UNIVERSITY OF
BIRMINGHAM

MECHANICAL PROPERTIES AND CHARACTERISATION OF SUBSTRATES FOR FLEXIBLE DISPLAYS

By

Konstantinos A. Sierros

A thesis submitted for the degree
of
Doctor of Philosophy

School of Metallurgy and Materials
The University of Birmingham
Birmingham, B15 2TT
United Kingdom

September, 2006

Abstract

This project is concerned with the electro - mechanical reliability and characterisation of ITO coated polyester substrates for use in touch screen and flexible display applications. Flexible display anode components such as ITO coated polyesters are common in almost all flexible display technologies.

However, these hybrid thin systems are unusual in mechanical terms. There is a mismatch between the mechanical properties of the inorganic coating and the organic substrate. It is therefore important to investigate the electromechanical response of such flexible anodes under various stress states and deformation modes. It is also important to develop new mechanical testing techniques for flexible displays.

Numerous experimental techniques were used in order to characterise and test the available ITO coated / uncoated PET and PEN substrates. Also, the development of new experimental mechanical testing methods, such as the biaxial 'bulge' apparatus, was undertaken.

During this work, various ITO coated polyester substrates were mechanically tested under uniaxial tension, controlled buckling and biaxial tension. In - situ electrical resistance monitoring and ex – situ atomic force microscopy, were used in order to detect and characterise ITO failure mechanisms. Tribological investigation of bare polyester substrates was undertaken. Preliminary nanoscratch and nanoindentation studies were also conducted on coated and uncoated systems.

Overall it was shown that ITO coated polyester flexible display electrodes can properly function up to relatively low strains. Electrical resistance generally does not recover during unloading in cyclic experiments. These factors currently limit the use of such components to slightly curved displays. Various ITO failure modes were observed, depending on the applied deformation mode. It was also shown, that the ITO adhesive failure is as critical as cohesive failure.

Acknowledgements

I would like to express my sincere thanks to my supervisor, Dr Stephen Kukureka for his support, invaluable discussions and constant encouragement during this project. His personal library was a constant source of useful books. During stressful times, he was always there to offer important advice.

Also, my sincere thanks are due to Professor Stuart Abell for his support and for fruitful meetings and discussions during this study.

In addition, I would like to thank Mr Frank Biddlestone for his outstanding technical support.

Furthermore, I am indebted to Professor Jim Hay because he was always available for important discussions.

Special thanks to my father, my mother and sister for their help, encouragement and financial support during the writing up stage.

Finally, I would like to thank Maria for her love and support during this work and particularly during the writing up stage.

" I know nothing except the fact of my ignorance "

Socrates

Contents

1. Introduction

1.1 The evolution of displays

The moment that Philo Farnsworth[1] first presented, in 1914, the idea for an electronic television to his high-school science teacher was the beginning of a new period, which can be characterized progressively through the years as a display-centric era. Displays can be defined as complex optical devices that render an image, graphics and text by electrically addressing small switching elements, which are called pixels. The display serves as an interface between human beings and machines[2].

Displays are present, in almost every part of our life, in the form of televisions, personal computers and mobile telephones to name but three. Their impact on our lives is high and display-users are becoming more familiar with new display applications. The first display technology, the cathode ray tube (CRT), is already more than a century old and technologies such as the thin active-matrix LCD, which is more than 25 years old, paved the path for future applications such as flexible flat-panel displays, as shown[3] in figure 1.1.

1.1.1: Flat panel displays

Flat panel displays, in general, consist of many different types of technologies. More specifically, they include, but are not limited to, glass-based panels that are mass-produced such as LCDs or plasma displays and display technologies, which are in an early production or development stage such as organic light-emitting diodes (OLEDs) or electrophoretic displays[4].

Industrialists and academics, worldwide, have covered much ground during the last few years, in research associated with different flat-panel display technologies. Electrochromic displays, for example, are discussed by Coleman et al who describe some initial attempts in pursuit of a simple economical method of mass-producing such displays[5].

Used purely as one illustration from many possible ones, and because it is an emerging technology with potential use of flexible components, the following considers the evolution of the flat panel OLED technology during, approximately, the last two decades.

In 1987 electroluminescence, at efficient levels, was first reported from an organic thin film at low drive voltage, and ten years later, after improvements in the efficiency and lifetime, OLEDs entered the commercial market competition, mainly with LCD displays, as monochrome emissive flat panels[6]. During the evolution of glass-based OLEDs many thin film materials and LED architectures, (figure 1.2), have emerged which led to OLEDs and the realization, in 2002, that organic electroluminescence is a viable display principle for a variety of applications[7]. Since then, rapid advances have been seen, both in materials and manufacturing, regarding thinner, lighter and higher-resolution flat panel OLEDs[8].

At this point, it is important, to note that flat panel displays are glass-based and hence flexibility, of any type, is not a display feature yet. However, right at the interface, between flat panel display and flexible flat panel display technology, stands touch-screen display technology. It is important, in display evolution terms, to inspect this particular technology before moving on to define and describe, flexible flat panel displays.

The resistive touch-screen, for example, as shown in figure 1.3, consists of a polymeric top-sheet and a bottom glass sensor; both are coated with a conductive coating, which are separated by dielectric spacers. When a current is applied to the top-sheet and a finger, or stylus, compresses the polymer film in order to contact the bottom glass conductive sensor, a controller detects the current flow to the four corners of the panel and calculates the position

of the finger or stylus. Touch-screens are becoming integral components of all display technologies[9].

1.1.2 Science and engineering of flexible flat panel displays

Continuing further with the resistive touch-screen example described in the previous section, a fundamental recognition arises, which subsequently evolves in order to shape the basis of a vital subject. This is the recognition that the polymeric thin touch-screen, topsheet component is compressed and hence deformed by an external force under service conditions. This leads to two kinds of display components: flexible display and non-flexible display components (which are both thin materials successfully assembled together in order to yield the final device).

Therefore, considering only flexible display components, a flat-panel display made using thin, flexible substrates, where the substrate can be bent to a radius of curvature of some centimeters without loss of key functional properties can be defined as a flexible flat-panel display[10].

The science and engineering of flexible displays[11], (figure 1.4), can be defined as a multidisciplinary, emerging, scientific and engineering field where physics, materials science and manufacturing technology converge.

1.2 Mechanical testing of display components

In order for flexible displays to become commercial, the mechanical issues involved when the display is stressed, or bent or generally deformed in service conditions have to be investigated experimentally. There are several test protocols that have been developed in this

work and in previous studies, as discussed in chapters 2 and 3. These experimental methods are mainly developed in order to test transparent conducting oxide (TCO) coated plastic display electrodes but they can also accommodate more complicated multilayer display flexible structures.

The flexible anode component is common to almost all display types[12] and therefore its mechanical behaviour, under different deformation modes and stress states, is of paramount importance. It is then apparent that investigating the mechanical performance of ITO coated polyester thin film electrodes serves as a general platform for the mechanical investigation of flexible displays.

Investigating the mechanics of flexible display anodes is also useful considering one-step roll-to-roll[13] processing of flexible displays. Roll-to-roll processing, as shown in figure 1.5, will be beneficial in the future because the fabrication technology for flexible displays is nowadays largely batch based and the move to a roll-to-roll process will reduce capital equipment costs, reduce display part costs, significantly increase throughput and eliminate component supply issues[14]. During roll–to–roll flexible display manufacturing the display materials will certainly undergo mechanical deformations under different stress states.

Identifying and simulating, in experimental terms, the different deformation modes and stress states during manufacturing and in service conditions is a major challenge, which is critical for commercialization of flexible display devices.

1.3 Other important properties of flexible display anode components

Flexible display anodes are usually two - material systems consisting of an inorganic TCO layer such as indium tin oxide, (ITO), and an organic flexible base substrate, on to which the ceramic conducting layer is deposited, such as polyethylene terepthalate, (PET), or polyethylene napthalate, (PEN). Such a hybrid system is unusual in terms of mechanical

properties since the conducting layer is brittle and the polymer substrate is both flexible and ductile.

There are also other important properties that directly, or indirectly, influence the flexible anode performance during service. These properties, which in most cases are interrelated, are summarized[15] in figure 1.6 and some of them, such as roughness and residual stress, are a result of the coating deposition on the polymer base substrate, process whereas some others are a result of the polymer substrate manufacturing process. The application of external forces in order to flex the display can cause cohesive and adhesive failure of the display anode component.

The tribological behaviour of the uncoated polyester surface and / or the ITO conductive surface is also important for the use of the polymer as a display top – sheet and for the adhesion of the ITO on to the polymer.

Therefore, in addition to the mechanical properties, tribological properties of display components as well as deposition methods, (physical or chemical), of conductive layers on base polymer substrates have to be synergistically investigated in order to understand flexible flat panel display behaviour during manufacturing and in service conditions.

1.4 Aim of this work

The primary aim of this work is to investigate the mechanical properties and functional reliability of ITO-coated (magnetron-sputtered) polyester substrates that are used as anodes in display and touch – screen applications. The present study aims to form a solid foundation for further research in this exiting new interdisciplinary field.

1.5: The scope of this project

The topics covered in this work are:

1. Reports on previous experimental and theoretical investigations related to this project.
2. General characterization of the ITO and / or polyester material properties such as crystallinity, adhesion and microstructure.
3. Preparation of ITO on polyester substrates by pulsed laser deposition (PLD) at room temperature, as an alternative to magnetron sputtering.
4. Development of new mechanical testing methods for flexible display components.
5. Investigation of the electro - mechanical behaviour of commercial ITO (sputtered on, polyester thin film anodes) under different deformation modes and stress states.
6. Investigation of the tribological behaviour of, mainly, the bare polyester substrates.

1.6: Structure of the thesis

The remaining chapters are organized as following:

Chapter 2 is an account of essential theoretical elements and previous experimental investigations mainly on coating / substrate thin systems for technological applications. More specifically, mechanical properties and failure processes, of thin composite systems, under various stress states and deformation modes, for example uniaxial tensile coating fragmentation, are mentioned. In addition, an introduction to polyesters is given with particular attention towards the production and characterization of PET and PEN films used in display applications.

Also, friction and wear of polymeric materials in general and of polyesters, mainly PET, in particular are reviewed. Furthermore, a review of transparent conducting oxides, mainly ITO film is conducted. Preparation methods including pulsed laser deposition and sputtering are

reviewed. Finally, this chapter includes some bulge-test background information as well as a review of bulge theoretical models used in order to extract thin-film mechanical properties such as biaxial modulus and initial stress.

Chapter 3 gives details of the materials used in this project. A wide range of experimental methods used in this study is also mentioned. Experimental development such as bulge testing of circular thin films and electromechanical testing of display anodes is described.

Chapter 4 is a description of results regarding general characterization of polyester substrates and / or ITO thin layers. Particular attention is directed towards surface characterization of the coated thin system, by contact mode AFM. Electrical and optical characterization of the ITO films is reported. Also, microstructural characterization of the ITO coating, by X – ray diffraction, is mentioned. Surface adhesion of different polyester substrates is covered. Finally, in-house preparation of ITO films on PEN substrates at room temperature is reported.

Chapter 5 is dedicated to electro–mechanical testing, under various stress states and deformation modes, and bulge test results. Monotonic and cyclic loading conditions are employed in order to investigate possible failure modes for thin flexible display anode components.

Chapter 6 is, mainly, related to tribological experimental results regarding the polyester substrates. Pure sliding, unlubricated conditions are employed by means of a pin – on – disc wear and friction tester. The polyester flat slides against a steel ball counterface. Also, scratch and Knoop hardness indentation results, for coating and / or substrate combinations, are reported.

Chapter 7 is a summary and a discussion of the most interesting results reported in the last three chapters. The chapter is divided into three parts. The first part is a discussion of the results obtained in chapter 4. The second part deals with the results obtained in chapter 5 and the third part with the results from chapter 6.

Chapter 8 gives some interesting conclusions obtained from this project. At first, conclusions regarding chapter 4 are drawn. Then, concluding remarks considering chapter 5 are mentioned. Also, conclusions regarding results obtained in chapter 6 are reported. Finally, some general conclusions from the flexible flat panel displays point of view are drawn.

Chapter 9 contains proposals regarding further work and development for this project. Some important recommendations for future, mainly experimental, work are highlighted.

2. Essential theory and previous experimental investigations

2.1 Introduction to polyesters

Thermoplastic polyesters are not, by any means, the largest group of commercially available synthetic polymers but they enjoy a leading market position because of their wide range of application[16].

The three principal members of the polyester family are polyethylene terephthalate (PET), polybutylene terephthalate (PBT) and polyethylene napthalate (PEN). PBT is not used in flexible display assemblies and it will not be discussed further.

Polyesters can be prepared, on a laboratory-scale, by polycondensation reactions such as direct esterification of alcohols with carboxylic acids, polyaddition such as reaction of diacids with diepoxides and chain polymerization with ring opening polymerization being an example[17].

However, there are certain fundamental differences between laboratory and industrial, large-scale, production of polyesters. For example a laboratory based polycondensation process examines whether the reaction can occur at all and what is the possibility that a polymeric material of useful average chain length can be produced. This is not the case for industrial processes that yield large amounts of material[18].

Market applications involving polyester materials, mainly PET, include fibres as textile filament yarn for clothing and tyre reinforcement. In the form of film, commercial uses of PET include food packaging, blow-moulded bottles for carbonated beverages, photographic films and magnetic tapes[19]. Recent commercial interest in PET and PEN films is shown by the flat-panel display industry where they are used as base substrates in thin display assemblies.

2.1.1 Production of PET and PEN thin films

The first polyester material, which was commercially available, was PET, figure 2.1, produced by reacting together terephthalic acid or dimethyl terephthalate as the diacid moiety with ethylene glycol as the dialcohol moiety. The original patent describing PET as a material, was filed in 1941 by Calico Printers Association[20]. As mentioned before, the first application was polyester fiber but recent applications such as magnetic tapes and displays require the use of semi-crystalline polyester thin films as a base substrate.

A sequential drawing process, figure 2.2, consisting of four steps, produces PET and PEN films, less than 180 μm thick. The first step, with the process temperature set above the glass transition temperature (T_g), is melt extrusion through a slot die and quenching to form an amorphous precursor film. Then, on-line drawing with respect to the machine direction (MD) is performed. The third step includes on-line drawing in the transverse direction (TD) and as a final step, on-line heat setting is conducted. Reheat of film above 80 °C takes place during the first three steps. Strain induced crystallization of up to 40-50%, can be achieved[21] during the second and third step of the process as discussed later. It was only 1973 that PEN, figure 2.3, became commercially available from Teijin Ltd., Japan[22].

2.2 Comparison of fundamental properties of PET and PEN related to display manufacturing

2.2.1 Melting and glass transition temperatures

The microstructure of polymeric materials can pass through two or more different states as the temperatures changes. The main transition temperatures are the glass transition temperature, T_g, and the crystalline melting, T_m, temperature.

In the case of PET, figure 2.4 shows the changes in its state with temperature[23]. From –200 °C to 78 °C the state is glassy and can be crystalline whereas from 79 °C to 265 °C the material may have crystallites and the amorphous matrix is a rubbery solid. From 266 °C to 323 °C the polymer becomes a liquid and from 324 °C up to 400 °C the polymer decomposes. The first transition of the amorphous material from glassy to rubbery solid is associated with the T_g and the second transition of the crystalline material to liquid is associated with the melting temperature, T_m.

Comparing glass and melting temperatures of PEN and PET one discovers the superiority of PEN values as opposed to PET. The glass transition of PET is 78 °C whereas the PEN value for glass transition is 120 °C. The melting temperature of PET is 265 °C whereas the T_m of PEN is approximately 274 °C. Therefore, PEN enjoys a higher (42 °C difference), Tg and a slightly higher T_m as compared to PET.

2.2.2 Optical properties

As discussed by MacDonald et al[24] the optical clarity of the polyester display film is vital, in the case of bottom-emissive displays, and typical requirements include total light transmission above 85 % in the 400 - 800 nm wavelength range coupled with a haze of less than 0.7 %. Both PET and PEN films exhibit a total light transmission above 85 % in the range of 400 – 700 nm. Their haze is also less than 0.7 %.

2.2.3 Dimensional stability

As discussed previously, polymer films undergo variable changes in their states at T_g. They undergo a change in physical and mechanical properties at T_g. However, for display manufacturing, the issue of primary importance is the control of the film dimensional

stability as it is cyclically loaded in temperature[24]. Dimensional stability is affected by film shrinkage, or expansion.

The dimensional stability of PET and PEN films can be altered by a heat stabilization method. The percentage of shrinkage is the percentage change of film dimension in a given direction before and after heating[25]. Heat stabilized PEN film exhibits minimal shrinkage, lower than 0.1 %, when exposed to temperatures of up to 180 °C for 30 minutes. On the other hand, PET film exhibit minimal shrinkage up to 150 °C.

2.2.4 Moisture and solvent resistance

During flexible display manufacturing, polyester substrate resistance to solvents and chemicals represent a real issue. Both PET and PEN exhibit good resistance to solvents such as ketones, alcohols and acids amongst others. However, resistance to alkalis is good for PEN but fair for PET. PET and PEN both typically absorb 1400 ppm at equilibrium[24] - the exact values depends on temperature and relative humidity.

2.3 Crystal structure and morphology of polyester films

2.3.1 Crystal structure of PET

When PET is melted and then quenched rapidly, it forms an isotropic amorphous solid. If annealed above the crystallization temperature, 140 °C, crystallization occurs when the material is drawn or slow cooled from the melt.

The crystal structure of PET was first investigated by Daubeny et al[26] who determined that the unit cell was triclinic and that it contains one chemical repeat unit of the monomer and dimensions a = 0.456 nm, b = 0.594 nm and c = 1.075 nm and angles $\alpha = 98.5^{\circ}$, $\beta = 118^{\circ}$ and $\gamma = 112^{\circ}$ as shown[27] in figure 2.5. Using these dimensions, the density of the crystalline material can be determined to be 1.455 g/cm^3.

2.3.2 Crystal structure of PEN

As in the case of PET, PEN can be quenched to the glass state and crystallization can occur from the glass by annealing or by slow cooling from the melt. A triclinic unit cell can describe the crystal structure[28] of PEN with one chemical repeat unit of the monomer and dimensions a = 0.651 nm, b = 1.575 nm and c = 1.32 nm and angles $\alpha = 81.33^{\circ}$, $\beta = 144^{\circ}$ and $\gamma = 100^{\circ}$ as shown[29] in figure 2.6. Using these dimensions, the density of the crystalline material can be determined to be 1.407 g/cm^3.

2.4 Morphology of semi-crystalline polyesters

The most common morphology[30] of semi-crystalline polyesters, such as PET and PEN that is observed with the aid of an optical microscope is the spherulitic one as figure 2.7c indicates. Spherulites are polycrystalline features with variable size ranging from several μm to several mm. The differentiation between amorphous and crystalline regions can be achieved by using high-resolution transmission electron microscopy, TEM. By using TEM it is possible to observe lamellae that are grouped in stacks embedded in the interstack amorphous material, as figure 2.7b shows. The lamellar stacks contain crystalline and amorphous regions as shown by figure 2.7a.

2.5 Orientation and drawing of polyester films

Molecular orientation and drawing, either uniaxial or biaxial, are of primary importance for the production of polyester films. As discussed by Ward[31], the changes in orientation and molecular conformation, for both crystalline and amorphous polyesters, which take place during drawing and annealing, govern the structure of the final oriented product.

The importance of the molecular orientation in determining the mechanical properties of the polymer is of paramount importance. Several spectroscopic techniques for the measurement of molecular orientation are possible. In order to define orientation it is essential to imagine a partially oriented polymer as an aggregate of units of structure. The orientation of each unit can be associated with three angles θ, φ, ψ. The orientation of the polymer is then described by an orientation distribution function $\rho(\theta, \varphi, \psi)$. As the polymer is drawn, preferred orientation of the molecular chain axis is described by $\rho(\theta)$, where θ is the angle between the chain axis within one unit and the draw direction. Equation 2.1 gives the orientation functions.

$$\left\langle P_n(\cos\theta) \right\rangle = \int_0^{\pi} \rho(\theta) P_n(\cos\theta) \sin\theta \, d\theta \qquad (2.1)$$

Where P_n is defined by Jarvis et al[205] and Everall et al[37].

De Vries et al[32] reported experimental results on uniaxial and biaxial orientation of polymer films and sheets under well-defined conditions of temperature and elongational strain rate. They concluded that as long as the degree of crystallinity remains relatively low, the mechanical behaviour of oriented semicrystalline polymers appears to be mainly determined by orientation in the amorphous regions. They also noted that not only the mechanical behaviour of polymer films but also other physical properties, such as transparency and thermal properties, are affected by the amount of uniaxial or biaxial orientation.

Biangardi and Zachmann[33] stretched amorphous PET samples at different temperatures, with different rates and stretching ratios. The samples were afterwards crystallized. They found that the stretching ratio generally does not characterize the orientation state. They also observed that the structure obtained after crystallization depends mainly on the birefringence of the samples after stretching and before crystallization. Stretching influences the conformations of the polymer chains in the non – crystalline regions of the sample. They concluded that the improvement of PET mechanical properties is not only a result of the increasing orientation but also a result of the increasing amount of taut tie molecules, which have relatively large end – to – end distances.

Cakmak and Lee[34] experimentally investigated the molecular mechanism, which is responsible for neck formation in the case of uniaxially stretched PEN films. They stretched the films between the glass transition temperature and the cold crystallization temperature and they observed that films exhibited necking. The molecular mechanism causing neck formation is associated with the highly localized cooperative orientation of flat naphthalene groups parallel to the film surface.

Kim et al[35] reported on the effect of composition on orientation, optical and mechanical properties of biaxially drawn PEN films. They found that the refractive indices, in the normal direction of the biaxially stretched films, decreased with increasing draw ratio. They attributed the latter to the orientation of naphthalene planes, which become parallel to the film surface as the draw ratio increases. More interestingly, they tested (in uniaxial tension) biaxially oriented PEN films in five different directions with respect to the film plane. The films were stretched 4 times in the machine direction and 1, 2, 3, 3.5, 4 times respectively in the transverse direction. They found, as figure 2.8 indicates, that moduli in all directions increase as the transverse direction stretch ratio increases.

Cole et al[36] demonstrated that it is possible to characterize the orientation in both uniaxially and biaxially oriented PET films by measuring front – surface reflection infrared spectra with polarization in two mutually perpendicular directions which can be the machine and

transverse directions respectively. They reported that the ratio of the complex ester band at 1330 – 1240 cm^{-1} with respect to the carbonyl band at 1729 cm^{-1} can be used in order to determine the orientation function.

A comprehensive account on measuring orientation of uniaxially and biaxially drawn PET films was given by Everall et al[37,38]. They used attenuated total reflection (ATR) infra – red, (IR) dichroism in order to measure surface orientation. This method is important since the birefringence of the film can be neglected. They showed that even simple systems such as uniaxially drawn films can display significant orientation gradients and biaxial orientation.

Finally, Goschel[39] reported on the structure development and mechanical behaviour during multistep uniaxial drawing of PET at pre – set temperatures. It was concluded that a strong increase of elastic modulus with increasing draw ratio exists. The modulus increase is related to a perfect alignment of the crystallites combined with the formation of taut tie molecules.

2.6 Indium tin oxide and display applications

As discussed by Paine et al[40], for display applications, indium, tin doped, oxide materials, in the form of thin films, are almost exclusively used due to their superior combination of environmental stability, relatively low electrical resistivity, (1 to $3*10^{-4}$ Ω cm), and high transparency, (> 90%), to visible light. In display applications, the basic function of ITO is as a transparent electrode. ITO is a member of the transparent conducting, wide – bandgap, oxide TCO family.

The role of dopant, tin in the case of indium oxide, is very important[41] and for example ZnO:Ga films have shown higher performance levels than previously obtained, with resistivities of about 10^{-4} Ω cm.

Although indium tin oxide, ITO, was first made by spray – pyrolysis, sputtering has become the preferred mode for its production. ITO may be preferred for deposition on thermally sensitive substrates, such as polyesters, whereas Cd_2SnO_4, for example, requires refractory substrates in order to develop its best properties[42].

The choice of sputter machine and geometry is dependent on the desired display application. Roll – to – roll polymer coating, typically with PET, has reached a commercial level with rolls up to 7 feet wide. However, low substrate temperatures and high deposition rates severely limit the quality of the as-deposited ITO by reducing the efficiency of the dopant[43].

In touch – screen applications for example, the overall sheet electrical resistance is not as important as its long term stability, since the resistance is used in order to map the vertical and parallel coordinates on the surface of the screen. If the resistance is not stable, in the long term, in any part of the screen, the contact position will appear to shift[44].

As recently summarized by Paine[45], flexible display device designers who wish to use temperature-sensitive polymer substrates must make do with the 5 to $7*10^{-4}$ Ω cm available from amorphous ITO until an alternative TCO becomes available or until new flexible substrate materials, which can withstand elevated temperatures, become available.

2.6.1 The sputtering process

In the sputtering process[46], as shown in figure 2.9, the positive gas ions, which are produced in a glow discharge, bombard the target material and dislodge groups of atoms which then pass into the vapour phase and deposit on to the substrate. The gas pressure of the glow discharge lies between 20 to 150 mTorr and the gas ions are usually argon ions. The deposition rate, for the sputtering process, varies between 2.5 to 1000 nm / min.

There are several sputtering systems[47] including dc diode and rf diode sputtering system as well as cylindrical magnetron and planar magnetron. In magnetron sputtering a magnetic field is superposed on the cathode and glow discharge producing an electron-trapping effect which in turn increases the collision rate between the electrons and sputtering gas molecules. This is crucial because it enables the lowering of the sputtering gas pressure as low as 10^{-5} torr.

In historical terms the first to report the magnetron sputtering process was Penning[48] in 1936. Therefore it is an old and well-established process for depositing thin metallic and ceramic thin layers on various substrates. Kukla[49] gave an interesting overview of the magnetron sputtering on large-scale substrates. He underlines that the advantages of magnetron sputter deposition include:

- The ability to deposit all kinds of metals and ceramic oxides with precise control of film composition and structure.
- The ability to deposit metal oxides, metal carbides and metal nitrides with precise control of the thin coating stoichiometry.
- The extremely high thickness uniformity, less than 2 % variation, that can be achieved even when using large substrate areas of 3.2 * 6 m size.

2.6.2 Preparation of ITO by sputtering

Minami et al[50] reported the preparation of very thin ITO layers on PET and glass substrates by DC magnetron sputtering. The oxide films that were prepared, at 60 °C, were initially amorphous and became crystalline when annealed at a temperature of 150 °C for 25 hours in air. The resistivity, of the ITO on PET films, is dependent on the SnO_2 content and is of the order of 10^{-3} Ω cm. An average transmittance above 97 % in the visible wavelength range was measured.

Kulkarni et al[51] studied the electrical optical and structural characteristics of ITO thin solid films that were deposited on glass, PET and PC substrates using the rf diode sputtering method. They found that sheet resistances for the ITO on PC films were at least an order of magnitude higher than those ITO films on glass substrates. However, when the ITO, on PC, films were annealed, for 1 hour at 100 °C, their sheet resistances decreased by 50 %. X-ray diffraction studies indicate polycrystalline films with grain orientations along (222) and (400) directions. Using TEM microscopy they observed two distinct regions of growth. The first region is characterized by a dense growth close to the substrate and a light growth away from the substrate. The growth is vertical, columnar and rod shaped. They finally observed that the type of the substrate and the annealing parameters used influence the sheet resistance, the grain size and the grain orientation.

The dependence of the sheet resistance of ITO thin films on grain size and grain orientation was studied in detail using X-ray diffraction[52]. The ITO films were deposited on glass, PET and PC substrates. A key finding indicates that larger grain sizes, almost 25 nm, in ITO films result in lower sheet resistance, 250 Ω / □, and high optical transmission, 86.7 %, at a wavelength of 550 nm.

Fahland et al[53,59] proposed a solution, in order to deposit low resistivity ITO on plastic at ambient temperatures, which includes the substitution of the single ITO layer by a more complicated three layer architecture consisting of ITO / Ag / ITO. They used a pilot roll sputter roll coated system and achieved films with sheet resistances below 16 Ω / □ at a transmittance over 80 % for a wavelength of 550 nm.

Shin et al[54] investigated the properties of dc magnetron sputtered ITO on polymeric substrates at room temperature. The polymer substrates were PC, acrylic, PET. Glass substrates were also used. The lowest resistivity value, for 1 mTorr of oxygen pressure, is 9.3 * 10^{-4} Ω cm on the PC substrate. The optical transmittance at visible wavelength, 550 nm, is 85 %.

Franz et al[55] characterized rf sputtered ITO layers on glass for substrate temperatures between 100 and 550 °C. The lowest resistivity was 2 * 10^{-4} Ω cm and achieved at a

temperature above 450 °C. The optical transparency was as high as 90 % in the wavelength range between 550 and 800 nm.

Henry et al[56] compared the structural and gas barrier properties of aluminium oxide and indium tin oxide coatings deposited on PET substrates by the dc reactive sputtering method. They found that both composite thin structures exhibited good resistance to water vapour transmission. They also observed that the ITO coating was significantly more effective as a gas barrier than the conventional aluminium oxide layer. Finally, they found, by using SEM and AFM, that the ITO layers featured smaller defects than the aluminium oxide films.

Sasabayashi et al[57] studied the microstructure of ITO, IZO and GZO films deposited by rf and dc magnetron sputtering on unheated glass substrates for various background pressures. They found that ITO films deposited at low pressures were polycrystalline whereas amorphous films have been deposited at high background pressures.

Hoshi and Kiyomura[58] used a novel kinetic energy controlled sputter deposition method in order to deposit ITO films on glass substrates at low temperatures, below 50 °C. They concluded that ITO films having resistivity as low as $3.5 * 10^{-4}$ Ω cm and average roughness, R_a, as low as 0.15 nm can be produced at low, 50 °C, temperature and low, 100 V, voltage

.

Yeom et al[60] reported on the effect of oxygen stoichiometry on the amorphous structure and crystallization kinetics of ITO on glass initially at room temperature and then annealed in air at 250 °C using reactive dc magnetron sputtering. They observed using bright field TEM, figure 2.10, that initially the material is in the amorphous state and then, after 5 min annealing at 250 °C, becomes partially crystalline. For 10 min annealing at 250 °C the ITO film is becoming more crystalline and after 30 min of annealing at 250 °C is fully crystallized.

Kim[61] prepared ITO thin films on PET using dc magnetron sputtering, using a negative metal ion source, at low substrate temperature. By varying the partial pressure he found that at low pressures the resistivity reached a value as low as $6.2 * 10^{-4}$ Ω cm and optical transmittance

of 87 % at a wavelength of 550 nm. AFM investigation of the ITO surfaces revealed a roughness range of values between 1.1 and 2.8 nm.

Carcia et al[62] compared the electrical and structural properties of ITO and indium oxide, IO, films deposited on polyester PET substrates by rf magnetron sputtering at room temperature. They measured minimum resistivity, for both ITO and IO films, of approximately $3 * 10^{-4}$ Ω cm. They also observed that both layer types had very similar structural properties. More specifically, they observed using TEM that crystalline features only formed on the layer surface and not through – out the film thickness. Using AFM they observed very fine surface features, approximately 30 nm in size. The AFM measured ITO roughness was 1.2 nm.

Qiao et al[63] prepared polycrystalline ITO films, with thickness varying between 40 nm and 1.7 μm, by direct current magnetron sputtering at 300 °C substrate temperature. They observed, using X-ray diffraction, that the thicker films, above 0.4 μm, exhibited similar texture of crystalline orientations whereas thinner films did not. The thicker films had also lower resistivities than their thinner counterparts although all the films were deposited at a high, 300 °C, temperature.

Wong et al[64] used a radio-frequency sputtering deposition method in order to grow ITO on unheated PET. The optimal ITO films had a transmittance of over 90 % in the visible range, 400 – 700 nm, and a resistivity of $5 * 10^{-4}$ Ω cm. They noted that at the initial stage of film formation, below 60 nm of thickness, the electrical conduction was provided by the limited connection between the ITO islands. As the film thickness increases the islands gradually coalesce and the film becomes continuous. At a film thickness of 120 nm a partially crystalline structure is observed. However, the crystalline behaviour is not maintained for thicker, 250 nm, ITO films because of the low deposition temperature.

Meng et al[65] deposited ITO films directly on glass-based colour filters, using dc magnetron sputtering at room temperature. The resulting thin structures can be used potentially in LCD and OLED display applications. The polycrystalline ITO films exhibited low, $2.2 * 10^{-4}$ Ω

cm, resistivity and very high, 96.7 %, optical transmission at 530 nm wavelength. They measured the ITO grain size to be 90 nm, using X-ray diffraction.

Finally, Guillen and Herrero[66] have compared the structure, morphology and electro – optical characteristics of ITO films grown on glass and PET substrates using rf magnetron sputtering at room temperature. It is observed that the sheet resistance, for optimal sputtering conditions, is lower, 7 Ω / □, for the ITO on PET than that of PET on glass. The optical transmittance in the visible range is the same, 85%, for both ITO on PET and ITO on glass.

2.6.3 ITO deposited by pulsed laser deposition

In an informative table[67] of the history of processes for making transparent conductors, Gordon suggests the deposition of Cd_2SnO_4 by pulsed laser ablation dates back to 1995. However, considering ITO films deposited by PLD, 1993 was the year that ITO films were grown by pulsed laser deposition on glass substrates.

At optimized oxygen pressures[68], films with resistivity values of $1.4*10^{-4}$ and $5.4*10^{-4}$ Ω cm were deposited at substrate temperatures of 310 and 20 °C, respectively. The optical transmission of the, 180 nm thick, ITO films were nearly 100% for the wavelength range of 600-800 nm.

Sun et al[69] studied the initial growth of ITO on glass substrates using the PLD method. They reported that a transition from a 3D island growth at low temperatures to 2D growth at higher temperatures exists. The critical temperature for the transition is around 150 °C. It is also interesting to note that the growth transition temperature coincides with the transition from amorphous to polycrystalline microstructure of the thin layers. The room temperature PLD method was applied in the case of ITO films on organic substrates and the lowest resistivity values obtained were of the order of ~ $4*10^{-4}$ Ω cm.

The relationship between electrical/optical properties of the film and the material stoichiometry was investigated[70] using Rutherford backscattering. Adurodija et al[71] have studied the PLD deposition of ITO films, between room temperature and 200 °C, using a glass base substrate. They obtained films with resistivity of ~ $3*10^{-4}$ Ω cm and transmittance, in the visible spectrum, above 87% for a narrow range of oxygen pressure of 10-15 mTorr. They also found that the films prepared below 100 °C were amorphous, while at a temperature above 150 °C the ITO thin films were polycrystalline. This last observation coincide with the observation made by Sun et al[69].

Yamada et al[72] studied the effect of He background gas on PLD deposition of indium oxide films on glass substrates at room temperature. They concluded that stoichiometric crystalline In_2O_3 films with excellent optical properties can be prepared at He background pressures higher than 1000 mTorr without the introduction of oxygen background gas.

Teghil et al[73] deposited ITO films on Si (100) substrates, for a temperature range of 25-700 °C, in an oxygen atmosphere using reactive pulsed laser ablation. They used an ICCD camera in order to image the plume under vacuum and gas background oxygen pressure conditions and they observed that the gas cloud is constrained in a smaller volume in the presence of an oxygen atmosphere.

Kim et al[74] studied the effect of target composition, substrate deposition temperature, background gas pressure and film thickness on the structural, electrical and optical properties of ITO films grown on glass substrates by PLD. They reported that the resistivity of ITO films, at room temperature, is $4*10^{-4}$ Ω cm at a background oxygen pressure of 10 mTorr. The average transmission in the visible range was 85%. Increasing the temperature to 300 °C the resistivity decreased to $2*10^{-4}$ Ω cm and the average transmission in the visible range increased to 92%. Kim et al[75] deposited, by PLD, high-quality ITO films on glass substrates without post-deposition annealing. The parameters of their experiments as well as the results and conclusions are the same as in reference[74].

Adurodija et al[76] have compared the properties of ITO films grown, by PLD, on glass and silicon substrates for temperatures ranging from room temperature up to 350 °C and oxygen background pressures from 0.75 – 50 mTorr. At room temperature and 9.75 mTorr of oxygen pressure they obtained films of resistivity $4.5*10^{-4}$ and $4.8*10^{-4}$ Ω cm for glass and silicon substrates respectively. They also confirmed that films deposited below 150 °C were amorphous, independently of the substrate used, while at temperatures above 150 °C crystalline films were obtained on both substrates. Adurodija et al[77] have also studied the influence of substrate temperature on the properties of indium oxide thin films. They deposited, using a PLD system, pure indium oxide and tin-doped indium oxide films on glass at different substrate temperatures ranging from room temperature up to 350 °C. They found that at low substrate temperatures, from room temperature up to 100 °C, pure indium oxide films yielded the lowest resistivity of $1.8\text{-}2.5*10^{-4}$ Ω cm and the resistivity increased sharply with an increase in temperature, above 100 °C. For the tin-doped indium oxide films, the resistivity decreased from $3.5*10^{-4}$ to $1.3*10^{-4}$ Ω cm with increasing temperature from room temperature up to 350 °C. Using atomic force microscopy they measured a minimum average surface roughness, 1.3 nm, for the films deposited at room temperature and above 200 °C.

In addition, Adurodija et al[78] investigated the effects of stress on the structure of indium tin oxide thin films grown by pulsed laser deposition. They used grazing incidence x-ray diffraction in order to investigate the microstructure of ITO films formed on a glass substrate at 200 °C and oxygen background pressures ranging from 0.75-20.25 mTorr. At low oxygen pressures significant changes in the film lattice constants occur when the thickness is larger than 150 nm. The splitting of the X-ray peaks only occurred in the 'bulk' of the films, while near the surface, single peaks were evident, indicating the existence of two layers.

Kim et al[79] investigated the effect of substrate deposition temperature and oxygen partial pressure on the structural, electrical and optical properties of transparent conducting indium tin oxide thin films grown by PLD on flexible polyethylene terephthalate (PET) substrates. They concluded that ITO films, 200 nm thick, deposited on PET at room temperature and oxygen partial pressure of 45 mTorr, exhibit low electrical resistivity, ~ $7*10^{-4}$ Ω cm, and high optical transmittance, ~ 87%, in the visible, 400-700 nm, range.

Izumi et al[80] examined the relation between electrical and structural properties of ITO films prepared by PLD with and without in situ laser irradiation. They estimated the residual stresses present on the films after deposition by using grazing incidence asymmetric Bragg and grazing incidence x-ray diffraction geometries. The films prepared with in situ laser irradiation showed very low resistivity, less than 10^{-4} Ω cm, which can be attributed to high crystallinity and low residual stress.

Adurodija et al[81] have also studied the effect of laser irradiation on the properties of indium tin oxide films deposited at room temperature, by PLD, and oxygen pressures ranging from 0.975 to 50 mTorr. Crystalline films with (111) preferred orientation were observed at all oxygen pressures, except for the 0.975 mTorr pressure. Minimum resistivities of $1.2*10^{-4}$ and $2.3*10^{-4}$ Ω cm were obtained on the laser irradiated and the non-irradiated parts of the deposited films respectively. They concluded that the low resistivity for the laser-irradiated part of the films was a consequence of both the high carrier concentration and Hall mobility of the films.

Suzuki et al[82] used a 5 wt.% SnO_2 dopant in order to deposit ITO on glass substrates by PLD. They observed that the lowest resistivity, $8.45*10^{-5}$ Ω cm, exists at a substrate temperature of 400 °C and an oxygen background pressure of 75 mTorr. The average surface roughness of their films, measured by AFM, was 1.26 nm.

Morales-Paliza et al[83] have explored the mechanisms of oxygen incorporation in ITO films deposited on graphite at room temperature by PLD. They concluded that the high oxygen component incorporated from the background gas suggests that not only is there direct incorporation of the oxygen gas into the plume via chemical reactions, but also there is exchange between target oxygen and gas oxygen.

Cracium et al[84] used in-situ ultraviolet-assisted PLD in order to grow ITO films on Si substrates in the range of temperatures of 50 °C up to 150 °C. They obtained root mean square roughness values below 0.5 nm. Fang et al[85] reported the effect of laser deposition

parameters on the resistivity and strain sensitivity in the case of ITO films deposited on glass. They concluded that ITO films exhibited a stable, hysteresis-free piezoresistive response. Annealing in a nitrogen atmosphere produced no significant change in piezoresistive response.

Izumi et al[86] have studied the electrical properties of crystalline ITO films prepared at room temperature by in situ laser irradiation PLD on polycarbonate substrates. They found that the polycarbonate substrates were coloured by in situ laser irradiation when the ITO layers were prepared on the substrates directly and therefore they pre-deposited a layer of Al_2O_3 and a layer of CeO_2 in order to prevent the colouring and achieve a low resistivity.

Choi et al[87] reported on the properties of ITO films fabricated on glass by PLD. Under an oxygen pressure of 20 mTorr, the lowest resistivity of $9.55*10^{-5}$ Ω cm was obtained for layers deposited at 500 °C. The transmittance of the films was about 80% at 20 mTorr pressure. Morales-Paliza et al[88] used nitrogen as background gas in PLD growth of indium tin oxide films, on graphite substrates, at room temperature. They found that the most conductive and transparent films incorporate nitrogen from the background and the amount of the nitrogen content in the films is related to the electron carrier concentration, which suggests that the embedded background gas favours the creation of oxygen vacancies.

Cracium et al[89] used PLD and ultraviolet PLD in order to grow ITO layers on Si and glass substrates at low temperatures, 40-180 °C. X-ray photoelectron spectroscopy showed uniform 'bulk' composition and minimal Sn segregation at the layer surface. Films deposited at temperatures lower than 70 °C were amorphous and exhibited high carrier mobility and low resistivity values.

Kim et al[90] investigated the effect of the oxygen pressure and the deposition temperature on the electrical and optical properties of the Sn-doped ITO films on quartz glass substrates by PLD. They obtained films of low resistivity, $2.49*10^{-4}$ Ω cm, and high optical transmission, 88% at 550 nm, at an oxygen background pressure of 10 mTorr and substrate temperature of 150 °C.

Lin et al[91] studied the changes in surface roughness and work function of ITO films due to KrF excimer laser irradiation. They concluded that the laser irradiation not only led to an increase in the surface work function, but also resulted in the reduction of root mean square roughness. This finding can be proved useful for enhancing the performance of organic light-emitting devices.

2.7: Mechanical properties of thin composite systems

2.7.1: Channelling crack process

There are several reviews on the mechanical properties of thin films. In 1987, Hardwick[92] wrote a comprehensive article on the mechanical properties of free-standing films. It should be noted that there are two distinct situations when considering mechanical properties of thin films. In the free-standing film case, both surfaces of the material are free and the mechanical behaviour is influenced only by the intrinsic properties of the film itself. In the second situation the film is deposited on to a substrate and therefore the stress is transmitted to the film by virtue of its adhesion to this substrate. In this work the second case is considered.

As figure 1.6 shows, there are numerous factors[15] that affect the mechanical reliability of the thin composite structure. These factors can be categorised as surface layer factors, 'bulk' film factors, film-substrate interface factors and polymer substrate factors that are interrelated. Regarding the surface of the coating the most notable properties are roughness, electronic properties and frictional characteristics. For the 'bulk' of the coating layer, the deposition-induced residual stress plays an important role. The cohesive and adhesive properties of the film are influenced by the interface quality as well as the roughness of the polymer substrate and its viscoelastic properties amongst other factors.

An interesting article, regarding cohesive and adhesive thin layer properties, written by Suo[93] describes a possible failure mode when a brittle film, thickness h, is under tension. The failure mode is cracking, cohesive failure, in the film. Starting from a surface flaw A, as shown in figure 2.11, in the film, a crack, B, runs across the film thickness as well as elongating laterally in the film until it meets a film edge or another crack. The type of such crack is termed as channelling crack. The crack morphology is somewhat difficult to quantify and some qualititative and semi-quantitative information, using contact-mode AFM, will be presented in the experimental section.

Furthermore, Hutchinson and Suo[94] give a broad summary of the fracture of thin-layered materials. Topics covered include mixed mode fracture, elasticity solutions for cracks in multilayers, laminate fracture test, cracking of pre-tensioned films, buckle-driven delamination of thin films, blister tests and failure modes of brittle joint and sandwich layers. In particular, the cracking processes and patterns of films, attached to dissimilar, in mechanical terms substrates, subjected to tensile or compressive external stresses, with appreciable levels of residual stress, are of great importance for the present research as well as buckle-driven delamination. The elastic mismatch between a soft organic substrate and a brittle inorganic layer, which underlines their difference in mechanical properties, is described by the Dundurs parameter α, equation 2.2 below.

$$\alpha = (E_c - E_s)/(E_c + Es) \qquad (2.2)$$

Where E_c is the elastic modulus of the coating and E_s is the elastic modulus of the substrate.

As discussed by Bouten et al[95], for the case of ITO coated PET, α is very close to 1 ($\alpha \rightarrow 1$). More precisely, they calculate α using $E_c = 119 \pm 5$ GPa and $E_s = 2.9$ GPa and they find that $\alpha = 0.95$.

Regarding crack patterns, the channelling crack process is unstable and once it is activated it would never arrest until it encounters another channel crack or an edge. In summary, considering the whole cracking process it is clear that there are two stages. At first, a surface flaw is activated by the externally applied tensile stress and grows towards the interface and then may stop if the substrate and interface are tough. With further increase in external stress the crack is channelled through the film.

Beuth[96] gave a relation which links the available energy at the channel crack front, G_{ss}, with the elastic mismatch α as shown in figure 2.12. It is important to note that β is a second Dundurs parameter, which is given below in equation 2.3.

$$\beta=[(1(\mu_c/\mu_s)(1-2\nu_s)-(1-2\nu_c)]/[2(\mu_c/\mu_s)(1-\nu_s)+(1-\nu_c)] \qquad (2.3)$$

Where μ_i, ν_i are shear moduli and Poisson's ratio for coating and substrate respectively.
The analysis considers a thin film bonded to a semi-infinite substrate with dissimilar elastic moduli. For the case of $\alpha \rightarrow 1$, it is clear that the compliant substrate provides less constraint and the available energy at the channel front is higher than that of $\alpha<0$.

It is also interesting to note that the Y-axis of the graph in figure 2.12, describes a unifying dimensionless driving force number Z that is given[94,97] in the following equation 2.4.

$$Z=(G\,E_f)/(\sigma^2 h) \qquad (2.4)$$

Where G is the crack driving force at the front of the crack, E_f is film's modulus, σ is applied stress and h is film's thickness.

The constraint parameter Z can be also calculated from the crack opening geometry using the equation, 2.5, below[96,97].

$$Z = \frac{\int_0^a \delta(y)dy}{\pi \frac{\sigma}{E_{film}} a\, h}$$

(2.5)

Where δ is crack tip displacement and a is the distance from the crack tip as presented in figure 2.13.

2.7.2: Coating buckling and delamination

When thin brittle coatings, bonded to compliant substrates, are loaded in compression, a combination of delamination and buckling failure is observed[98]. The buckling pattern morphology, shown in figure 2.14 (a) and (b), can consist of a closed, figure 2.14 (a), tip or an open, figure 2.14 (b), tip.

The buckle base width, 2b, and deflection, δ, can be measured by AFM and the buckling critical strain can be estimated. However, this approach leads to an overestimation of the critical strain of ITO on polymer as compared to hot – stage microscopy results for ITO on glass[99].

2.7.3: Uniaxial tensile testing of coated thin composite films

Thin oxide coatings deposited on polymer films, by physical or chemical routes, have experienced considerable development for a large variety of technological applications, ranging from food packaging to displays and microelectronics. The in – service reliability of these applications, upon application of external tensile stresses, is mainly influenced by the coating cohesive properties and the substrate / coating adhesive characteristics.

In order to assess experimentally coating cohesive and substrate / coating adhesive behaviour, tensile testing of the composite thin structure has been conducted by various researchers in the past and some indicative examples, for various coated systems, are presented below.

Jankowski et al[100] used uniaxial tensile testing of Cu / Ni multilayers, deposited by dc magnetron sputtering on mica substrates, in order to measure their yield and ultimate stresses as well as their Young's modulus. Their results confirmed the existence of an enhanced modulus effect in metallic multilayer films. They also observed that the stiffest films were the most brittle.

Leterrier and Manson[101] used experimental stress – strain curves of uncoated and SiO_x coated PET in order to calculate the experimental work of fragmentation, W_f, of the thin coating on the polymer substrate. The work of fragmentation is equal to the energy, which is dissipated at the interface, W_{int}, minus the cohesive energy, W_{coh}, of the coating material. They compared the experimental W_f with a modelled W_f based on the Kelly – Tyson model[102]. They assumed that a) the coating is perfectly elastic, b) there is not any Poisson's effect and c) delamination of the coating from the substrate starts after the onset of fragmentation. They concluded that most of the fragmentation work is spent in plastic flow at the interface.

Leterrier et al[103] investigated the effect of substrate properties on coating's tensile fragmentation process regarding the adhesion of silicon oxide layers, 100 nm thick, on PET substrates. They observed, using in-situ optical microscopy, that upon unloading the samples that were strained to less than 4 % uniaxial strain, strain recovery leads to the closure of coating cracks. They have also determined the coating fragmentation onset strain at 1.15 %. Primary cracks perpendicular to the loading direction are then formed. At about 6 % strain, transverse cracking of the fragments is initiated. These cracks develop in the straining direction due to the lateral contraction of the sample resulting from Poisson's effects. At 10 % uniaxial strain, tertiary cracks, parallel to the primary cracks, appear and are stopped by the secondary cracks. At this strain partial debonding also appears along the secondary cracks. Then the coating fragments tend to overlap and debonding is enhanced. The whole

fragmentation process regarding SiO_x coatings deposited, by PVD, on PET is presented in figure 2.15.

Leterrier et al[104] have also investigated the effect of SiO_x, deposited on PET, layer thickness on adhesive and cohesive strengths. They measured the crack density, CD, as a function of the applied strain[103]. The adhesive strength was modelled using the CD at saturation assuming plastic flow of the substrate, according to the Kelly – Tyson model. The adhesion was found to be independent of coating thickness and equal to substrate shear stress at saturation. In addition, the coating cohesive strength and the crack onset strain are proportional. As the coating thickness decreases the cohesive strength and the crack onset strain are both increase.

Yanaka et al[105] analyzed the cracking behaviour of brittle SiO_x coatings on PET substrates using a shear lag model and taking into account the residual coating stresses present due to deposition. They found that the difference of residual strains in the film and substrate increased as the thickness of the film decreased. They noted that SiO_x layers, 200 nm thick, failed at roughly constant values of a critical stress ranging from 200 – 300 MPa. For film thicknesses below 200 nm, layer critical stress values were higher than 300 MPa. Finally, some discrepancies of the experimental data from the model were attributed to the yielding of the polymer substrate.

Handge et al[106] analyzed theoretically and experimentally the influence of disorder in thin SiO_x coatings, deposited on biaxially oriented PET, on their uniaxial fragmentation kinetics. They showed that the mean fragment length, L, scales with the applied strain, e, such as L is proportional to $e^{-\alpha}$, with α depending on the degree of disorder in the coating. They found good agreement between theory and experiment and concluded that α ranges from 0.333 to 0.5. Values close to 0.333 indicate coating strong disorder whereas values close to o.5 indicate coating weak disorder.

Volynskii et al[107] investigated the mechanical buckling instability of thin coatings deposited on soft polymer substrates. Specifically natural rubber and amorphous PET substrates were

coated with platinum or gold and tested in tension. Folding of the coating, at relatively high strains and temperatures, leading to a wave – like pattern was observed, as figure 2.16 presents, for all the cases. Regarding the PET substrate the mechanism of folding is different than that in rubber – based composite films. Folding appears near cracks in the coating. In addition, it is noted that coating fragmentation is observed.

Cairns et al[108] were the first to report that the electrical resistance of ITO, deposited on polymer flexible display substrates, depended on applied uniaxial tensile strain. The increase in electrical resistance is due to cracking of the ITO layer with increasing strain. Tensile fragmentation coupled with in-situ optical microscopy and electrical resistance monitoring was conducted. The onset of cracks between 2 % and 2.5 % uniaxial tensile strain correlates with the sudden increase in the electrical resistance, which is presented in figure 2.17(I). They also found that the resistance remains finite even after cracks were observed to propagate across the entire sample length. The reason for the finite character of the resistance is probably a result of the crack being bridged by some conducting material as figure 2.17(II) indicates. Three possible mechanisms for bridging are also discussed. The first mechanism indicates that particulate debris from the brittle fracture process falls to the bottom of the crack and provides a conducting path. The second mechanism can be that the intergranular fracture path of the ITO results in an interlocking of neighboring ITO fragments. Finally the third mechanism, which seems to be the most probable because of AFM crack opening evidence, indicates that an interfacial conducting ductile layer exists on the polymer surface.

In addition to electromechanical monotonic uniaxial tensile testing of ITO coated PET flexible display anode components, Cairns et al[109] reported results for cyclic tensile loading of such components. They showed that, under increasing cyclic loading, very little resistance is recovered after the occurrence of cracking. The sample was strained and then released to 1 % strain, 2 % strain and 2.4 % strain. They also reported that using polyamide as an additional surface coating results in improving the integrity of the ITO layer.

Cairns et al[110] also reviewed various mechanical reliability issues regarding sputter coated ITO polyester substrates which are used in flexible display and touch – screen applications.

They concluded that the mechanical properties of the ITO film are dominated by the properties of the substrate and that the deformation of the substrate is mapped by the crack patterns in the ITO. Furthermore, the mechanical reliability of the ITO layer is dependent on the film thickness. Finally, it was stated that the thickness and hence sheet resistance of the ITO layer limits the maximum allowable substrate deformation.

Fortunato et al[111] reported the influence of the strain on the electrical resistance of zinc oxide doped thin films deposited on PET substrates. The crack onset strain, using in – situ optical microscopy and resistance monitoring, was found to be equal to 2 % and to depend on the film thickness. At 8 % of tensile strain transverse buckling was observed due to the lateral contraction of the sample. The finite character of the electrical resistance was explained using the interlocking fragment mechanism[108]. It was finally concluded that the resistance is not directly proportional to the number of cracks but rather to the width of cracks, which also depends on the layer thickness.

McGuigan et al[112] measured the debonding of cracked glass coated PET films by ultrasonic force microscopy, UFM. They investigated the subsurface fracture mechanisms of the films during tensile loading. AFM and UFM microscopies are compared in order to accurately identify debonded regions of the glass film from the PET substrate. They concluded that debonding occurred for tensile strains greater than 6 %. In some cases it was observed that debonding increased with increasing applied strain.

Rochat et al[113] studied the tensile fragmentation, in situ in a SEM, of 10 nm thick silicon oxide coatings deposited by plasma enhanced chemical vapour deposition on PET substrates. In order to prevent undesirable charging effects, an additional conductive gold coating was sputtered onto the silicon oxide coating. The gold coating did not influence the initiation of the oxide tensile failure. However, in the high strain regime the uniaxial tensile failure behaviour of the oxide coating was influenced by the gold coating.

Rochat et al[114] have also investigated the influence of substrate morphology on the cohesion and adhesion of thin SiO_x coatings on semicrystalline PET and polyamide, PA, substrates.

Coating failure is initiated at coating defect sites such as pinholes. In the case of PA, large surface spherulitic structures are shown to lead to preferential oxide delamination at spherulites boundaries. For both substrates, the interfacial shear strength is found to be comparable to the bulk shear strength of the polymer.

Leterrier et al[115] studied the tensile fragmentation behaviour of ITO coatings sputtered on a high temperature aromatic polyester, Arylite, with or without 4000 nm thick hard coats. The coating was in - situ optically and electrically monitored. They concluded that the loss of ITO functional performance was controlled by crack propagation features rather than by crack initiation. They also found that amorphous as well as fine grained polycrystalline film structures are beneficial for the cohesive ITO properties. On the other hand, relatively large surface grains acted as stress concentrators and decreased the crack onset strain. However, a major parameter that influences the cohesive properties of the ITO film to a large extent is the surface quality of the polymer. Therefore, the use of a hard coat was found to significantly increase the ITO failure strain.

Li et al[116] studied the stretchability of thin gold metal films on elastomeric, silicone, substrates. A 5 nm thick chromium layer was deposited on the elastomer substrate in order to improve the adhesion of the gold layer to the substrate. Their experiment shows that, when stressed in tension, the composite films rupture at strains larger than those reported for freestanding films. They also showed, using finite element simulations, that the metal film on an elastomer substrate may develop an array of necks before rupture whereas a freestanding metal film ruptures by forming a single neck. The electrical resistance of the gold, 50 nm thick, layer changed little when the tensile strain was below 3 % and increased linearly with the strain up to 6 %. The sample became electrically open at 8 % uniaxial applied tensile strain, corresponding to cracks traversing the gold stripe.

Bouten et al[117] reported on the mechanics of ITO on polymer, Arylite, substrates for flexible displays. They concluded that, under applied tensile stress, failure of ITO is mainly propagation controlled. Failure strains are measured around 1 %. However, failure initiation was found to occur at strain levels below 1 %. They proposed in order to increase the ITO

failure strain: a) the reduction of layer thickness, b) the use of a high – modulus non-brittle undercoat between the ITO and the substrate, c) the introduction, during coating deposition, of a moderate level of compressive internal stress and d) the fine patterning of ITO lines, instead of a fully coated area, because they can accommodate larger amount of externally applied tensile strains without cracking.

Cairns[118] compared the tensile properties of ITO coated PET and PEDOT: PSS coated PET samples under monotonic uniaxial tensile loading conditions. The conclusion is that while ITO on PET critical strain, approximately 3%, is limiting for flexible displays, it may still be suitable for use in conformable displays. On the other hand, in the case of PEDOT: PSS coated PET flexible display anode the electrical resistance does not increase significantly with increasing tensile strain.

2.7.4: Bending and controlled buckling of thin film substrate systems

Important composite thin-film deformation modes, in addition to uniaxial tensile deformation, are bending and controlled buckling under uniaxial stress states. It is vital for flexible display thin structures to address this field of experimental mechanics with the attention being focused mainly on previous experimental investigations.

Suo et al[119] reported on the mechanics of rollable and foldable film – on – foil electronics in the context of thin film transistors, TFTs, on steel and plastic substrates. They observed that transistor islands deposited on, 25 μm thick, steel foil could function well until some critical radii. When transistors are under compression, they can function till 2.5 mm of bending radius and when they are under tension, they can function till 1.5 mm of bending radius. It is important to note that bending to a 1.5 mm radius adds a net tensile strain of $4 * 10^{-3}$ when the transistors face out. Consequently, when the transistor islands face in, the net compressive, in this case, strain is $13 * 10^{-3}$. The authors summarized that when TFTs are placed on the surface of a foil substrate, the smallest bending radius is set by the failure strain

of the TFT materials. When the TFTs are placed on a low elastic modulus substrate, for example polymer, the smallest bending radius can be reduced.

Cotterell and Chen[120] investigated, using theory and finite element simulations, the buckling and cracking behaviour of thin films on compliant substrates under compression. They noted, using SEM, that when ITO-coated PET film is bent cylindrically so that the ITO coating surface is in compression, cracks grow behind delaminated buckles, as figure 2.18 indicates, and propagate parallel to the cylindrical axis of bending. They mentioned two different ITO failure cases. Buckling of ITO, on PET, without cracking and buckling of ITO, on PET, with cracking. In both cases, the energy released from the substrate can be very much more than the energy stored in the film itself. They estimated the delamination energy for ITO on PET, with the Dundurs parameter α equal to 0.97, to be $32 - 36$ J / m^2.

Chen et al[121,122] studied experimentally the fracture properties of thin brittle ITO coatings, deposited on PET, under controlled buckling conditions. They used the controlled buckling test because the PET film is extremely flexible and the usual three or four point bend tests were inappropriate. The most common test of straining, under compression, is by displacement controlled buckling with either simply supported or clamped ends. By buckling the PET film so that the ITO coating is on the convex or the concave sides, the conducting layer can be tested either in tension or compression. The electrical resistance of the coating can be monitored in – situ. They found that the critical failure strain for the coating under tension was 1.1 % and under compression was 1.7 % as figure 2.19 shows. They concluded that the mechanism of ITO coating failure under tension is by channelling cracks whereas under compression, the coating is delaminating and buckling and then it can crack.

Gorkhali et al[123] conformed an ITO / PET sample around a 50.8 mm pipe. The conformed shape was a spiral. They evaluated the electro – optic performance of the sample, at room temperature, before and after the conformal process and they observed a lower threshold voltage and lower contrast for the deformed sample.

Auch et al[124] studied the buckling deformation behaviour of ultrathin glass, with and without a polymer coating, used as an encapsulating cover in flexible displays. They found that the fracture of the glass substrate initiates at either the surface or an edge flaw. The average buckling strain for the thin glass was calculated to be 0.26 % and when the glass is coated with a thin polymer the buckling strain increases to 0.3 %.

In addition, Bouten[125] experimentally investigated the failure of ITO on PC substrates using the two – point bend test, originally developed for optical fiber characterization, coupled with electrical resistance monitoring. The ITO films were of the form of uniform coatings and narrow lines. It was determined that ITO layers, 100 nm thick, exhibited a critical failure strain at about 1.2 %. Narrow ITO lines show a quite sudden increase in electrical resistance at the critical strain. In the case of wider lines, a more gradual increase in resistance was observed. It was concluded that the onset to resistance increase does not depend on the width of the ITO lines.

Furthermore, Paetzold et al[126] fabricated OLEDs on a 125 μm thick PET substrate coated with 100 nm ITO. They investigated the luminance – current – voltage performance and the emission spectrum of the devices in the bent state under mechanical stress at different bending radii. They observed no significant degradation of the properties, as compared to the undeformed case and to glass – based devices, down to a bending curvature of 15 mm. Also, the mechanical behaviour of the anode, ITO on PET, was investigated separately and was compared to a polymer, 120 nm thick PEDOT on PET, anode. It was found that ITO has a critical bending radius of about 8 mm. They noted that this value is below the bending limit of many possible applications. However, this border is not sufficient for rollable displays, which need at least a bending radius of 5 mm. The PEDOT coated PET anode's electrical resistance is not affected by bending at all. However, the absolute value of the resistance is 5 – 6 times higher compared to ITO and therefore is too high for potential display applications.

Lewis et al[127] studied the monotonic and cyclic bending behaviour of ITO – Ag – ITO stacks sputtered on PET substrates. They concluded that even after repeated bending to a 3 mm radius the electrical resistance increased by only 1.2 – 2.7 times after relaxing. This response

was attributed to the ductile nature of Ag, 8 nm thick, that provides effective electrical conductivity even after the ITO is beyond its failure strain (approximately 0.8 %). Also, it was observed that the electrical conductivity recovered after large increases in electrical resistance due to bending.

Finally, Menard et al[128] reported on the frontward and backward bending behaviour of single crystal silicon thin film transistors formed by printing on ITO coated PET. The maximum value of the tensile strain at which the device can be operated is limited by the failure of the ITO layer, around 0.9 %. The device performs satisfactorily at compressive strains as high as 1.4 %.

2.7.5: Fragmentation of biaxial tensile – tested coatings

Biaxial tensile testing of coated thin materials for technological applications has not attracted as much attention as uniaxial tensile testing of such materials. However, during the last five years significant activity, in this experimental field, has taken place mainly for silicon oxide, SiOx, coated PET films used for O_2 barrier purposes, in packaging applications.

Leterrier et al[129] reported experimental results of the biaxial fragmentation of thin silicon oxide coatings, 53 and 103 nm thick, on biaxially oriented PET, 125 μm thick. They performed biaxial fragmentation tests, at room temperature, using circular specimens, 36 mm diameter, mounted on a PMMA bulging cell. The device was pressurized by means of a precision pressure controller. The bulging cell was installed on an optical microscope stage to allow observations of the SiO_x surface. The examination of the fragmentation process of the coating under increasing pressure reveals that the crack onset strain of the oxide thin layer is similar to that measured under the uniaxial tension mode. In addition, the coating biaxial fragmentation is characterized by complex dynamic phenomena resulting in considerable broadening of the fragment size distribution as figure 2.20 shows.

Alaca et al[130] investigated in – situ the fracture patterns of nanoscale Al coatings, 150 nm thick, deposited on 4.6 μm thick polyimide substrates using a bulge testing apparatus. They observed crack channelling and branching, as figure 2.21 shows, a phenomenon, involving a biaxial stress state, previously reported in much larger scales and examples ranging from drying coffee – water mixture to dessiccating muds and clays.

Andersons et al[131] studied the initial fragmentation stage of silicon oxide coatings, 100 nm thick, on PET, PP and PA substrates using a bulging apparatus with in – situ microscopical monitoring. Fragment areas are found to follow the exponential distribution at low strains close to the cracking onset. With the increase of equibiaxial strain, the distribution is observed to change as a result of stress transfer and crack propagation. In the case of SiO_x on PP and PA, coating fragment breakup due to crack propagation always leads to generation of two new fragments. On the other hand, in the case of silicon oxide on PET, crack branching occurs, as biaxial strain increases, as an additional failure process.

Cieslar et al[132] investigated the biaxial deformation of thin Al polycrystalline films prepared by magnetron sputtering. Films were deposited on photoresist-covered glass plates and released from the substrate in an acetone bath. The influence of film thickness, 0.5 – 4.4 μm, and testing temperature, from room temperature up to 240 °C, were investigated. TEM was used in order to observe biaxial deformation mechanisms. They concluded that the film thickness has an important impact on plasticity of thin Al films. Also, no grain boundary sliding was observed using TEM.

Andersons and Leterrier[133,134] also studied the advanced fragmentation stage of oxide coating, SiO_x, on a PP substrate. The fragment area distribution at an advanced fragmentation stage is shown to scale with the average fragment area with the latter being a power function of the applied biaxial strain. They also compared two plausible cracking scenarios, caused by flaws randomly distributed over the area of the coating or along the coating fragment edges. They concluded that fragment pattern due to perimeter fragmentation exhibits ordinary scaling behaviour at advanced fragmentation. On the other hand, fragment distribution under area fragmentation becomes multi – scaling with increasing crack density.

Finally, Sierros et al[135] reported preliminary results considering the crack onset strain for biaxial fragmentation of ITO coatings on PEN flexible display substrates using an in – house built bulge test apparatus coupled with electrical resistance, two point, monitoring. This method did not require in – situ optical monitoring since the coating is electrically conducting. They calculated the critical onset ITO biaxial strain, using the spherical cap model, to be 1.4 %. They also observed, using c – m AFM, that the complex biaxial stress state lead to a deformation of the coating islands and to a rougher surface.

2.8: Biaxial bulge testing of thin flexible structures

2.8.1: Background

A thin film sample subjected to a circular bulge test can be described as a pressurised, thin, circular plate, or membrane, clamped at its periphery. This is a widely studied problem, in solid mechanics, which has been examined rigorously for many different materials and material systems. In this study, the bulge test is primarily associated with the mechanical characterization of thin composite functional substrates for flexible displays. It is not intended to present the full history of the bulge test but only summarize the work done in the past with illustrative examples of experimental and theoretical research, covering a range of material systems and applications.

2.8.2 Material systems and applications of the bulge test

Almost 25 years ago, Tsakalakos et al[136] measured the biaxial elastic modulus of Cu-Ni thin foils, containing short-wavelength composition modulations from vapour deposition, by bulge testing. Since the measurement of biaxial properties in thin films is of paramount interest in many areas of microfabrication Bromley et al[137] determined intrinsic stress, elastic biaxial modulus and yield strength by measuring pressure-deflection responses of circular, low pressure chemical-vapour-deposited, silicon-rich silicon nitride, membranes.

Mechanical properties, including fracture strength, of polycrystalline diamond membranes with a potential application in optical windows have been studied, with the use of bulge test, by Aikawa et al[138]. They measured the burst pressure and Young's modulus and estimated the fracture strength of the diamond films.

Y. von Kaenel et al[139] also researched diamond thin films, as well as silicon and aluminium films, used in IR and optical windows, with the aid of the bulge technique. They used numerical modelling, instead of analytical models, in order to interpret pressure-deflection curves and they concluded that uncertainties in predicting the biaxial modulus are relatively large, (10%-15%), because the method is highly sensitive to certain test parameters such as the initial stress state which is only known by approximation.

A.F. Jankowski et al[140] researched the enhancement of biaxial modulus in multi-layered thin, Ag-Pd and Cu-Pd, material systems using a circular geometry bulge system. Hydrostatic bulging of metal sheets is another area where the bulge test method can be reliably applied, in order to determine the strain-hardening characteristics of metals. Ahmed and Hashmi[141] have used bulge test principles combined with finite element analysis with the aim of simulating bulge metal forming processes.

The mechanical properties of micro-electromechanical systems, MEMS consisting of thin film materials, can be determined by using the bulge method. Loy et al[142] obtained an

analytical load-deflection relation for a circular membrane using a series solution for the case of MEMS materials.

The studies published by Pai-hui I. Hsu et al[143,144,145] are related to the present work. They used the bulge test technique in order to deform, plastically, polyamide substrates with amorphous silicon islands into spherical shapes. These studies are a consequence of a growing interest in the application of large area electronics on curved surfaces. Their goal is to achieve permanent spherical deformation without cracking the pre-fabricated, brittle semiconductor device materials. When the inorganic semiconducting materials were of the form of continuous layers and not patterned as isolated islands, they fractured during deformation. Also, it was concluded that the strain in the island increases with increasing island size.

The development of metallic actuators, as discussed by Basrour et al[146], requires rigorous mechanical characterization of electroplated thin films, which can be accomplished by means of the bulge experimental method. Interference fringes, with the aid of computer processing, allow a measure of the bulge shape and the applied pressure is measured via a pressure sensor. Thus, residual stresses and biaxial moduli of electroplated nickel coatings can be determined and compared with respective values obtained by a dynamic technique which is based on the study of the variations of eigenfrequencies of vibration modes when stresses are present in the plate.

W. D. Zheng et al[147] reported bulge testing results of both dense and porous poly-arylethers, PAE, and low dielectric constant films, used in the microelectronics industry, which can replace SiO_2 interlayer dielectric, ILD, materials. In summary, they have extended the bulge testing method to polymeric thin films of sub-micron thickness and they have obtained biaxial modulus values.

The bulge test experiment is not confined into using circular samples. This is confirmed by the works of Yang et al[148] and Xiang et al[149]. Firstly, Yang et al used bulge testing of silicon-nitride thin film, in rectangular membrane form in order to determine their fracture

properties. Secondly, Xiang et al used square electroplated Cu films in order to obtain biaxial stress-strain data. The yield stress, Young's modulus and residual stress were determined as a function of film thickness and microstructure.

An interesting application is a biomedical device that consists of a silicon substrate into which micro-reservoirs, containing individual doses of drug, are etched. In order to achieve controlled release of the drug, the biaxial mechanical stresses and strains have to be evaluated using a bulge test system[150].

Alaca et al[130] reported the manufacture of a bulge testing apparatus which can conduct monotonic and cyclic tests and also can be utilized to study fracture patterns, with the aid of an optical microscope, in nano-scale, spin-coated polyamide diaphragms under biaxial stress states. The most interesting feature, of this particular apparatus, is that cyclic fatigue experiments can be performed.
Bulge systems for testing free-standing Al films between room temperature and 300 °C and between room temperature and 240 °C have been demonstrated by Kalkman et al[151] and Cieslar et al[152] respectively. The former apparatus consists of a pressure cell, made from a Ampcoloy 940 alloy, of good heat conductivity. The pressure cell is heated using eight 125 W resistive heaters in parallel, positioned symmetrically in the wall of the pressure cell. In the latter system the circular sample is mounted on a heating stage located above the cavity to which a motor driven syringe and a pressure gauge were attached.

Finally J. Andersons et al[131] published work most close to the present project on the bulge test in a research report in 2003 concerning material systems and applications. The specimens are mounted in a transparent PMMA bulging cell, which is installed on the stage of an optical microscope. Three different materials were investigated. The first two were a 12 μm thick PET and the third was a biaxially oriented PP, 21 μm thick, film. All three films were coated, on one side, with a thin SiO_x layer. PET/SiO_x composite films can be used in flexible displays applications. The function of the inorganic coating is to act as a gas barrier whereas in our case the inorganic coating acts as an anode electrode.

2.8.3: Bulge theoretical models and previous experimental investigations

There is a wealth in the literature involving, analytical and finite element predicted, bulge test models and experimental investigations applying these models to real thin film material systems. It is first useful to describe the bulge test method. In simple terms, a circular thin film, of radius a, is placed over a die and is firmly clamped around the perimeter. An increasing differential pressure, p, is applied to one side of the circular film, causing it to bulge through the aperture, as figure 2.22 indicates. From the measured central, vertical film deflection in the z-direction it is possible to obtain biaxial stress and strain characteristics of the thin film under biaxial tension.

Hill[153] gave one of the first accounts of the bulge test for the case of circular sheet metal diaphragm under biaxial stress. It was found that the influence of the work hardening on the shape of the bulge profile and on the relation between polar strain and curvature, agreed well with experimental data. A simple equation was also developed for the instability strain at which a secondary bulge begins to form over about the top half of the diaphragm. A general solution for the case of cold – worked metals was reported.
Beams[154] was the first to report, using the bulge test, that it is possible to measure the mechanical properties of thin films deposited on substrates. Some simple equations, 2.6 and 2.7, were derived in order to calculate stress and strain in a bulged film. The model assumes that the shape of the bulged film attains spherical cap geometry.

$$\sigma = \frac{P\alpha^2}{4ht} \qquad (2.6) \qquad\qquad \varepsilon = \frac{2h^2}{3a^2} \qquad (2.7)$$

The sample geometry is shown in figure 2.22, where P is the applied differential pressure, σ is the film stress, R is the bulge radius of curvature and t is film thickness.

Timoshenko[155] approached the thin film bulging problem using the energy minimization method. The energy minimization approach assumes that the shape of the deformed film is that of a clamped circular plate under uniform loading, as equation 2.8 indicates. The vertical deflection of the film, w, the central bulge height, h, and the radial displacement, r, are linked in order to yield the plate shape behaviour.

$$w = h\left[1-\left(\frac{r}{a}\right)^2\right]^2 \qquad (2.8)$$

The load – deflection behaviour is calculated, equation 2.9, by minimizing the strain energy of the system.

$$P = \frac{16\,M\,t^2}{3\,a^4(1+\nu)}h\left(1 + 0.488\,\frac{h^2}{t^2}\right) \qquad (2.9)$$

Where M is the biaxial modulus and ν is the Poisson's ratio.

Papirno[156] reported evidence, which indicates that the strains measured in bulged aluminium alloy diaphragms, by means of strain gauges, vary considerably from those, predicted on the basis of sphericity and uniform strain. It was concluded that the bulge surface could be more closely approximated by a surface of revolution of a general quadratic whose form can be obtained by analysing the deflections of the bulge centre and the quarter – chord distance respectively. However, it was noted that it is not possible to derive an exact analytic expression of the strain distribution in the bulge surface since the mathematical investigation involved analysis of an ellipse.

Ranta – Escola[157] reported on the effect of the hydraulic bulge test and the measuring procedure on the determination of biaxial stress – strain curves. It was shown that the shape of the top of the bulge is nearly spherical irrespective of the anisotropy of the sheet. The strain rate is found to influence the accuracy and reproducibility of the bulge test. The samples under investigation were steel and brass sheets and the fluid used was oil.

Tsakalakos[158] solved the boundary value problem for an initially flat linear elastic membrane, with no initial stress, which is clamped over a circular orifice. The resulting differential equations were solved numerically using the appropriate boundary condition, i.e. clamped edge. However, the lack of a simple analytical solution is a barrier in using this model despite the fact that the shape and the stress and strain distributions are calculated rather than assumed as in the spherical cap model.

Williams[159] investigated the bulge film problem from the membrane theory point of view. A membrane is considered as a thin sheet which is not able to resist shear forces and hence must always have zero bending moments at all points. Therefore, direct forces in the plane of the film support all loads. The spherical cap assumption is used and mean stress and strain equations are derived, equations 2.10 and 2.11.

$$\sigma = \left(\frac{PR}{2t}\right)\left(1 + h^2/a^2\right) \qquad (2.10)$$

$$\varepsilon = ln\left(1 + h^2/a^2\right) \qquad (2.11)$$

Where R is the radius of curvature given by equation 2.12 below:

$$R = \frac{a^2 + h^2}{h^2} \qquad (2.12)$$

Bromley et al[160] used the spherical cap model, equation 2.13, in order to calculate the intrinsic stress, σ_o, biaxial modulus and yield stress of silicon nitride thin films assuming that the deflection of the membrane is small compared with its radius.

$$P = \frac{4\,t\,\sigma_o}{a^2}h + \frac{8\,M\,t}{3\,a^4}h^3 \qquad (2.13)$$

Small and Nix[161] in an interesting review regarding the bulge test commented that while the apparatus required for the bulge test is relatively simple, interpretation of bulge test data is not. In order to assess the accuracy of the bulge test they used the finite element method to model the deformation behaviour of a thin film for a variety of initial conditions and material properties. They concluded that the film would be more compliant at the edge than at the centre, where the stress state is equi – biaxial. Since it is assumed by the spherical membrane equations that the stress in the film is everywhere equibiaxial, it is evident that the biaxial modulus predicted will be lower than the actual biaxial modulus. They propose that using equation 2.14 will considerably improve the accuracy of the biaxial modulus prediction.

$$M = \frac{M_{calculated}}{1 - 0.24\,\nu - 0.00027\,(1 - \nu)\,\sigma_0} \qquad (2.14)$$

Fichter[162] investigated the stresses and large deflections of a clamped circular membrane for two types of loading. At first the classic Hencky[163] series solution of uniform lateral loading was analyzed. Also, the uniform pressure loading was investigated. Results for the two types of loading have been shown to agree quite closely when the membrane is lightly loaded and to diverge slowly as load intensity is increased. The deflection shapes from the uniform pressure solution are observed to be more nearly spherical than those from the solution to Hencky's problem at high loads.

Sheplak and Dugundji[164] investigated the large deflections of clamped circular plates under initial tension and transitions to membrane behaviour. They introduced an initial tension parameter k, equation 2.15. The transition from plate behaviour to membrane behaviour for small deflections is a function of k. Plate behaviour dominating for $k < 1$. For $k > 20$, membrane behaviour dominates in the majority of the clamped plate. However, near the edge, the zero – slope boundary condition is met.

$$k = \frac{a}{t}\sqrt{12\ \varepsilon_o\ (1 - \nu^2)} \qquad (2.15)$$

Hohlfeder[165] in his PhD thesis summarized, as shown in table 2.1, the available analytical bulge models and finite element predicted models using the generalized bulge equation 2.16.

$$P = c_1\ \sigma_o\ t\ \frac{h}{a^2} + c_2\ M\ t\ \frac{h^3}{a^4} \qquad (2.16)$$

Where c_1 and c_2 are parameters, which account for the shape the film's Poisson ratio.

Finally, Leterrier et al[129] correctly reported that the relations reported by Small and Nix[161] are relevant to the case of a small bulge, for which the bulge top displacement is much less than the film radius. They noted that this condition is not necessarily met in their experimental case, which was associated with the biaxial deformation of thin silicon oxide coatings deposited on PET.

Therefore, they derived stress and strain equations 2.17 and 2.18 respectively, that account for large strain and film thickness reduction. The biaxial strain ε is related to the ratio

between initial and final film surface area and expresses via the measured displacement d of the top of the inflated sample. The radial displacement d was measured using optical microscopy.

$$\sigma = P\frac{(d^2 + a^2)^2}{4dta^2} \qquad (2.17)$$

$$\varepsilon = \frac{1}{2}Ln\left(\frac{d^2 + a^2}{a^2}\right) \qquad (2.18)$$

2.9: Friction and wear of polymeric materials

Tribology is defined as the science and technology of interacting surfaces in relative motion and embraces the study of friction, wear and lubrication[168]. In this work, the primary concern is the friction and wear of a steel ball bearing against a polyester surface in dry-sliding contact. Therefore, external lubrication issues and their study are excluded and the tribological investigation is limited to friction and wear mechanisms.

2.9.1: Friction of polymers

As discussed by Lancaster[169], the two basic friction laws stated by Amonton, i.e. first that the frictional force between sliding surfaces is proportional to the applied load and second that the frictional force is independent of the apparent contact area, are basically valid in most cases involving metals but serious questions arise when considering soft polymeric surfaces and metal-polymer combinations.

Bowden and Tabor[170] expressed the frictional resistance force as the sum of two terms, namely the shearing term and the ploughing term. The first term, is associated with the energy losses arising from shearing of adherent junctions, produced by adhesive forces over the regions of true contact and the second term is related to losses due to elasto-plastic deformation of the contacting asperities between the hard, eg. steel ball, and the soft, eg. polyester film, surface. In the case of metals and generally hard surfaces the first term dominates whereas in the case of dry steel-polymer contact, in air, the second term may become very significant.

Briscoe and Tabor[171] disconnect the two processes and treat them individually. They state that the ploughing mechanism is associated with relatively large volume-deformations and small strains, as seen in figure 2.23, whereas the shearing of adhesive bonds, formed at the interface of the two surfaces, involves very thin interfacial regions and large strains. In terms of energy considerations for the case of the ploughing process, when a single circular asperity traverses the surface of an elastomeric polymer as shown in figure 2.24, energy is fed into the polymer ahead of the slider and some of this is restored at the rear of the circular asperity because of the elastic recovery effect. To summarise, the total frictional force can be presented as the sum of two different processes as shown in equation 2.19 below:

$$F_{\text{frictional(total)}} = F_{\text{adhesion}} + F_{\text{displacement}} \qquad (2.19)$$

However, it is important to note that there are numerous factors[172] that influence the friction of polymers and in particular polymer-polymer or metal-polymer systems in contact as shown in figure 2.25. The ratio of elastic modulus, E, over the hardness, H, of the material determines the extent of plasticity in the contact region[173] and is related to the mechanical properties of the polymer and to the adhesion term of the total frictional force. Also, the adhesion term is influenced by the surface roughness and hence the number of the polymer surface asperities as well as the temperature effects which play an important role due to the usually low glass transition, T_g, temperatures observed for polymeric materials. Along with the material's characteristic mechanical properties H and E the surface roughness and temperature factors describe the development of the contact area and its elastic, plastic or elasto-plastic deformation.

Another feature, which influences the adhesion parameter, is the geometrical arrangement of the contact between the surface under investigation and the counter-body. It is possible to have single asperity contact or multiple asperity contacts. The latter is a more realistic situation in topographical terms.

However, as discussed by Meyer et al[174], even surfaces which appear smooth on a macroscopic scale are indeed rough on the microscopic scale containing a number of micro-asperities. If we bring two of these surfaces in contact, figure 2.26, only the highest asperities of each surface really touch each other and therefore the real area of contact is smaller than the apparent area of contact. This is an important fact when considering the modelling of a frictional process and depends on the normal load acting between the surfaces. For a zero normal load, F_N, the real contact area cannot be defined whereas for a finite load small asperities can be plastically deformed.

Additionally, the surrounding environment plays an important role in terms of the strength of the adhesive junctions that are formed during sliding and under external lubrication. In our case the experimental investigation took place in air and dry conditions at room temperature.

As mentioned earlier, the displacement term on the right hand side of equation 2.19 may play a significant role in the case of polymeric materials, which are by nature visco-elastic. Mechanical properties, surface roughness, load, temperature and speed are all inter-related. This means that there is little value on listing coefficients of friction for particular polymer-polymer or metal-polymer sliding systems[172,173].

2.9.2 Sliding wear of polymers

Wear, when two surfaces move over each other, is the resulting damage, to one or both surfaces, which involves progressive loss of material[168]. When a polymer slides against a hard counterface the induced deformation, due to contact and sliding, takes place solely within the polymeric material. The hard counterface strongly affects the mechanism(s) of the resulting wear. For a smooth counterface, the wear mechanism is adhesion, between the two surfaces, and the polymer solely accommodates the deformation. If the counterface is rough, the wear results from either abrasion, linked with polymer plastic deformation, or fatigue in the deformed zone[175].

Pooley and Tabor[176] presented an experimental study of some thermoplastic polymers, in the form of rods with a hemispherical cap end, sliding against smooth flat surfaces of glass or polished metals. The sliding speed was 1 mm / sec and the normal load was 9.8 N. For PTFE, once sliding has commenced and the slider has acquired a preferred orientation, the coefficient of friction is low, less than 0.1, and the polymer transfer, to the counterbody, is in the form of an extremely thin film. In the case of high density PE, discrete streaks, less than 10 nm thick, are transferred to the smooth flat surface. This behaviour was found to be independent of the degree of crystallinity or the crystalline morphology of the polymer.

Lancaster[172] gave an interesting overview of the basic wear mechanisms of plastic materials. Some of the key elements of this paper are discussed below. As mentioned previously, the three main mechanisms are:

- Abrasive wear which is caused by hard asperities on the counterface or by hard particles between the two surfaces
- Fatigue wear representing the detachment of the material as a result of a localized cyclic stress.
- Adhesive wear, which is highlighted by the transfer of material from one surface to the other as a result of the interacting adhesion forces between the polymer and the counterbody.

For abrasive wear, one has to distinguish between a rough and a soft counterface sliding against polymers. When a rough counterface, or a cone, is sliding against a soft polymeric surface the likely mode of deformation and therefore material removal and displacement will be elasto-plastic. On the other hand, when the counterbody's surface roughness is low, the deformation should be almost totally elastic. When the deformation is elastic the wear of the polymer is likely to be much lower than when considering mixed elastic – plastic or fully plastic deformation.

Another major factor that can influence the wear behaviour of polymers is fatigue wear. Again the topography and hence surface roughness of the hard counterpart is of paramount importance as well as the polymer surface roughness. The localized nature of this particular wear process suggests that the mechanical properties of the polymer play an important role.

However, abrasive and fatigue wear are interrelated in the sense that abrasion, which comprises of ploughing and micro-cutting, is a limiting case of fatigue in which failure results from a single application of stress.

Finally, adhesive wear is also difficult to be categorized as an individual wear process. However, when both surfaces are smooth, adhesive force interactions play their most

significant role for pure sliding conditions. During repetitive sliding of polymers on metals, polymeric material is transferred on to the metal surface. In ductile thermoplastic polymers, the transferred fragments can be deformed during repeated cycles and the wear rate may decrease as the experimental time increases.

Briscoe and Tabor[171] also gave an interesting review for the wear mechanisms of basic polymer, mainly thermoplastics but also elastomers. They concluded that changes in the structure of the polymer near the surface, when the counterface has extremely fine asperities, might significantly influence the microdeformations occurring during sliding. They also concluded that the adhesion wear process involves possible electrostatic effects, van der Waals forces as well as viscoelastic losses. When polymers are below their T_g, the associated tensile stresses may lead to crack formation and detachment of relatively large polymer fragments.

Briscoe[177] reviewed some fundamental aspects of the wear mechanisms that occur in organic polymers. He mentioned two general categories of wear processes namely interfacial wear and cohesive wear as figure 2.27 indicates. However, a sharp distinction between the previous two categories is difficult to be made. The basic elements of the natural adhesive, or transfer, wear process are discussed. More specifically the basic elements are:

- The nature and magnitude of the initial adhesion between the polymer and the counterface
- The locus of the junction failure (mainly for brittle and highly cross-linked polymers)
- The thickness and molecular organization of the transferred material and subsequent changes during cyclic loading
- The final or equilibrium adhesive bonding of the transferred material to the counterface after multiple deformations
- The mechanism associated with the material removal
- The displacement of transfer debris from the contact region

In addition, Briscoe[178] reported on the state of an art regarding polymer tribology and paid attention to the effect of frictional heating during pure sliding conditions. Local surface thermal softening often occurs when the ambient temperature is well below any thermally induced transition region. This may result to a polymer surface melting effect. It is noted that it is not clear if such substantial thermal effects play a role at low sliding speeds in the case of semicrystalline polymers and more specifically PTFE and polyethylenes. He concluded by giving an extensive account of the polymer tribology fields that were well understood, up to that date, and those which needed more attention. Deformation mechanisms, viscoelastic contacts and fatigue processes are included in the former case whereas abrasive wear and transfer wear mechanisms are included in the latter case.

Chow[179] developed a model based on a fatigue-abrasive wear mechanism in order to calculate the wear of a polymeric surface due its interaction with small particles when a rotating foam roll compresses them. The wear behaviour is related to the contact deformation and fatigue resistance with respect to material and geometrical parameters. In summary, a weak dependence of the foam modulus on the wear behaviour is found. The wear process is dominated by the particle – polymer surface interactions.

Belyi and Nevzorov[180] studied experimentally the transfer wear of high density PE when it slides against a steel counterface. The varying experimental parameters were load and sliding velocity. They investigated the nature of the polymer to metal transfer process and recorded variations in the molecular weight distribution of the high density PE using light – scattering data. They observed that primarily the applied load influences the macromolecular dispersion whereas the effect of the sliding velocity is indirect and is related to the metal-polymer contact areas.

Eiss and Potter[181] investigated the wear of polycarbonate, polyvinyl chloride, ultra – high molecular weight polyethylene, siloxane modified epoxies and polyimides using a steel ball bearing, which was slid repeatedly on a rotating polymer disc. They observed that under low loads, 5 and 10 N, the polymer is subjected primarily to fatigue wear.

Buckley and Aron[182] reviewed the available techniques, which can be used in order to characterize and measure polymer wear. Experimental methods include visual observation tools such as SEM and optical microscopy. Wear quantification tools such as profilometry and ellipsometry can be used. Chemical wear issues can be studied using XPS and SIMS.

Briscoe and Stolarski[183] reported on the wear of polymers in the pin on disc configuration. Several polymers including PTFE, PMMA and linear – low-density PE sliding in the form of pin on a rotating disc. The load range was 25 to 150 N and the sliding velocity varied from 50 to 1500 rpm. They concluded that the motion is complex and results in an intrinsic rotation of the contact area. This intrinsic rotation appears to influence the wear behaviour pf PTFE and linear – density polyethylenes. These two polymers are observed to be sensitive to the orientation of their molecular chains in the contact region. The wear transfer process is not observed to be spin sensitive. The radius of the wear path seems to be an interesting variable and provides a clear indication of the presence of interface molecular or morphological reordering.

Yamada and Tanaka[184] studied experimentally the effect of the degree of crystallinity on the friction and wear of PET. The PET, in the form of pin, is slid against a smooth steel disc. It was found that the friction was little dependent on the crystallinity whereas the wear rate increased with increase in crystallinity. The wear rate increased remarkably for crystallinity above 40 %. Low crystallinity PET, as low as 8 %, was found to exhibit mainly transfer wear whereas high crystallinity PET was observed to exhibit surface fatigue during sliding.

Yamada and Tanaka[185] have also experimentally compared the friction and wear behaviour of water lubricated and unlubricated PET samples with various crystallinities. Sliding speed was in the range of 0.01 to 0.1 m / sec and the load kept constant at 10 N. The coefficients of friction of the lubricated PET were lower than those for unlubricated conditions and little dependence observed on the degree of crystallinity. On the other hand, the wear rates of the unlubricated samples were lower than those obtained in the case of the water lubricated conditions. Figure 2.28 summarizes the friction and wear results.

Omar et al[186] investigated the role of crack resistance parameters in wear of PMMA and PES. The wear rates were determined using a 6.35 mm diameter polymer pin sliding against a 25 mm diameter rotating ring. A relationship is derived to predict the adhesive and fatigue wear rates from measurements of the fracture mechanics parameters characterizing fatigue crack growth. They concluded that the wear rate should be proportional to $1 / K_{IC}^2$.

Tanaka[187] presented some interesting problems that remained unsolved in his work on polymer tribology. He mentioned the following areas:

- Relationships between molecular structure and tribological properties
- Relationships between morphological structure and tribological properties
- Relationships between tribological characteristics and sliding conditions
    - Effect of molecular profile on friction
    - Effect of crystallinity on polymer wear
    - Effect of spherulitic size on wear of semi – crystalline polymers
    - Effect of counterface roughness on wear of various polymers

Also, Unal et al[188] investigated the wear characteristics of some industrial polymers against steel counterface using a pin – on – disc arrangement. The influence of test speed and applied pressure on the friction and wear behaviour of polyamide 66, polyoxymethylene, ultra – high molecular weight polyethylene and aliphatic polyketone was studied. They concluded that the sliding speed should be low in order to restrict the temperature rise of the polymeric materials under investigation. The lowest specific wear was observed in the case of PA 66 and the highest in the case of POM. Finally they observed that, in general, the wear rate is not influenced by the change in applied pressure.

2.9.3 Tribology of polyesters

When one focuses on tribological properties of polyester materials, either in their bulk or thin film form, it is essential to mention some examples of previous experimental investigations involving such materials.

Chalmers and Knox[189] investigated the wear of a biaxially oriented polyester film surface using, as figure 2.29 presents, an abrasion apparatus, which can also be linked with roll-to-roll processing of flexible displays. During manufacture, processing and use the film surface is subjected to damage by scratching. The authors observed the scratched films using SEM. The film passed at high speed over stationary smooth metal pin surfaces of 150 nm rms surface roughness. A controlled film tension between the different abrasion pins was applied. At slow roller speed, 3.8 m / sec, wear was significant. On the other hand, at a higher roller speed, 10.2 m / sec, little wear was observed to occur. Wear debris particles generated during scratching were found to exhibit a typical platelet form. They started as small white specs in the interface between film and metal, grew in size and then broke loose from the metal surface. Failure on the semi-crystalline biaxially oriented film surface occurred by separation of the upper surface layers.

Yamada and Tanaka[184,185] investigated the effect of the degree of crystallinity on friction and wear of unlubricated and water lubricated PET. This research is discussed in the sliding wear of polymers section and therefore will not be further discussed in this part.

Weick and Bushan[190] reported on the tribological characteristics of thin magnetic tape substrates such as PET and PEN. Macro - scale friction measurements based on a reciprocating friction apparatus were reported. The PET, 14.4 μm thick, substrate found to exhibit lower friction coefficient, 0.29 when slid against a ferrite surface, than the friction coefficient, 0.59, measured for the case of PEN. However, it is mentioned that the PET film surface contains anti – slip agents. On the other hand, the PEN surface does not contain any anti – slip agents.

Yang et al[191] studied the tribological properties, against a 3mm diameter steel ball, of 25 μm thick ion implanted and unimplanted PET films. The applied normal load was 2 N. Sliding was conducted in the direction from left to right for a sliding distance of 1.5 cm. After each pass, the steel ball was removed automatically from the PET substrate and was reset to the initial contact point. Both static and kinetic friction coefficients were recorded. For the case of the unimplanted PET, the initial friction coefficient of 0.31 is observed and then it slightly decreased as the number of passes increased. Polymer transfer to the steel surface was observed. The wear rate of the unimplanted PET sample was 0.076 mm^3 / (Nm) after 20 passes and 2 N applied normal load.

Ling et al[192] investigated the biaxially oriented PET film surface morphologies and their tip – induced nanoscale wear using contact and non – contact scanning force microscopy, SFM. Two different PET film surfaces were studied. The first surface contained silicate additive particles whereas the second was additive free. Regarding surface morphology they concluded that the polymer orientation had no influence.

Wear ridges were observed to form on the polymer surface in the case of contact – mode experiments and loads as high as 45 nN. The debris that accumulated at the bottom of the scanned region was found to yield high contrast in lateral force microscopy, LFM, images suggesting that it differed from the rest of the polymer surface. It was suggested that the debris material was either low molecular weight polymeric material or polymer chain fragments produced by bond rupture during the wear experiment. They concluded that tip – induced wear is caused by deformation due to the applied load and adhesion due to the presence of a capillary force between the tip and the sample.

Frictional properties of PET film surfaces containing silicate particles were also investigated by Beake et al[193] using SFM. The measured friction coefficient, for applied loads ranging from 1 to 35 nN, yields a value of 0.027. Beake et al[194] also investigated the nanotribology of additive – free biaxially oriented PET films using contact – mode SFM. They found that under repeated scanning of the film surface at low to moderate loads, less than 50 nN, well-

defined ridges are formed as figure 2.30 shows. They concluded that both the spacing between the ridges and the rms roughness exhibited power law dependence on the load. Also, they noted that scanning at higher load above 50 nN, led to more extensive surface disruption and to material removal to the periphery of the scan region.

Neogi et al[195] investigated the role of PET in improving the wear properties of PP in dry sliding conditions. The sliding wear of isotactic PP, PET and their blends was studied as a function of applied pressure and composition against a steel counterface. A flat - ended polymer pin on steel disc configuration was used. As far as PET is concerned they concluded that PET showed minimum wear loss, as compared to PET / PP blends and PP, for pressures ranging from 0.3 – 0.9 MPa and 1.33 m / s sliding speed. In addition PET shows the minimum coefficient of friction, approximately 0.35, for 0.4 MPa of applied pressure and 1.33 m / s sliding speed.

Finally, Samyn et al[196] studied the sliding behaviour of pure polyester and polyester – PTFE filled bulk composites in overload conditions. They presented results that were obtained using large – scale test samples and extremely high loads ranging from 190 to 3380 kN. They used a large – scale tribotester which consist of two polymer sample counterfaces sliding against each other in a flat – on – flat reciprocating motion. They observed that pure PET shows high friction and unstable wear due to stick – slip. They also observed that, compared to small scale cylinder – on – plate and block – on – ring tests, friction coefficients measured on large scale tests are much lower due to large polymer transfer, while wear rates are much higher.

2.10 Nanoscratch and nanoindentation of ITO thin films

There have been a few investigations regarding the nanoscratch and nanoindentation mechanical response of ITO thin films deposited on glass and polymer substrates. Wu et al[197] investigated the microhardness, pull – off strength and scratch adhesion strength of r.f.

magnetron sputtered ITO films on rigid glass and flexible polycarbonate substrates. They concluded that ITO coatings on polycarbonate substrates improve the hardness of the substrate. Also, it was noted that films on polycarbonate substrates have smaller adhesion strength than those on glass substrates.

In addition, Shin et al[198] found that the friction force, as measured by the scratch adhesion test as a function of dc sputtering power, of ITO on PET substrate increases almost linearly, as dc power increases. However, the friction force for ITO on glass and acrylic seems to increase slightly with increasing dc power. It is observed that the friction force of as – deposited ITO films grown on PET and acrylic substrates is always greater than that on glass. This means that adhesion of ITO on polymer substrates is better than that on glass.

Finally, Zeng et al[199] reported on the nanoindentation determined elastic modulus and hardness of ITO and IZO sputtered on unheated glass substrates. They presented average elastic modulus and hardness values of ITO films on glass substrate of 99.8 ± 13.6 GPa and 6.5 ± 1.6 GPa respectively.

3. Materials, experimental methods and development

3.1: Materials used in this study

3.1.1: Polyester substrates

There are four different semicrystalline polyester substrates[24] used in this study all supplied by DuPont Teijin Films[215]. Two PET (PET Melinex 506 and PET Melinex ST506) and two PEN (PEN Kaladex S1020 and PEN Teonex Q65) surface heat – treated grades[24], presented in table 3.1. Samples were received in the form of A4 sheets. The thickness of all substrates is 0.125 mm. They are all biaxially oriented and have been produced using a similar method to that described in section 2.1.1.

3.1.2: ITO coated polyester substrates

Thin ITO coatings[200] (10% Sn) were deposited on the top sides of the polyesterA4 sheets, using magnetron sputtering, by Diamond Coatings Ltd[216]. All four different substrates were coated during the same run, at room temperature, using a dedicated commercial sputtering machine, which can coat areas of up to 1000 mm x 1000 mm. The resistivity of ITO can be expressed either in Ω / □ as defined by Eite et al[200] or Ω cm. The latter unit is used in this study.

3.2: Experimental techniques

3.2.1: Microscopy

There is extensive use of several microscopes, in order to investigate surface morphology, in this project.

- SEM microscopical investigations conducted using a conventional tungsten electron gun JEOL 6060 microscope[217]. Also, a conventional JEOL JSM-7000F FE-SEM[217] with Schottky emitter was used. The maximum resolution that can be achieved is 1.5 nm at 15 kV. In both cases, the samples were gold coated before the investigation. It should be noted[202] that thin silver 'dag' lines should provide a continuous path down the sides of the specimen to the 'stub' in order to achieve efficient conduction all the way, from the area under the electron beam to the earthed specimen stage. The operating voltage can be set between 0.5-30 kV. The working distance, WD, between the detector and the sample is normally set equal to 10 mm. It is also important to note that the SEM chamber can accommodate relatively large specimens, typically 10 mm across. The specimen is adhered to a 'stub' using a fast–setting adhesive. The adhesive must not attack, in chemical terms, the polymer surface.

- AFM microscopical studies were conducted using a Dimension 3100 atomic force microscope[218] operating in contact – mode conditions. Silicon nitride cantilevers with spherical tips (~50 nm radius) were used. It is important to note that a slow scan rate (<1.5 Hz) should be employed in order to acquire good quality images. Also, the sample preparation is not particularly demanding because the 'stub', which is used in the case of SEM, can be used in this case in order to accommodate the thin sample.

In general[219], a very fine tip (radius approximately 50 nm) positioned on the end of a flexible cantilever is rastered over the surface of the sample in a direction perpendicular to the longest axis of the cantilever. The tip and cantilever are displaced vertically upon encountering the surface. A laser detects the latter movement, as figure 3.1 shows. The laser maintains the deflection and the applied load of the cantilever at a constant value. The z – displacement of the sample can be displayed as a function of x and y position to provide a morphological image of the sample.

- Optical images were taken using the AFM microscope, without engaging the tip, by clicking the Vision toolbar.

3.2.2: Polyester characterisation

PET biaxial orientation characterisation was conducted using a Nicolet Magna IR 860 FTIR spectrometer[220] operating in ATR mode using a diamond golden gate (Specac). This makes use of a diamond crystal in a specially designed objective lens that is placed in direct contact with the surface of the sample.

The attenuated total reflectance (ATR) spectroscopic method is used mainly in the near infrared region in order to acquire spectra of thin film materials and measure molecular orientation. The sample, of refractive index n_1, is positioned in contact with a diamond anvil cell, of refractive index $n_2 >> n_1$. Using polarized infrared radiation and ATR spectroscopy the molecular orientation of biaxially oriented polyester films can be measured. The radiation, figure 3.2, can be totally reflected if the incidence angle, i, is greater than a critical value. The radiation penetrates the sample to a certain depth, usually less than 20 μm, and absorption may take place at a specific wavelength at which n_1 changes in a rapid fashion and the greater the change the greater the attenuation of the radiation. Therefore, the intensity of the reflected light varies with respect to a wavelength resulting in an absorption spectrum[201].

Advantages when using the ATR-FTIR technique include the fact that is more specific when compared to the transmission mode because it analyses only the sample surface and can be applied to samples irrespective of their thickness and absorbance. However, it must be noted that when using the ATR method an uncertainty arises because of the contact between the sample and the high refractive index crystal[221]. Such uncertainty can be corrected, as will be explained in the experimental section, by normalizing the intensity of the bands of interest with respect to a nondichroic band in the spectrum[37].

Polyester substrate crystallinities were determined using a DSC 7 Perkin Elmer differential scanning calorimeter[222]. When a substance undergoes a physical or chemical change, a corresponding change in enthalpy is observed. DSC primarily measures the thermal properties of the material and allows calculation of the enthalpy (ΔH) changes which occur when transformations such as crystal melting occur[202].

The sample, a few mg in mass, is placed in a heating block and warmed at a uniform rate. The sample temperature is monitored by means of a thermocouple and compared with the temperature of an inert reference (an empty aluminium pan), which is subjected to the same linear heating programme. As the temperature of the block increases at a constant rate (5 to 20 K min^{-1}) the sample temperature, T_s, and that of the reference, T_r, will keep pace until a change in the sample takes place. The resulting temperature difference is recorded and transmitted to a chart recorder where changes such as melting or crystallization are recorded as peaks[223].

3.2.3: ITO characterisation

ITO resistance measurements were conducted using an in - house four point – probe system with 1 mm probe spacing. The four-point probe is a simple device used to measure resistivity of a thin film.

The four-point probe station consists of a probe station (four probe tips), an ohm- meter, a DC current source and a voltmeter. This set up can measure resistivity of thin film material. The four probes are arranged in a linear fashion, where the two outer probes are connected to a current supply, and the inner probes to a voltage meter. As current flows between the outer probes, the voltage drop across the inner probes is measured. The relationship of the current and voltage values is dependent on the resistivity of the material under test, and the geometrical characteristics of the probe[203].

Optical transmission was measured using a laser diode and photocell system at 638 nm wavelength. The system consists of a laser diode, a polarizer, a beam splitter and two photodiodes as figure 3.3 shows. A computer is connected to the system and displays the optical transmission % of the sample under investigation. It should be noted that care has to be taken in order to properly clamp, using 'blue tac' adhesive, the sample on the system without cracking the ITO layer. Also, the surrounding environment should be relatively dark in order to achieve accurate measurements.

The microstructure of ITO coatings was also investigated using a Siemens X–ray diffractometer (Hilton Brookes). The operating step size was 0.05 and the counting time was 3 sec. Measurements on bare and ITO coated samples were conducted and a comparison of the respective diffraction intensities was made. The sample plane and the sample holder plane must be parallel.

X-ray powder diffraction (XRD) is an instrumental technique[204] that is generally used in order to study crystalline materials. The three-dimensional structure of non-amorphous materials is defined by regular, repeating planes of atoms, which form a crystal lattice. When a focused X-ray beam interacts with these planes of atoms, a part of the beam is transmitted, another part is absorbed by the sample, another part is refracted and scattered, and another part is diffracted. When an X-ray beam hits a sample and is diffracted, one measures the

distances between the planes of the atoms that constitute the sample by applying Bragg's Law.

3.2.4: Pulsed laser deposition of ITO on polyester substrates

ITO films were deposited on unheated PEN Kaladex S1020 substrates using a KrF Lambda Physic) excimer laser[224]. The system is shown in figure 3.4. The laser was operated at 10 Hz pulse frequency and the energy density of the laser beam at the target surface was 3 J/cm. For the pre-ablation of the target 500 shots were fired and for the actual deposition 4000 shots were fired. The PEN samples were prepared by cutting a circular section, of 0.8 cm radius, from a PEN biaxially oriented sheet.

The substrates were cleaned, prior to deposition, for 15 min using acetone and 15 min using ethanol and then they were rinsed with distilled water and dried using compressed air. The cleaned substrate was attached to the substrate holder using blue-tac adhesive, which can be easily removed after deposition at room temperature. Care has to be taken when removing the coated sample from the sample holder for the ITO layer to remain intact.

The diameter of the circular ceramic target, 90% In_2O_3 and 10% SnO_2 by weight, was 25 mm and its thickness 5 mm. The vacuum created in the chamber was of the order of 10^{-6} Torr. The deposition pressures, PO_2, used were in the range of 2.5-20 mTorr.

3.2.5: Tribological techniques

Friction and wear testing of bare polyester substrates was conducted using a conventional unidirectional pin – on – disc tribotester, using a normal constant load of 9.8 N and a sliding

cycle range of 925 to 12630 cycles. Stainless steel balls of approximately 4 mm radius were used as the counterbody.

After each test a new steel surface was used for the next experiment. The environment was dust – free and the relative humidity was measured before and after each test. Relative humidities measured were in the range of 34% – 63%. The temperature was also measured before and after each experiment. Measured temperatures ranged between 15 °C and 28 °C.

Friction coefficient data were monitored during the tests. Polymer discs, 11.5 cm diameter, were cut from the A4 sheets and were adhered on smooth austenitic steel discs (316L), 12 cm in diameter, using adhesive tape which was applied carefully around the discs edges. Care was taken when adhering the polymer on the steel discs in order to avoid film wrinkling.

The resulting wear track depths were measured, ex – situ, using a Mitutoyo stylus profilometer[225] operating in contact mode.

Nanoindentation and nanoscratch tests, on coated / uncoated samples, were performed using a Micromaterials Nanotest platform[226]. Knoop hardness values were obtained using a normal load of 5 mN and loading rate of 0.06 mN / s. A standard Knoop indenter was used[227]. ITO scratch adhesion profiles were also obtained. In the test process, a diamond tip is driven over a coated surface in order to produce a scratch. The load on the diamond tip is increased linearly to induce a shear force in the film that is proportional to the applied load. As the mechanical properties of the film and the substrate differ, the high discontinuity in the shear stress at the interface induces adhesive failure at a critical load[227].

3.3: Experimental development

3.3.1: Electromechanical tensile and controlled buckling test development

The uniaxial tensile, figure 3.5, and buckling electro-mechanical test development is based on slight technical modifications, of a commercial, Instron 5500 series mechanical test machine[228] (model 5520).

The tensile testing machine consists of a dual column tabletop frame, accommodating a 10 kN load cell and the upper grip, joined with a compression base which houses the lower grip, the machine motor and control unit. Applied stress-strain data are collected by a computer, which operates using Merlin software[228]. Standard tensile dumb-bell specimens can be accurately cut from the polyester sheet using a Moore Hydraulic Press.

When the sample is mounted between the upper and lower grip of the Instron, particular care has to be taken so that the composite thin film under investigation forms a 90^0 angle with respect to the compression base plane. Also, in order to avoid premature failure originating from the edges of the film, the sample edges have to be, lightly, rubbed with sand paper.

However, the commercial Instron machine available is capable of testing structures under tensile and compressive stress states but does not include any electrical resistance-monitoring unit when testing conductive coatings. Therefore, some minor modifications were needed in order to incorporate in-situ electrical resistance measurement capabilities, figure 3.6. First of all a plastic PTFE thin sheet was placed between the machine compression base and the lower grip in order to create a closed electrical circuit between the two grips. Then, two copper wires each attached to each grip, were connected to a multi-meter that monitors ITO electrical resistance changes. The electrical resistance data, measured in Ω, was collected by a computer and can be combined with stress-strain data, if mechanical test and resistance monitoring start simultaneously, in order to describe the electro-mechanical performance of flexible display components.

3.3.2: Development of biaxial bulge apparatus

The biaxial test apparatus, as shown in figure 3.7, consists of a cylindrical, thin walled pressure vessel made of brass, of 16 cm height and 34 mm inner diameter. The sample is

clamped on the open orifice of the vessel using a circular brass ring of 38 mm outer diameter and 34 mm inner diameter and hence sample free surface, α. An O – ring, 34mm inner diameter, is used in order to prevent gas leakage. The sample is pressurized, manually, by means of a N_2 gas cylinder, via a flow meter, and the differential total pressure, P, applied on the thin circular sample, thickness t, is monitored using a pressure transducer.

When pressure is applied to the circular specimen its central area deforms, figure 3.8, in order to acquire a near hemi-spherical cap shape and the central deflection, h, is measured using a linear voltage displacement transducer. The output voltage, in mV, from the transducer is converted to displacement, in mm, using the calibration plot presented in figure 3.9. In addition, data are collected, with the aid of a computer that operates using Lab View software, every two seconds. Experimental time is monitored and load as well as deflection history curves can be plotted.

Furthermore, the biaxial bulge testing equipment can be coupled, using thin wires and silver dag adhesive, with a multi-meter which monitors electrical resistance changes for tests on conductive surfaces, figure 3.10. The thin wires and silver dag material are assumed to have a negligible weight.

Some practical considerations, to be discussed further in the discussion section, include the fact that the applied pressure must be sufficient to deform the sample under investigation. Also, it is important to note that subjecting circular films to differential pressure care has to be taken in order to approach the ideal end conditions of rigid clamping along the periphery of the circular sample. The assumptions of no film slipping at the edge and no N_2 gas leakage have to be updated often by performing regular checks on the equipment, figure 3.11.

4. General characterisation and ITO preparation by PLD

4.1: AFM investigation of polyester substrate surfaces

It is necessary to characterize the surface morphology of the bare polyester substrates in order to understand the role that the substrate surface plays when ITO is deposited on polyester by physical or chemical methods. Contact – mode AFM is used in this case because it offers high resolution and accuracy for characterization of small surface features.

Figure 4.1 shows the top PET 506 surface as observed by c – m AFM. Extended long surface features are present. Their shape varies and generally can be characterized as angular. However, some rounded features can also be observed. The root mean square roughness, figure 4.5, of the top, adhesion pre – treated, PET 506 film surface is around 4 nm and its maximum roughness is approximately 28.6 nm.

In addition, the back PET 506 surface has also been characterized by means of c – m AFM. The reason for this is that the back surface is also adhesion pre – treated and therefore it is interesting to observe if its morphology and roughness differs from the top surface.

Figure 4.2 shows the back PET 506 surface. It is observed that little difference exists. However, the long features observed in the case of the PET 506 top surface, now appear to be more concentrated. The c – m AFM roughness analysis, figure 4.6, of the back PET 506 display film surface reveals a slightly higher rms roughness, 5.3 nm, as compared with the rms roughness of the top PET 506 substrate. It is also observed that the maximum roughness of the back PET 506 surface is higher, 39.1 nm, than that measured in the case of the top PET 506 surface.

Figure 4.3 shows the adhesion-treated PEN Kaladex S1020 surface. Long surface features are observed as well as rounded surface particles. The surface morphology is similar to that of PET 506 but the features are shorter and smaller. Roughness analysis, as figure 4.7 shows, of the PEN Kaladex surface reveals a significantly lower surface rms roughness, 1.5 nm, as compared with both top and back PET 506 surfaces. It is important to mention that the PEN Kaladex S1020 measured area is larger, 6.25 μm^2, than that of PET 506 which is equal to 4 μm.

Figure 4.4 shows the treated surface of PET ST506 as obtained by using c – m AFM. It is evident that the rounded surface features prevail in this case. The surface rms roughness, figure 4.8, is higher, 4nm, than that observed for PEN Kaladex S1020 and comparable to that obtained in the case of the top PET 506 surface. The maximum roughness measured equal to approximately 43 nm.

Figure 4.9 presents the back PET 506 surface as measured by c – m AFM. It is important to note that the measured area is large, 10000 μm^2. Some surface scratches can be observed and are present probably because of the contact between the machine surface and the polymer surface. Note good agreement between box measured rms roughness and rms roughness reported for PET 506 earlier.

In addition, long surface scratches are observed to exist, as figure 4.10 shows, also in the case of PEN Kaladex S1020 top surface for a large measured area, 10000 μm^2. This is puzzling since the top surface is not in contact with the roller surface(s) of the manufacturing equipment. Therefore, the scratches could be also a product of film handling after processing.

Furthermore, figure 4.11 presents the PEN Teonex Q65 top surface. It is interesting to observe that the long extended features and the rounded features do not exist in this case. On the other hand a few large lumps exist as well as some smaller ones. The rms roughness of the PEN Teonex top surface, figure 4.12, is approximately 5.6 nm. This value seems relatively high and can be attributed to the presence of the lumps.

4.2: AFM investigation of ITO layer surfaces

Contact – mode AFM was used in order to investigate the ITO surface morphology and possible differences regarding sputtering of ITO on different polyester film display substrates. Four different ITO coating surfaces were investigated.

The first surface under investigation, as figures 4.13 and 4.17 indicate, is an ITO layer deposited on PET 506 substrate. The root mean square roughness of the, 4 μm^2 area, conductive layer is equal to 8.4 nm. The surface morphology of the layer consists of a population of rounded islands, which have coalesced. These islands are of different heights. The higher of these features show a diminishing shape at their peak whereas the lower islands remain relatively rounded.

The surface morphology of ITO deposited on PET ST506 is presented in figures 4.14 and 4.18. The ITO layer morphology is similar to that observed in the case of ITO on PET 506. However, the measured rms roughness is lower than in the previous case and equal to approximately 7 nm. Also, the maximum roughness is equal to approximately 43.2 nm whereas in the case of ITO on PET 506 is equal to 54.8 nm.

A significant change is observed when ITO is sputtered on PEN Kaladex S1020 flexible substrates. As figures 4.15 and 4.19 indicate, the ITO islands are significantly smaller and shorter than their ITO on PET 506 and PET ST506 counterparts. Also, the root mean square roughness, approximately 2 nm, measured by contact mode AFM is significantly lower. The maximum roughness measured is around 16.3 nm.

When ITO is deposited, by magnetron sputtering, on PEN Teonex Q65 the islands are observed to have a rounded shape and are smaller and shorter than their ITO on PET substrates counterparts as presented by figures 4.16 and 4.20. However, the average island dimensions seem to be larger than those observed in the case of ITO on PEN Kaladex S1020.

The measured rms roughness is around 2 nm, a value similar to that measured for the case of ITO on PEN Kaladex S1020. The maximum roughness measured is approximately equal to 23.3 nm.

4.3: X–ray diffraction of ITO on polyester substrates

X–ray diffraction studies of bare polyester substrates and coated film substrates, were conducted in order to examine the microstructural characteristics of the ITO coatings sputtered on various PET and PEN substrates. The bare polymer substrates were investigated first and the respective coated systems afterwards. The aim of the experiment was to compare the resulting diffraction peaks of the bare substrates and the resulting peaks of the respective coated systems.

Figure 4.21 shows the diffraction graph of the bare PET 506 surface and the diffraction graph of the ITO, deposited on PET 506, surface. Two main diffraction peaks, in the range of 20 to 70 2θ degrees, were observed for both the bare surface and the ITO coated surface. Both peaks, 26 and 54 2θ degrees correspond to the semi – crystalline polyester substrate. Therefore, the lack of any distinct ITO diffraction peak indicates an amorphous ITO microstructure.

Figure 4.22 presents the X–ray diffraction graph of the bare PET ST506 surface and the X–ray diffraction graph of the ITO, sputtered on PET ST506, surface. As observed in the case of PET 506 the two diffraction peaks are the same for both coated and uncoated material and correspond to the semi – crystalline polyester substrate. Therefore, the conductive coating is observed to exhibit an amorphous microstructure.

Figure 4.23 shows the X–ray diffraction graph for the bare PEN Kaladex S1020 surface and the ITO, deposited on PEN Kaladex S1020. Again the microstructure of the ITO layer is observed to be amorphous. It is important to note the higher intensity of the 54^{o} 2θ peak as compared to the intensity of the respective PET 506 diffraction peak observed in figure 1.

Finally, figure 4.24 presents the X–ray diffraction data of the ITO coated and uncoated PEN Teonex Q65 surface. The comparison of the uncoated and coated sample, in terms of the resulting diffraction peaks, leads to the same result as mentioned in the three previous cases,.

4.4: FTIR – ATR investigation of PET 506 substrates.

The following calculation of orientation parameters for PET 506 biaxially drawn film is based on the proposed calculation method given by Everall and Bibby[37]. The absorbance versus wavenumber results, for the four different geometries, is shown in figures 4.25, 4.26, 4.27 and 4.28.

At first the R1 and R3 values, given by equations 4.1 and 4.2 respectively, have to be determined for the 875 cm^{-1} dichroic band.

$$R1 = \frac{\left[\frac{A(TE_y)}{A(TE_y)_{1410}}\right]}{\left[\frac{A(TE_x)}{A(TE_x)_{1410}}\right]} \qquad (4.1) \qquad R3 = \frac{\left[\frac{A(TM_y)}{A(TM_y)_{1410}}\right]}{\left[\frac{A(TE_y)}{A(TE_y)_{1410}}\right]} \qquad (4.2)$$

The beam can be polarized in such a way that the electric vector is perpendicular to the plane of incidence, TE, or lies in the plane of incidence, TM. Thus, the notation TM_x, for example, indicates that the sample x axis is perpendicular to the plane of incidence and the electric vector lies in the plane of incidence.

For 875 cm^{-1}, R1 is 0.954 and R3 is 2.118. The same procedure can be followed in order to calculate R1 and R3 for 1019 cm^{-1} and yields 1.24 and 0.3 respectively. In order to proceed with the calculations, one needs to compute the ratios k_x / k_z and k_y / k_z. The latter is given by the following equation 4.3.

$$\frac{k_y}{k_z} = \frac{C4}{\left[R3 - \frac{C3}{R1}\right]} \qquad (4.3)$$

However, before the calculation of k_y / k_z, it is essential to compute the parameters C3 and C4 which are given by equations 4.4 and 4.5 respectively.

$$C3 = \frac{\beta_y}{(\beta_y + \gamma_y)} \qquad (4.4)$$

$$C4 = \frac{\gamma_y}{(\beta_y + \gamma_y)} \qquad (4.5)$$

Using equations 4.6 and 4.7, which give β_y and γ_y respectively, the calculation of C3 and C4 is possible. It is important to note that θ is taken equal to 45°. Also, $n_x = n_y = n_z = 1.57$ and $n_1 = 2.4$.

$$\beta_y = \frac{-4 n_x n_z \left[1 - \frac{n_z^2}{n_1^2 \sin^2\theta}\right]}{n_1^2 \tan\theta \sqrt{\left[1 - \frac{n_z^2}{n_1^2 \sin^2\theta}\right]\left[1 - \frac{n_z^2}{n_1^2 \sin^2\theta} + n_x^2 n_z^2 \frac{\cot^2\theta}{n_1^4}\right]}} \qquad (4.6)$$

$$\gamma_y = \frac{-4 n_x n_z}{n_1^2 \tan\theta \sqrt{\left[1 - \frac{n_z^2}{n_1^2 \sin^2\theta}\right]\left[1 - \frac{n_z^2}{n_1^2 \sin^2\theta} + n_x^2 n_z^2 \frac{\cot^2\theta}{n_1^4}\right]}} \qquad (4.7)$$

Therefore, C3 is found to be equal to 0.1256 and C4 is 0.8743. Now, if we return to equation 4.3, the computation of k_y / k_z yields 0.44 for the 875 cm^{-1} band and 4.372 for the 1019 cm^{-1} band. Then the k_x / k_z ratios can be calculated, since R1 is the k_y / k_x ratio, and yieldS 0.46 for the 875 cm^{-1} band and 3.5 for the 1019 cm^{-1} band.

The orientation functions can be calculated using equations 8 and 9 below.

$$\frac{2\frac{k_y}{k_z} - \frac{k_x}{k_z} - 1}{\frac{k_y}{k_z} + \frac{k_x}{k_z} + 1} = 2 p_{200}(\beta) P_{200} + 4 (p_{200}(\beta) - 1) P_{202} \qquad (4.8)$$

$$\frac{\frac{k_x}{k_z} - 1}{\frac{k_y}{k_z} + \frac{k_x}{k_z} + 1} = 4 P_{200}(\beta) P_{220} + \frac{4}{3}(P_{200}(\beta) - 1) P_{222} \qquad (4.9)$$

Where $p_{200}(\beta) = 0.5\,(3\cos^2\beta - 1)$. For the 875 cm^{-1} band, $\beta \sim 85°$, $p_{200}(\beta)$ is equal to 0.488 and for the 1019 cm^{-1} band, $\beta \sim 20°$, is calculated equal to 0.8245.

Equations 4.8 and 4.9 can be set as four equations with four unknowns and can be solved simultaneously in order to yield P_{200}, P_{220}, P_{202} and P_{222}. In our case, P_{200} was calculated equal to 0.29 and P_{220} equal to 0.0885.

Therefore, the direction cosines, using equations derived by Jarvis et al[205], yield:

$(\cos^2[yY]) = 0.52$ Machine direction

$(\cos^2[yX]) = 0.41$ Transverse direction

$(\cos^2[yZ]) = 0.06$ Thickness direction

It is observed that the biaxial stretching of the PET 506 film has induced more orientation in the machine direction as compared with the transverse direction. The orientation in the thickness direction is small as compared with the other two directions.

4.5: Measurement of T_g, T_m and degree of crystallinity of polyester films

Two different polyester films were used in order to measure their glass transition temperature and their degree of crystallinity. The first film to be considered is biaxially oriented PET 506

and the second is biaxially oriented PEN Kalabex S1020. The measurement was performed using a differential scanning calorimeter (Perkin Elmer DSC 7).

The sequence of the experiment, for PET 506, was first to hold the sample of 6.59 mg weight at a temperature of 30 °C for 1 min. Then the sample was heated from 30 °C to 280 °C at a heating rate of 10 °C / min. Finally the sample was held at a temperature of 280 °C for 2 min. For the PEN Kaladex S1020 sample of 5.03 mg weight, a very similar sequence was followed with the only difference being the upper heating temperature, which in this case was 290 °C.

Figure 4.29 presents the T_g related peak in the case of PET 506. The observed T_g is equal to 78.8 °C . The respective value for PEN Kaladex S1020 is 120.2 °C. It is clear that the T_g of PEN Kaladex S1020 is higher than that of PET 506. The agreement of the observed T_g values with previously published data will be considered in the discussion of the results chapter.

Figure 4.30 shows the melting peak of the PET 506 sample. At first it is important to note that the melting temperature, T_m, of PET 506 is 254.6 °C. Secondly and most important, the area under the melting peak represents the heat of fusion, ΔH_f, of the sample under investigation. In this case ΔH_f is equal to 37.0435 J / g. This value can be used in order to calculate, if the heat of fusion of the 100 % crystalline material is known, the degree of crystallinity of the sample. Mehta et al[206] have reported the theoretical value of 100 % crystalline PET to be equal to 140 J / g. Therefore, the crystallinity of PET 506 is found to be equal to 26.46 %.

In addition, figure 4.31 presents the melting peak of the PEN Kaladex S1020 film sample. The T_m is observed to be 264.8 °C and is therefore 10 °C higher than that of PET 506. The area under the melting peak is equal to 37.9482 J / g. Using a previously reported theoretical value[207] of the heat of fusion of 100 % crystalline PEN which is 103.4 J / g, the crystallinity of the PEN Kaladex film sample can be calculated. The calculated value yields 36.7 % crystallinity. This value is significantly, (10 %) higher than the respective value of PET 506.

4.6: Local adhesion measurements of bare substrates by AFM

Measuring surface adhesive properties of display polyester substrates is important when additional display layers, in this case ITO conductive coating, are deposited on top of the polymer base.

In this section the local adhesive pull – off force, measured by contact – mode AFM, of the surface treated PET ST506 and the PEN Kaladex S1020 is measured. The aim is to compare the adhesion of the two surfaces. The adhesive force F, is calculated by multiplying the cantilever spring constant K, 0.12 N / m, with the tip displacement, x. Using Hooke's law, F = K x. Silicon nitride cantilevers were used with tips of 50 nm radius. Seven measurements for each sample are considered in this experiment. The original scanned surface area was 1 nm^2 for all measurements.

Figures 4.32 and 4.33 present typical force calibration plots for PET ST506 and PEN Kaladex S1020 samples respectively. The ramp size is equal to 1.163 μm for both cases. Also, the scan rate was set to 1.163 Hz for both cases.

Figure 4.34 summarizes the measurements for both substrates. PET ST506 is found to show a higher adhesive force, 39.3 ± 3.07 nN, as compared to PEN Kaladex S1020, 33.6 ± 0.47 nN. However, the PET ST506 measurements showed a larger deviation than those of PEN Kaladex. This can be attributed to the higher rms roughness of the PET ST506 substrate. As will be discussed in detail in chapter 7 these measurements provide only a rough indication of the surface adhesive properties since they represent local behaviour.

4.7: Electrical and optical properties of ITO on polyester substrates

The electrical resistivity of ITO layers, which are deposited on polyester substrates, is a critical parameter that determines the electrical properties of the conductive display layer. Electrical resistivity, (equation 4.10), of various samples, as table 4.1 indicates, was measured using a built in - house four-probe system to measure resistance R, with probe spacing of 1 mm.

The thickness of the ITO was determined by performing weight measurements, employing a microbalance of four decimal places accuracy, on coated and uncoated samples and by using the theoretical density[208] of ITO which is 7.1 g / cm^2.

$$\text{Resistivity} = R\, t_f \qquad (4.10)$$

The lowest resistivity values are observed for ITO deposited on PET 506. The second lowest resistivity is noted for ITO on PET ST506. The third best resistivity minimum and maximum value is observed for ITO on PEN Teonex Q65. The highest minimum and maximum resistivity values are observed for the case of ITO on PEN Kaladex S1020.

In addition, table 4.2 shows the transparency values, at 613 nm wavelength, obtained for ITO coated and uncoated polyester substrates. The measurements were conducted using a laser diode at 638 nm. Bare PET 506 substrate exhibits 89 % optical transparency. The transparency of PEN Kaladex S1020 flexible substrate is 8.5 %. ITO coated PET 506 exhibits 90 % transparency and ITO coated PEN Kaladex S1020 display anode is 87 % transparent. It is worth mentioning that the coated substrate optical transparency values are normalized with respect to the bare substrate values.

4.8: ITO deposition on PEN Kaladex S1020 by PLD at room temperature

Indium tin oxide thin films were prepared by pulsed laser deposition on PEN Kaladex S1020 substrates at room temperature. ITO films were prepared using a *KrF* excimer laser (Lambda Physik). The laser was operated at 10 Hz frequency and the energy density of the laser beam at the target surface was 3 J/cm. For the pre-ablation of the target, 500 shots were fired and for the actual deposition 4000 shots were fired.

The PEN samples were prepared by cutting a circular section, of 0.8 cm radius, from a PEN biaxially oriented sheet. The substrates were cleaned, prior to deposition, for 15 min using acetone and 15 min using ethanol and then they were rinsed with distilled water and dried using compressed air. The cleaned substrate was attached to the substrate holder using 'blue-tak' adhesive, which can be easily removed after deposition at room temperature.

The diameter of the circular ceramic target, 90% In_2O_3 and 10% SnO_2 by weight, was 25 mm and its thickness 5 mm. The vacuum created in the chamber was of the order of 10^{-6} Torr. The deposition pressures, PO_2, used were in the range of 2.5-20 mTorr.

The film thickness, t_f, was measured by performing weight measurements, employing a microbalance of four decimal place accuracy, before and after deposition and by using, for the thickness calculations, the density of the ceramic target, which is 7.1 g/cm^2. Typical film thicknesses were 240 ± 35 nm with no significant change or trend with oxygen background pressure.
The average electrical resistance, R, of the films was measured, in eight different but symmetrical places on each sample, using a four-probe system with probe spacing of 1mm.

Microstructural studies were performed using x-ray diffraction (XRD) and the surface of the films was studied using an atomic force microscope (AFM, Digital Instruments) in contact-mode.

Optical transmittance measurements were conducted using a 638 nm laser diode and photocell system and the average of five measurements, for each film, is considered in this work. The adhesive surface force properties of the produced films were measured using AFM and a mean value of six measurements at different symmetrical places, for each sample, is presented.

Figure 4.35 shows the electrical resistivity (ρ) and optical transmittance dependence on oxygen background pressure for ITO films deposited at room temperature on PEN substrates. Low resistivity and high optical transmission values are observed for pressures ranging from 7.5 mTorr to 12.5 mTorr. The lowest resistivity, $\rho = R\ t_f$, is $1.04*10^{-4}\ \Omega$ cm for 7.5 mTorr oxygen pressure whereas, the maximum resistivity and lowest optical transmission are both observed to occur at 2.5 mTorr pressure. The highest optical transmission, 90.4 %, occurred at 10 mTorr background pressure.

Also, figure 4.36 shows X-ray diffraction data which reveal the lack of distinct ITO diffraction peaks and the reduced peak intensity of the characteristic semi-crystalline PEN peak, at $\sim 26^0\ 2\theta$, for the coated film is consistent with the presence of an amorphous ITO coating.

In addition, figure 4.37 shows the ITO surface layer morphology and growth mode, in the case of 10 mTorr background oxygen pressure, as studied by contact-mode AFM. The existence of coalesced and post-coalesced amorphous islands in the nano-scale is evident in the film. The lowest surface root mean square (rms) roughness, 1.3 nm, is observed at 10 mTorr PO_2.

The adhesive force, as shown in figure 4.38, plotted against oxygen background pressure is observed to reach a maximum, 35.5 ± 0.5 nN, at 10 mTorr.

5. Mechanical properties

5.1: Uniaxial tensile testing of bare substrates

PET 506 and PEN Kaladex S1020 polyester substrates were tested, using an Instron 5520 mechanical testing machine, under uniaxial tension and at 1 mm / min crosshead speed.

Dumb - bell samples, 25 mm long and 5 mm wide, were cut at different angles, with respect to x – axis, which is defined in figure 5.1. Young's modulus values were extracted from the initial linear regime of stress – strain curves.

The Young's moduli, for different angles, are compared for both materials as shown in figure 2. Generally, PEN Kaladex S1020 exhibits higher elastic modulus values, as compared to PET 506, for all angles. The mean Young's modulus for PET 506 is 2.35 ± 0.29 GPa. The mean elastic modulus for PEN Kaladex S1020 is 3.3 ± 0.37 GPa. It is therefore apparent that PEN Kaladex S1020 has a mean value, which is 1 GPa higher than that of PET.

PET 506 display substrate exhibits highest and comparable modulus values, around 2.7 GPa, at 0^{o} and 90^{o} degrees with respect to the A4 sheet x – axis. Similar behaviour is exhibited by PEN Kaladex S1020 film with highest modulus value, being at 0^{o} with respect to x – axis, around 3.9 GPa.

The modulus value for 90^{o} is lower and equal to 3.5 GPa. Lower elastic moduli, as compared with values measured at 0^{o} and 90^{o}, were obtained at 30^{o}, 45^{o}, 60^{o} and 75^{o} for both film substrates. This may be related to the biaxial orientation that both films exhibit, and this will be discussed further in chapter 7.

5.2: Tensile testing of coated and uncoated samples

The Young's modulus of the ITO coating, $E_{coating}$, can be determined using the rule of mixtures, equation 5.1.

$$E_{composite} = f\,E_{coating} + (1 - f)\,E_{substrate} \qquad (5.1)$$

Where $E_{composite}$ is the modulus of the coated system, f is the film thickness to substrate ratio and $E_{substrate}$ is the Young's modulus of the bare substrate[103,129].

It is therefore relatively easy to conduct tensile tests using bare and ITO coated polyester substrates, at the same crosshead speed, in order to extract the modulus of the ITO film.

Figure 5.3 shows a typical example for ITO coated and uncoated PET 506 tensile tested films at a crosshead speed of 0.03 mm / min. The modulus of the coated system is higher than that of the uncoated substrate.

Using equation 5.1 and the thickness value of the ITO film, obtained from weight measurements and ~120 nm in this case, the Young's modulus is calculated to be 220 GPa. Following the same procedure for ITO on PET ST506 the coating modulus is similar, 215 GPa.

The modulus of ITO, when deposited on PEN Kaladex S1020, is found to be 180 GPa. When ITO is deposited on PEN Teonex Q65 the conductive layer's elastic modulus is slightly lower than previously, 175 GPa. Table 5.1 summarizes the experimentally determined ITO Young modulus values for different polyester substrates. The crosshead speed for all experiments was 0.03 mm / min.

5.3: Uniaxial tensile electromechanical testing of flexible display anodes

5.3.1: Uniaxial tensile monotonic behaviour of ITO coated PEN Kaladex S1020 at low applied strains

The uniaxial tensile behaviour of ITO coated PEN Kaladex S1020 flexible display anodes and the resulting ITO surface was assessed ex – situ by contact – mode AFM on the same day. Electrical resistance was not monitored in – situ. The primary aim of this experiment was to observe, optically, at which applied uniaxial strain cracks are formed.

Figure 5.4 shows the relation of the c – m AFM measured crack depth with the applied uniaxial tensile strain. Up to 2 % strain, employing a crosshead speed of 0.3 mm / min, no cracks are formed. Then the crack depth is increasing to approximately 15 nm at 3 % strain and 20 nm at 4 % strain. When strain is increased to 6 % the crack depth is increasing to approximately 45 nm. This suggests a 55 % increase in experimentally measured crack depth.

Furthermore, figure 5.5 presents an AFM image of an ITO surface, on PEN Kaladex S1020, which has been tensile tested to 2 %. There are no cracks formed at 2 % uniaxial tensile strain. However, ITO inter – island minor separation occurs, as compared to virgin samples.

Figure 5.6 shows an AFM image and measurement of, perpendicular to the tensile direction, cracking and transverse buckling zone development at 3 % applied tensile strain. It is interesting to observe an unusual crack cross – sectional view. It appears that either ITO folding occurred or fractured ITO brittle fragments gathered at the crack edges. The edge – to – crack depth is approximately 140 nm.

Additionally, figure 5.7 presents an ITO intact region as imaged by ex – situ c – m AFM. There is no strong evidence of inter – island deformation. It is important to note that 20 nm deep cracks have been formed at this stage.

Also, figure 5.8 shows an AFM measured cross – section and image of an ITO - PEN Kaladex S1020, surface uniaxially strained to 6 %. Similar crack morphology, as in figure 5.6, is observed in some limited cases. However, the ITO layer exhibits strong transverse buckling behaviour. The intact ITO region, investigated for this particular applied strain, is presented in the 3D AFM image in figure 5.9. It is apparent in this case, that island tensile straining occurs. The ITO behaviour and failure mechanisms at the relatively low applied strain regime will be further discussed in chapter 7.

5.3.2: Monotonic uniaxial tensile electromechanical behaviour of flexible anodes

This section is related to the electromechanical response of ITO coated polyester anodes, which are tested under uniaxial tension. Results are compared for the different substrates used. The electrical resistance of the ITO coating is monitored in – situ. Changes in the electrical resistance of the layer, critical onset strain (COS), are associated with structural changes of the composite system. Two different crosshead speeds are employed. A low crosshead speed equal to 0.03 mm / min and a higher equal to 03 mm / min. The samples are cut from the A4 sheet using a hydraulic press in 'dog – bone' shape and their gauge length is 15 mm. Their width is 4.5 mm. Uniaxial tension is applied parallel to the machine direction for all samples.

The electromechanical response of ITO coated PET 506, PET ST506 and PEN Kaladex S1020 for 0.03 mm / min crosshead speed is presented in figure 5.10. The measured, normalized, electrical resistance is plotted against uniaxial tensile applied strain. Increase in electrical resistance is not desirable in flexible display applications and is generally associated with coating cohesive and / or adhesive mechanical failure.

ITO coated PET 506 and PET ST506 substrates exhibit similar electromechanical behaviour. Their electrical resistance increases gradually after approximately 2.2 % uniaxial strain. However, a sudden increase in the electrical resistance, at a lower strain, is observed for ITO coated PEN Kaladex S1020 as compared to ITO coated PET 506 and PET ST506 anodes.

When a higher, 0.3 mm / min, crosshead speed is employed, the electromechanical behaviour of ITO coated PEN Kaladex S1020 and PEN Teonex Q65 is similar to previous behaviour and is shown in figure 5.11. The electrical resistance increases suddenly in both cases. On the other hand, the resistance increase for ITO coated PET 506 is more gradual as compared to the two previous cases. However, ITO coated PET ST506 shows the best behaviour but when the resistance increases it follows a gradual pattern similar to the ITO / PEN case.

Figure 5.12 summarizes the critical onset strain mean values when various coated substrates are tested in tension using a crosshead speed of 0.03 MPa. ITO coated PET 506 and PET ST506 flexible display anodes have similar mean COS values around 2.2 %. PET ST506 substrate seems to be the best candidate. ITO coated PEN Kaladex S1020 exhibits a significantly lower COS mean value around 1.4 %.

In addition, figure 5.13 summarizes the COS mean values for different coated substrates when a higher crosshead speed of 0.3 mm / min is employed. The highest COS value is observed for ITO coated PET ST506 and is around 2.1 %, a similar value observed in the lower speed case. ITO coated PET 506 and PEN Teonex Q65 anodes have similar COS mean values, around 1.6 %. As compared to the lower speed value, ITO coated PET 506 exhibits lower COS. The lowest mean strain, at which conductive failure initiates, is observed for ITO coated PEN Kaladex S1020 and is around 1.3 %. However, it is important to note that the standard deviation of the measured data is the largest for ITO coated PEN Kaladex S1020 samples.

Furthermore, figures 5.14 and 5.15 show typical stress – strain – electrical resistance graphs for ITO coated PET 506 and ITO coated PEN Kaladex S1020 composite films respectively for 0.03 mm /min crosshead speed. It is possible to locate the substrate tensile stress at which

electrical resistance increases. Results are summarized in figure 5.16. The mean tensile stress at the critical onset strain is similar for all substrates used and lies between 40 to 50 MPa.

Figures 5.17 and 5.18 present typical stress – strain – electrical resistance graphs for ITO coated PETST 506 and ITO coated PEN Teonex Q65 composite films respectively for 0.3 mm /min crosshead speed. However, large deviation of the corresponding tensile stresses is observed, when the crosshead speed is 0.3 mm / min, for ITO coated PEN Kaladex S1020 as figure 5.19 shows.

5.3.3: Uniaxial tensile coating ex – situ microscopical investigation

After uniaxial tensile electromechanical testing of ITO-coated polyester substrates, SEM and contact – mode AFM investigations were carried out in order to observe the ITO, deposited on various polyester substrates, failure mechanisms at various applied tensile strains.

Figure 5.20 shows cracking and transverse buckling perpendicular to the tensile direction for an ITO surface deposited on PET ST506 substrate, strained at 75 %. De - cohesion and de - adhesion of the ITO are evident. In the polymer substrate underneath the ITO surface, darker regions, are visible.

In addition, figure 5.21 presents failure mechanisms for ITO, on PEN Kaladex S1020, strained to 35 % uniaxial tensile strain. Perpendicular to the applied stress direction, cracking is evident. Transverse buckling zone formation is also present. However, the level of delamination is not as strong as in the previous case, i.e. figure 5.20. There are relatively large edge - shaped regions, around 10 μm in length, where the ITO coating material has been totally removed. In these parts the underlying substrate is visible. Furthermore, figure 5.22 shows a contact – mode AFM image of an ITO surface, sputtered on PET 506. A crack and a part of a transverse buckling deformed zone are presented. The tensile deformed islands are also visible. It is interesting to note the absence of ITO debris inside the crack.

Also, it is important to underline that the lower part of the ITO coating, which forms the interface with the PET 506 substrate, does not seem to exhibit ITO island morphology. This issue will be discussed further in chapter 7. The depth of the measured crack can be measured using contact – mode AFM, as figure 5.23 indicates. The measured depth is found to be approximately 116 nm. The crack cross –sectional view may suggest that the crack initiated from a surface flaw and arrested at the ITO / polymer interface.

Also, figure 5.24 shows a contact – mode AFM image of an ITO surface, on PET 506, strained till 20 %. Primary and tertiary cracks, perpendicular to the applied force direction, are observed. A buckling zone, parallel to the straining direction, exists in the imaged part. Close and open buckling morphology can be observed.

Additionally, figure 5.25 presents a cross – sectional view of crack formation perpendicular to the tensile direction, on an ITO, deposited on PET 506, surface strained till 30 % of its original length. Various cracks of approximately 115 maximum depth are observed. Open buckling transverse zone formation is also evident.

Figure 5.26 shows a contact – mode AFM buckling zone measurement for an ITO, on PET ST506 display substrate, surface uniaxially strained till 10 %. The measured tip deflection height in this particular case is approximately 218 nm. The buckling zone base width can be also determined. As will be discussed in chapter 7, buckle tip height and base width ex –situ contact – mode AFM measurements can be used in order to calculate, roughly, the strain at which buckling occurs.

Furthermore, figure 5.27 shows the cracking cross –sectional view of an ITO, deposited on PET ST506 substrate, surface strained till 20 %. Maximum recovered crack depth is approximately 100 nm in this case. Open buckling morphology, parallel to the tensile force direction, can be also observed. A buckling zone cross – sectional view, obtained by c – m AFM, is presented in figure 5.28 for an ITO coating on PEN Kaladex S1020 strained till 12 %. The measured vertical buckle tip deflection is approximately 160 nm.

Figure 5.29 shows a contact mode AFM 2D image of an ITO, on PEN Kaladex S1020 substrate, surface strained till 30 % in uniaxial mode. It is interesting to note that a crack, which forms a 45° angle with the tensile direction, is observed. There is some bridging ITO material within this particular crack. Transverse buckling zone formation is also evident.

In addition, figure 5.30 presents a 3D AFM image of an ITO on PEN Teonex Q65 flexible display substrate, surface uniaxially strained till 20 %. Perpendicular to the tensile direction cracking is observed. Also, transverse buckling zone formation can be detected. It is important to note the cracks 'climbing up' the buckling zone deflected area. Tip height values vary in different position of the buckled zone.

Finally, figure 5.31 shows a buckling zone cross – sectional view measured by contact – mode AFM for an ITO, sputtered on PEN Teonex Q65, surface strained till 30 %. Measured buckle tip height is approximately 315 nm. Perpendicular, to the tensile direction, cracks are observed to cut through the buckled zone.

5.3.4: AFM measurements of failure patterns for uniaxially tensile tested flexible anodes

Various ex – situ measurements were conducted using contact – mode AFM after the electromechanical uniaxial tensile testing of various surfaces of ITO on polyester substrates. Measurements include non - recovered coating crack depth, crack opening, crack spacing, number of cracks, number of buckling zones, buckling zone tip heights and buckling zone base widths. All these are characteristic parameters of cohesive and adhesive ITO failure and can be plotted against applied strain in order to study the coating's mechanical behaviour when deposited on various polyester display substrates.

Figure 5.32 shows the non - recovered crack depth dependence with applied tensile strain for ITO-coated PET 506 and PET ST 506 substrates and crosshead speeds of 0.03 mm / min. Up to 6 % applied strain no measurable crack depth exists for ITO on PET ST506. However, the crack depth at 6 % strain was measured and was found to be approximately 18.5 nm. As the applied strain increases, the non - recovered coating crack depth increases for both base substrates. At a relatively large applied strain of 20 %, the crack depth reaches 75 nm for ITO PET ST506 and 40 nm for ITO PET 506 respectively. Large deviations in measurements at high strains are observed.

Additionally, figure 5.33 presents measured crack depth as a function of applied uniaxial tensile strain when PET 506, PEN Kaladex S1020 and PEN Teonex Q65 substrates are used at 0.3 mm / min crosshead speed. No crack depth was detected at 10 % strain for ITO coated PET 506. On the other hand crack depths around 11 nm were measured for the other two substrates. When applied strain increases, measured non – recoverable crack depth increases. It reaches approximately 110 nm when the applied strain is equal to 30 % for ITO on PEN Kaladex S1020 and Teonex Q65. The measured crack depth for ITO on PET 506 is the lowest at 30 %. On the other hand, the highest measured crack depth, at 20 % and 30 % applied strains, is that of PEN Teonex Q65. However, it is evident, as previously observed, that large deviations in measured crack depth occur when high strains are employed.

Furthermore, figure 5.34 shows the variation of, c – m AFM measured, non – recoverable crack opening against applied uniaxial strain for ITO deposited on PET 506 and PET ST506 substrates and 0.03 mm / min crosshead speed. For 6 % strain only the crack opening of ITO on PET 506 is measurable and equal to approximately 370 nm. As the applied strain increases the crack opening increases for ITO on PET ST506 and reaches a mean value of approximately 1775 nm at 20 % applied tensile strain. However, the value for ITO on PET 506 does not exceed 740 nm for a strain of 20 %.

Also, figure 5.35 presents the non – recoverable crack opening dependence on applied strain for ITO deposited on PEN Kaladex S1020 and PEN Teonex Q65 for 0.3 mm / min crosshead

speed. At a relatively low strain of 3 % the crack opening value of ITO on PEN Teonex Q65 is approximately 223 nm whereas for ITO on PEN Kaladex S1020 is 524 nm. As the strain increases the crack opening increases and reaches approximately 2154 nm for ITO deposited on PEN Kaladex S1020 at 30 % applied tensile strain.

In addition, figure 5.36 presents the variation of crack spacing with respect to the applied uniaxial tensile applied strain for ITO coated PET 506 and PET ST506 and 0.03 mm / min crosshead speed. At a relatively low strain, 6 %, the crack spacing for ITO on PET 506 is approximately 5 μm. As the applied strain increases the crack spacing decreases and reaches a mean value of 2.6 μm for ITO on PET ST506 and applied strain 20 %.

Also, figure 5.37 presents the crack spacing against the applied tensile strain for ITO on PET 506, PEN Kaladex S1020 and PEN Teonex Q65 substrates for 0.3 mm / min crosshead speed. For 10 % applied strain, the crack spacing is approximately 3.5 μm for ITO on PEN Teonex Q65 and a comparable value for ITO on PEN Kaladex S1020 is observed. As strain increases the crack spacing decreases for ITO on PET 506 and ITO on PEN Kaladex S1020 remains almost stable.

Furthermore, figure 5.38 shows the number of cracks, per 10 μm, with respect to applied tensile strain for ITO deposited on PET 506 and PET ST506 and crosshead speed of 0.03 mm / min. At relatively high applied strains, above 12 %, more cracks are observed for ITO on PET ST506 as compared with ITO on PET 506.

Additionally, figure 5.39 presents the number of cracks, per 10 μm, with respect to applied tensile uniaxial strain for ITO deposited on PEN Kaladex S1020 and PEN Teonex Q65 and crosshead speed of 0.3 mm / min. For ITO on PEN Teonex Q65 the number of cracks shows a linear increase with respect to applied strain whereas for ITO on PEN Kaladex S1020 the number of cracks saturates after 20 % tensile strain.

Also, figure 5.40 shows the number of transverse buckling zones, per 250 μm, against applied tensile uniaxial strain for ITO sputtered on PET 506 and PET ST506 and crosshead speed 0.03 mm / min. For a relatively low applied strain, 6 %, 14 buckling zones are observed for ITO on PET ST506. When the applied strain increases the number of transverse buckling zones increase and reaches 30 for ITO on PET 506 at a strain of 20 %.

Furthermore, figure 5.41 presents the number of transverse buckling zones, per 250 μm, against applied tensile uniaxial strain for ITO sputtered on PET 506, PEN Kaladex S1020 and PEN Teonex Q65 and crosshead speed 0.3 mm / min. At high applied tensile strains, above 20 %, ITO on PET 506 is observed to exhibit the most buckled zones whereas ITO on PEN Kaladex S1020 exhibits the least. However, at low applied strains, below 10 % strain, the previous situation is reversed.

Additionally, figure 5.42 shows the, c – m AFM measured, buckle tip vertical height with respect to applied tensile strain for ITO deposited on PET 506 and PET ST506 and crosshead speed equal to 0.03 mm / min. For a relatively low applied uniaxial tensile strain, 6 %, the tip heights are comparable, around 100 nm, for both composite systems whereas for higher strains, such as 20 %, ITO on PET 506 buckle vertical deflection is measured equal to 530 nm and ITO on PET ST506 buckle vertical deflection was found to be 360 nm.

The buckle tip vertical deflection, with respect to applied uniaxial tensile strain, for ITO on PET 506, PEN Kaladex S1020 and PEN Teonex Q65 for 0.3 mm / min crosshead speed is presented in figure 5.43. Relatively low tip deflections are observed for ITO sputtered on PET 506. At high applied strains the highest vertical deflections are observed for ITO on PEN Kaladex S1020.

Also, figure 5.44 presents the buckling zone base width, as measured ex - situ by c – m AFM, plotted against applied tensile strain for ITO on PET 506 and PET ST506 and 0.03 mm / min crosshead speed. ITO on PET 506 is observed to exhibit lower base width values as

compared to ITO on PET ST506. As the strain increases the base width increases for both composite systems and reaches 2.5 μm at 20 % strain for ITO on PET ST506.

Finally, figure 5.45 shows the buckling zone base width, as measured ex - situ by c – m AFM, plotted against applied tensile strain for ITO on PET 506, PEN Kaladex S1020 and PEN Teonex Q65 and 0.3 mm / min crosshead speed. Comparable base width values are observed for all three different systems at applied strains up to 20 %. However, at the highest applied strain, 30 %, ITO sputtered on PEN Teonex Q65 exhibits the highest base width whereas ITO on PET 506 is observed to exhibit the lowest base width value. As will be discussed in chapter 7, base width and buckle tip heights can be used in order to roughly approximate critical coating buckling strains.

5.3.5: Electromechanical tensile cyclic investigation of flexible display anodes

It is important to investigate the electromechanical response of flexible display anodes under a cyclic tensile stress and observe if the electrical resistance recovers when unloading the sample. ITO sputtered on PET 506, PET ST506 and PEN Kaladex S1020 samples, with the same dimensions with those used in monotonic experiments, was investigated under tensile cyclic conditions, at low applied tensile strains, with in – situ electrical resistance monitoring. Ex – situ contact mode AFM and optical microscopy were employed, after testing, in order to examine the ITO surfaces and detect possible failure mechanisms.

Figure 5.46 shows the stress – strain – electrical resistance response for ITO on PET 506, composite film which was strained between 0 % and 3 % for 8 loading – unloading cycles using 0.05 mm / min crosshead speed. The resulting applied cyclic stress was between 0 and 88 MPa. The normalized electrical resistance increases to about 240 kΩ for the first cycle. However, during the first cycle electrical resistance recovery is observed. Electrical resistance is observed to exhibit a linear increase till the start of the 6^{th} cycle. After the 6^{th} cycle large increases and consequent decreases of the monitored coating resistance are

observed till a final value of approximately 5600 kΩ is reached. When the ITO surface is investigated, after testing, by c – m AFM, as figure 5.47 shows, transverse buckling is clearly evident. Perpendicular, to the tensile direction, conductive layer folding is also visible. It is important to note the absence of cracking.

Furthermore, figure 5.48 presents the electromechanical response of ITO deposited on a PET 506 substrate, which is strained between 0 and 2 % tensile strain for 6 cycles and 0.05 mm / min crosshead speed. For the 1st cycle the electrical resistance increases at 0.7 % strain and then increases significantly at about 1.1 % strain and continues to increase upon unloading. As more cycles are applied to the sample the electrical resistance exhibits a tendency to increase further. No significant resistance recovery is observed. After almost 6 cycles the resistance reaches 250000 Ω.

An intact coating area was investigated by AFM, as figure 5.49 shows, and revealed the tendency of ITO to de – adhere from the underlying substrate. A clearer representation of the ITO failure mechanism(s), was obtained when a larger surface area, 1600 μm^2, was examined using contact – mode AFM, as figure 5.50 indicates. Parallel and perpendicular to the tensile direction, adhesive failure as well as coating folding is clearly visible.

In addition, figure 5.51 shows the electromechanical response of ITO on PET 506, strained between 0 and 1.5 % uniaxial strain for 11 cycles and crosshead speed equal to 0.05 mm / min. During the first cycle, electrical resistance increases during loading, at approximately 1 % strain and then levels till 1.5 % applied strain. During unloading, the electrical resistance further increases. At a relatively high number of cycles, above 8, electrical resistance increase levels. The highest normalized resistance observed is 1300 Ω for 11 cycles. Microscopical investigation, figures 5.52 and 5.53, reveals formation of a non – recovered buckling zone, which is approximately 300 nm high.

Behaviour similar to that observed previously is exhibited for ITO on PET ST560 strained between 0 and 1.8 % for 12 cycles and 0.05 mm / min crosshead speed, as figure 5.54 shows. However, the highest electrical resistance is 4600 Ω in this case. The presence of buckled

zones, parallel to the tensile direction, is evident as figures 5.55 and 5.56 indicate. The absence of coating cohesive failure, perpendicular to the tensile direction, should be noted.

When ITO deposited on PEN Kaladex S1020 is tested for 5 cycles between 0 and 2 % tensile strain and 0.05 mm / min crosshead speed, electrical resistance does not recover, as figure 5.57 shows. The highest normalized electrical resistance in this case is measured to be approximately 60000 Ω. Contact-mode 3D AFM image, figure 5.58, shows ITO transverse buckling formation and non - recovered folded cracking. The observed folded crack depth was measured, using AFM as figure 5.59 shows, and is equal to approximately 16 nm.

5.4: Controlled buckling electromechanical testing of ITO coated polyester electrodes

5.4.1: Single - cycle electromechanical response

It is important to monitor the electromechanical behaviour of flexible display anodes when they are loaded and unloaded under buckling. This section is concerned with ITO coated polyesters when they are compressed, with the ITO being on the convex and then concave side of the two – layer system, for one loading – unloading cycle. During the experiment ITO electrical resistance was monitored in – situ. The crosshead speed was 1 mm / min and the sample dimensions are the same as the ones used in tensile experiments.

Figure 5.60 shows the electromechanical behaviour of ITO on PET 506 surface under compression. Upon loading an increase in electrical resistance is observed at around 1.1 % buckling strain. Then, the resistance increases linearly until the end of the loading portion of the cycle. During unloading the resistance shows little increase till the final stages where a more sudden increase is observed.

When the surface is placed under tension, monitored electrical resistance is observed to initially decrease and then it increases till it reaches approximately 0.9 % buckling strain as figure 5.61 indicates. At this strain, the measured resistance is higher than the initial value. The resistance continues to increase for the remaining loading part. During unloading, the ITO electrical resistance further increases. When the sample approaches the initial flat shape, some resistance recovery is exhibited.

Furthermore, when the conductive ITO layer (deposited on PET ST506) and its surface is placed under compression, an interesting response, in electrical resistance terms, is observed as figure 5.62 presents. During the loading portion, a significant decrease in ITO resistance is exhibited. The measured resistance exceeds the initial value at approximately 1.9 % buckling strain. Further resistance increase is observed up to the end of the loading portion. During unloading, the layer resistance further increases but towards the finish of the unloading it fully recovers.

Also, figure 5.63 shows the electromechanical buckling behaviour of an ITO on PET ST506 surface in tension. After a short decrease, electrical resistance increases and exceeds the initial value at around 0.5 % buckling strain. Then the resistance increases almost linearly until the end of the loading part. During unloading, further electrical resistance is noted and little recovery is observed towards the final stages.

In addition, figure 5.64 presents the electromechanical buckling behaviour of an ITO on PEN Kaladex S1020 surface in compression. The resistance increases at around 1.3 % buckling strain and continues to increase gradually till the end of the loading part. During unloading, little electrical resistance increase is observed and some recovery is noted when the sample tends to attain its initial flat shape.

Finally, figure 5.65 shows the electromechanical buckling behaviour of an ITO on PEN Kaladex S1020, surface under tension. At 0.4 % buckling strain, a large gradual increase in monitored resistance is observed until the end of loading. During unloading a further increase

in resistance is noted initially but towards the latter stages some significant resistance recovery is observed.

5.4.2: Controlled buckling under cyclic loading

An important deformation mode for in - service flexible displays, is buckling. This section is concerned with cyclic controlled buckling testing of 'dog bone' ITO-coated polyester samples, with the same dimensions as in the tensile experiments, and with in – situ resistance monitoring. The ITO surface can be placed under tension or under compression during testing. Ex – situ AFM, SEM and optical microscopy was also conducted in order to observe possible ITO coating failure mechanism(s).

Figure 5.66 shows the electromechanical buckling response of a surface of ITO on PET 506 which has been under compression for two cycles and 1 mm / min crosshead speed. The electrical resistance linearly increases to about 4.7 kΩ for the first loading part at a buckling strain equal to 2.45 %. During unloading, the normalized resistance further increases to approximately 8.8 kΩ and then decreases to approximately 6.3 kΩ till the full first cycle is completed. During the second cycle, electrical resistance further increases and the same behaviour is observed during unloading.

The final measured resistance is 18.5 kΩ. It is therefore apparent that limited resistance recovery occurred during the late stages of unloading. Contact – mode AFM investigation, (as figure 5.67 shows), of an intact ITO surface fragment does not suggest any change of the coating surface island topography.

However, figure 5.68 shows buckling failure of the ITO coated surface parallel and perpendicular to the compressive force direction. The measured vertical tip deflection of the buckled coating regions, as shown in figure 5.69 and obtained by c – m AFM, is approximately 100 nm. An SEM investigation, of an individual buckling zone (as shown in

figure 5.70), reveals open and closed buckling adhesive failure as well as delamination of the ITO coating from the underlying polyester substrate.

Furthermore, figure 5.71 shows the electromechanical buckling behaviour of ITO, sputtered on PET 506, surface when is under tension for 10 cycles between 0 and 2.45 % buckling strain. Interesting behaviour, in electrical resistance terms, is observed in this case. During the first loading, the ITO electrical resistance decreases until 1.3 % buckling strain and then gradually increases and is 3.45 kΩ when loading is completed. During unloading, the resistance further increases and reaches a final value of approximately 5 kΩ. The same pattern occurs during the second and the subsequent cycles. No electrical resistance recovery is observable.

However, an interesting point is that, unlike the previous experiment when the coating is under compression, the resistance during the later stages of unloading is observed to further increase. After 10 cycles, the final resistance reached is 670 kΩ. The failure mechanisms observed differ than those observed in the previous case. As revealed by using optical microscopy, figure 5.72, perpendicular to the applied force direction cracking, cohesive failure occurs as well as transverse buckling, adhesive failure. The depth of the non - recovered cracks is found to be approximately 16 nm as figure 5.73 shows.

Also, figure 5.74 presents the buckling behaviour of an ITO surface under compression, on a PET 506 flexible transparent electrode which is loaded and unloaded for 9 cycles with 1 mm / min crosshead speed. During the first loading, the resistance increases at around 1.7 % buckling strain to 200 Ω and then gradually increases to 2000 Ω at a strain of 2.45 %. During unloading the resistance further increases to 2200 Ω. The same behaviour is observed for the subsequent loading and unloading cycles. However, it is important to note that after the 4^{th} cycle significant electrical resistance recovery is observed in the unloading parts. During the 9^{th} unloading cycle the resistance is observed to significantly decrease from approximately 425 kΩ to 120 kΩ.

However, as will be discussed in detail in chapter 7, even after such recovery, electrical resistance has been significantly degraded after 9 cycles. SEM investigation, as shown in figure 5.75, of the tested ITO surface reveals a rather unusual buckling pattern, for uniaxial loading, parallel and perpendicular, to the loading axis. Closed and open buckling zones parallel and perpendicular to the applied compressive stress dominate ITO adhesive failure as shown in figure 5.76.

In addition, figure 5.77 shows the electromechanical buckling behaviour of an ITO, , on PET ST506 composite display electrode tested under compression for 10 cycles at 1 mm / min crosshead speed. During the first loading half – cycle, a decrease in electrical resistance is observed until 2.1 % buckling strain. Then the resistance increases to 3.2 kΩ at 2.45 % buckling strain. When the first unloading is completed, the resistance is observed to decrease to 1.4 kΩ. When the 10^{th} cycle is completed, electrical resistance has reached approximately 160 kΩ. Minor resistance recovery is observed during all the unloading portions.

ITO buckling is observed parallel and perpendicular to the uniaxial force direction, as figure 5.78 indicates. At a junction point which the parallel and perpendicular buckles form, cracking and ITO fragment delamination is observed, as figure 5.79 shows.

Furthermore, figure 5.80 shows the buckling behaviour in tension of an ITO surface, sputtered on PET ST506 anode material, which is repeatedly compressed for 10 cycles using a crosshead speed of 1 mm / min. After 4 cycles total electrical resistance degradation is observed.

Figure 5.81 shows the existence of cohesive failure cracking, perpendicular to the compression direction as well as transverse buckling zone formation. Observation of an individual buckling zone, as figure 5.82 presents, reveals periodic open and closed buckled regions.

Also, figure 5.83 presents the electromechanical buckling behaviour under compression of an ITO, surface, deposited on PEN Kaladex S1020 composite film, which is tested for a total of

10 cycles. The resistance increases at around 1.4 % buckling strain during the first loading. During unloading no significant resistance recovery is observed. After the 10^{th} cycle, the electrical resistance approaches 200 kΩ. The coating failure mechanisms include adhesive and minor, cohesive failure at buckling zone junction points as shown in figure 5.84. The buckling zone vertical tip deflection, figure 5.85, is approximately 155 nm as measured by c – m AFM.

Finally, figure 5.86 presents the electromechanical buckling behaviour under tension of an ITO, surface, on PEN Kaladex S1020 thin anode, which is tested for 10 cycles. Total electrical degradation is observed during the 8^{th} cycle of the experiment.

However, significant resistance recovery is observed, upon unloading, after the 3^{rd} cycle. As shown in figure 5.87, coating cracking occurs, perpendicular to the loading axis, and buckling zone formation which is parallel to the compressive force direction. The non – recovered crack depth is found to be approximately 15 nm as obtained by c – m AFM. Figure 5.88 shows that buckling zones consist of closed and open parts. There is also limited ITO fragment detachment from the substrate.

5.5: Biaxial tensile electromechanical testing – preliminary results

In this section we test the ITO coating under equibiaxial tension with in-situ monitoring of the resistance. We aim to determine the crack onset biaxial threshold strain. We have built our own bulge test apparatus and have developed a simple technique to measure the resistance of the conductive layer as described in chapter 3.
We use a simple analytical model, the spherical cap model[154], in order to calculate the biaxial stress and strain of our composite film.

Figure 5.89 shows a typical biaxial stress-strain curve and the in-situ resistance measurement for ITO on PEN Kaladex S1020. The ITO layer is observed to have a critical onset biaxial strain at 1.4%. The resistance curve shows an increase at 1.4% which means that the cracking initiation process starts at that threshold strain. It should be pointed out that the resistance increases to 0.05 and then remains constant as soon as the test starts. Such increase can be attributed to the radial stresses that are present due to clamping of the sample in the bulging apparatus.

Furthermore, figure 5.90 shows an AFM image of the coating surface after testing. The final strain is calculated to be approximately equal to 3%, and reveals biaxially deformed island morphology. It is observed that the complex biaxial stress state lead to a deformation of the coating islands and to a rougher surface.

Finally, figure 5.91 presents a detailed image, acquired by FEG – SEM, of the coating failure pattern after biaxial tensile testing. Cracks are observed to propagate with curved trajectories until reaching another crack, which they intercept at almost right angles.

5.6: Comparison of experimentally measured bulge shapes for bare polyester substrates

In this section the experimentally measured bulge shapes, for between 0.01 and 0.12 MPa applied pressure, for three different substrates are compared. It is important to note that the deflection was measured, for each pressure, at four different points, 4.25 mm distance between two points, starting from the centre of the flat circular film and towards the clamped edge. At the clamped edge of the film the vertical deflection is assumed to be zero. Therefore five points in total can be plotted.

It is assumed that symmetry exists in the bulge shape, if slipping of the film from the edge is negligible, and therefore the whole bulge shape can be plotted in two – dimensional form with the x – axis representing the distance from the centre of the circular film, i.e. the bulge

diameter, and the y – axis representing the vertical displacement which is experimentally measured.

Figure 5.92 shows the two – dimensional bulge shape of three different bare substrates, namely PET 506, PET ST506 and PEN Teonex Q65 for a low differential pressure of 0.01 MPa. At first note that the central deflection of PET 506 is the highest out of the three measured. The lowest central deflection is that of PET ST506.

Also, in terms of the shape in general, the PET 506 shows a 'wavy' shape as compared with the PET ST506 shape. On the other hand, PET ST 506 and PEN Teonex Q65 shapes, at 0.01 MPa differential pressure, both show cap formation in the vicinity of the centre and as the edge is approached a change in the slope of the bulge profile is observed for both cases.

Figure 5.93 gives the bulge profile of the three substrates when pressure is increased to 0.02 MPa. It is observed that the profiles of PET 506 and PET ST506 have converged. It is also important to note that the shape of PEN Teonex Q65 substrate shows a restriction in the vicinity of the clamped edges. All three film profiles tend to converge in the centre close vicinity. Again the shortest profile, out of all three, appears to be that of PEN Teonex Q65.

As pressure increases to 0.03 MPa of differential applied pressure, figure 5.94, the same profile pattern for all the three films is observed as previously. The PET 506 substrate remains the tallest profile.

When pressure is increased to 0.04 MPa, as figure 5.95 indicates, a slight transition is observed in the centre of the bulge centre considering the convergence of the three bulge profiles. Also, the edge constraint seems to influence the profile of the PET ST506 substrate in the vicinity of 7.5 to 10 mm distance from the centre. This is not particularly observed in the case of PET 506. Regarding the bulge profile of PEN Teonex Q65 the edge constraint has a profound effect in the edge vicinity as before.

Figure 5.96 presents the two – dimensional experimentally measured bulge shapes in the case of 0.05 MPa of differential pressure. It is observed that the PET ST506 and PEN Teonex Q65 shapes converge as the centre is approached and diverge quite dramatically towards the edge. Profile convergence for the case of PET 506 and PET ST506 in the close edge vicinity is also observed.

Figure 5.97 shows another transition, at 0.06 MPa pressure, associated with the central deflection of PEN Teonex Q65, which is higher than that of PET ST506 for the first time but still lower than that of PET 506. As pressure increases above 0.06 MPa, figure 5.98 to figure 5.103, the relative shape patterns do not seem to change behaviour for all three film substrates. In terms of central bulge height, PEN Teonex Q65 approaches PET 506 as pressure increases.

5.6.1: PET 506: Comparison of experimentally measured bulge profiles with theories

Taking the PET 506 experimentally measured bulge profile into account, it is important to compare it with the perfect spherical shape and the shape predicted by Timoshenko[155]. This comparison will aid the understanding of how the actual shape of the film material evolves, as differential applied pressure increases, with respect to theoretical predictions. The pressure range used spans from 0.01 MPa to 0.16 MPa.

As figure 5.104 presents, the experimentally measured two – dimensional shape is the shortest, in terms of bulge height, as compared to the other two theoretical profiles. It should be note that at the edge vicinity the experimental shape coincides with the Timoshenko predicted shape.

When pressure increases to 0.02 MPa, as figure 5.105 shows, a transition is observed. This transition is two – fold. At first, the experimental profile does not coincide any more in the edge vicinity with the shape predicted by Timoshenko. However, in the centre vicinity, the

experimental shape converges with that of Timoshenko as it approaches the ideal spherical profile. The experimental profile is observed to sit in between the two theoretical predictions.

With further increase in pressure to 0.03 MPa, figure 5.106, the experimentally measured bulge profile is observed to be in between the two theoretically predicted shapes with the spherical shape being the upper boundary and the shape predicted by Timoshenko being the lower boundary. The Timoshenko predicted shape seems to be the most influenced in edge constraint terms. However, at the close centre vicinity all three profiles are observed to converge.

When the differential applied pressure increases from 0.04 MPa to 0.06 MPa, figure 5.107 to figure 5.109, a similar trend is followed as before with no particular change in the behaviour of the experimental shape as compared with the two theoretically predicted shapes. When differential applied pressure increases further to 0.07 MPa, as figure 5.110 presents, the main behaviour of the experimentally measured shape remains similar as before. However, there is a tendency for the experimentally measured bulge profile to converge with the spherical shape at the fixed edge vicinity.

For the differential pressure range of 0.08 MPa to 0.12 MPa, figure 5.111 to figure 5.115, the tendency of the experimental two – dimensional profile to converge with the ideal spherical shape, and at the same time diverge from the Timoshenko profile, increases.

Figure 5.116 shows the experimentally measured bulge profile and the two theoretically predicted shapes when the pressure reaches 0.13 MPa. It is evident that the experimental shape has almost converged with the ideal spherical profile. When the applied pressure has reached 0.14 MPa, figure 5.117, the convergence with the spherical shape becomes stable.

It is important to note that the same behaviour is observed for the pressure of 0.15 MPa, as figure 5.118 shows, and the applied pressure of 0.16 MPa as figure 5.119 indicates. At this high-pressure range a slightly higher experimental bulge profile, as compared to the ideal shape, is observed to exist in all areas except the close centre vicinity.

5.6.2: PET ST506: Comparison of experimentally measured bulge profiles with theories

The evolution of experimentally measured bulge profile for surface treated PET ST506 substrate, for pressures ranging from 0.01 MPa to 0.16 MPa, is also compared with the ideal spherical profile and the profile predicted by Timoshenko's theory. It is vital to observe how this particular substrate behaves as compared to the PET 506 grade.

Figure 5.120 presents the experimentally measured shape, the ideal spherical shape and the Timoshenko predicted theoretical shape. It is evident that the experimental profile is similar to that of Timoshenko at this early pressure, 0.01 MPa, stage. The three bulge shapes converge at the bulge centre close vicinity.

When the pressure increases to 0.02 MPa as figure 5.121 indicates, the experimentally measured bulge profile is observed to diverge from the Timoshenko shape in the fixed edge vicinity and therefore a minor transition seems to take place. However, in the bulge centre vicinity the Timoshenko and experimental shapes are almost identical.

In the pressure range from 0.03 to 0.04 MPa, figure 5.122 and figure 5.123, the same behaviour, for experimentally measured bulge profile as above is observed.

However, when the applied pressure reaches 0.05 MPa, as figure 5.124 shows, a minor transition is observed for the experimental two – dimensional shape case. It is observed that the experimental shape acquires (in bulge vertical deflection terms) a position between the upper ideal spherical profile boundary and the lower Timoshenko predicted theoretical shape boundary. This behaviour was also observed, at a pressure as low as 0.02 MPa, in the case of PET 506 film substrate.

As the differential pressure increases to 0.06 MPa, figure 5.125, the previously mentioned behaviour stabilizes. The three bulge profiles converge close to the vicinity of the centre.

Further increase of pressure, from 0.07 to 0.16 MPa, reveals the tendency of the experimentally measured shape to approach the ideal spherical situation as figures 5.126 to 5.135 show. However, the PET ST 506 bulge shape does not fully converge with the ideal spherical profile for the actual experimental pressure range employed in this work.

5.6.3: PEN Teonex Q65: Comparison of experimentally measured bulge profiles with theories

The experimentally measured bulge profile of PEN Teonex Q65 bare substrate is also compared with the ideal spherical shape and the shape predicted by Timoshenko.

As figure 5.136 presents, for a differential applied pressure of 0.01 MPa, the experimentally measured shape is observed to significantly deviate from both the Timoshenko predicted shape and the ideal spherical shape. This case was not observed for PET 506 and PET ST506 samples.

As pressure increases to 0.02 MPa, figure 5.137, the experimental bulge profile seems to tend to attain the Timoshenko shape but still is far from converging with the ideal spherical shape.

When the pressure reaches 0.03 MPa, as figure 5.138 indicates, the experimentally measured PEN Teonex Q65 bulge shape has almost fully converged with the Timoshenko shape. This convergence is fully achieved for a differential pressure of 0.04 MPa as showed in figure 5.139. When the pressure reaches 0.05 MPa, figure 5.140, the same trend is observed for the experimentally measured bulge shape.

In the pressure range from 0.06 to 0.12 MPa, as figures 5.141 to 5.147 indicate, the shape of the experimentally measured bulge profile is located in between the upper ideal spherical profile boundary and the lower Timoshenko predicted profile boundary.

This behaviour was also observed for both PET 506 and PEN Teonex Q65 samples. It is also interesting to note that the fixed edge effect is observed to significantly influence the PEN Teonex Q65 circular substrate two – dimensional shape even at relatively high applied differential pressures.

5.6.4: Deviation of experimental bulge shape from theories

It is important to compare the deviation of the experimentally measured bulge shape with theoretical bulge shapes. In this section the % deviations of the experimentally measured bulge deflection shape values, for various bare polyester substrates, from the perfect spherical shape and Timoshenko's plate shape prediction are presented. It is worth noting that the minus sign in the deviation axis means that the experimentally measured bulge deflection is lower than its theoretical counterpart whereas the opposite applies for the case of the positive sign. Therefore, good agreement of theory and experiment exists near zero.

Figure 5.148 presents the % deviation from spherical shape against increasing applied differential pressure for the case of PET 506 bare substrate. Three sample regimes are considered. The first regime, in blue colour, corresponds to the sample regime, which is close to the bulge edge. The second regime is in between the bulge edge and the bulge centre vicinity. The third regime, the black line, represents the bulge centre vicinity with the vertical deflection being measured 4.25 mm from the circular sample centre.
When the vertical deflection is measured at 12.75 mm away from the bulge centre, it shows a large deviation from the spherical shape. For an applied differential pressure of 0.01 MPa the deviation is 57 %. As the pressure increases the deviation becomes smaller and at a pressure

of 0.05 MPa is equal to 20.6 %. Further increase in pressure leads to further decrease of deviation and when differential pressure reaches 0.1 MPa the deviation is found to be only 2.7 %. At 0.12 MPa of applied pressure the deviation is 0 %, which means that theory and experiment are in total agreement for this particular sample regime.

However, further increase of pressure leads to renewed deviation, now the vertical sample deflection is higher than that of the theoretical shape. At 0.16 MPa of applied pressure the deviation of experimental shape from the ideal spherical shape is – 6.3 %. For the vertical deflection measured at 8.5 mm away from the sample centre the deviation at low pressures is lower than that of the previous case. However, significant deviation is still found to exist. At a differential pressure of 0.01 MPa the deviation is 31 % and decreases to 12 % when the applied pressure increases to 0.05 MPa. At 0.13 MPa of bulge pressure total agreement of experiment and spherical shape is observed, i.e deviation is equal to 0 %. As pressure increases further the experimentally measured shape surpasses the ideal spherical shape and at 0.16 MPa of applied differential pressure the deviation is – 2.6 %. When the vertical deflection, 4.25 mm away from centre, is measured at the low pressure of 0.01 MPa significant deviation found and is equal to approximately 29 %.

However, as pressure increases good agreement between theory and experiment is observed and the deviation is around 2 –3 % from the ideal spherical shape. At a pressure of 0.16 MPa the deviation is 1%. It is worth noting that the experimental shape does not surpass the theoretical shape for this particular deflection measured.

Figure 5.149 shows the % deviation from spherical shape against increasing applied differential pressure for the case of PET ST506 bare substrate for the three different deflections measured. For the deflection measured near the bulge edge zone, 12.75 mm from the sample centre, large deviation around 40 % is observed at 0.01 MPa pressure. Then it decreases rapidly to 15 % at 0.07 MPa applied differential pressure. For a pressure of 0.08 MPa up to 0.11 MPa deviation lies in between 10 – 15 % and remains like that till a final pressure of 0.16 MPa is reached. When the measured deflection is 8.5 mm away from the bulge centre, a similar behaviour is observed regarding the % deviation from the circular

deflection shape. However, when measuring the deflection close to the centre vicinity a totally different behaviour is found to exist. Deviation from the spherical case is between 1 – 6 % for all pressures and therefore a relatively good agreement between spherical deflection shape and experimental measurement is observed.

Figure 5.150 presents the % deviation from spherical shape against increasing applied differential pressure for the case of PEN Teonex Q65 bare substrate. A large deviation is observed for the vertical deflection measured at 12.75 mm far from the sample centre. At a pressure as low as 0.01 MPa the deviation from the spherical theory is as large as 75 %. As pressure increases, deviation is decreasing but not lower than 50% for 0.12 MPa of applied differential pressure. For the vertical deflection measured at 8.5 mm far from the centre, the deviation is still large, but smaller than previously, and equal to approximately 53 % at a pressure of 0.01 MPa. However, the deviation decreases significantly as pressure increases and lies between 10 – 20 % for higher pressures up to 0.12 MPa. Again, the best relative agreement between theory and experiment is found when the, 4.25 mm away from the centre, vertical deflection is measured. It is calculated to be around 10 % for low pressures and then lies around 4 –5 % for higher pressures.

Figure 5.151 shows results regarding % deviation of experimentally measured vertical deflections, along the sample surface at different distances from the centre, from Timoshenko's predicted plate shape, for the case of PET 506 substrate film. Timoshenko's model is derived for small vertical bulge deflections but assumed to also work for large deflections, i.e bulge height >> sample thickness. For the vertical deflection measured near the bulge edge vicinity, a total agreement of experiment and theory is observed for the applied pressure of 0.01 MPa. However, when pressure increases to 0.02 MPa a large deviation increase equal to –50 % is observed to occur. Until a pressure of 0.07 MPa is reached the deviation from Timoshenko's theory lies in between –50 % and –100 %. Further deviation increase up to –150 % is observed for high-applied differential pressures. A different behaviour is noted when the measured deflection is 8.5 mm away from the sample centre. At a pressure of 0.01 MPa the deviation from Timoshenko's theory is approximately 8 % and as the pressure increase it surpasses the theoretical deflection and eventually reaches

– 38% for the case of the highest applied pressure, which is equal to 0.16 MPa. Near the bulge centre vicinity the experimental behaviour seems to agree even more closely with theory and lies within – 5 % deviation after a relatively poor deviation, approximately 25%, at the starting pressure of 0.01 MPa.

Figure 5.152 presents the % deviation from Timoshenko's predicted deflection shape against increasing applied differential pressure for the case of PET ST506 bare substrate. Similar behaviour with that reported for PET 506 is observed in this case. However, the deviation, when vertical deflection is measured near the bulge fixed edge, reaches –100 % at high-pressures and is lower than the respective value measured in the case of PET 506. Moving towards the bulge centre, 8.5 mm from the centre, relatively better agreement of theory and experiment is observed. However, the deviation from Timoshenko's theoretical prediction is still significant, between 0% and –20.6% as pressure increases. Moving further towards the bulge centre vicinity, 4.25 mm distance, the best agreement between theory and experiment is found. In all pressures deviation does not exceed the –6% boundary.

Figure 5.153 shows the results regarding % deviation of experimentally measured vertical deflections, along the sample surface at different distances from the centre, from Timoshenko's predicted plate shape, for the case of PEN Teonex Q65 substrate display film. For the deflection measured near the film edge a large deviation variation ranging from 40% to –40 % is observed as applied pressure increases. At 0.05 MPa pressure total agreement between theory and experiment is found to exist. When the measured vertical deflection is 8.5 mm away from the bulge centre, similar behaviour is observed.

However, the deviation values are lower than previously at higher applied pressures. Total agreement between theory and experimental measurement exist at 0.04 MPa of applied pressure in this particular case. As the measured deflection is more close to the bulge centre vicinity, the deviation of theoretical prediction and experiment appears to be small and stable with respect to the pressure range applied. For high applied pressures, the deviation is as low as –1.2 %.

Figure 5.154 compares the deviation of experiment and theory, for the case of the spherical shape, for the three different film materials near the bulge centre vicinity. The most satisfactory agreement is observed for the case of PET ST506. However, all substrates exhibit relatively good experimental behaviour, as compared with theory, near the bulge centre vicinity.

Figure 5.155 compares the % deviation of experiment and theory, for the case of the spherical shape, for the three different film materials when the measured deflection is 8.5 mm away from the bulge centre. In this case PET 506 display substrate shows the best behaviour. The second best behaviour is exhibited by PET ST506 bare substrate and PEN Teonex Q65 is following.

Figure 5.156 compares the % deviation of experiment and theory, for the case of the spherical shape, for the three different film materials when the measured deflection is 4.25 mm far from the bulge fixed edge. At low applied pressures, less than 0.05 MPa, large deviations for all polyester films are observed. However, at relatively high pressures, above 0.06 MPa, PET 506 shows improved behaviour. PET ST506 follows PET 506 but PEN Teonex Q65 still appears to deviate largely from the spherical deflection shape.

Figure 5.157 compares the % deviation of experiment and theory, for the case of the Timoshenko's prediction, for the three different film materials when the measured deflection is 4.25 mm far from the bulge centre. All substrates exhibit relatively small deviations as pressure increases. An exception is that of PET 506, which deviates from Timoshenko's prediction, approximately 25%, when the applied differential pressure is 0.01 MPa.

Figure 5.158 compares the % deviation of experiment and theory, for the case of the Timoshenko's prediction, for the three different film materials when the measured deflection is 8.5 mm far from the bulge centre. At pressures higher than 0.05 MPa, PET ST506 and PEN Teonex Q65 exhibit relatively low but significant deviations whereas PET 506 shows increasing deviation as pressure increases.

Figure 5.159 compares the % deviation of experiment and theory, for the case of the Timoshenko's prediction, for the three different film materials when the measured deflection is close to the bulge edge vicinity. Large deviations, as differential pressure increases, are observed for PET 506 and PET ST506 substrates. PEN Teonex Q65 shows a relatively better behaviour but still far from ideal as far as Timoshenko's film vertical deflection shape is concerned.

5.7: The use of different bulge models in determining mechanical properties

Mechanical properties of bare thin substrates tested under biaxial conditions, such as biaxial modulus and initial stress, can be determined using the bulge test.

The obtained pressure – deflection data can be fitted to the generalized bulge equation, 2.16, in order to acquire the A and B parameters as shown in figure 5.160.

$$A = \frac{C_1 \sigma_o t}{\alpha^2} \qquad (5.2)$$

$$B = \frac{C_2 M t}{\alpha^4} \qquad (5.3)$$

The obtained value of A, as shown in equation 5.2, can lead to the determination of σ_o which is the initial stress. Similarly, the value of B leads to the determination of biaxial modulus M as shown in equation 5.3.

The values obtained from the analytical spherical cap model[154], $C_1 = 4$ and $C_2 = 8/3$, do not depend on the Poisson's ratio. Figure 5.161 presents the mean biaxial modulus plotted against Poisson's ratio for PET 506 bare substrate using the analytical spherical cap model. The average initial stress, $\sigma_{o,}$ is 7 MPa and the mean biaxial modulus, M, is 3.75 ± 0.3 GPa.

Also, figure 5.162 shows the variation of PET 506 biaxial modulus with the Poisson's ratio, ν, as obtained using the energy minimization reported by Lin[166]. It is important to note that in this case $C_1 = 4$ and $C_2 = (7 - \nu) / 3$. It is apparent that the obtained initial stress value is the same, 7 MPa, as the one obtained using the spherical cap model. Biaxial modulus varies with Poisson's ratio and is 4.41 ± 0.44 GPa when the Poisson's ratio is 0.2. As the Poisson's ratio increases, the biaxial modulus slightly increases and reaches 4.54 ± 0.46 GPa for 0.4 Poisson's ratio.

Furthermore, figure 5.163 shows the variation of PET 506 biaxial modulus with Poisson's ratio, ν, as obtained using the finite element method, which was presented by Small[161]. Small's model does not present a value for C_1 and therefore the initial stress cannot be predicted. C_2 is equal to 8/3 (1 – 0.241 ν) and therefore the computed biaxial modulus, M, ranges between 3.94 ± 0.39 GPa and 4.15 ± 0.4 GPa for 0.2 to 0.4 Poisson's ratio respectively.

In addition, figure 5.164 presents the variation of PET 506 biaxial modulus with Poisson's ratio, ν, as obtained using a finite element model, which was presented by Pan[167]. For this model $C_1 = 4$ and $C_2 = 8/3$ (0.974 – 0.233 ν). It is therefore apparent that the obtained initial stress, 7 MPa, is the same as the one predicted from spherical cap and Lin models. The biaxial modulus is increasing from 4.03 ± 0.4 GPa to 4.23 ± 0.4 GPa as the Poisson's ratio increases from 0.2 to 0.4.

Also, figure 5.165 shows the variation of PET 506 biaxial modulus with Poisson's ratio, ν, as obtained using Hencky's analytical solution[165]. The same initial stress, as in previous models, is predicted by this model for which $C_1 = 4$. However, the biaxial modulus, $C_2 = 8/3$ (1.015 – 0.247 ν), is found to vary between 3.88 ± 0.38 GPa and 4.09 ± 0.39 GPa as Poisson's ratio increases from 0.2 to 0.4.

Furthermore, figure 5.166 presents PEN Kaladex S1020 biaxial modulus plotted against Poisson's ratio as obtained using the spherical cap model. The mean biaxial modulus, M, is

constant and found to be equal to 4.55 ± 0.4 GPa. Average initial stress, σ_o, is computed equal to 2.8 MPa.

Additionally, figure 5.167 shows the variation of PEN Kaladex S1020 biaxial modulus with the Poisson's ratio, ν, as obtained using the energy minimization method reported by Lin. The average initial stress is 2.8 MPa, the same as the one predicted by the spherical cap model. The mean biaxial modulus increases with increasing Poisson's ratio and ranges between 5.35 ± 0.46 GPa and 5.51 ± 0.49 GPa.

Also, figure 5.168 presents the variation of PEN Kaladex S1020 biaxial modulus with Poisson's ratio, ν, as obtained using the finite element method, which was presented by Small. The biaxial modulus ranges between 4.78 ± 0.41 GPa and 5.03 ± 0.44 GPa as ν increases from 0.2 to 0.4. As mentioned before, this model does not predict initial stress.

Furthermore, figure 5.169 presents the computed biaxial modulus, with respect to Poisson's ratio, for PEN Kaladex S1020 using Pan's finite element model. The average initial stress, C_1 = 4, is 2.8 MPa. Biaxial modulus varies with Poisson's ratio and ranges between 4.9 ± 0.43 GPa and 5.16 ± 0.45 GPa as Poisson's ratio increases.

Using Hencky's analytical solution, as shown in figure 5.170, the mean biaxial modulus of PEN Kaladex S1020 is found to lie between 4.71 ± 0.41 GPa and 4.96 ± 0.43 GPa as Poisson's ratio increases from 0.2 to 0.4. As usual the average initial stress is 2.8 MPa, a similar value predicted from all models. PEN Kaladex S1020 exhibits a higher mean biaxial modulus, when using the spherical cap analytical model, than PET 506 as shown in figure 5.171. The difference in measured biaxial moduli is of the order of 0.8 GPa.

The same trend is observed when using Lin's model as figure 5.172 indicates. The difference observed using this model is approximately 0.95 GPa. According to Small's finite element model, figure 5.173, a biaxial moduli difference of approximately 0.86 GPa in favour of PEN Kaladex S1020 is noted. Pan's model, figure 5.174, shows a biaxial moduli difference, in favour of PEN Kaladex S1020, of the order of 0.9 GPa.

Finally, using Hencky's analytical solution the observed difference is approximately 0.85 GPa. The average initial stress is 4.2 MPa higher for PET 506, as shown in figure 5.175.

5.8: Biaxial stress and strain for pressurized coated and uncoated systems

Biaxial stress and strain behaviour against applied pressure can be derived using Williams[159] and Leterrier's[129] analytical equations for large film bulging. In this section the stress and strain behaviour, against applied differential pressure, of bare and ITO coated PET 506, PET ST506 and PEN Kaladex S1020 substrates is presented. The applied pressure rate was 0.1 bar per minute for all tests. It is important to note that the stress equation for both Williams and Leterrier yields the same result and therefore only the Williams solution is presented. However, Williams's strain solution differs from that of Leterrier and therefore both strain solutions are presented.

Figure 5.176 presents the biaxial stress against applied differential pressure for bare PET 506 substrate, ITO coated PET 506 with the coating being in tension and ITO coated PET 506 with the ceramic layer being under compression. The highest biaxial stress is achieved by the ITO coated PET 506 when the conductive layer is placed under tension. The biaxial stress, in this case, reaches a maximum value of 295 MPa at a pressure of 1.27 bar. Then, ITO coated PET 506 with the ITO surface in compression, follows with a maximum biaxial stress, at 1.27 bar, of 290 MPa. The bare PET 506 substrate is observed to reach the lowest biaxial stress values, for the whole range of applied pressure, and reaches a maximum biaxial stress of 281 MPa.

Figure 5.177 shows the biaxial stress against applied differential pressure for bare PET ST506 substrate, ITO coated PET ST506 with the coating being in tension and ITO coated PET ST506 with the ceramic layer being under compression. The maximum mean biaxial stress when the coating is under compression was found to be equal to 289 MPa. For the bare

substrate the maximum biaxial stress, at 1.27 bar differential pressure, is equal to 297 MPa. The maximum biaxial stress observed when the coating is under tension is equal to 303 MPa. This is the highest value out of all three samples.

Figure 5.178 presents results obtained for the biaxial stress against applied differential pressure for bare PET 506 substrate, ITO coated PET 506 with the coating being in tension and ITO coated PET 506 with the ceramic layer being under compression. When the coating surface is under tension, the maximum mean biaxial stress observed is equal to 336 MPa. For the case of the coating under compression, the maximum stress observed is approximately equal to 306 MPa. In addition, the bare PEN Kaladex S1020 substrate exhibits a maximum biaxial stress, at 1.27 bar differential applied pressure, of 303 MPa.

Figure 5.179 shows the biaxial strain, using William's equation, against applied differential pressure for bare PET 506 substrate, ITO coated PET 506 with the coating being in tension and ITO coated PET 506 with the ceramic layer being under compression. When the coating is under tension, a biaxial strain equal to 2.25 %, for 1.25 bar of applied pressure, is observed. The biaxial strain increases to 2.35 %, for the same applied differential pressure, in the case of ITO, surface under compression, PET 506. The highest biaxial strain, 2.4 %, is observed for the bare PET 506 substrate.

Furthermore, figure 5.180 presents the biaxial strain, using William's analytical strain equation, against applied differential pressure for bare PET ST506 substrate, ITO coated PET ST506 with the coating being in tension and ITO coated PET ST506 with the ceramic layer being under compression. When the ITO conductive layer is under tension, the maximum biaxial strain, at a reference pressure of 1.25 bar, is equal to 2.15 %. For the case of bare PET ST506 substrate, the maximum strain is 2.28 %. The highest strain value is observed when the coating is under compression and is equal to 2.4 %.

Figure 5.181 shows the biaxial strain, using William's equation, against applied differential pressure for bare PEN Kaladex S1020 substrate, ITO coated PEN Kaladex

S1020 with the coating being in tension and ITO coated PEN Kaladex S1020 with the ceramic conducting layer being under compression. Comparable biaxial strain values are observed when the coating is under compression, 2.14 %, and when no coating exists, 2.15 % for a reference applied pressure equal to 1.25 bar. However, when the ITO conductive layer is under tension, the biaxial strain value, at 1.25 bar differential pressure, is significantly lower and equal to 1.65 %.

In addition, figure 5.182 presents the biaxial strain, as predicted by Leterrier, against differential pressure for bare PET 506, ITO, surface in tension, coated PET 506 and ITO, surface in compression, coated PET 506 flexible display substrate. The highest biaxial strain value, at a pressure of 1.24 bar, is observed for the case of bare PET 506 substrate and is equal to 1.22 %. When the coating is under compression, for the same applied differential pressure, the maximum biaxial strain is 1.17 %. The lower strain value observed when the coating layer is under tension and is equal to 1.12 %.

Figure 5.183 shows the biaxial strain, using the Leterrier equation, against applied differential pressure for bare PET ST506 substrate, ITO coated PET ST506 with the coating being in tension and ITO coated PET ST506 with the ceramic conducting layer being under compression. When the coating is under compression, the maximum strain, calculated at 1.27 bar differential pressure, was found equal to 1.22 %. When a bare PET ST506 substrate was tested, the biaxial strain, according to Leterrier, is 1.15 % for the same reference pressure. The lowest strain value is observed when the coating is under tension and is equal to 1.09 %.

Finally, figure 5.184 presents the biaxial strain, using Leterrier's equation, against applied differential pressure for bare PEN Kaladex S1020 substrate, ITO coated PEN Kaladex S1020 with the coating being in tension and ITO coated PEN Kaladex S1020 with the ceramic conducting layer being under compression. When the coating is under tension the maximum strain, at a pressure of 1.24 bar, is equal to 0.82 %. When the ITO layer is under compression the biaxial strain, as predicted by Leterrier's analytical strain equation, is equal to 1.05 %. A similar biaxial strain value, 1.06 %, is noted for the case of bare PEN Kaladex S1020 display substrate for a differential applied pressure equal to 1.24 bar.

6. Tribological investigations

6.1 Tribological investigation of polyester bare substrates

Little research has been reported to date on the tribological properties of polyester top-sheet display components. The aim of this section is to investigate the unlubricated tribological response of biaxially oriented PET and polyethylene napthalate (PEN) films developed for use in display device assemblies.
Wear track depths were measured, after testing, with a contact-mode stylus profilometer. Ex-situ microscopical studies were performed on virgin and worn surfaces using scanning electron microscopy (SEM) and contact-mode atomic force microscopy (AFM).

Friction and wear testing was conducted using a conventional unidirectional pin – on – disc tribotester using a normal constant load of 9.8 N and a sliding cycle range of 925 to 12630 cycles. Stainless steel balls of approximately 4 mm radius were used as the counterbody. After each test a new steel surface was used for the next experiment. The environment was dust – free and the relative humidity was measured before and after each test. Relative humidities measured, were in the range of 34% – 63%. The temperature was also measured before and after each experiment. Measured temperatures ranged between 15 °C and 28 °C. Friction coefficient data were monitored during the tests. Polymer discs, 11.5 cm diameter, were cut from the A4 sheets and were adhered on smooth austenitic steel discs (316L), 12 cm in diameter, using adhesive tape which was applied carefully around the discs edges. Care was taken when adhering the polymer on the steel discs in order to avoid film wrinkling.
Resulting wear track depths were measured, ex – situ, using a stylus profilometer operating in contact mode. An average of four measurements, for each wear track, was considered in this study.

Figure 6.1 shows a c – m AFM image of the steel ball counterbody. A relatively large area, 25 μm^2, was obtained in this case. The RMS roughness of the hard steel ball is measured to

be 8.6 nm, a value that indicates that the steel ball is relatively smooth and which is comparable to the RMS values obtained for the two polyester substrates and presented in 4.1 section in chapter 4.

Also, figure 6.2 presents the variation of PET and PEN friction coefficients for 4500 sliding cycles. Although the mean value is nearly the same for both materials, 0.49 for PET and 0.48 for PEN, it is evident that the initial running – in period is significantly larger for PET than for PEN and extends to approximately 250 cycles. It can be also observed that the steady – state period is significantly interrupted further on two occasions, shortly after its introduction and at about 3300 sliding cycles. This phenomenon is observed frequently for PET and is not observed in the case of PEN, which exhibits lower surface roughness.

In addition, figure 6.3 shows the mean values of measured friction coefficients for PET and PEN films, against number of sliding cycles. Generally, the measured values lie in the range from 0.1 to 0.5. However, there are two interesting regimes, of behaviour, observed for both materials. Up to 6450 sliding cycles higher mean friction coefficient values are observed, for both films. On the other hand, above 8000 cycles lower friction coefficient values are measured. This is a dramatic decrease in the case of PEN.

Furthermore, figure 6.4 presents a typical example of PET and PEN wear track measurement, using a contact mode stylus profilometer, for 12600 sliding cycles. These measurements can be used in order to calculate the wear rates for PET and PEN samples, as figure 6.5 indicates.

In general, the wear rates for PET show nearly stable wear up to 8000 cycles whereas PEN's wear rate increases as the number of sliding cycles increases. However, PEN exhibits lower wear rates as compared with PET up to 6450 cycles. Above 6450 cycles the wear rate of PEN is higher than that of PET.

Using SEM, wear particle debris generation is observed for both materials at low sliding cycles, as figures 6.6 and 6.7 indicate, mainly on the central part of the wear track. A closer observation of the debris particles reveals two distinct particle groups. Larger - edged

particles form one group whereas smaller rounded particles form the other. After testing, it was observed visually that polymer transfer to the steel ball occurred. It can also be observed, as figure 6.8 shows, that ductile micro - cutting occurred at low sliding cycles for PET. This was not observed to a large extent, in the case of PEN.

In addition, as the number of sliding cycles increases, limited fatigue wear and cracking is exhibited by PET, in the centre of the wear track, as shown in figure 6.9. It is also clear that most of the larger edged debris particles have been removed from the worn central area by the action of the rigid counterbody.

This is further demonstrated for the case of PEN, as figure 6.10 shows, where a considerable number of debris particles have been displaced beyond the wear track edges. Plastic deformation and delaminated surface layer fragments are also evident. When the number of sliding cycles further increases (figure 6.11) wear debris particles have been totally displaced from the wear track centre and alignment of the biaxially oriented molecular chains in the direction of sliding may occur.

6.2 Nanoscratch and nanoindentation experimental investigation

Nanoscratching of ITO, on different polyester substrates, and nanoindentation of ITO coated and uncoated polyester substrates were undertaken using a commercial nanotest platform (described in chapter 3).

Nanoscratch testing of ITO surfaces was accomplished using a linearly increasing normal load from 0 to 30 mN and a standard conical stylus. The aim was to determine the critical load at which the ITO layer fractures.

Figure 6.12 shows the normal load variation as the scanning distance increases for ITO on PET 506. It is observed that at about 17 mN, the normal load slightly decreases. This is an

indication of coating failure. It is therefore apparent that the critical normal load, at which ITO on PET 506 fails, is 17 mN.

Similarly, as figure 6.13 shows for ITO on PEN Kaladex S1020, the observed critical normal load at which ITO fails is 28 mN after a ~260 μm distance is travelled by the conical stylus.

Furthermore, figure 6.14 presents a contact – mode AFM image of a scratched ITO, deposited on PET 506, surface. The coating is observed to buckle inwards in the early stages of the experiment and when the load is smaller. At a later stage, ITO is observed to fracture in a brittle manner. When the brittle fracture stage is initiated, the depth, which the indenter penetrated, is around 285 nm as measured by contact – mode AFM and shown in figure 6.15.

It is also important to note significant material displacement at the edge of the groove. The morphology of the groove, in the second stage, is characterized by the formation of peaks and valleys with approximately 120 nm height difference as measured by contact mode AFM and shown in figure 6.16.

Similarly, as figure 6.17 shows, ITO failure behaviour is observed when the conductive layer is deposited on PEN Kaladex S1020 flexible display substrate by magnetron sputtering at room temperature. During the first stage the ITO buckles inwards whereas during the second stage ITO remnants show brittle behaviour. However, during the second stage, interplay between the polymer and the ceramic is observed and will be discussed in detail in chapter 7.

Table 6.1 summarizes the observed ITO failure critical loads for three different substrates. The highest critical load is measured when ITO is deposited on PEN Kaladex S1020 polyester substrate. The second highest critical load, 17 mN, is observed for ITO on PET 506 and the lowest load is measured when ITO is sputtered on PET ST506 flexible display substrate.

Figure 6.18 shows a part of a Knoop indentation for an ITO on PET 506, surface as imaged by contact – mode AFM using a 5 mN normal load, 0.06 mN / s loading rate and a standard

Knoop nano – indenter. The non – recovered depth, due to indentation, is measured by c – m AFM to be approximately 1.35 μm. It is therefore apparent that the polymer substrate properties dominate at such a depth. As will be discussed in chapter 7, the thin ITO layer mechanical properties can be determined accurately at significantly lower indentation depths on the order of a few nanometers.

Figure 6.19 presents an optical micrograph of a Knoop indent for ITO on PEN Kaladex S1020 substrate. The length of the indentation is approximately 600 μm and its width, at the centre, is approximately 45 μm. The depth is also large, 1.5 μm, in this case as previously.

Table 6.2 summarizes the mechanical properties, hardness and Young's modulus, of ITO coated and uncoated polyester substrates, as measured by nanoindentation, for two different maximum normal loads, 5 mN and 30 mN and loading rate equal to 0.06 mN / sec. It is observed that at the higher load the hardness of the uncoated substrates is similar and approximately equal to 0.28 GPa. The hardness of the ITO surface also exhibits similar values of hardness.

However, as mentioned previously, the ITO surface mechanical properties cannot be determined accurately in this case since the indentation depth is too high. The bare substrates Young's moduli obtained for 30 mN are all below 3GPa. The lowest value is observed for PET 506 and is 2.5 GPa. The second lowest elastic modulus is that of PET 506 and the highest modulus is observed for PEN Kaladex S1020.

When the maximum load is 5 mN, no change in elastic modulus is noted for PET 506. The Young's modulus of PEN Kaladex S1020 is significantly higher as well as the elastic modulus of PET ST506. It is also noted that PEN Kaladex is harder than PET 506 and PET ST506. Also, PET ST506 is observed to be harder than PET 506.

7. Discussion

7.1 PART A – Discussion of general characterization and preparation of ITO by PLD

As mentioned in chapter 4 (section 4.1), the RMS surface roughness values of the PEN Kaladex S1020 substrates are lower than those obtained for the PET 506 and PET ST506 substrates. In particular, the roughness difference, for the case of PET 506 against PEN Kaladex S1020, is 2.5 nm. Letterier[209] in his review, reports that various measurements, using AFM, led to mean surface roughness, for PET film, of the crystalline regions in the range 2.3 – 13 nm and of the amorphous regions in the range 23 – 38 nm. Also, RMS roughness as low as 1.13 nm has been reported[209] for biaxially oriented PET films. It is therefore apparent that our measurements are comparable with those reported elsewhere. It is also important to note, when depositing subsequent layers on the substrate, the lower RMS roughness of the PEN Kaladex S1020 substrate as compared to both PET films.

In addition, the PET film surface (figure 4.1) is observed to contain several elongated features that protrude a few nm above the film surface. A similar topography was observed by Beake et al[210], using tapping – mode AFM, who proposed that these plate – like structures could be putative crystallites. For all the remaining substrates that were investigated, using contact – mode AFM, the presence of similar long features is not as pronounced as in the case of PET 506.

The calculation of orientation parameters, as presented in section 4.4, for the case of PET 506 reveals that the biaxial stretching of the initially amorphous film has induced more orientation in the machine direction as compared to the transverse direction.

Comparing our calculated direction cosine values with those obtained by Everall and Bibby[37] for a biaxially drawn PET film (identical draw ratios ~ x3), we observe that our machine direction value, i.e. ($\cos^2$ [yY]), is a little bit higher whereas both transverse direction values, i.e. ($\cos^2$ [yX]), are close. It can be therefore concluded that the PET 506 film, investigated in this work, is stretched more than 3 times in the machine direction and approximately 3 times in the transverse direction.

The glass transition temperature, T_g, and melting temperature, T_m, of PET 506 and PEN Kaladex S1020 as measured by DSC (section 4.5) agree closely with respective values reported by MacDonald[24]. It is evident that the PEN grade is in the upper temperature range for the semi – crystalline thermoplastic polymers that can still be melt processed.

The crystallinity of PET 506, 26.46 %, is lower than that calculated for PEN Kaladex S1020 which is 36.7 %. When the degree of crystallinity remains relatively low, the mechanical behaviour appears to be mainly determined by orientation in the amorphous regions[32]. However, the measured crystallinity of PEN Kaladex S1020 is close to 40 %, which is a typical crystallinity value when polyester films are produced by sequential drawing[21].

Clarity of the film is important for bottom emissive displays and a total light transmission greater than 85 % is required[24]. Both PET 506 and PEN Kaladex S1020 meet this criterion and measured optical transmittance values are above 85 % as presented by table 4.2.

The surface adhesion of PET ST506, as measured by contact – mode AFM, is slightly higher than that of PEN Kaladex S1020 (section 4.6). However, it should be noted that these measurements are of limited value since they are of a local nature.
Also, they cannot be easily compared with previously reported values because different cantilevers with different tip radii are used and a strong dependence on the tip radius and humidity has been observed in the past[211].

When ITO is sputtered on polyester substrates at room temperature (section 4.2), the RMS surface roughness of the ITO is lower when PEN substrates are used. This indicates that PEN substrates maybe a better choice when low ITO RMS roughness is required. The lowest RMS roughness, of ITO on PEN, measured in this study, is around 2 nm. This value is higher than that observed by Hoshi and Kiyomura[58] who reported a roughness as low as 0.15 nm when ITO is deposited on glass at 50° C. However, when ITO is deposited on PET at room temperature, as reported by Kim[61] and Carcia et al[62], the RMS roughness measured values lay in the range 1.1 – 2.8. These values are comparable to those obtained in this work.

The surface morphology of the ITO layer is dependent on the base substrate surface. Smaller ITO islands are observed when ITO is deposited on PEN substrates. Therefore, the effect of the substrate is crucial in this case. X-ray diffraction (section 4.3) can help in order to study the ITO microstructure. ITO is observed to be amorphous when sputtered on all available polyester substrates at room temperature (figures 4.21 – 4.24). This is consistent with Yeom et al[60] who reported that ITO is amorphous when deposited on glass at room temperature using magnetron sputtering. It is also consistent with the study of Minami et al[50] who deposited ITO on PC substrates.

It is important to note that annealing of ITO films for 1 hour at 100° C, after deposition, may lead to polycrystalline film formation[51]. However, in this study annealing of ITO film was not performed and may be a useful future investigation.

ITO on PET 506 exhibits the lowest resistivity whereas the highest resistivity is observed for ITO on PEN Kaladex S1020 (section 4.7). The measured values are comparable with those reported by Minami et al[50] except from the ITO on PET 506 value which is slightly lower. The latter is comparable with the value reported by Shin et al[54] for ITO deposited on PC at room temperature and with the value presented by Hoshi and Kiyomura[58]. Also, Wong et al[64] reported a resistivity value, for ITO on PET, equal to 5×10^{-4} Ω cm which is in close agreement with the respective value obtained in this study.

Also, the optical transmission, at 638 nm wavelength, is higher for ITO on PET 506 than that of ITO on PEN Kaladex S1020. Both values are lower than that reported by Minami et al[50]. They are comparable with that reported by Kulkarni et al[52], Shin et al[54], Kim[61] and Wong et al[64]. When ITO is deposited on PEN Kaladex S1020 by pulsed laser deposition at room temperature (section 4.8), the lowest resistivity obtained is equal to 1.04×10^{-4} Ω cm. This is lower than the value reported by Zheng and Kwok[68] for ITO on glass, Sun et al[69] for ITO on organic substrates, Kim et al[74] for ITO on glass.

The highest optical transmission value for ITO on PEN Kaladex S1020 is 90.4 % and is lower than that reported by Zheng and Kwok[68]. However, the optical transmission value is higher than that reported by Adurodija et al[71] for ITO on glass and Kim et al[79] for ITO on PET.

It is worth noting that maximum optical transmission and resistivity values for the pulsed laser deposition sample are superior to those measured for the magnetron sputtered ITO on PEN Kaladex samples. This observation may highlight that pulsed laser deposition can produce high quality inorganic conductive coatings for display applications.

The pulsed laser deposited samples are observed to be amorphous, using X–ray diffraction. This is in agreement with Adurodija et al[71,76] and Sun et al[69] who also observed that the ITO films, prepared on glass, below 100° C were amorphous.

In conclusion, we have demonstrated the possibility of using a different flexible substrate, PEN Kaladex S1020, on which ITO with low resistivity, $1.04*10^{-4}$ Ω cm, and high optical transmittance, 90.4 %, can be deposited at room temperature in the narrow regime of 7.5 mTorr-10 mTorr of oxygen pressure. ITO deposited on PEN Teonex Q65 by radio frequency sputtering[212] with resistivities around 10^{-3} Ω cm and optical transmittances of ~85% is inferior to the samples obtained in this work. Some of the results, presented in this study, can be attributed to the high surface quality and lower surface roughness of the PEN Teonex Q65 as compared to other available rigid and flexible substrates. Our results agree closely with previous studies which report that at ~9 mTorr of oxygen pressure, at room temperature,

there is an optimum in the carrier concentration[83] and high quality ITO can be deposited, on glass substrates, by PLD at room temperature using 10 mTorr as background oxygen pressure[90].

The microstructure and growth characteristics of the ITO have been explored and the deposited layer surface adhesion measured with attention being focused on multilayer flexible display structures.

7.2 PART B Discussion of mechanical properties

The Young's moduli measured in this study, for the polyester substrates (section 5.1), are found to be lower than those reported previously[24] for the case of PET 506. However, it should be noted that values for PEN Kaladex S1020 have not been reported in the past and a comparison cannot be made. Kim et al[35] reported values of biaxially stretched (4x3) PEN film, figure 2.8, that are comparable with the results obtained in this work.

In general, PET Young's moduli equal to 2.2 GPa in amorphous regions and 11.8 GPa in crystalline regions have been reported[209]. Also, a Young's modulus value around 4 GPa for biaxially oriented PET has been reported previously[103,121]. The latter value is also higher than 2.35 ± 0.29 GPa obtained by this investigation. It is important to underline that Young modulus measurements are dependent on the sample length over sample width ratio for samples, which are less than 10 mm in width[103] and also the uniaxial tensile direction when working with biaxially oriented films.

The ITO Young's modulus (section 5.2) is higher than that of the polymer substrate and is reported previously[95] to be equal to 119 ± 5 GPa for ITO on polyester (Arylite). This is lower if compared with the values obtained in this work (Table 5.1). However, for ITO deposited on PET substrate, the Young's modulus is reported[121] equal to 250 GPa, which is higher than the present's work respective values that are approximately equal to 220 GPa.

The measure[94] of the mismatch in the modulus between the coating and the substrate is described by the Dundur's parameter α, given by equation 2.2, which in our case is ~0.97 for ITO on PET 506 and ~0.96 for ITO on PEN Kaladex S1020. The energy at the channel front[96], when considering a channelling crack propagating on the ITO film surface, is very high for $\alpha \rightarrow 1$ as figure 2.12 shows.

Section 5.3 deals with the electromechanical uniaxial tensile testing of flexible display anodes. At first, as presented in section 5.3.1, the monotonic uniaxial tensile behaviour of ITO on PEN Kaladex S1020 is considered. The ITO electrical resistance is not monitored in this case and ex – situ AFM is performed in order to assess the resulting ITO failure mechanisms at relatively low applied uniaxial tensile strains ($\leq 6\%$).

Up to 2 % uniaxial tensile strain no cracks were observed. It has been reported in a previous study[103] that upon unloading, the samples that were strained to less than 4 % uniaxial strain, cracks tend to close due to strain recovery. When the applied strain is increased to 3 %, cracking perpendicular to the tensile direction and transverse buckling is the dominant ITO failure mechanism. The latter is surprising since it has been reported in the past[103,118] that transverse buckling occurs at strains around 6 %. Another, interesting pattern observed is the ITO cracking (figure 5.6). It is observed that either ITO folding occurs or fractured ITO material has gathered at the crack edges. The latter is unlikely since the ITO debris is difficult to adhere at the edges and most probably the ITO folding is a consequence of the substrate deformation. This is in agreement with Cairns et al[110] who noted that the deformation of the polymer substrate is mapped by the failure patterns in the ITO.

However, an advantage when testing conductive layers is the in–situ electrical resistance monitoring (section 5.3.2). Various flexible display anodes were tested in uniaxial tension and their electrical resistance was monitored during testing. An increase in electrical resistance is associated with ITO cracking[108] at a threshold strain that is called the critical onset strain for failure (COS).

In this work ITO on PET 506 and PET ST506 substrates are observed to be more reliable than ITO on PEN Kaladex S1020 for the lower crosshead speed used whereas ITO on PET ST506 is the most reliable for the higher crosshead speed used, with a critical onset strain around 2% which is consistent with previously reported values[108,111]. The increase in electrical resistance is gradual rather than a catastrophic loss.

It is interesting to investigate the ITO failure mechanisms at high-applied uniaxial tensile strains (section 5.3.3) in order to better understand the ITO coating failure modes. As figure 5.22 shows, there is no evidence of ITO debris inside the crack. However, as reported in a previous study[108], there should be a bridging mechanism because ITO is electrically conducting after the onset of failure. As shown by figures 5.22, 5,24 and 5.29, the two possible bridging mechanisms are; (i) interlocking of neighbouring ITO fragments and (ii) existence of an interfacial conducting ductile layer. It is possible that these two mechanisms may act synergistically.

The transverse buckling failure mechanism observed represents another major issue in reliability terms. It is even more interesting in this particular work since it appears to exist not only at high applied strains but also at relatively low strains (< 4%) as mentioned above. At high applied strains our observations are similar to those of Volynskii et al[107] who described two possible mechanisms of transverse buckling for gold coated PET composites. The first mechanism is related to yielding of the coating under compression. The second mechanism may be related to cracking of the coating. Under a tensile strain, the volume of the substrate is constant and its width reduces with strain. The coating is rigid and cracks. Hence the lateral contraction of the coating is lower than that of the substrate and as a result the coating is compressed and buckles. This can lead first to crack formation and then initiation of transverse buckling by the cracks thus formed. However, in the present study closed and open buckling zones are observed. Therefore, it may be possible that different adhesion levels exist between the coating and the amorphous and crystalline substrate regions respectively. Lower adhesion levels may exist when the coating forms an interface with an amorphous and hence more compliant substrate region, leading to an open buckle formation.

Ex–situ AFM measurements (section 5.3.4) are important in order to compare in a more quantitative manner the mechanical behaviour of the available flexible anodes. It is important to note large deviations of the measured crack depth at high strains as figures 5.32 and 5.33 show. Since the cracks initiate from surface defect sites[114], the crack depth may vary with the defect size as well as the defect morphology. The crack opening increases with increasing strain for ITO coated on PEN Kaladex S1020, figure 5.35. As mentioned by Fortunato et al[111], the coating electrical resistance may be directly proportional to the width of cracks. This proposition cannot be fully supported by the present work since the crack width measured is the strain recovered crack width and not the original width. The number of cracks against applied strain increases with increasing applied strain for ITO on PEN Teonex Q65 as figure 5.39 shows. For all other coating / substrate combinations the number of cracks saturates at high applied strains. This is consistent with previous reports[103,104,108]. ITO on PET 506 exhibits the lowest buckling zone tip deflection and base width, at high applied strain, as compared to ITO on PEN Kaladex S1020 and ITO on PEN Teonex Q65, as figures 5.43 and 5.45 show respectively. As was mentioned by Bouten et al[117], the length scale of the delamination patterns depends on the stiffness of the coating. More specifically, using the buckle deflection and the base width of the buckle, the buckling strain can be predicted[117]. However, this approach leads to an overestimation of the buckling strain since it neglects the strain release in the coating next to the buckle itself. Chen et al[121] offered a plug–in solution in order to calculate the coating buckling strain. According to that solution the larger the base width the lower the buckling strain.

In considering the mechanical reliability another important parameter is the maximum strain a device can be deformed to many times without causing degradation with repeated mechanical cycling[213,118] (section 5.3.5). During uniaxial tensile cyclic conditions the absence of cohesive failure perpendicular to the tensile direction is evident in most cases. Also, no significant electrical resistance recovery is observed. The latter is consistent with a previous study by Cairns et al[109] who reported very little resistance recovery. In the absence of cracking, the increase in resistance can be attributed to transverse buckling formation and hence coating thinning and also to changes in sample dimension. The latter has also been reported elsewhere[213,118]. The non – recoverable electrical resistance, when cyclic loading is

employed, represents a significant limitation regarding potential flexible devices that have to be deformed more than one time during service.

Another deformation mode that plays a significant role in flexible display development in terms of device flexibility and reliability, is monotonic (section 5.4.1) and repeated cyclic controlled buckling (section 5.4.2). It is important to determine the critical onset strain at which the ITO fails and to observe the possible ITO failure patterns.

For single–cycle electromechanical measurements (section 5.4.1) the ITO on PET 506 (coating in compression) critical onset strain is observed at around 1.1 %. This value is lower than the respective value obtained by Chen et al[121,122] who reported 1.7 %. When ITO surface is under tension a COS value equal to 0.9 % is observed. This is comparable with the value obtained by Chen et al[121,122] (around 1.1 %). However, in both cases during unloading the electrical resistance does not recover. A remarkable full resistance recovery is observed, during unloading, for ITO on PET ST506, when ITO is under compression, figure 5.62. This may be due to compressive internal coating stresses generated during deposition. The critical onset strain recorded, is comparable to that reported in a previous study[121,122].

In addition, when flexible display anodes are compressed repeatedly (section 5.4.2), a new failure pattern (figures 5.68 and 5.75) is observed. Parallel and perpendicular to the compressive direction buckling is evident. This failure pattern is not reported in previous studies. However, Cotterell and Chen[120] noted that cracks grow behind delaminated ITO buckles. This case is evident in this study as figure 5.70 shows for ITO surface in compression. For an ITO surface in tension, (figures 5.71 and 5.72), after 10 cycles of loading and unloading, perpendicular to the uniaxial compressive direction cracking is noted. Also, transverse buckling formation is evident. Cotterell and Chen[120] mention buckling of ITO, on PET, with and without cracking. In both cases the energy released from the substrate can be very much more than the energy stored in the coating itself. They estimated the delamination energy, for $\alpha = 0.97$, to be $32 - 36$ J / m^2. They report a buckling base width around 1 μm, which is comparable with values obtained in this study. Therefore, the adhesion energy reported[120] is much higher than 1.9 J / m^2 which is reported by Bouten et al[117]. When

an ITO surface, deposited on PET ST506 and PEN Kaladex S1020, is under tension (figures 5.80 and 5.86), total electrical degradation is observed after some cycles during loading. This indicates that ITO deposited on PET 506 is a relatively better candidate. However, it is essential to highlight the fact that once electrical resistance is increased, the flexible device degrades and is questionable how flexible display designers can capitalise on a potential resistance recovery.

Electromechanical testing should not be limited to uniaxial tensile and compressive deformation modes but extended to biaxial tension experiments (section 5.5). ITO coated polyester thin systems have not been tested in the past under biaxial tension. This work presents some preliminary results for ITO on PEN Kaladex S1020. As shown in figure 5.89, the ITO electrical resistance can be monitored in situ and the critical biaxial onset strain can be determined. The value obtained, 1.4 %, is comparable with the uniaxial tensile and buckling respective COS values. Leterrier et al[129] have reported a biaxial COS equal to 1.8 ± 0.2% for silicon oxide on PET. The ITO failure pattern as figure 5.91 shows, for 3 % applied biaxial strain, observed using FEG – SEM, is consistent with previously reported patterns[129,130,131,117] (figures 2.20 and 2.21). The failure pattern is characterised by crack channelling and branching. However, improvements need to be accomplished when testing conductive surfaces under biaxial tension[135].

The bulge test method has been used extensively in the past for various applications[136-152]. Of particular importance to this study are the works of Pai – hui I. Hsu et al[143,144,145] who have used the bulge method in order to permanently deform polyamide substrates into three – dimensional shapes as a consequence of a growing interest in the application of large area electronics on curved surfaces. It is therefore important to investigate the evolution of the three - dimensional substrate surface as a function of applied pressure (sections 5.6, 5.6.1, 5.6.2 and 5.6.3).

In general, the PET 506 substrate exhibits the highest central vertical deflection (section 5.6) out of the three experimentally measured substrates (PET 506, PET ST506 and PEN Teonex Q65). This means that PET 506 is the most compliant substrate if film slipping is neglected

in all three cases. PEN Teonex Q65 is influenced the most by the fixed edge effect. It is also apparent that PET ST506 tends to converge with PET 506. The differences of the two – dimensional profiles exist mostly between the PET substrates and the PEN Teonex Q65.

However, it is also interesting to compare the experimentally measured profiles with those obtained from the ideal spherical shape and the Timoshenko[155] predicted thin film shape (sections 5.6.1, 5.6.2 and 5.6.3). The ideal spherical shape is used because most of the existing reviews and models[154,159,161,129,165] assume spherical film deformation. At relatively high applied pressures (>1.3 bar) PET 506 attains a nearly spherical shape (figure 5.116). Below 1.3 bar, the bulge profile is between those of the ideal sphere and Timoshenko. Above 1.5 bar pressure the experimental PET 506 shape tends to attain a higher profile than that of an ideal sphere. In addition, PET ST506 does not fully converge with the ideal spherical shape but it is more stable compared to PET 506 during the initial pressure regime. However, for most of the time it remains in between the ideal spherical profile and the predicted shape. Finally, the PEN Teonex Q65 substrate (figures 5.136 – 5.147) exhibits a different behaviour, which appears to be a little closer to the Timoshenko theory. The fixed edge effect significantly influences the experimental shape even at relatively high applied pressures.

Section 5.6.4 summarises the shape measurements and their deviation from the theoretical profiles. The circular samples are divided in three regions. The first region is near the edge, 12.75 mm from the sample centre, the second is between the sample centre and the fixed edge, 8.5 mm from the centre, and the third is close to the film centre, 4.25 mm. As figure 5.156 shows, PET 506 exhibits the most satisfactory behaviour, near the fixed edge, when compared to the ideal spherical profile. As we move towards the centre of the film, fig 5.155, all three substrates exhibit improved behaviour, which is further improved at a distance of 4.25 mm from the substrate centre. Large deviations are exhibited by the PET substrates near the fixed edge region when compared with Timoshenko theory. PEN Teonex Q65 exhibits relatively better behaviour (figure 5.159). A relatively improved behaviour is exhibited as the bulge centre is approached and significant improvement is observed when the distance from the centre is 4.25 mm (figure 5.157).

From the above data is evident that the polymer substrates do not acquire the ideal spherical shape in the pressure regime used, except for PET 506 under high applied pressures. It is therefore not straightforward to assume equi-biaxial substrate deformation. It is maybe more correct to assume that equi-biaxial deformation exists only in a very narrow film area at the sample centre. This is in agreement with Papirno[156] who reported that the actual strains in a bulged system vary considerably from those that are predicted on the basis of sphericity and equi–biaxial strain. Tsakalakos[158] tried to use the actual bulge shape in order to arrive at a simple analytical solution but failed to reach a satisfactory solution.

Using the equations presented in table 2.1 initial stresses and biaxial moduli of the polyester films can be computed (section 5.7). The three analytical models; spherical cap[154], Hencky[165] and energy minimization[166] predict the same initial stress, which is a function of the film residual stress and the clamping stress, but different biaxial modulus values.

The stiffest response is predicted from the spherical cap model. However, the latter is the only model that works without the Poisson's ratio input, which is difficult to measure. The potential problem using the spherical cap model lies in the fact that it assumes equi–biaxial stress throughout the circular film. As we saw above this is not the case because constraints are imposed near the fixed edge at relatively high-applied pressures. Using the other models a more compliant response is expected.

An experimental consideration when using the bulge test is that the thin film sample is assumed to be flat at zero applied pressure. It is therefore apparent, as discussed by Small and Nix[161], that bulge testing on slack films should not be conducted.

As figure 5.160 shows, the initial linear pressure deflection data can be fitted to the generalized bulge equation 2.16 in order to calculate the initial stress and biaxial modulus. Satisfactory agreement is observed for the case of PET 506 when using the spherical cap model. If we set E = 2.35 GPa, measured by tensile testing, and $\nu = 0.33$ we can verify that M = 3.5 GPa which is comparable to 3.75 ± 0.3 GPa obtained using the spherical cap model. Good agreement is also found for PEN Kaladex S1020 using E = 3.3 GPa and $\nu = 0.33$. The

biaxial modulus is equal to 4.9 GPa and comparable to the 4.55 ± 0.4 GPa that is obtained using uniaxial tensile testing.

However, it is important to note that only the initial linear portion of the pressure / deflection versus squared deflection data must be fitted into equation 2.16. If the whole data are fitted to the generalized equation, an underestimation of the biaxial modulus will be achieved. It is therefore essential that the bulge pressure gauge must exhibit good resolution at the early stages of the introduction of pressure.

Also, relatively good agreement for the case of PET 506 biaxial modulus is observed using Small's and Hencky's models for $v = 0.33$. However, Pan's and Lin's models yield higher values. For PEN Kaladex S1020 the same models as in the case of PET 506 appear to be in relatively good agreement for $v = 0.33$. However, if the PET Young's moduli are set equal to those reported in other studies[24,103,121], the biaxial moduli computed from all the bulge models will be an underestimation of the actual value for $v = 0.33$. The deviation can be as large as 50%.

The last section (5.8) of the bulge test aims to demonstrate the different biaxial tensile behaviour of ITO coated and uncoated substrates. Using the spherical membrane assumption, Williams[159] and Leterrier[129] derived biaxial stress and strain equations for large bulge displacements. Both stress equations yield the same result. However, William's strain solution predicts larger strain as compared to Leterrier's. The contribution of the ITO coating on the stress and strain response of the composite system is evident, due to elastic mismatch, for the case of ITO on PET 506 and PET ST506 and PEN Kaladex S1020 when ITO is placed under tension. When the ITO surface is placed under compression, there is no significant difference observed in the ITO on PEN Kaladex S1020 case. The latter may indicate the presence of little residual stress in the coating.

7.3 PART C - Discussion of tribological investigation

The friction and wear of polyester substrates, using a pin-on-disc apparatus, has been little studied in the past. Section 6.1 aims to investigate some fundamental aspects of the tribological response of PET 506 and PEN Kaladex S1020 substrates sliding against a relatively smooth steel ball. As figure 6.2 shows, the steady-state period for PET 506 is significantly interrupted - a case not observed frequently for PEN Kaladex S1020. This may be attributed to the presence of putative crystallites on the surface of PET 506 and their rearrangement during sliding. The running-in period is dependent on the contact between the polymer and the counterbody and how carefully they are aligned on initiation of testing[183]. However, misalignment of the ball and film is unlikely, as compared to polymer pin–steel disc systems, because of the smaller contact area. In addition, the fact that further interruptions occurred, even when steady–state running was reached, highlights the role of the surface features and roughness of PET 506 which are higher as compared to those of PEN Kaladex S1020. Further study at a low number of cycles might be interesting.

There are two regimes of behaviour of measured friction coefficients (figure 6.3), for both films, against number of sliding cycles. Up to 6450 sliding cycles, higher mean friction coefficients are observed. When polymers slide over clean and smooth counterfaces the adhesion between the polymer and the counterface is of sufficient magnitude to inhibit sliding[177]. Appreciable interlocking between the higher surface features and asperities of the steel counterface may exist. On the other hand, above 8000 cycles lower friction coefficient values are measured. This is a dramatic increase in the case of PEN Kaladex S1020.

In general, the wear rate for PET shows nearly stable wear up to 8000 cycles whereas the PEN Kaladex S1020 wear rate increases, but is lower than the wear rate of PET 506, as the number of sliding cycles increases (figure 6.5). This may be attributed to the higher crystallinity and lower surface roughness of PEN Kaladex S1020 as compared with PET 506. The measured wear rate of PET 506 shows good agreement with results obtained by Tanaka et al[184,185].

It has been reported[214] that debris particles, figures 6.6 and 6.7, modify the topography of the counterface and as a consequence the measured wear rate becomes sensitive to the gross contact geometry. After testing, it was observed that polymer transfer to the steel ball occurred. A similar observation has been reported in the past for the case of biaxially oriented PET films[189]. The micro–cutting mechanism observed for PET 506, as figure 6.8 shows, leads directly to wear[178]. As the number of sliding cycles increases, most of the larger-edged wear particles have been removed from the worn central area by the action of the steel ball (figures 6.9 and 6.10). Similar behaviour is observed for PET films, using nanotribology, by Beake et al[194]. Since the influence of the wear debris particles is diminished, this phenomenon can be correlated with the decrease in friction coefficient values for both polyester substrates.

Nanoscratch and nanoindentation of coated and uncoated systems (section 6.2) provide useful information in coating adhesion terms as well as mechanical properties, mainly of bare substrates. Table 6.2 shows results of hardness and Young's modulus values of coated and uncoated substrates.

Most of the coated substrate results cannot be used since the nanoindentation depth exceeded the limit of a few tens of nm. When, the nanoindentation depth exceeds a few tens of nm, the measured mechanical properties are dominated by the substrate behaviour. However, satisfactory agreement, especially in the case of PET 506 bare substrates, of Young moduli measured by nanoindentation and tensile testing, is noted. Finally, ITO on PEN Kaladex S1020 exhibit higher scratch adhesion than ITO on PET 506 as shown by figures 6.12 and 6.13.

8. Conclusions

8.1 General concluding remarks

This work was motivated by the need to investigate the mechanical properties of ITO-coated, polyester, display anode components. The anode component is common to almost all flat panel display technologies and therefore the evolution from flat panel displays to flexible flat panel displays is directly linked with the mechanical reliability of such a component.

Before describing the mechanical issues involved, it is important to note that a part of this project was dedicated to the characterisation of the coated and / or uncoated substrates. The investigation was undertaken in order to determine potential differences in behaviour and performance between PET and PEN and the effect of different polyester substrates on the ITO performance. Also, some preliminary work was conducted on depositing ITO on PEN by pulsed laser deposition as an alternative to magnetron sputtering.

However, it is recognized that thin ITO films, sputtered on polymer substrates, are brittle and fail at relatively low externally applied strains. The mismatch between mechanical properties of coating and substrate represents a major issue in utilizing flexible displays. It is therefore interesting, since the flexible device can be deformed in many different ways during service, to test flexible display anodes under different stress states and deformation modes and investigate potential failure mechanisms.

A considerable amount of effort was directed towards testing such thin structures under different stress states and deformation modes. This effort was divided between the development of new testing techniques and the actual testing of various coated and uncoated systems. Specifically, the biaxial 'bulge' test was built in order to accommodate biaxial testing of thin display substrates. Satisfactory progress was achieved towards the use of

different bulge models for extracting bare substrate mechanical properties, which are compared with uniaxial tensile testing results. Also, a commercial mechanical tester was modified in order to accommodate electromechanical testing of display anodes under uniaxial tension and compression using monotonic and cyclic loads. It had been shown previously that electrical resistance monitoring offers a significant advantage in determining the electrical functionality of the substrates. This latter fact was fully capitalized in this project. Particular attention was paid towards ex–situ microscopical investigation of electromechanically tested thin surfaces. Numerous surface failure mechanisms were detected and failure patterns were measured with the aid of an AFM.

Finally, it is predicted that the tribological reliability of display components may play an important role in the future, since more demanding display applications will be developed. These devices may need to operate in harsh environments, in tribological terms. Also, substrate and/or coating properties can be determined using nanoindentation and nanoscratch methods. This highlights the importance of using nano–scale tribological techniques in characterising flexible display components. This study also presented work in this field.

8.2 PART A – Conclusions from general characterisation and preparation of ITO by PLD (Chapter 4)

PEN Kaladex S1020 bare substrates exhibit lower roughness than both the PET substrates. This is an important feature since deposition of subsequent display layers requires the presence of a smooth base substrate surface. The roughness difference can be attributed to the presence of putative crystallites that are present mainly on the PET 506 substrate.

In addition, the biaxial stretching of the PET 506 has induced more orientation in the machine direction as compared to the transverse direction. The T_g and T_m values are higher for PEN Kaladex S1020. This is important in display manufacturing terms. Also, PEN

Kaladex S1020 is more crystalline as compared to PET 506. This may have an effect on the mechanical properties.

The ITO RMS roughness is lower when PEN substrates are used. This suggests that the substrate topography is transferred on to the ITO layer and underlines the importance of a smooth base substrate surface. Furthermore, ITO films sputtered on polyester substrates at room temperature were found to be amorphous. However, when annealed at around 100° C for a few minutes, amorphous ITO can become polycrystalline. PEN substrates can be used at this temperature since they exhibit minimum shrinkage.

Additionally, ITO on PET 506 exhibits the lowest electrical resistivity whereas ITO on PEN Kaladex S1020 exhibits the highest resistivity value. Also, the optical transmission, at 638 nm wavelength, is higher for ITO on PET 506 than that of ITO on PEN Kaladex S1020. Finally, the ability to deposit high quality ITO films on PEN Kaladex S1020 substrates at room temperature by pulsed laser deposition has been demonstrated.

8.3: PART B – Conclusions from mechanical properties (Chapter 5)

Higher Young's moduli are measured for PEN substrates as compared with PET display substrates. On the other hand, a higher elastic modulus is observed for ITO when is sputtered on PET substrates.

ITO on PET 506 and ITO on PET ST506 flexible anodes are the most reliable when tested, monotonically, under uniaxial tension. The critical onset strain at which ITO failure initiates is around 2 %. A gradual electrical resistance increase is observed suggesting a synergistic effect of two different ITO bridging mechanisms.

Ex–situ microscopical investigations of ITO, under monotonic uniaxial tension, surfaces suggest cohesive and adhesive failure. It was shown that ITO transverse buckling is a real

issue even at strains as low as 3 %. Also, it is important to note that as the applied uniaxial tensile strain increases, the number of cohesive cracks increases.

Cyclic uniaxial tensile testing of various flexible display anodes showed that resistance does not recover significantly during the unloading portion of each cycle. The absence of cohesive failure is noted in this case. In the absence of cracking, the increase in resistance is attributed to transverse buckling formation and hence coating thinning and also to changes in sample dimension.

When flexible anodes are subjected to controlled monotonic buckling, COS values are lower than those observed under uniaxial tension. Also, electrical resistance recovery is observed for ITO on PET ST506 after a single – cycle deformation. When flexible anodes are compressed repeatedly, a new failure pattern is observed to exist. This pattern is characterized by open and closed buckles both perpendicular and parallel to the compression direction.

The ability to conduct biaxial electromechanical testing of flexible display anode electrodes has been demonstrated. The coating fails at a critical onset biaxial strain equal to 1.4 %. The failure pattern is characterised by crack channelling and branching.

The evolution of the two – dimensional bulge shape with respect to applied pressure was investigated, using the biaxial 'bulge' test, for various bare substrates. It was found that PET 506 substrate exhibits the highest central vertical deflection. The experimentally measured profiles were compared with the ideal spherical profile and the profile predicted by Timoshenko. It is evident that equi - biaxial deformation exists only in a very narrow film area at the sample centre.

Good agreement, in measuring the biaxial modulus M, is found by using the spherical cap model, Small's model and Hencky's model. However, the spherical cap model, although simplified, does not need the Poisson's ratio as an input parameter.

8.4 PART C – Conclusions from tribological investigation

An attempt to compare the tribological response of PET and PEN display substrates has been undertaken. The larger initial running in period for PET friction is attributed to surface topography differences between the two polyester substrates. Higher coefficient of friction values for both materials, up to 6450 sliding cycles, is attributed to high adhesion between the polymer and the steel counterbody.

The decrease of friction coefficient, for both materials, after a considerable number of sliding cycles can be correlated with the wear debris displacement towards and beyond the wear track edges. Adhesive wear at a low number of sliding cycles is observed, and also a mixture of plastic deformation, micro - cutting and fatigue wear. At a high number of sliding cycles polymer chains may realign towards the sliding direction and displacement of wear debris towards the wear track periphery occurs. Lower measured wear rates of PEN, at a low number of sliding cycles, can be attributed to its higher crystallinity as compared with PET.

Finally, nanoindentation of bare substrates revealed that PEN Kaladex S1020 is harder than PET 506. Good agreement between Young's moduli measured by nanoindentation and Young's moduli measured by uniaxial tensile testing, especially in the case of PET 506, is observed. ITO on PEN Kaladex S1020 is observed to exhibit better scratch resistance than ITO on PET 506.

8.5 Conclusions from the flexible display point of view

In order to evaluate the results (Chapter 4, 5 and 6), it is important to consider some key elements related to flexible display technology and manufacturing. It is almost certain that no single display technology will serve all display applications. Therefore, the choice of the

substrate will depend on the particular display application need(s) and the related manufacturing route(s).

A flexible display application will not require, for example, the use of a frame, which holds together the structure. This implies that the substrate must be as stiff as possible. The higher Young's modulus of PEN as compared to that of PET indicates that PEN may be a better candidate. Better thermal properties of PEN indicate that it can withstand higher manufacturing temperatures. As far as optical properties are considered, both polyester substrates are good candidates for bottom – emissive displays. The deposition of subsequent layers on polyester substrates, i.e. display manufacturing, also presents key challenges. The roughness of the substrate, for example, is critical in order to deposit smooth functional layers. ITO on PEN substrates is less rough as compared to ITO on PET substrates. As shown, the sputtered layer acquires the topography of the substrate.

However, looking at conductive substrate resistivities, it is observed that ITO on PET ST506 exhibits lower electrical resistivity and thus higher electrical conductivity, which is desirable in all display applications. The larger islands formed, when ITO is deposited on PET 506 are a consequence of the underlying substrate surface morphology, provide better electrical conduction as compared to ITO on PEN Kaladex S1020 case. On the other hand they may form larger surface defects.

Flexible devices can be divided into three categories: (i) curved or conformed, but not flexed during use, (ii) mildly flexible, but not designed for severe treatment such as rolling and (iii) fully flexible, like paper.

The limiting strain of around 1 % for ITO-coated polyester flexible display electrodes suggests that slightly curved displays, i.e. category (i), can be manufactured at the moment. The challenge lies mostly in the improvement of the mechanical durability of the brittle ITO coating for higher applied external strains. Critical uniaxial tensile stresses and strains for failure can be used as design input parameters for roll–to–roll display manufacturing. Electromechanical testing under various stress states and deformation modes is essential in

order to determine failure strains and understand the failure mechanisms involved. This represents a significant step towards utilizing roll–to–roll flexible display processing.

In this study, electromechanical controlled buckling of flexible anodes was investigated. The critical onset strain values at which electrical resistance degradation initiates are lower than those observed in uniaxial tensile experiments. This finding suggests that the flexible display, in service conditions, will fail at a lower strain if compressed. However, the compression mode is quite complex in the sense that the ITO layer can be actually put under uniaxial tension or uniaxial compression. Under controlled buckling a new failure pattern was observed. Periodic open and closed buckling zones, parallel and perpendicular to the applied force direction, were detected.

The fact that, in most cases, electrical resistance does not recover during unloading, in both uniaxial tensile and buckling cyclic experiments, limits the use of ITO coated polyester electrodes for mildly flexible (category (ii)) and fully flexible (category (iii)) display applications. However, even if electrical resistance were to recover during unloading, the degradation of conductivity during the loading portion of the cycle represents an initial limiting factor.

The development of the biaxial 'bulge' test technique for display applications can be proved significant in the future, especially towards the direction of three – dimensional permanently curved displays. It is an initial step towards the determination of mechanical stresses as well as shape profiles introduced during three-dimensional shaping of polymer based conformal displays, (which at a higher temperature can be permanent).

Also, this work is the first to present results of ITO on PEN Kaladex S1020 biaxial electromechanical response. This is important because during manufacturing the substrate will, almost certainly, be subjected to a biaxial stress rather than a uniaxial one. ITO biaxial coating failure detection was also achieved in this study for the first time.

In addition, the use of various bulge models in determining the mechanical properties of bare substrates was beneficial because the biaxial moduli of the substrates were measured and some models proved more appropriate than others for this process. This is a positive step towards extracting the mechanical properties of more complicated display structures which should not be limited to ITO coated polyesters but also include other flexible display materials.

Flexible displays and touch screens may be susceptible to scratching if the user is inexperienced or if they operate in tough conditions and harsh environments. Potential flexible display applications such as drawing touch - pads and flexible expedition electronic maps are strong candidates for this special category. It is therefore interesting to conduct macro–scale tribological testing of bare substrates. In this project some such work was carried out. Friction and wear of polyester films was investigated and a range of wear mechanisms described. PEN Kaladex S1020 seems to exhibit lower wear rates than PET 506 at low sliding cycles. Also, Knoop indentation measurements revealed that PEN Kaladex S1020 is harder than PET 506. This is important if we consider a resistive touch – screen polyester top – sheet in contact with a rigid stylus. The elastic moduli measured by indentation are in good agreement with those obtained by uniaxial tensile testing, in particular for the case of PET 506.

8.6 Overall conclusions

It is believed that this work forms a solid foundation on to which further research, in the subject, will be based. Following a thorough coverage of the previous literature, new experimental techniques, with considerable room for further development, were established and also several standard experimental techniques were used. Various experimental results were presented and the most interesting were discussed in more detail. It is hoped that useful conclusions, from the display point of view, were drawn. It is necessary to underline that this

is a rapidly growing field and is almost certain that new and exciting display materials, which will require mechanical and tribological investigation, will appear in the future.

9. Further work and development

In order to further this work, a number of areas suggest themselves for immediate development. Annealing of ITO films sputtered at room temperature on PEN substrates should be attempted in order to observe potential microstructural changes of ITO from amorphous to crystalline. An indicative annealing temperature at which the substrate can survive[24] may be 150 °C; that is a temperature at which the amorphous to crystalline ITO transition has been reported in the past. It will be interesting to characterise and compare amorphous and crystalline ITO films deposited on polyester substrates.

In addition, thermal cycling of flexible anodes can be conducted using an appropriate oven, for a temperature range between −100 to +160 °C. Thermal fatigue cycling may reveal ITO potential failure patterns that in turn have to be observed ex-situ by SEM and AFM. These patterns may be compared with those obtained from uniaxial and/or biaxial tensile and uniaxial compressive testing.

It is important that the development of the biaxial 'bulge' test technique be continued in the future. More specifically, the development of an optical technique is essential, in order to measure accurately the biaxial strain. Mounting an optical microscope on the apparatus and measuring the evolution of the shape of a circle drawn at the central area of the sample should be able to achieve that. The optical microscope can be used in order to monitor, in–situ, the coating failure process. Also, the electro–mechanical testing can be improved by measuring the resistance at four symmetrical points, similarly to the Van der Pauw method[229]. Finally, a pressure controller can be installed in the system in order to automatically introduce gas pressure into the vessel at small but equal increments. This will significantly improve the pressure resolution, particularly in the low-pressure regime.

It will perhaps be interesting to investigate the electromechanical properties of alternative flexible display anodes such as PEDOT: PSS coated polyester since it has been reported[118]

recently that conductive organic coatings significantly improve the mechanical reliability of coated substrates under monotonic and cyclic loads. However, conductivity and thermal stability of PEDOT: PSS are significantly low up to date and inferior to the respective ITO values.

Another approach is to continue using ITO coated polyesters but pattern the coating in the form of thin and long serpentine–like structures. It has been recently reported[230] that by using these serpentine–like film shapes, large elongations of the substrate induce small strains in the film. The challenge lies in the accurate patterning of the ITO film, which is beyond the scope of the present project. Also, testing of ITO patterned lines[117] and/or patterned spherical islands might be interesting. Additionally, the two – point electromechanical bending, using fibre fragmentation equipment, can be added to the variety of electromechanical tests available.

Pulsed laser deposition of ITO on PEN substrates, at moderate temperatures, should be continued since preliminary results are encouraging. Since the PEN substrate can survive at around 120 - 150 °C, it will be attractive to deposit ITO films at this temperature. It will be also interesting to deposit the functional oxide on dumbbell specimens in order to test them under tension and / or compression. The comparison of mechanical properties of sputtered and pulsed laser deposited ITO on polyester samples should be a good contribution. The central area of circular bulge samples can also be coated in order to test the pulsed laser deposited ITO coating under biaxial stress conditions.

The use of transmission electron microscopy, TEM, in order to investigate the oxide's thickness direction morphology represents a significant challenge. The substrate – coating interface may also be investigated by using TEM. Sample preparation, especially when a thin polymer substrate and a brittle coating are involved, is demanding.

Finally, more work is needed on the tribological investigation of coated and uncoated substrates. In particular, attention should be directed towards using the AFM as a tribological investigation tool. The nanotribology of coated and uncoated systems can provide

fundamental information for the adhesion, friction and wear of such systems. Friction force maps can be obtained using contact - mode AFM. Macroscale wear testing should be also conducted using lower loads (i.e. less than the ~10 N used in this study). It is important to note that nano-indentation experiments should be conducted. When testing the ITO surface, a very shallow indent (not more than 1/5 of the coating thickness) must be produced in order to determine accurately the properties of the coating.

References

1. The boy who invented television. A story of inspiration, persistence and quite passion. Paul Schatzkin, Teamcom Books, Sep. 2000, ISBN: 1928791301
2. G. Crawford, Lecture Notes, Brown University, Photonics Group, 2003, www.brown.edu
3. Gregory P. Crawford, Flexible Flat Panel Display Technology Chapter1, flexible flat panel displays edited by G. P. Crawford, SID series in display technology, Wiley, 2005, pp 1-2
4. Advanced Flat-Panel Displays and Materials, Yue Kuo and Kouji Suzuki, Guest Editors, Materials Research Society Bulletin, November 2002, pp. 859-863
5. Printed, flexible electrochromic displays using interdigitated electrodes. James P. Coleman, Anne T. Lynch, Puttanachetty Madhukar, John H. Wagenknecht, Solar Energy Materials & Solar Cells 56 (1999) 395-418
6. Prospects and Applications for organic light-emitting devices. Paul E. Burrows, Stephen R. Forrest and Mark E. Thompson, Current Opinion in Solid State & Materials Science, 1997, 2:236-243
7. Passive-Matrix Polymer Light-Emitting Displays. Elian I. Haskal, Michael Buchel, Paul C. Duineveld, Aad Sempel and Peter van de Weijer, Materials Research Society Bulletin, November 2002, pp. 864-869.
8. Developments in Organic Displays, John K. Borchardt, Materials Today, September 2004, Elsevier, pp. 42-46
9. Wear resistance of Indium Tin Oxide Coatings on Polyethylene Terepthalate substrates for Touch Screen Applications. Darran R. Cairns, Gregory P. Crawford and Anthony F. Chernefsky, Society of Information Display 00 Digest, pp 1-4
10. Bending the display rules: Options and Challenges for Flexible Displays. Peter J. Slikkerveer, Eurodisplay 2002, pp. 273-276
11. K.A. Sierros, J. S. Abell and S.N. Kukureka, Novel Applications of Surface Modification, IOP, Chester, 2005

12. Mechanical reliability of conductive polymers for rollable display applications. Darran R. Cairns. Chapter 9 in flexible flat panel displays edited by G. P. Crawford, SID series in display technology, Wiley, 2005, p. 165
13. Roll to roll manufacturing of flexible displays. Abbie Gregg, Lara York and Mark Strnad. Chapter 21 in flexible flat panel displays edited by G. P. Crawford, SID series in display technology, Wiley, 2005, pp. 409 – 445
14. Flexible flat panel technology. Gregory P. Crawford. Chapter 1 in flexible flat panel displays edited by G. P. Crawford, SID series in display technology, Wiley, 2005, pp. 1 – 9
15. Evaluation of coatings. S. J. Bull, D. S. Rickerby. British ceramic. Transactions and Journal 88, Institute of Materials, 1989, pp.177-183
16. Handbook of Thermoplastic Polyesters, Volume 1, Preface, S. Fakirov, Edited by S. Fakirov, Wiley-VCH, 2002
17. Handbook of Thermoplastic Polyesters, Volume 1, E. Marechal, Chapter 1: Synthesis and Chemical Aspects, Edited by S. Fakirov, Wiley-VCH, pp 3-45
18. Handbook of Thermoplastic Polyesters, Volume 1, S. M. Aharoni, Chapter 2: Industrial Scale Production of Polyesters, Especially PET, Edited by S. Fakirov, Wiley-VCH, p. 59
19. Molecular Orientation in Biaxially Drawn PET film. Duncan H. Gordon, PhD Thesis, University of Leeds, Department of Physics, September 1992
20. New Developments in Polyester Films for Display Applications. W.A. MacDonald, J.M. Mace and N.P. Polack, 45th Annual Technical Conference Proceedings (2002), Society of Vacuum Coaters, pp. 482-486
21. Handbook of Thermoplastic Polyesters, Volume 1, PET Fibers, Films and Bottles, Chapter 7, V.B. Gupta and Z. Bashir, Edited by S. Fakirov, Wiley-VCH, p. 363
22. Handbook of thermoplastic polyesters, Volume 1, PEN: Structure and Properties. M. Ito and T. Kikutani, Edited by S. Fakirov, Wiley-VCH, p. 463
23. Plastics: Microstructure and engineering applications. N. J. Mills. Arnold, 2nd Edition, 1993, pp. 31 – 32
24. Engineered films for display technologies. Bill A. MacDonald, Keith Rollins, Duncan MacKerron, Karl Rakos, Robert Eveson, Katsuyuki Hashimoto and Bob

Rustin. Chapter 2 in Flexible flat panel displays edited by Gregory P. Crawford, Wiley, SID, Series in display technology, 2005, pp. 13-14

25. Engineered films for display technologies. Bill A. MacDonald. Journal of materials chemistry, 14, 2004, pp. 4-10

26. The crystal structure of polyethylene terepthalate. R. de P. Daubeny, C. W. Bunn and C. J. Brown. Proceedings of Royal Society (London), A226, 1954, pp. 531-542

27. Crystal structure, morphology and orientation of polyesters. P. H. Geil. Chapter 3 in Handbook of Thermoplastic Polyesters, Volume 1, Edited by S. Fakirov, Wiley-VCH, 2002, p. 133

28. Crystal structure, morphology and orientation of polyesters. P. H. Geil. Chapter 3 in Handbook of Thermoplastic Polyesters, Volume 1, Edited by S. Fakirov, Wiley-VCH, 2002, p. 175

29. Crystal structure, morphology and orientation of polyesters. P. H. Geil. Chapter 3 in Handbook of Thermoplastic Polyesters, Volume 1, Edited by S. Fakirov, Wiley-VCH, 2002, p. 183

30. Microstructural characterization of PEN based on the amorphous and crystalline phase properties. Z. Denchev, I. Sics, A. Nogales and T. A. Ezquerra. Chapter 11 in Handbook of Thermoplastic Polyesters, Volume 1, Edited by S. Fakirov, Wiley-VCH, 2002, p. 488

31. The measurement of molecular orientation in polymers by spectroscopic techniques. I. M. Ward. Journal of Polymer Science: Polymer Symposium 58, 1977, pp. 1 – 21

32. Uniaxial and biaxial orientation of polymer films and sheets. A. J. De Vries, C. Bonnebat and J. Beautemps. Journal of Polymer Science: Polymer Symposium 58, 1977, pp. 109 – 156

33. Influence of the arrangement of the crystals and the structure of the non – crystalline regions on the mechanical properties of PET. H. J. Biangardi and H. G. Zachmann. Journal of Polymer Science: Polymer Symposium 58, 1977, pp. 169 – 183

34. Molecular mechanism of neck formation in uniaxially stretched PEN films. M. Cakmak and S. W. Lee. Polymer, Volume 36, Number 21, 1995, pp. 4039 – 4054
35. Effect of composition on orientation, optical and mechanical properties of biaxially drawn PEN and PEN / PEI blend films. J. C. Kim, M. Cakmak and X. Zhou. Polymer, Volume 39, Number 18, 1998, pp. 4225 – 4234
36. A new approach to the characterization of molecular orientation in uniaxially and biaxially oriented samples of PET. K. C. Cole, H. Ben Daly, B. Sanschagrin, K. T. Nguyen, A. Ajji. Polymer, 40, 1999, pp. 3505 – 3513
37. Improvements in the use of attenuated total reflection Fourier transform infrared dichroism for measuring surface orientation in polymers. Neil J. Everall and Arran Bibby. Applied Spectroscopy, Volume 51, Number 8, 1997, pp. 1083 – 1091
38. Characterization of biaxial orientation gradients in PET films and bottles using polarized attenuated total reflection FTIR spectroscopy. Neil Everall, Duncan MacKerron, Derek Winter. Polymer, 43, 2002, pp. 4217 – 4223
39. Structure development and mechanical behaviour during uniaxial drawing of PET. U. Goschel. Chapter 6 in Handbook of Thermoplastic Polyesters edited by Stoyko Fakirov, Volume 1, 2002, Wiley – VCH, p. 314
40. Transparent conducting oxide materials and technology. David C. Payne, Hyo – Young Yeom and Burag Yaglioglu. Chapter 5 in flexible flat panel displays edited by G. P. Crawford, SID series in display technology, Wiley, 2005, p. 79
41. Transparent conducting oxides. David S. Ginley and Clark Bright (Guest editors). MRS Bulletin, Material Research Society, August 2000, p. 17
42. Criteria for choosing transparent conductors. Roy G. Gordon. MRS Bulletin, Material Research Society, August 2000, pp. 53 – 54
43. Applications and processing of transparent conducting oxides. Brian G. Lewis and David C. Paine. MRS Bulletin, Material Research Society, August 2000, p. 23
44. Applications and processing of transparent conducting oxides. Brian G. Lewis and David C. Paine. MRS Bulletin, Material Research Society, August 2000, p. 24

45. Transparent conducting oxide materials and technology. David C. Payne, Hyo – Young Yeom and Burag Yaglioglu. Chapter 5 in flexible flat panel displays edited by G. P. Crawford, SID series in display technology, Wiley, 2005, p. 96

46. Evaporation: Processes, bulk microstructures and mechanical properties. Rointan F. Bunshah. Chapter 4 in Thin film deposition: Handbook of deposition technologies for films and coatings – Science technology and applications, Edited by R. F. Bunshah, 2nd Edition, 1994, William Andrew Publishing / Noyes, pp. 163-164

47. Thin film processes. Thin film materials technology. Sputtering of compound materials. Wasa Kiyotaka, Kitabatake Makoto, Adachi Hideaki, 2004, William Andrew Publishing / Noyes, pp. 39-42

48. F. M. Penning, U.S. Patent 2, 146, 025, February 1935

49. Magnetron sputtering on large scale substrates: an overview on the state of the art. Reiner Kukla. Surface and Coatings Technology, 93, 1997, pp. 1-6

50. Physics of very thin ITO conducting films with high transparency prepared by DC magnetron sputtering. T. Minami, H. Sonohara, T. Kakumu and S. Takata. Thin Solid Films, 270, 1995, pp. 37-42

51. Electrical, optical and structural characteristics of indium-tin-oxide thin films deposited on glass and polymer substrates. A. K. Kulkarni, K. H. Schulz, T. –S. Lim and M. Khan. Thin Solid Films, 308 – 309, 1997, pp. 1-7

52. Dependence of the sheet resistance of indium-tin-oxide thin films on grain size and grain orientation determined from X-ray diffraction techniques. A. K. Kulkarni, Kirk H. Schulz, T. S. Lim and M. Khan. Thin Solid Films, 345, 1999, pp. 273 – 277

53. Low resistivity transparent electrodes for displays on polymer substrates. M. Fahland, P. Karlsson and C. Charton. Thin Solid Films, 392, 2001, pp. 334 – 337

54. Properties of dc magnetron sputtered ITO films on polymeric substrates at room temperature. J. H. Shin, S. H. Shin, J. I. Park and H. H. Kim. Journal of Applied Physics, Volume 89, Number 9, 1 May 2001, pp. 5199 – 5203

55. Characterization of sputtered indium tin oxide layers as transparent contact material. Gerhard Franz, Benjamin Lange and Stefan Sotier. Journal of Vacuum Science and Technology, A 19 (5), Sep / Oct 2001, pp. 2514 – 2521

56. Characterization of transparent aluminium oxide and indium tin oxide layers on polymer substrates. B. M. Henry, A. G. Erlat, A. McGuigan, C. R. M. Grovenor, G. A. D. Briggs, Y. Tsukahara, T. Miyamoto, N. Noguchi and T. Niijima. Thin Solid Films, 382, 2001, pp. 194 – 201

57. Internal stress of ITO, IZO and GZO films deposited by rf and dc magnetron sputtering. T. Sasabayashi, P. K. Song, Y. Shigesato, K. Utsumi, A. Kaijo and A. Mitsui. Materials Research Society Symposium Proceedings, Volume 666, 2001, MRS, pp. F2 4.1 – 4.6

58. ITO thin films deposited at low temperatures using a kinetic energy controlled sputter – deposition technique. Yoichi Hoshi and Takakazu Kiyomura. Thin Solid Films, 411, 2002, pp. 36 – 41

59. Deposition technology of transparent conductive coatings on PET foils. M. Fahland, C. Charton and A. Klein. 45th Annual Technical Conference Proceedings, Society of Vacuum Coaters, 2002, pp. 487 – 491

60. A study of the effect of process oxygen on stress evolution in dc magnetron deposited tin-doped indium oxide. Hyo – Young Yeom, Natasha Popovich, Eric Chason and David C. Paine. Thin Solid Films, 411, 2002, pp. 17 –22

61. Influence of negative metal ion bombardment on the properties of ITO / PET films deposited by dc magnetron sputtering. Daeil Kim. Journal of Non – Crystalline Solids, 331, 2003, pp. 41 – 47

62. Resistivity and microstructure issues in indium – oxide based films grown by rf magnetron sputtering on flexible polyester substrates. P. F. Carcia, R. S. McLean, M. H. Reilly, Z. G. Li, D. E. Wilmington, L. J. Pillione and R. F. Messier. 46th Annual Technical Conference Proceedings, Society of Vacuum Coaters, 2003, pp. 195 – 199

63. Thickness dependence of In_2O_3:Sn film growth. Z. Qiao, R. Latz and D. Mergel. Thin Solid Films, 466, 2004, pp. 250 – 258

64. Flexible organic light - emitting device based on magnetron sputtered indium tin oxide on plastic substrate. F. L. Wong, M. K. Fung, S. W. Tong, C. S. Lee and S. T. Lee. Thin Solid Films, 466, 2004, pp. 225 – 230

65. Room temperature deposition of thin film ITO on micro – fabricated colour filters and its application to flat panel displays. Zhiguo Meng, Huajun Peng, Chunya Wu, Chengfeng Qiu, Kuen Kuen Li, Man Wong and Hoi Sing Kwok. Journal of the SID, 12 / 1, 2004, pp. 113 – 118

66. Comparison of study of ITO thin films deposited by sputtering at room temperature onto polymer and glass substrates. C. Guillen and J. Herrero. Thin Solid Films, 480 – 481, 2005, pp. 129 – 132

67. Criteria for choosing transparent conductors. Roy G. Gordon, MRS Bulletin, August 2000, p. 52.

68. Low resistivity indium tin oxide films by pulsed laser deposition. J. P. Zheng and H. S. Kwok, Applied Physics Letters, 63 (1), 5 July 1993.

69. On the initial growth of indium tin oxide on glass. X. W. Sun, H. C. Huang and H. S. Kwok, Applied Physics Letters, 68 (19), 6 May 1996.

70. Resistivity and oxygen content of indium tin oxide films deposited at room temperature by pulsed laser ablation. Y. Wu, C. H. M. Maree, R. F. Haglund, Jr., J. D. Hamilton, M. A. Morales Paliza, M. B. Huang, L. C. Feldman and R. A. Weller, Journal of Applied Physics, Volume 86, Number 2, 15 July 1999, pp. 991-994

71. High-quality indium tin oxide films at low substrate temperature. Frederic O. Adurodija, Hirokazu Izumi, Tsuguo Ishihara, Hideki Matsui and Muneyuki Motoyama, Applied Physics Letters, Volume 74, Number 20, 17 May 1999, pp. 3059-3061

72. Stoichiometric indium oxide thin films prepared by pulsed laser deposition in pure inert background gas. Yuka Yamada, Nobuyasu Suzuki, Toshiharu Makino and Takehito Yoshida, Journal of Vacuum Science and Technology, A, 18 (1), Jan/Feb 2000, pp. 83-86

73. Reactive pulsed laser ablation and deposition of thin indium tin oxide films for solid-state compact sensors. R. Teghil, V. Marotta, A. Giardini Guidoni, T. M. Di Palma and C. Flamini, Applied Surface Science, 138-139, 1999, pp. 522-526

74. Electrical, optical and structural properties of indium tin oxide thin films for organic light-emitting devices. H. Kim, C. M. Gilmore, A. Pique, J. S. Horwitz, H. Mattoussi, H. Murata, Z. H. Kafafi and D. B. Chrisey, Journal of Applied Physics, Volume 86, Number 11, 1 December 1999, pp. 6451-6461

75. Indium tin oxide thin films for organic light-emitting devices. H. Kim, A. Pique, J. S. Horwitz, H. Mattoussi, H. Murata, Z. H. Kafafi and D. B. Chrisey, Applied Physics Letters, Volume 74, Number 23, 7 June 1999, pp. 3444-3446

76. Low-temperature growth of low-resistivity indium tin oxide thin films by pulsed laser deposition. F. O. Adurodija, H. Izumi, T. Ishihara, H. Yoshioka, H. Matsui and M. Motoyama, Vacuum 59, 2000, pp. 641-648

77. Influence of substrate temperature on the properties of indium oxide thin films. F. O. Adurodija, H. Izumi, T. Ishihara, H. Yoshioka, M. Motoyama and K. Murai, Journal of Vacuum Science and Technology, A, 18 (3), May/Jun 2000, pp. 814-818

78. Effects of stress on the structure of indium tin oxide thin films grown by pulsed laser deposition. F. O. Adurodija, H. Izumi, T. Ishihara, H. Yoshioka and M. Motoyama, Journal of Materials Science: Materials in Electronics, 12, (2001), pp. 57-61

79. Indium tin oxide thin films grown on flexible plastic substrates by pulsed laser deposition for organic light-emitting diodes. H. Kim, J. S. Horwitz, G. P. Kushto, Z. H. Kafafi and D. B. Chrisey, Applied Physics Letters, Volume 79, Number 3, 16 July 2001, pp. 284-286

80. Electrical and structural properties of indium tin oxide films prepared by pulsed laser deposition. Hirokazu Izumi, Frederick O. Adurodija, Takahiro Kaneyoshi, Tsuguo Ishihara, Hideki Yoshioka and Muneyuki Motoyama, Journal of Applied Physics, Volume 91, Number 3, 1 February 2002, pp. 1213-1218

81. Effect of laser irradiation on the properties of indium tin oxide films deposited at room temperature by pulsed laser deposition. F. O. Adurodija, H. Izumi, T.

Ishihara, H. Yoshioka, M. Motoyama and K. Murai, Vacuum, 67, 2002, pp. 209-216

82. Highly conducting transparent indium tin oxide films prepared by pulsed laser deposition. Akio Suzuki, Tatsuhiko Matsushita, Takanori Aoki, Akihito Mori and Masahiro Okuda, Thin Solid Films, 411, 2002, pp. 23-27

83. Mechanisms of oxygen incorporation in indium tin oxide films deposited by laser ablation at room temperature. M. A. Morales-Paliza, R. F. Haglund Jr. and L. C. Feldman, Applied Physics Letters, Volume 80, Number 20, 20 May 2002, pp. 3757-3759

84. Low temperature growth of smooth indium tin oxide films by ultraviolet assisted pulsed laser deposition. V. Cracium, C. Chiritescu, F. Kelly and R. K. Singh, Journal of Optoelectronics and Advanced Materials, Volume 4, Number 1, March 2002, pp. 21-25

85. The effect of strain on the resistivity of indium tin oxide films prepared by pulsed laser deposition. Hui Fang, Timothy M. Miller, Robert H. Magruder III and Robert A. Weller, Journal of Applied Physics, Volume 91, Number 9, 1 May 2002, pp. 6194-6196

86. Electrical properties of crystalline ITO films prepared at room temperature by pulsed laser deposition on plastic substrates. Hirokazu Izumi, Tsuguo Ishihara, Hideki Yoshioka and Muneyuki Motoyama, Thin Solid Films, 411, 2002, pp. 32-35

87. Properties of ITO films on glass fabricated by pulsed laser deposition. Jin Baek Choi, Jong Hoon Kim, Kyung Ah Jeon, SangYeol Lee, Materials Science and Engineering, B102, 2003, pp. 376-379

88. Nitrogen as background gas in pulsed laser deposition growth of indium tin oxide films at room temperature. M. A. Morales-Paliza, M. B. Huang and L. C. Feldman, Thin Solid Films, 429, 2003, pp. 220-224

89. Transparent and conducting indium tin oxide thin films grown by pulsed laser deposition at low temperatures. V. Cracium, D. Cracium, X. Wang, T. J. Anderson and R. K. Singh, Journal of Optoelectronics and Advanced Materials, Volume 5, Number 2, June 2003, pp. 401-408

90. Electrical and optical characteristics of ITO films by pulsed laser deposition using a 10 wt.% SnO_2-doped In_2O_3 ceramic target. Sang Hyeob Kim, Nae-Man Park, TaeYoub Kim and GunYong Sung, Thin Solid Films, 475, 2005, pp. 262-266

91. Changes in surface roughness and work function of indium tin oxide due to KrF excimer laser irradiation. Yow-Jon Lin, Iain D. Baikie, Wei-Yang Chou, Shih-Ting Lin, Hsing-Cheng Chang, Yao-Ming Chen and Wen-Fung Liu, Journal of Vacuum Science and Technology, A 23(5), Sep/Oct 2005, pp. 1305-1308

92. The mechanical properties of thin films: A review. D. A. Hardwick. Thin Solid Films, 154, 1987, pp. 109-124

93. Fracture in thin films. Z. Suo. Encyclopedia of Materials: Science and Technology, 2nd Edition, Elsevier Science, 2001, pp. 3290-3296

94. Mixed mode cracking in layered materials. J. W. Hutchinson and Z. Suo. Advances in Applied Mechanics, Volume 29, 1992, pp. 63-191

95. Mechanics of ITO on plastic substrates for flexible displays. Piet C. P. Bouten, Peter J. Silkerveer and Yves Leterrier. Chapter 6 in Flexible flat panel displays edited by Gregory P. Crawford, Wiley, SID, Series in display technology, 2005, p. 102

96. Cracking of thin bonded films in residual tension. J. L. Beuth Jr. International Journal of Solids and Structures, Volume 29, Issue 13, 1657, 1992

97. Constrain effects on thin film channel cracking behaviour. Ting Y. Tsui, Andrew McKerrow and Joost Vlassak. Journal of Material Research, Volume 20, Number 9, Sep 2005, MRS, pp. 2266-2273

98. Mechanics of ITO on plastic substrates for flexible displays. Piet C. P. Bouten, Peter J. Slikkerveer and Yves Leterrier. Chapter 6 in flexible flat panel displays edited by G. P. Crawford. SID series in display technology, Wiley, 2005, pp.112 - 113

99. Mechanics of ITO on plastic substrates for flexible displays. Piet C. P. Bouten, Peter J. Slikkerveer and Yves Leterrier. Chapter 6 in flexible flat panel displays edited by G. P. Crawford. SID series in display technology, Wiley, 2005, pp.114 – 115

100. Elastic property dependence on layer periodicity in Cu / Ni superlattices. Alan F. Jankowski, Edward M. Sedillo and Jeffrey P. Hayes. Japanese Journal of Applied Physics, Volume 33, 1994, pp. 5019 – 5025

101. Work of fragmentation of a thin oxide coating on a polymer film. Y. Leterrier and J. –A. E. Manson. Journal of materials science letters, 16, 1997, pp 120 – 121

102. Tensile properties of fibre – reinforced metals. Copper / Tungsten and Copper / Molybdenum. A. Kelly and W. R. Tyson. Journal of the Mechanics and Physics of Solids, Volume 13, 1965, pp. 239 – 350

103. Adhesion of silicon oxide layers on PET. I: Effect of substrate properties on coating's fragmentation process. Y. Leterrier, L. Boogh, J. Andersons and J. –A. Manson. Journal of Polymer Science, Part B: Polymer Physics, Volume 35, Issue 9, 1997, pp. 1449 – 1461

104. Adhesion of silicon oxide layers on PET. II: Effect of coating thickness on adhesive and cohesive strengths. Y. Leterrier, L. Boogh, J. Andersons and J. –A. Manson. Journal of Polymer Science, Part B: Polymer Physics, Volume 35, Issue 9, 1997, pp. 1449 – 1461

105. Cracking phenomena of brittle films in nanostructure composites analysed by a modified shear lag model with residual strain. M. Yanaka, Y. Tsukahara, N. Nakaso and N. Takeda. Journal of Materials Science, 33, 1998, pp. 2111 – 2119

106. An analysis of disorder in thin silicon oxide coatings. U. A. Handge, Y. Leterrier, J. –A. Manson, I. M. Solokov and A. Blumen. Europhysics Letters, 48 (3), 1999, pp. 280 –285

107. Mechanical buckling instability of thin coatings deposited on soft polymer substrates. A. L. Volynskii, S. Bazhenov, O. V. Lebedeva and N. F. Bakeev. Journal of Materials Science, 35, 2000, pp. 547 – 554

108. Strain – dependent electrical resistance of tin – doped indium oxide on polymer substrates. Darran R. Cairns, Richard P. White II, Daniel K. Sparacin, Suzzane M. Sachsman, David C. Paine, R. R. Newton and Gregory P. Crawford. Applied Physics Letters, Volume 76, Number 11, 2000, pp. 1425 – 1427

109. Electrical studies of mechanically deformed indium tin oxide coated polymer substrates. Darran R. Cairns, Daniel K. Sparacin, David C. Paine and Gregory P. Crawford. SID 00 Digest, Society of Information Display, 2000, pp. 274 – 277

110. The mechanical reliability of sputter coated indium tin oxide polyester substrates for flexible display and touch – screen applications. Darran R. Cairns, David C. Payne and Gregory P. Crawford. Materials Research Society Symposium Proceedings, Volume 666, 2001, MRS, pp. F3.24.1 – F3.24.12

111. Influence of the strain on the electrical resistance of zinc oxide doped thin film deposited on polymer substrates. Elvira Fortunato, Patricia Nunes, Antonio Marques, Daniel Costa, Hugo Aguas, Isabel Ferreira, Maria E. V. da Costa, Maria H. Godinho, Pedro L. Almeida, Joao P. Borges and Rodrigo Martins. Advanced Engineering Materials Communications, 4, Number 8, 2002, pp. 610 – 612

112. Measurement of debonding in cracked nanocomposite films by ultrasonic force microscopy. A. P. McGuigan, B. D. Huey, G. A. D. Briggs, O. V. Kolosov, Y. Tsukahara and M. Yanaka. Applied Physics Letters, Volume 80, Number 7, 2002, pp. 1180 – 1182

113. Mechanical analysis of ultrathin oxide coatings on polymer substrates in situ in a scanning electron microscope. G. Rochat, Y. Leterrier, P. Fayet and J. –A. Manson. Thin Solid Films, 437, 2003, pp. 204 – 210

114. Influence of substrate morphology on the cohesion and adhesion of thin PECVD oxide films on semi – crystalline polymers. G. Rochat, A. Delachaux, Y. Leterrier, J. –A. E. Manson and P. Fayet. Surface and Interface Analysis, 35, 2003, pp. 984 – 952

115. Mechanical integrity of transparent conductive oxide films for flexible polymer – based displays. Y. Leterrier, L. Medico, F. Demarco, J. –A. E. Manson, U. Betz, M. F. Escola, M. Kharazi Olsson, F. Atamny. Thin Solid Films, 460, 2004, pp. 156 – 166

116. Stretchability of thin metal films on elastomer substrates. Teng Li, Zhenyu Huang, Z. Suo, Stephanie P. Lacour and Sigurd Wagner. Applied Physics Letters, Volume 85, Number 16, 2004, pp. 3435 – 3437

117. Mechanics of ITO on plastic substrates for flexible displays. Piet C. P. Bouten, Peter J. Silkkerveer and Yves Leterrier. Chapter 6 in Flexible flat panel displays edited by Gregory P. Crawford, SID series in display technology, SID, 2005, John Wiley and Sons, pp. 99 – 120

118. Mechanical reliability of conductive polymers for rollable display applications. Darran R. Cairns. Chapter 9 in Flexible flat panel displays edited by Gregory P. Crawford, SID series in display technology, SID, 2005, John Wiley and Sons, pp. 163 – 177

119. Mechanics of rollable and foldable film – on – foil electronics. Z. Suo, E. Y. Ma, H. Gleskova and S. Wagner. Applied Physics Letters, Volume 74, Number 8, 1999, pp. 1177 – 1179

120. Buckling and cracking of thin films on compliant substrates under compression. B. Cotterell and Z. Chen. International Journal of Fracture, 104, 2000, pp. 169 – 179

121. A mechanical assessment of flexible optoelectronic devices. Zhong Chen, Brian Cotterell, Wei Wang, Ewald Guenther and Soo – Jin Chua. Thin Solid Films, 394, 2001, pp. 202 – 206

122. The fracture of brittle thin films on compliant substrates in flexible displays. Zhong Chen, Brian Cotterell and Wei Wang. Engineering Fracture Mechanics, 69, 2002, pp. 597 – 603

123. Conformable polymer dispersed liquid crystals (C – PDLC) displays with indefinitely captured form. S. P. Gorkhali, D. R. Cairns, S. Esmailzadeh, J. Vendrine and G. P. Crawford. SID 02 Digest, Late news paper, Society of Information Display, 2002, pp. 1004 – 1007

124. Ultrathin glass for flexible OLED application. Mark Dai Joong Aush, Ong Kian Soo, Guenther Ewald, Chua Soo – Jin. Thin Solid Films, 417, 2002, pp. 47 – 50

125. Failure test for brittle conductive layers on flexible display substrates. Piet C. P. Bouten. Eurodisplay 2002, Society of Information Display, 2002, pp. 313 – 316

126. Performance of flexible polymeric light – emitting diodes under bending conditions. Ralph Paetzold, Karsten Heuser, Debora Henseler, Stephan Roeger,

Georg Wittman and Albrecht Winnacker. Applied Physics Letters, Volume 82, Number 19, 2003, pp. 3342 – 3344

127. Highly flexible transparent electrodes for organic light – emitting diode – based displays. Jay Lewis, Sonia Grego, Babu Chalamala, Eric Vick and Dorota Temple. Applied Physics Letters, Volume 85, Number 16, 2004, pp. 3450 –3452

128. Bendable single crystal silicon thin film transistors formed by printing on plastic substrates. E. Menard, R. G. Nuzzo and J. A. Rogers. Applied Physics Letters, Volume 86, 2005

129. Biaxial fragmentation of thin silicon oxide coatings on polyethylene terepthalate. Y. Leterrier, D. Pellaton, D. Mendels, R. Glauser, J. Andersons, J. –A. E. Manson. Journal of Materials Science, 36, 2001, pp. 2213 – 2225

130. Biaxial testing of nanoscale films on compliant substrates: Fatigue and fracture. B. Erdem Alaca, John C. Selby, M. T. A. Saif and Huseyin Sehitoglu. Review of Scientific Instruments, Volume 73, Number 8, 2002, pp. 2963 – 2970

131. Analysis of the initial fragmentation stage of oxide coatings on polymer substrates under biaxial tension. J. Andersons, Y. Leterrier, I. Fescenko. Thin Solid Films, 434, 2003, pp. 203 – 215

132. Plasticity of thin Al films as a function of temperature. M. Cieslar, V. Oliva, A. Karimi and J. –L. Martin. Materials Science and Engineering, A 387 – 389, 2004, pp. 734 – 737

133. Advanced fragmentation stage of oxide coating on polymer substrate under biaxial tension. J. Andersons, Y. Leterrier. Thin Solid Films, 471, 2005, pp. 209 – 217

134. The effect of defect location on coating fragmentation patterns under biaxial tension. J. Andersons, Y. Leterrier. Probabilistic Engineering Mechanics, 20, 2005, pp. 103 – 108

135. Biaxial testing of thin functional structures used in flexible display and touch – screen applications. Konstantinos A. Sierros, J. Stuart Abell and Stephen N. Kukureka. Eurodisplay 2005, Society of Information Display, Edinburgh, 2005

136. Elastic modulus in composition-modulated copper-nickel foils. T. Tsakalakos and J. E. Hilliard. J. Appl. Phys. 54 (2), February 1983, pp. 734-737

137. A technique for the determination of stress in thin films. E. I. Bromley, J. N. Randall, D. C. Flanders and R. W. Mountain. J. Vac. Sci. Technol. B, Vol. 1, No. 4, Oct-Dec 1983, pp. 1364-1366

138. Mechanical properties of diamond membranes. Jpn. J. Appl. Phys. Vol. 32 (1993), Part 1, No 10, October 1993, pp. 4680-4683

139. A new interpretation of bulge test measurements using numerical simulation. Y. von Kaenel, J.-Ch. Giacheto, J. Stiegler, J. –M. Drezet, E. Blank. Diamond and Related Materials 5 (1996) pp. 635-639

140. Effects of deflection on bulge test measurements of enhanced modulus in multilayered films. A. F. Jankowski and T. Tsakalakos. Thin Solid Films, 290-291, 1996, pp. 243-247

141. Finite-element analysis of bulge forming applying pressure and in-plane compressive load. M. Ahmed and M. S. J. Hashmi. Journal of Materials Processing Technology, 77, 1998, pp. 95-102

142. A series solution approach to an analytical load-deflection relation for the measurement of mechanical properties of thin films. C. T. Loy, S. C. Pradhan, T. Y. Ng and K. Y. Lam. J. Micromech. Microeng. 9, 1999, pp. 341-344

143. Plastic deformation of thin foil substrates with amorphous silicon islands into spherical shapes. Pai-hui I. Hsu, Min Huang, Sigurd Wagner, Zhigang Suo and J. C. Sturm. Mat. Res. Soc. Symp. Proc. Vol. 621, 2000 Materials Research Society, Q8.6.1-Q8.6.6

144. Spherical deformation of compliant substrates with semiconductor device islands. P. I. Hsu, M. Huang, Z. Xi, S. Wagner, Z. Suo and J. C. Sturm. Journal of Applied Physics, Volume 95, Number 2, 15 January 2004, pp. 705-712

145. Effects of mechanical strain on TFTs on spherical domes. Pai-hui I. Hsu, M. Huang, H. Gleskova, Z. Xi, Z. Suo, S. Wagner and James C. Sturm. IEEE transactions of electron devices, Vol. 51, No.3, March 2004, pp. 371-377

146. Measurement of residual stresses in a plate using bulging test and a dynamic technique: application to electroplated nickel coatings. S. Basrour, L. Robert and P. Delobelle. Materials Science and Engineering, A288, 2000, pp. 160-163

147. Mechanical property measurement of thin polymeric-low dielectric constant films using bulge-testing method. D. W. Zheng, Y. H. Xu, Y. P. Tsai, K. N. Tu, P. Patterson, Bin Zhao, Q. –Z. Liu and Maureen Brongo. Applied Physics Letters, Volume 76, Number 15, 10 April 2000, pp. 2008-2010

148. Fracture properties of LPCVD silicon nitride films from the load-deflection of long membranes. Jinlng Yang and Oliver Paul. Sensors and actuators A 97-98, 2002, pp. 520-526

149. The mechanical properties of electroplated Cu thin films measured by means of the bulge test technique. Yong Xiang, Xi Chen and Joost Vlassak. Mat. Res. Soc. Symp. Proc. Vol. 695, 2002 Materials Research Society, L4.9.1-L4.9.6

150. Mechanical testing of gold membranes on a MEMS device for drug delivery. Yawen Li, Rebecca S. Shawgo, Robert Langer and Michael J. Cima. 2nd Annual International IEEE-EMBS Special Topic Conference on Microtechnologies in Medicine and Biology, May 2-4, 2002, Madison, Wisconsin, USA, pp. 390-393

151. High-temperature bulge-test set up for mechanical testing of free-standing thin films. A. J. Kalkman, A. J. Verbuggen and G. C. A. M. Janssen. Review of scientific instruments, Volume 74, Number 3, 2003 American Institute of Physics, pp. 1383-1385

152. Plasticity of thin Al films as a function of temperature. M. Cieslar, V. Oliva, A. Karimi, J. –L. Martin. Materials science and engineering, A 387-389, 2004, pp. 734-737

153. A theory of the plastic bulging of a metal diaphragm by lateral pressure. R. Hill. Philosophical Magazine, Series 7, Volume 41, Number 322, November 1950, pp. 1133 – 1142

154. Mechanical properties of thin films of gold and silver. J. W. Beams. Structure and Properties of Thin Films, edited by C. A. Neugebauer, J. B. Newkirk and D. A. Vermilyea, John Willey and Sons, New York, 1959, pp. 183 – 192

155. Theory of Plates and Shells. S. Timoshenko and S. Woinowski – Krieger. McGraw – Hill, New York, 1959, p.345 and 400

156. Stress and strain in thin films bulged over circular openings. Ralph Papirno. Journal of Applied Physics 32, Letters to the editor, 1961, pp. 1175 – 1176

157. Use of the hydraulic bulge test in biaxial tensile testing. A. J. Ranta – Escola. Journal of Mechanical Science, Volume 21, 1979, pp. 457 – 465

158. The bulge test: A comparison of theory and experiment for isotropic and anisotropic films. T. Tsakalakos. Thin Solid Films, Volume 75, Number 3, 1981, pp. 293 – 305

159. Stress analysis of polymers. J. G. Williams. Longman, London, 1973, pp. 210 – 220

160. A technique for the determination of stress in thin films. E. I. Bromley, J. N. Randal, D. C. Flanders and R. W. Mountain. Journal of Vacuum Science and Technology, B 1 (4), 1983, pp. 1364 – 1366

161. Analysis of the accuracy of the bulge test in determining the mechanical properties of thin films. Martha K. Small and W. D. Nix. Journal of Materials Research, Volume 7, Number 6, June 1992, pp. 1553 – 1563

162. Some solutions for the large deflections of uniformly loaded circular membranes. W. B. Fichter. National Aeronautics and Space Administration, Technical Paper 3658, July 1997

163. On the stress state in circular plates with vanishing bending stiffness. H. Hencky. Zeitschrift fur Mathematic und Physic, Volume 63, 1915, pp. 311 – 317

164. Large deflections of clamped circular plates under initial tension and transitions to membrane behaviour. Mark Sheplak and John Dugundi. Journal of Applied Mechanics, Volume 65, March 1998, pp. 107 – 115

165. Bulge and blister testing of thin films and their interfaces. Robert J. Hohlfeder. PhD thesis, 1999, Stanford University

166. The in – situ measurement of mechanical properties of multilayer coatings. Pinyen Lin. PhD thesis, 1990, MIT

167. Verification of FEM analysis of load – deflection methods for measuring mechanical properties of thin films. Jeffrey Y. Pan, Pinyen Lin, Fariborz Maseeh and Stephen D. Senturia. IEEE Solid – State Sensor and Actuator Workshop, South Carolina, 1990, pp. 70 – 73

168. Tribology: Friction and wear of engineering materials. I. M. Hutchings. Edward Arnold, p.1, 1992, ISBN: 034056184x

169. Basic mechanisms of friction and wear of polymers. J. K. Lancaster. Plastics and polymers, Vol. 41, December 1973, paper read at the conference on plastics in bearings, Solihull, 21 February 1973, p. 297

170. The friction and lubrication of solids. F. P. Bowden and D. Tabor. Chapter V, p.90, Oxford classic texts in the physical sciences, Oxford University press, 2001, ISBN: 0198507771

171. Friction and wear of polymers. B. J. Briscoe and D. Tabor. Polymer surfaces, Ch. 1, D.T. Clark and W. J. Feast (editors), John Wiley & Sons, 1978, Chichester

172. Basic mechanisms of friction and wear of polymers. J. K. Lancaster. Plastics and polymers, Vol. 41, December 1973, paper read at the conference on plastics in bearings, Solihull, 21 February 1973, p. 299

173. Tribology: Friction and wear of enginnering materials. I. M. Hutchings. Edward Arnold, p.51, 1992, ISBN: 034056184x

174. Nanoscience: Friction and rheology on the nanometer scale. E. Meyer, R. M. Overney, K. Dransfeld and T. Cyalog. Chapter 1, p. 12, World Scientific, 1998, ISBN: 981-02-2562-8

175. Tribology: Friction and wear of engineering materials. I. M. Hutchings. Chapter 5: Sliding wear, Arnold, 1992, p. 122

176. Friction and molecular structure: the behaviour of some thermoplastics. Christine M. Pooley and D. Tabor. Proceedings of the Royal Society of London A, Volume 329, 22 August 1972, Plates 15 to 20, pp. 251-260

177. Wear of polymers: an essay on fundamental aspects. B. Briscoe. Tribology International, August 1981, pp. 231 – 243

178. Tribology of polymers: State of an art. B. J. Briscoe. Physicochemical Aspects of Polymer Surfaces edited by K. L. Mittal, Volume 1, Plenum press, New York and London, 1983, pp. 387 – 412

179. A fatigue – abrasive wear mechanism for polymeric surfaces. T. S. Chow, Chapter 5 in Polymer wear and its control edited by L. H. Lee, American Chemical Society, Washington DC, ACS symposium series 287, 1985, pp. 67 – 74

180. Molecular features of transfer fragments when high-density polyethylene is rubbed against metals. V. A. Belyi and V. V. Nevzorov. Chapter 14 in Polymer wear and its control edited by L. H. Lee, American Chemical Society, Washington DC, ACS symposium series 287, 1985, pp. 205 – 212

181. Fatigue wear of polymers. N. S. Eiss Jr. and J. R. Potter III. Chapter 4 in Polymer wear and its control edited by L. H. Lee, American Chemical Society, Washington DC, ACS symposium series 287, 1985, pp. 59 – 66

182. Characterization and measurement of polymer wear. Donald H. Buckley and Paul R. Aron. Chapter 19 in Polymer wear and its control edited by L. H. Lee, American Chemical Society, Washington DC, ACS symposium series 287, 1985, pp. 287 – 302

183. Wear of polymers in the pin – on – disc configuration. B. J. Briscoe and T. A. Stolarski. Chapter 20 in Polymer wear and its control edited by L. H. Lee, American Chemical Society, Washington DC, ACS symposium series 287, 1985, pp. 303 - 313

184. Effect of the degree of crystallinity on friction and wear of PET. Yoshinory Yamada and Kyuichiro Tanaka. Chapter 24 in Polymer wear and its control edited by L. H. Lee, American Chemical Society, Washington DC, ACS symposium series 287, 1985, pp. 363 – 374

185. Effect of the degree of crystallinity on the friction and wear of PET under water lubrication. Yoshinory Yamada and Kyuichiro Tanaka. Wear, 111, 1986, pp. 63 – 72

186. The role of crack resistance parameters in polymer wear. M. K. Omar, A. G. Atkins and J. K. Lancaster. Journal of Physics D: Applied Physics, 19, 1986, pp. 177 – 195

187. Some interesting problems that remain unsolved in my work on polymer tribology. Kyuichiro Tanaka. Tribology International, Volume 28, Number 1, 1995, pp. 19 – 22

188. Dry sliding wear characteristics of some industrial polymers against steel counterface. H. Unal, U. Sen and A. Mimaroglu. Tribology International, 37, 2004, pp. 727 – 732

189. Wear of polyester film. D. J. Chalmers and K. L. Knox. Wear, 18, 1971, pp. 101 – 108

190. The tribological and dynamic behaviour of alternative magnetic tape substrates. Brian L. Weick and Bharat Bushan. Wear, 190, 1995, pp. 28 – 43

191. Tribological properties of nitrogen, carbon and titanium ion implanted PET against steel. Shengrong Yang, Shangkui Qi, Weimin Liu, Changlin Li and Youmei Sun. Wear, 211, 1997, pp. 64 – 69

192. Scanning force microscopy of polyester films: contact versus non – contact imaging and tip – induced wear experiments. John S. G. Ling, Graham J. Leggett and Andrew J. Murray. Polymer, Volume 39, Number 24, 1998, pp. 5913 – 5921

193. Frictional, adhesive and mechanical properties of polyester films probed by scanning force microscopy. Ben D. Beake, Graham J. Leggett and Philip H. Shipway. Journal of Surface and Interface Analysis, 27, 1999, pp. 1084 – 1091

194. Nanotribology of biaxially oriented PET film. Ben D. Beake, Graham J. Leggett and Philip H. Shipway. Polymer, 42, 2001, pp. 7025 – 7031

195. Role of PET in improving wear properties of PP in dry sliding condition. Somit Neogi, S. A. R. Hashmi and Navin Chand. Bulletin of Materials Science, Volume 26, Number 6, 2003, pp. 579 – 583

196. Sliding behaviour of pure polyester and polyester – PTFE filled bulk composites in overload conditions. Pieter Samyn, Jan Quintelier, Wouter Ost, Patrick De Baets, Gustaaf Schoukens. Polymer Testing, 24, 2005, pp. 588 – 603

197. Mechanical properties of r.f. magnetron sputtered indium tin oxide films. Wen – Fa Wu, Bi – Shiou Chiou. Thin Solid Films 293, 1997, pp. 244 –250

198. Properties of dc magnetron sputtered indium tin oxide films on polymeric substrates at room temperature. J. H. Shin, S. H. Shin, J. I. Park and H. H. Kim. Journal of Applied Physics, Volume 89, Number 9, 1 May 2001, pp. 5199 – 5203

199. Investigation of mechanical properties of transparent conducting oxide thin films. Kaiyang Zeng, Furong Zhu, Jianqiao Hu, Lu Shen, Keran Zhang and Hao Gong. Thin Solid Films, 443, 2003, pp. 60 – 65

200. Indium tin oxide for transparent EMC shielding and antistatic applications. J. Eite and A. G. Spencer. Presented at EMCUK 2004, Newbury, UK, 2004 (www.diamondcoatings.co.uk)

201. Modern spectroscopy. J. Michael Hollas. 3^{d} Edition, John Wiley and Sons, 1996, p. 55

202. Polymer characterization. Physical techniques. D. Campbell, R. A. Pethrick and J. R. White. 2nd Edition, Stanley Thornes, 2000, p. 362

203. Measurement of sheet resistivities with the four – point probe. F. M. Smits. The Bell System Technical Journal, May 1958, pp. 711 – 718

204. Polymer characterization. Physical techniques. D. Campbell, R. A. Pethrick and J. R. White. 2nd Edition, Stanley Thornes, 2000, p. 194

205. Characterization of biaxial orientation in polyethylene terephthalate by means of refractive index measurements and Raman and infra – red spectroscopies. D. A. Jarvis, I. J. Hutchinson and I. M. Ward. Polymer, 1980, Vol 21, January 1980, pp. 41 – 54

206. Equilibrium melting parameters of polyethyleneterepthalate. Aspy Mehta, Umesh Gaur and Bernhard Wunderlich. Journal of Polymer Science: Polymer Physics Edition, Volume 16, Issue 2, 1978, pp. 289 – 296

207. Glass transition and melting behaviour of PEN. Stephen Z. D. Cheng and Bernhard Wunderlich. Macromolecules, 21, 1988, pp. 789 - 797

208. Elastic properties of indium tin oxide films. T. Wittkowski, J. Jorzick, H. Seitz, B. Schroder, K. Jung, B. Hillebrands. Thin Solid Films, 398 – 399, 2001, pp. 465 – 470

209. Durability of nanosized oxygen – barrier coatings on polymers. Yves Leterrier. Progress in Materials Science, Volume 48, Number 1, 2003, pp. 1 – 55

210. Tapping mode and phase imaging of biaxially oriented polyester films. B. D. Beake, G. J. Legget, P. H. Shipway. Surface and Interface Analysis, 31, 2001, pp. 39 – 45

211. Thin film friction and adhesion studies using atomic force microscopy. Bharat Bhusan and Chatan Dandavate. Journal of Applied Physics, Volume 87, Number 3, 1 February 2000

212. Characterization of the physical and electrical properties of indium tin oxide on polyethylene napthalate. H. Han, Daniel Adams, J. W. Mayer and T.L. Alford, Journal of Applied Physics, 98, 083705, 2005

213. Electromechanical properties of transparent conducting substrates for flexible electronic displays. Darran R. Cairns and Gregory P. Crawford. Proceedings of the IEEE, Volume 93, No 8, August 2005, pp. 1451 – 1458

214. Materials aspects of polymer wear. B. J. Briscoe. Scripta Met. Et Mat, 24, 1990, pp. 839 – 844

215. www.dupontteijinfilms.com, Wilton, UK

216. www.diamondcoatings.co.uk, Birmingham, UK

217. www.JEOL.com

218. www.veeco.com

219. Surface forces, surface chemistry and tribology. Kirill Feldman, Michaela Fritz, Georg Hahner, Andreas Marti and Nicholas D. Spencer. Tribology International, Volume 31, Number 1 – 3, 1998, pp. 99 – 105

220. www.thermo.com/spectroscopy

221. Infrared spectroscopy in analysis of polymer crystallinity. Surya K. Mallapragada and Balaji Narasimhan. Encyclopedia of Analytical Chemistry, R. A. Meyers (Ed.), John Wiley & Sons Ltd, Chichester, 2000, pp. 7644-7658

222. www.perkinelmer.com

223. Polymers: Chemistry and physics of modern materials. J. M. G. Cowie. 2nd Edition, Nelson Thornes, 1991, p. 226

224. www.lambdaphysik.com

225. www.mitutoyo.co.uk

226. www.micromaterials.co.uk

227. Toughness measurement of thin films: a critical review. Sam Zhang, Deen Sun, Yongqing Fu, Hejun Du. Surface and Coatings Technology, 198, 2005, pp. 74 – 84

228. www.instron.com

229. A method for measuring the resistivity and Hall coefficient on lamellae of arbitrary shape. L. J. van der Pauw. Philips Technical Review 20, 1958, pp. 220 – 224

230. Compliant thin film patterns of stiff materials as platforms for stretchable electronics. T. Li, Z. Suo, S. P. Lacour, S. Wagner. Journal of Materials Research, 20, 2005, pp. 3274 - 3277

Appendix 1

(Figures and tables from Chapter 1)

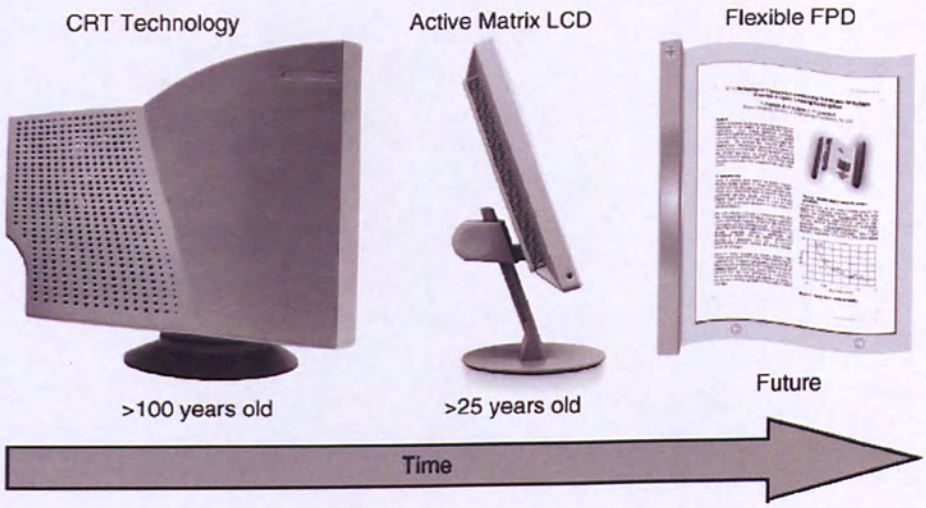

Figure 1.1: The evolution of displays[3].

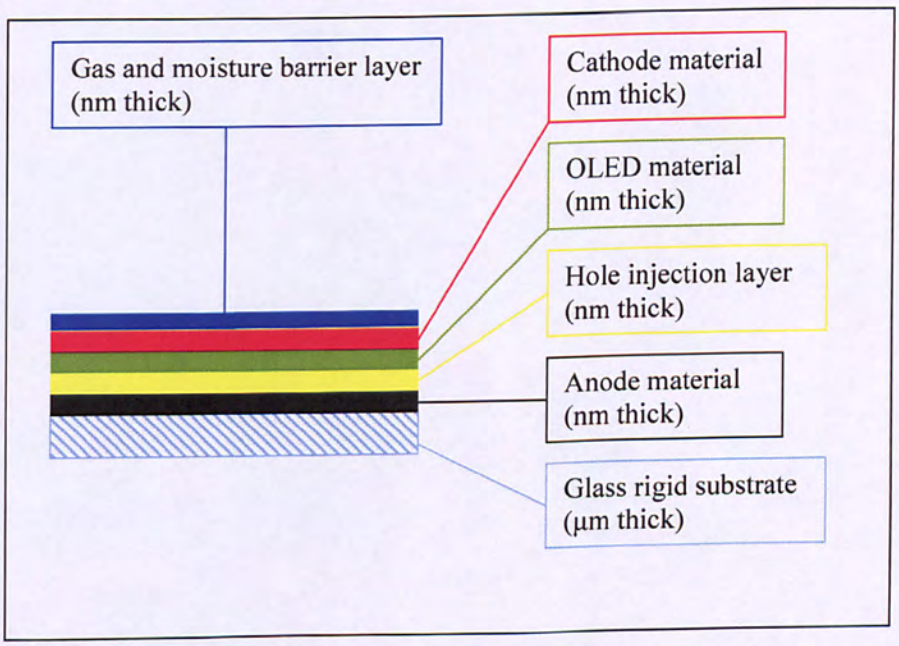

Figure 1.2: Assumed glass-based thin OLED cross-section[6].

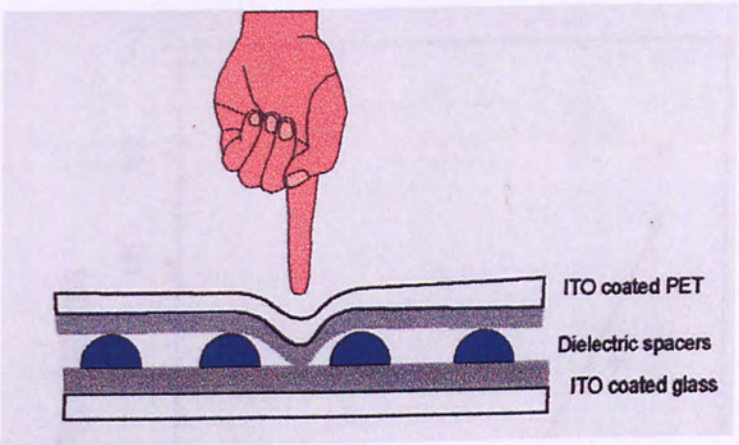

Figure 1.3: Architecture of a resistive touch-screen[9].

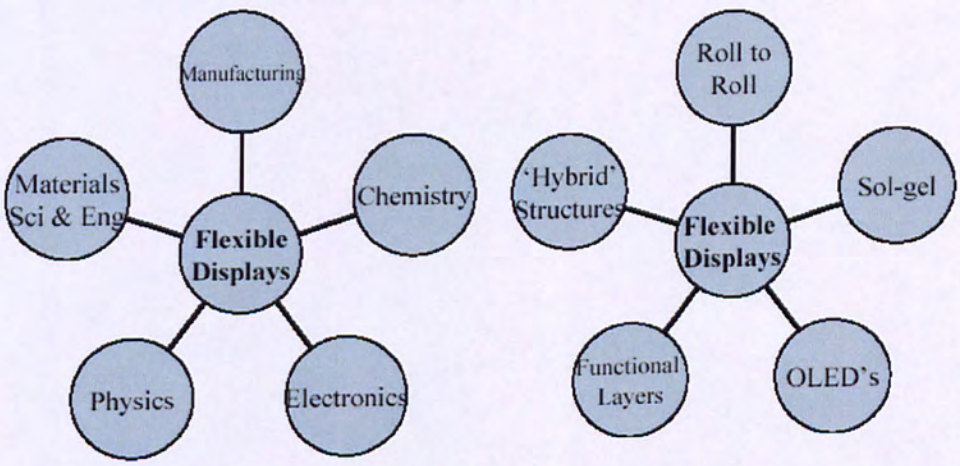

Figure 1.4: Flexible display related scientific and engineering fields[11].

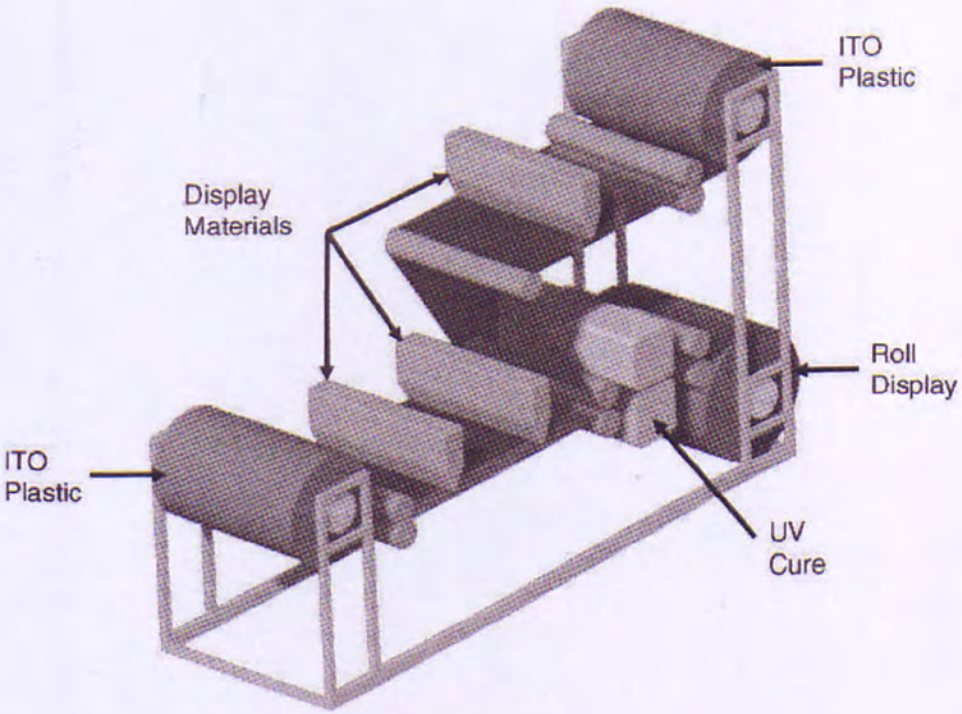

Figure 1.5: A simple schematic illustration of a roll – to – roll manufacturing process[14].

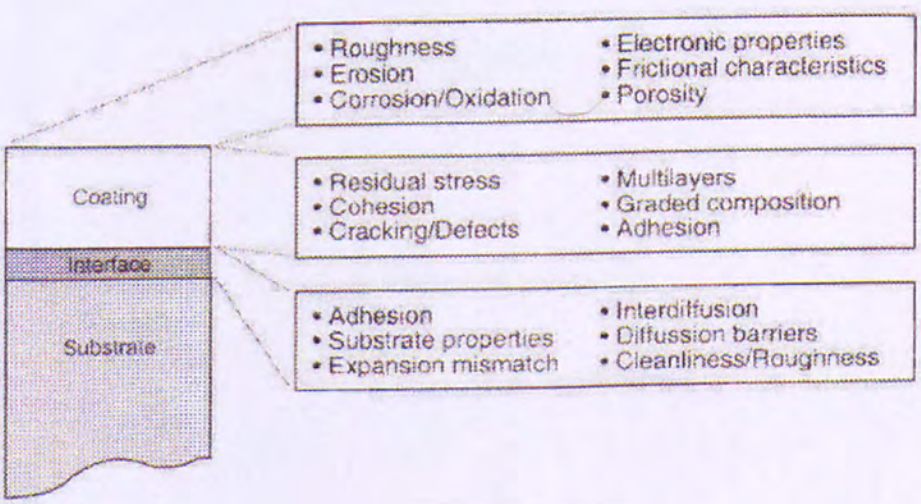

Figure 1.6: Important coating / substrate properties for technological applications[15].

Appendix 2

(Figures and tables from Chapter 2)

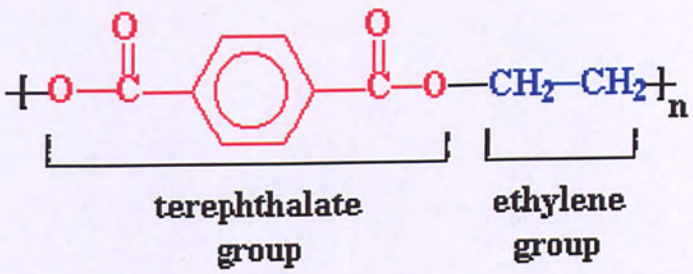

Figure 2.1: Chemical structure of PET.

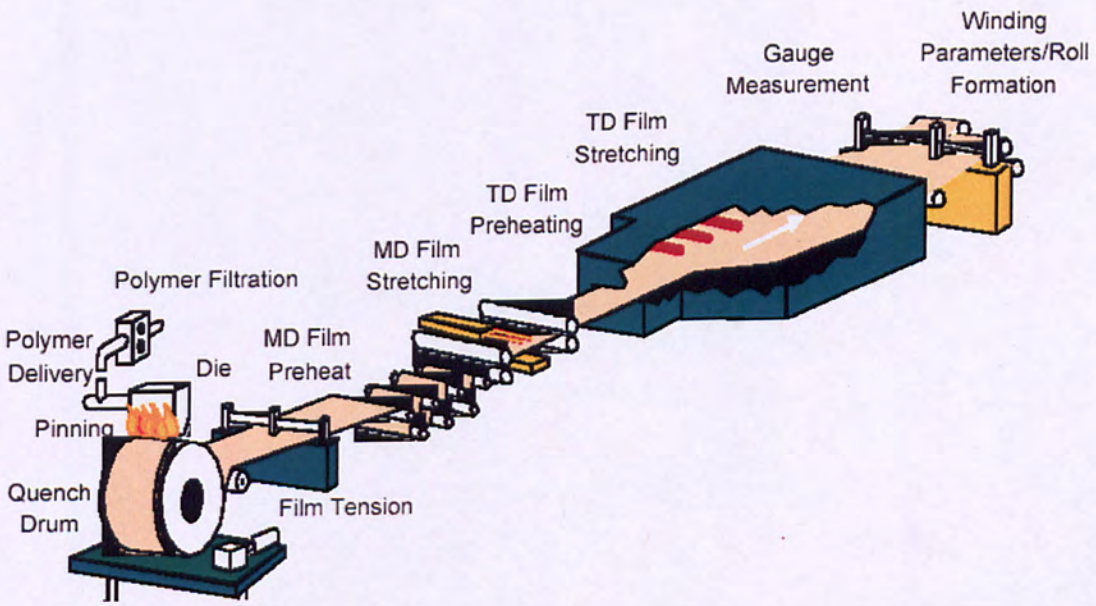

Figure 2.2: Biaxial drawing process yielding PET/PEN oriented film (Image courtesy of DuPont Teijin films).

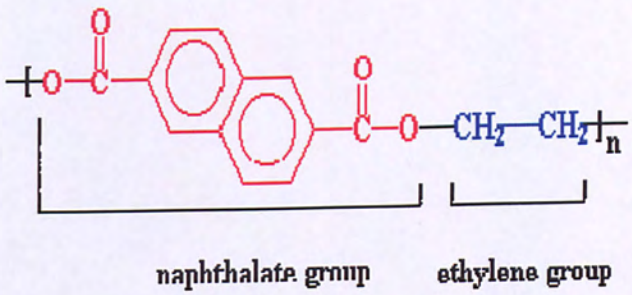

Figure 2.3: Chemical structure of PEN.

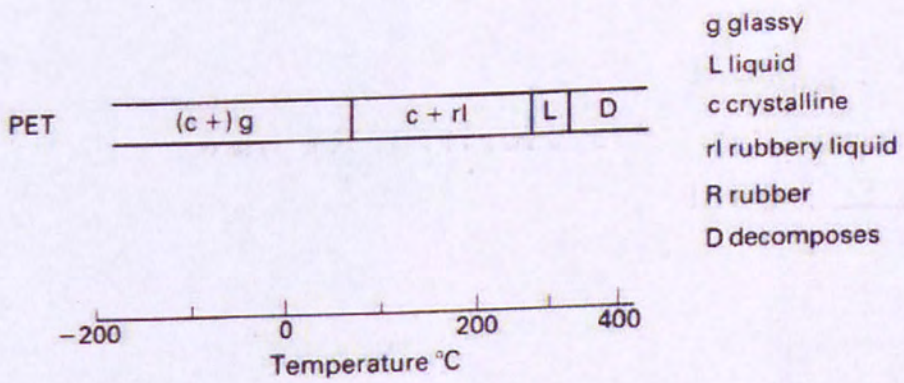

Figure 2.4: Modified[23] figure showing the changes in the state of PET with respect to temperature.

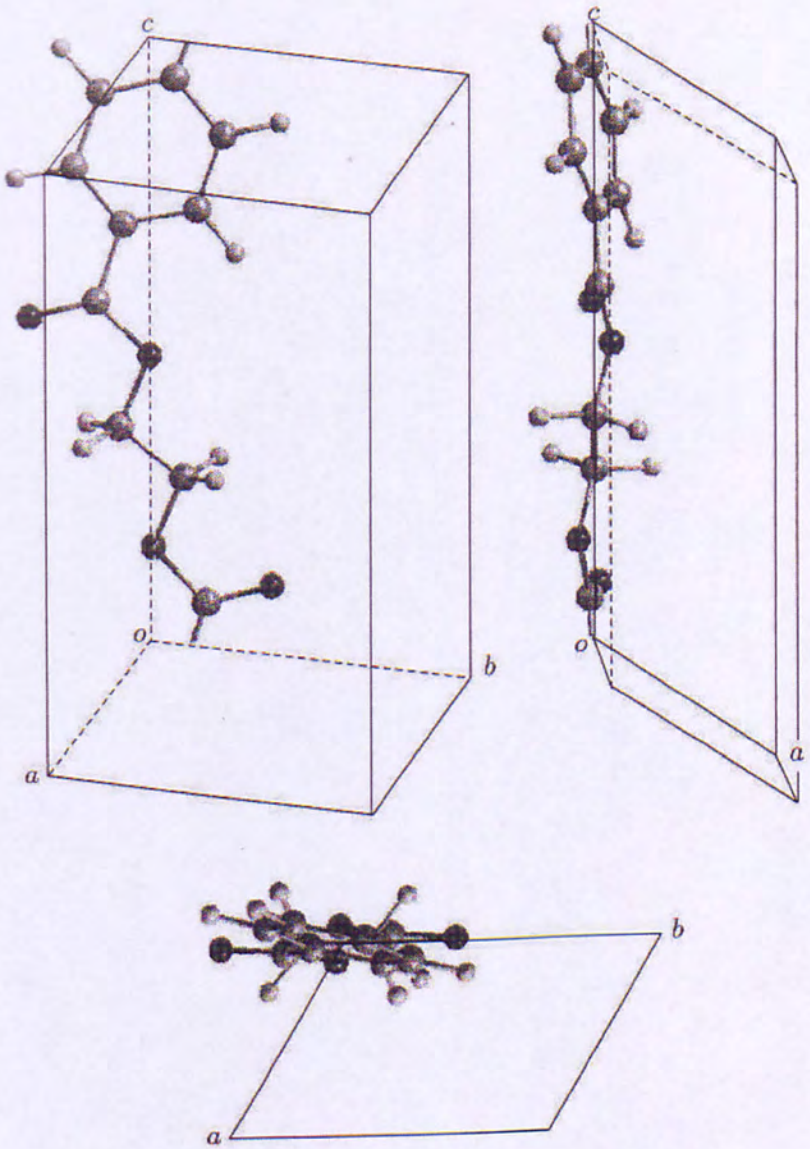

Figure 2.5: Conformation of a single PET chemical repeat unit and its packing in the unit cell[27].

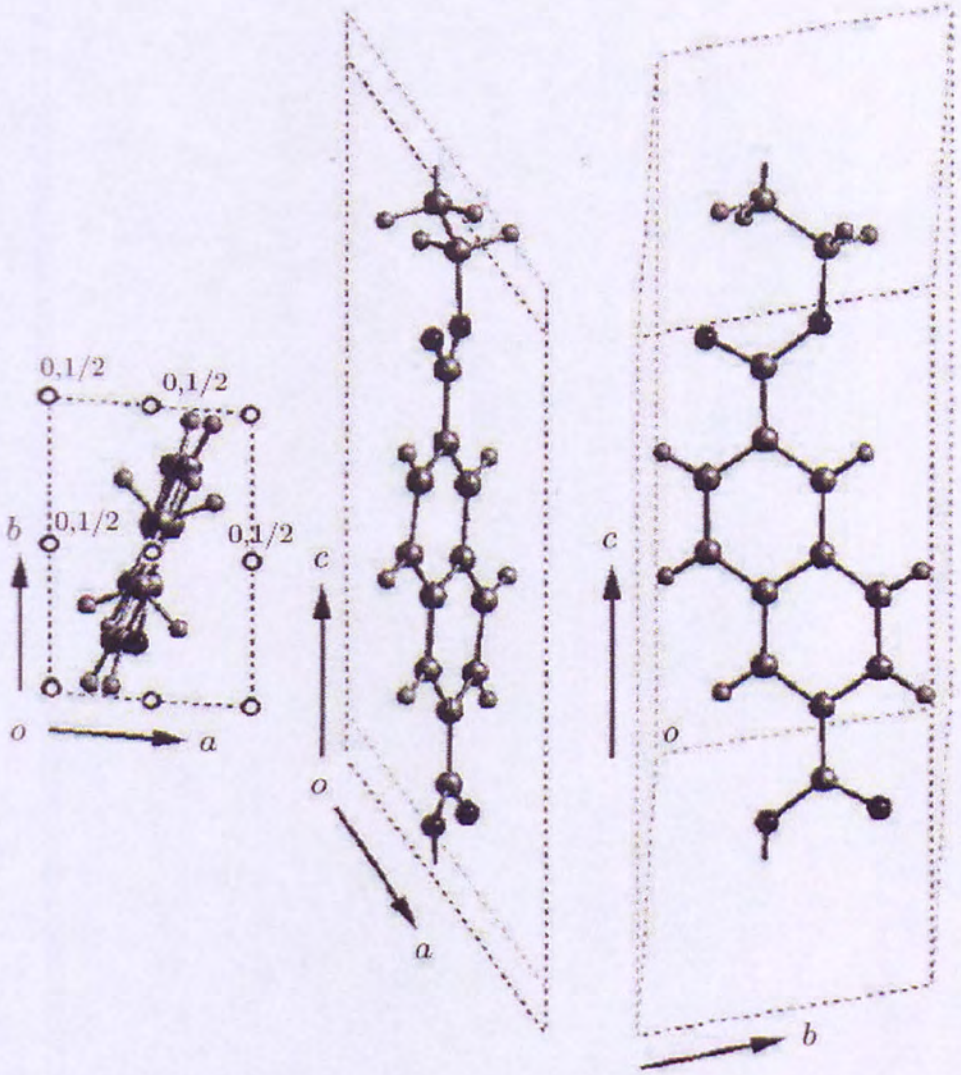

Figure 2.6: Conformation of a single PEN chemical repeat unit and its packing in the unit cell[29].

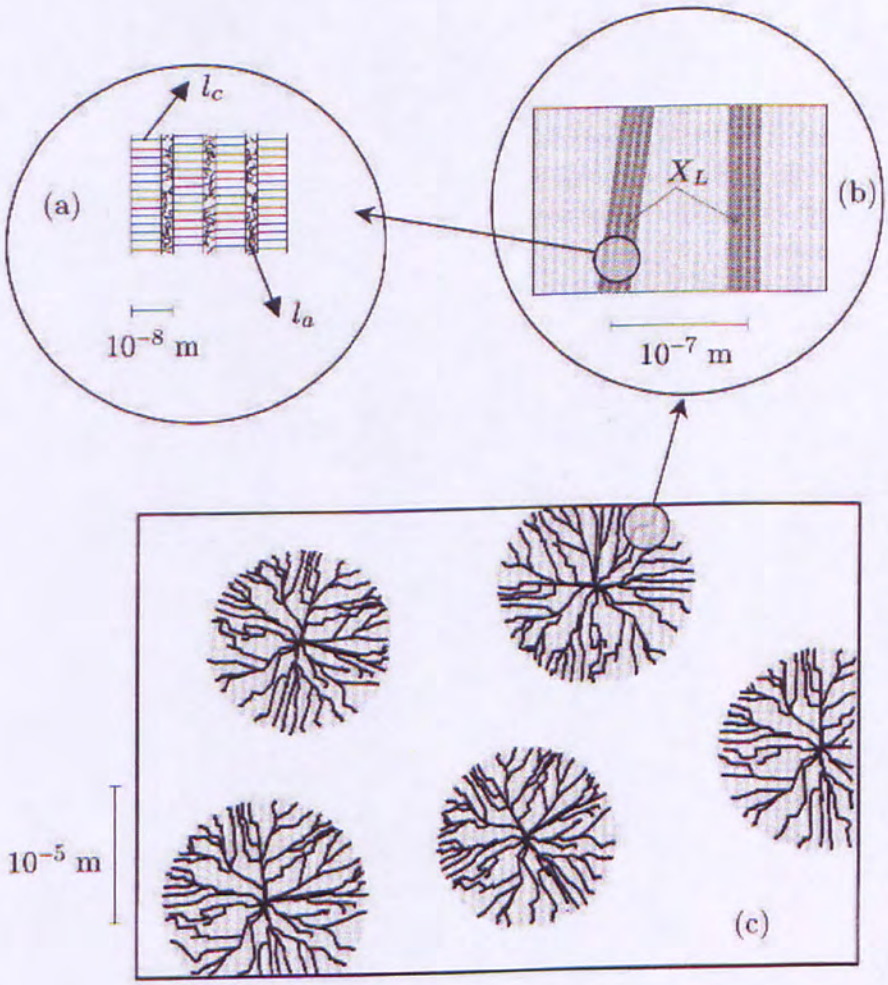

Figure 2.7: Spherulitic morphology[30] of PET and PEN: (a) lamellar structure, l_α is thickness of amorphous region and l_c is thickness of crystalline region; (b) lamellar stacks, X_L, and interstack amorphous phase; (c) spherulites.

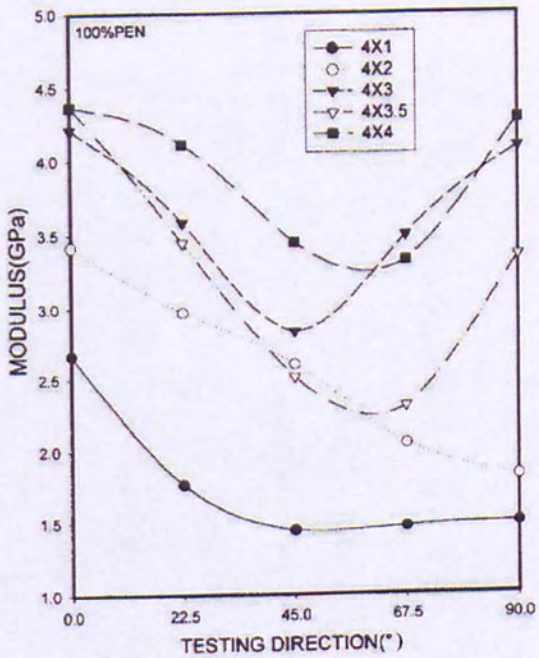

Figure 2.8: The development of in – plane modulus anisotropy in biaxially stretched PEN films for different drawing ratios[35].

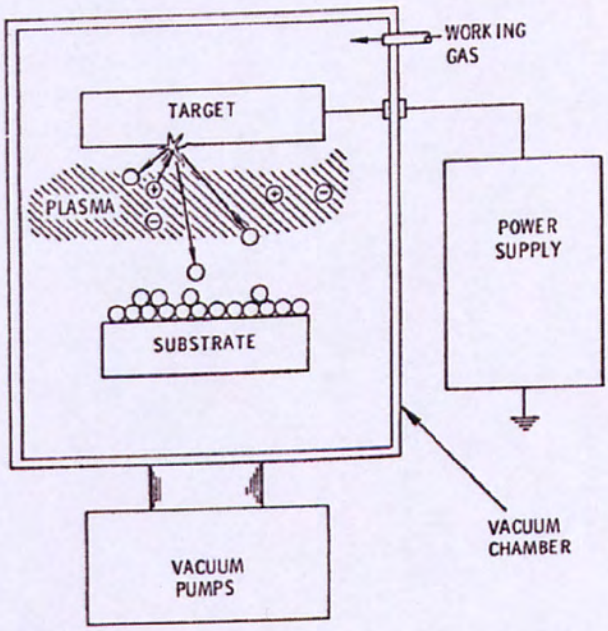

Figure 2.9: The basic sputtering technique[46].

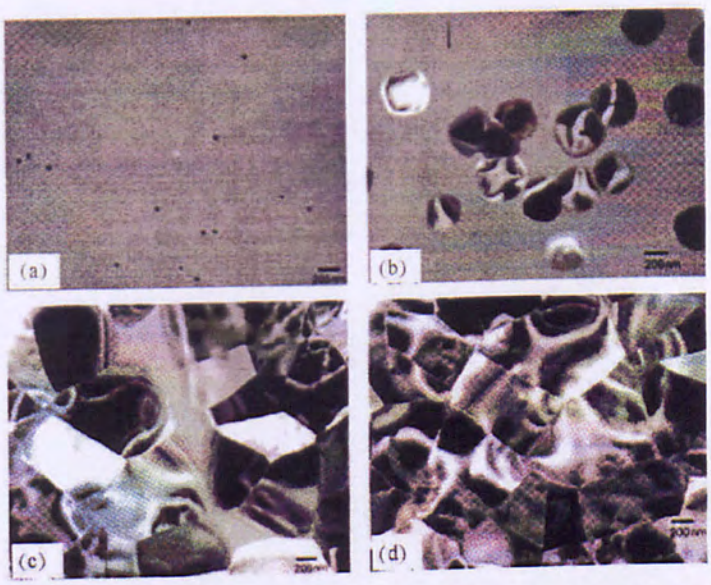

Figure 2.10: Plan view TEM image[60] presenting ITO deposited on glass in (a) the as – deposited amorphous state, (b) partially crystallized film after 5 min annealing at 250 °C, (c) 10 min at approximately 250 ° C and (d) in the fully crystallized state.

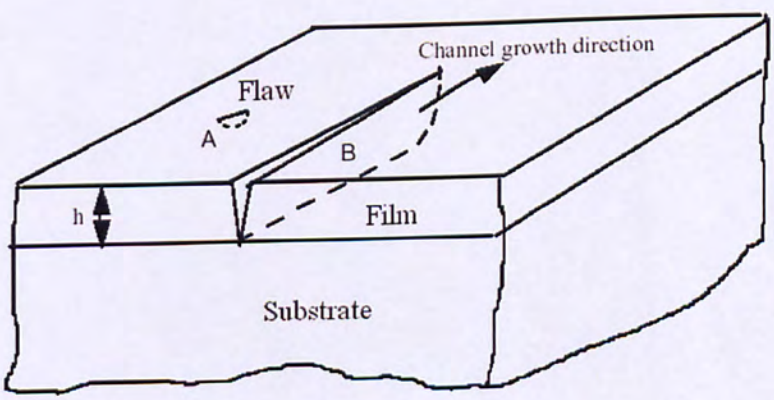

Figure 2.11: Coating of thickness h, channeling crack (B) and initial surface flaw (A)[93].

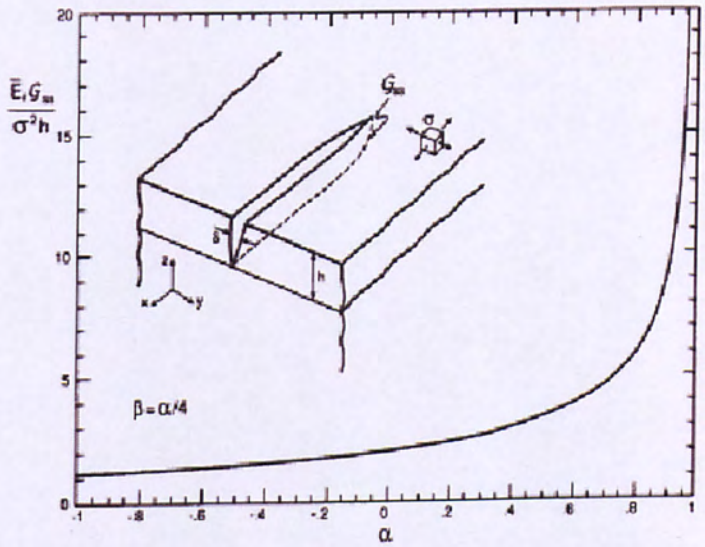

Figure 2.12: The relation between the energy at the channel front against the Dundurs parameter α. The insert shows a channeling crack[96].

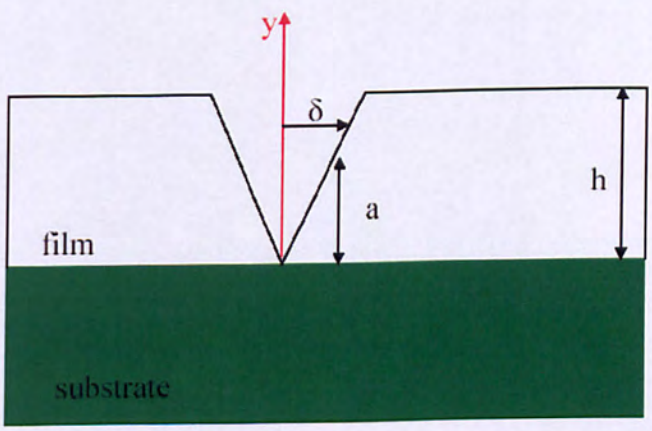

Figure 2.13: Cross – sectional view of a cracked thin film bonded to a substrate.

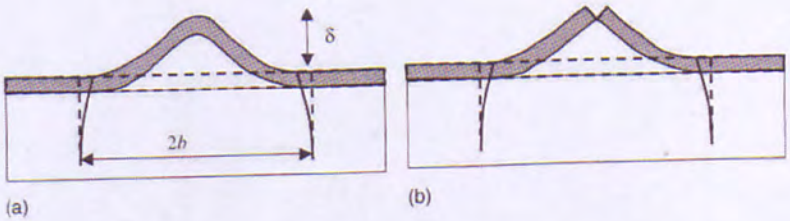

Figure 2.14: Closed (left) and open (right) buckling patterns[98].

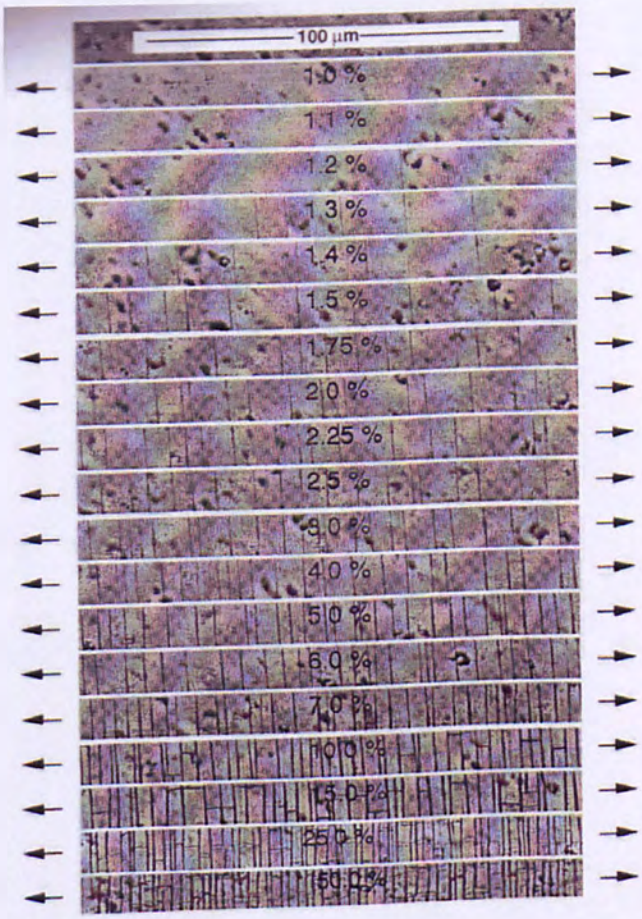

Figure 2.15: Tensile fragmentation of SiO_x coating on PET substrate at different strains using in situ optical microscopy[103]. Arrows indicate the direction of the applied uniaxial tensile stress.

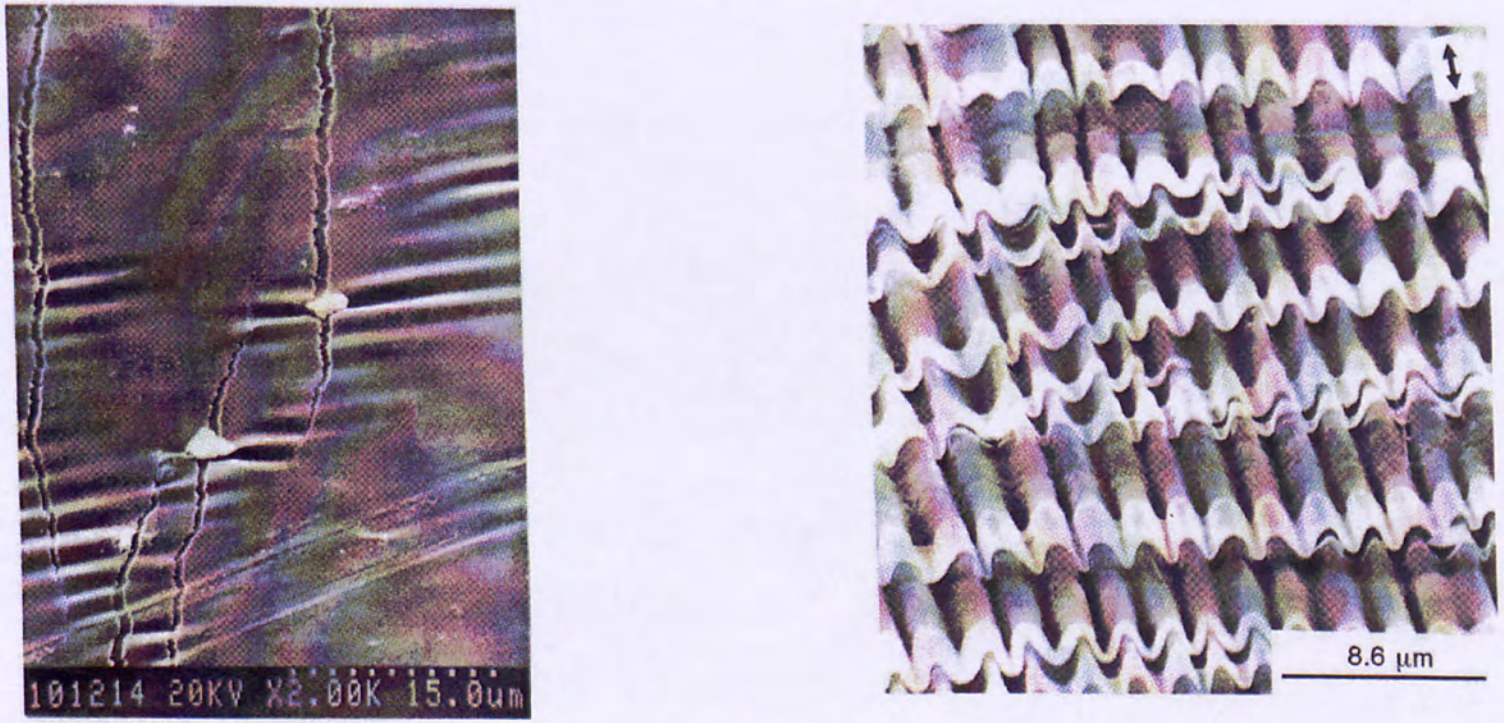

Figure 2.16: SEM image[107], left, showing a Pt / PET surface uniaxially strained to 5 % at 90 % and SEM micrograph[107], right, of a gold – coated PET elongated to 300 % at 85 °C.

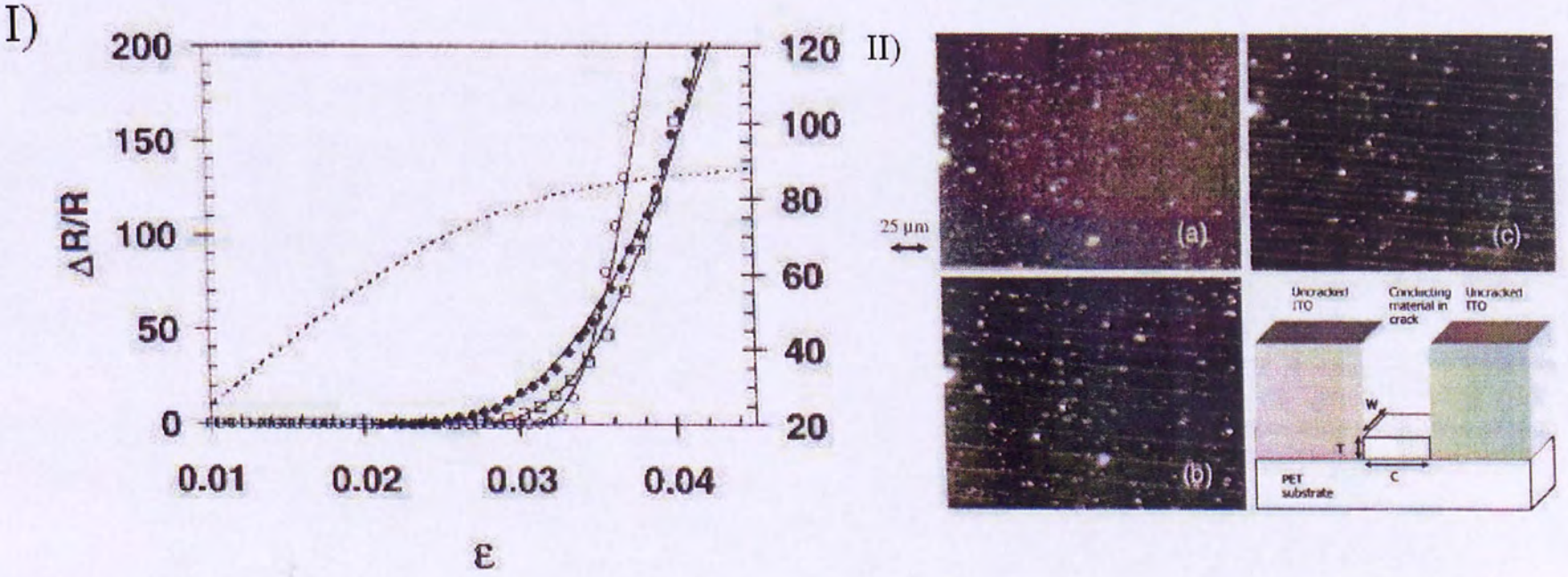

Figure 2.17: **(I):** Change in resistance of ITO coated PET for three different thicknesses shown as points. The composite film stress – train curve is also shown as dotted line. **(II):** Optical images of ITO coated PET at 2 %(a), 2.5 % (b) and 3 % (c). A schematic diagram showing bridging ITO material is also included[108].

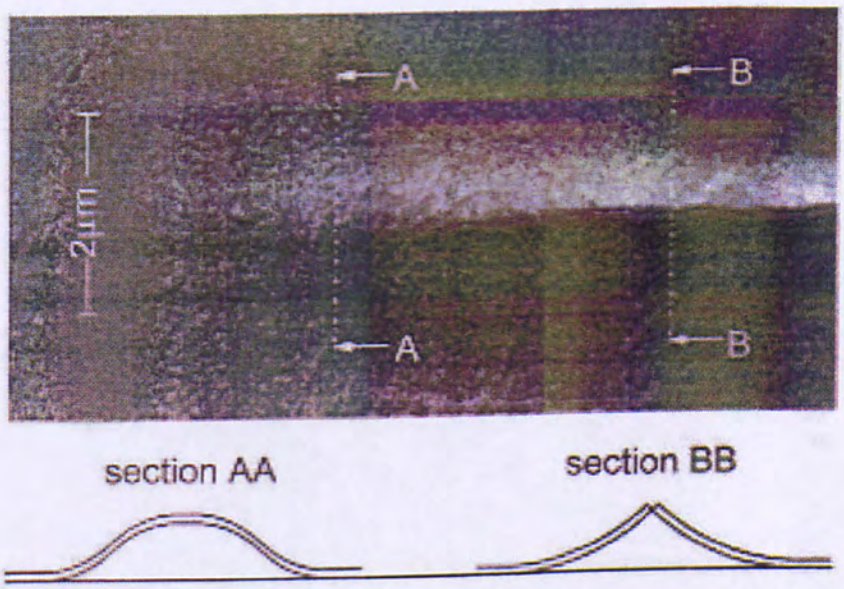

Figure 2.18: SEM image showing ITO on PET surface tunneling delamination – buckle – crack[120].

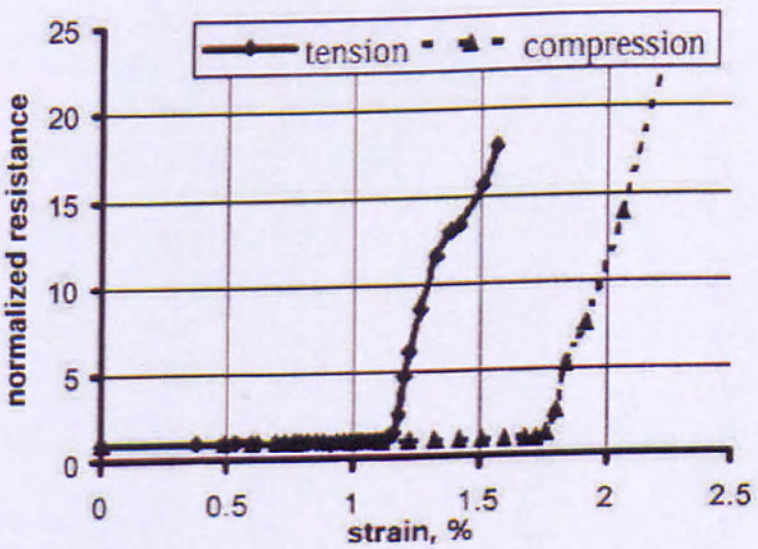

Figure 2.19: Electrical resistance as a function of buckling strain for ITO coated PET, surface under tension and compression[121].

Figure 2.20: SEM micrograph of 53 nm thick SiO_x biaxial fragment morphology at saturation[129].

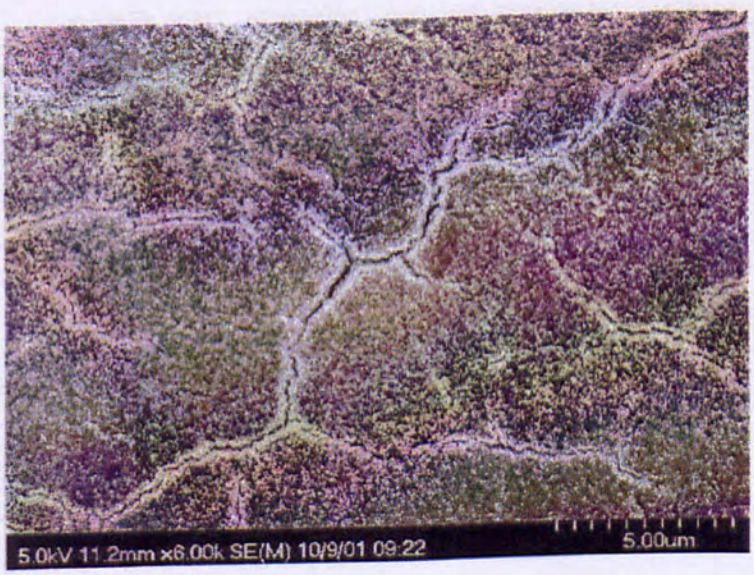

Figure 2.21: SEM image of the Al surface biaxial fracture pattern[130].

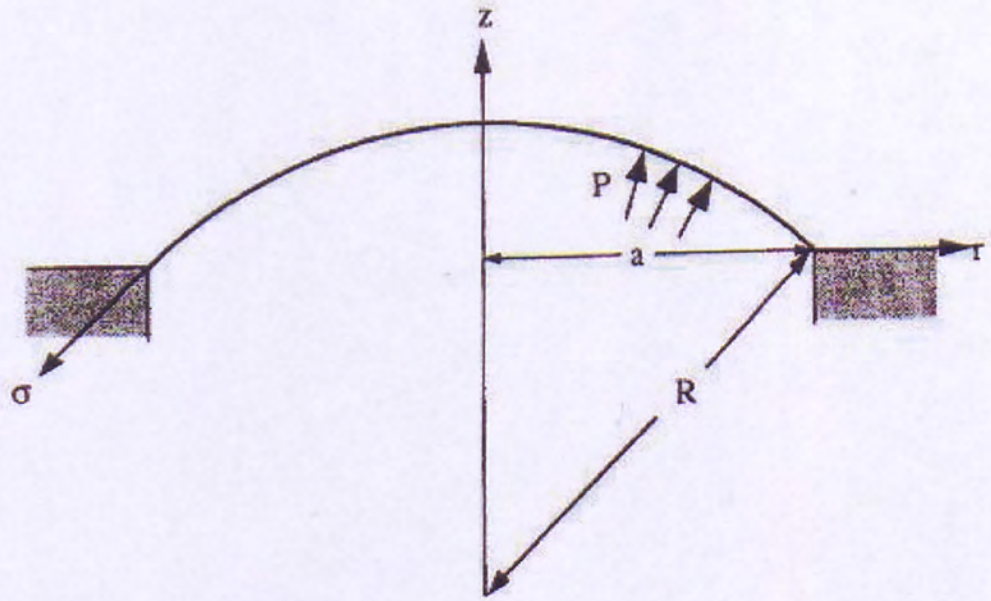

Figure 2.22: The bulge test geometry[161].

Type of Model	C_1	C_2
Spherical cap	4	8/3
Energy minimization (Lin[166])	4	$(7 - \nu)/3$
Finite – element (Small[161])	-	$(8/3)*(1 - 0.241\ \nu)$
Finite – element (Pan[167])	4	$(8/3)*(0.974 - 0.233\ \nu)$
Hencky[165]	4	$(8/3)*(1.015 - 0.247\ \nu)$

Table 2.1: Parameters of generalized bulge equation[165].

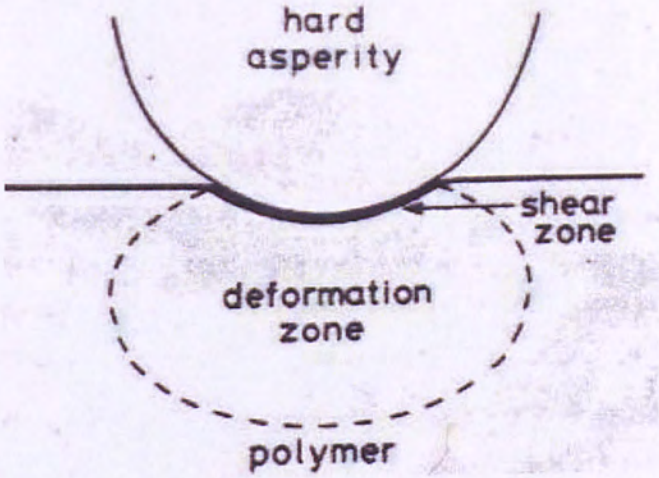

Figure 2.23: Sliding of a hard sphere over a polymer surface[171].

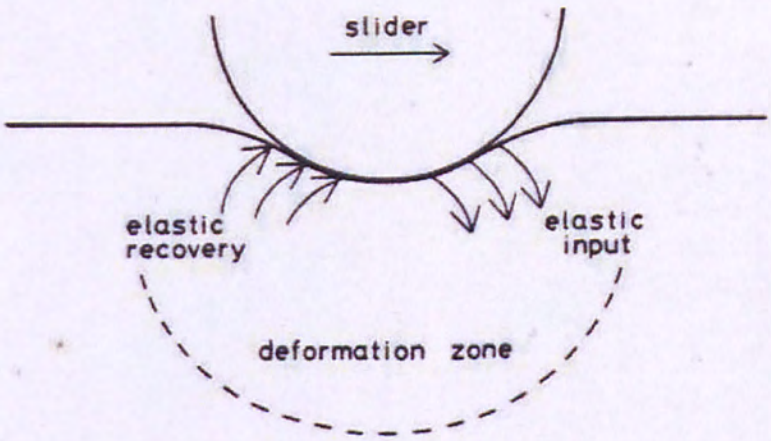

Figure 2.24: A hard asperity traverses the surface of an elastomeric material[171].

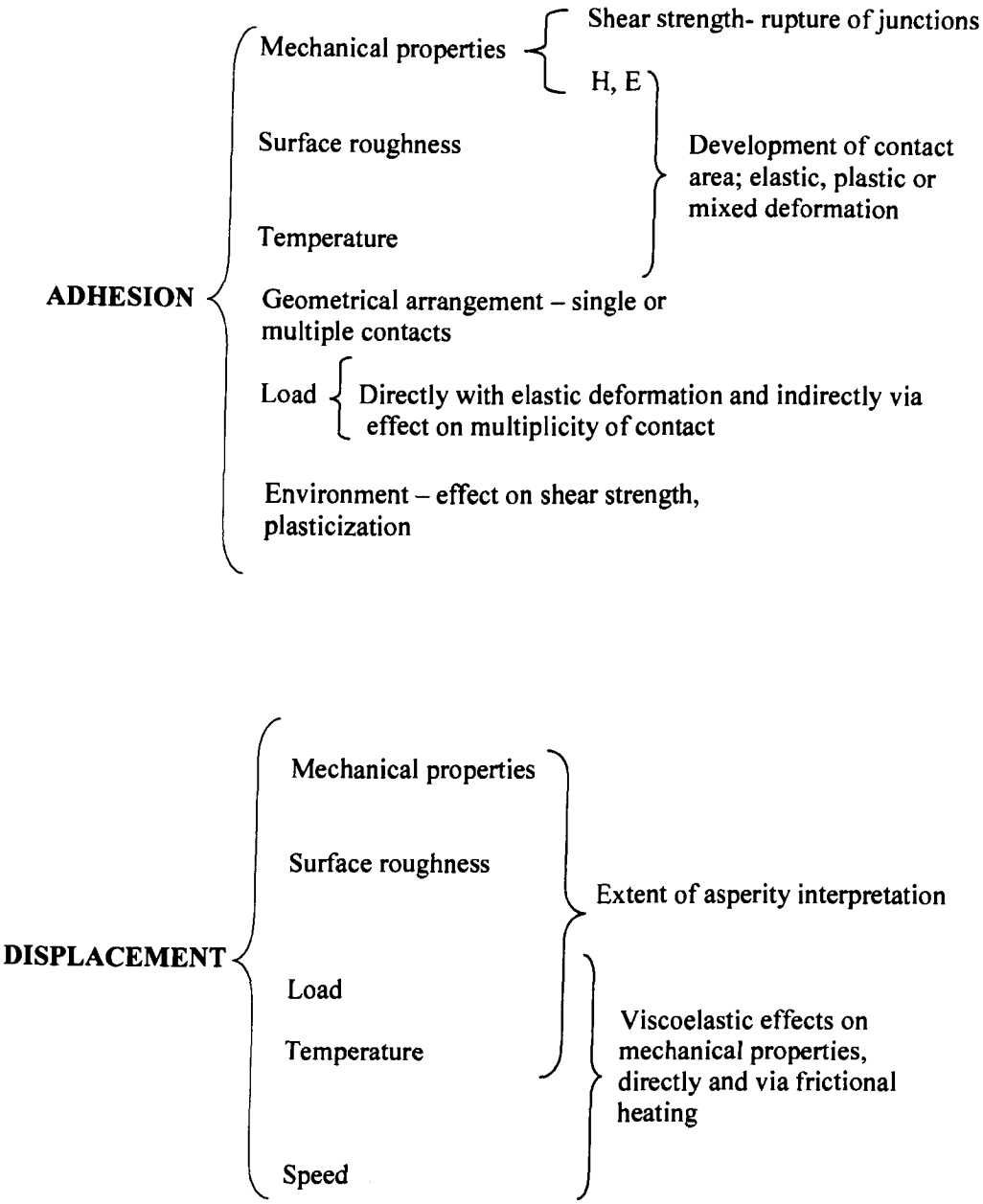

Figure 2.25: Factors affecting the friction of polymers, from Lancaster[172].

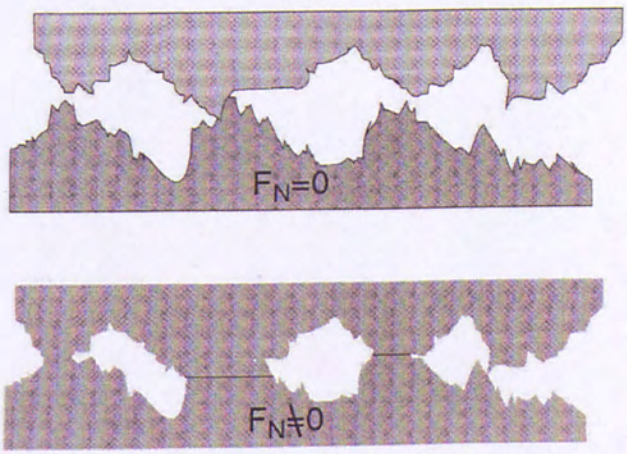

Figure 2.26: Multiple asperities in contact under zero normal force and under finite normal force[174].

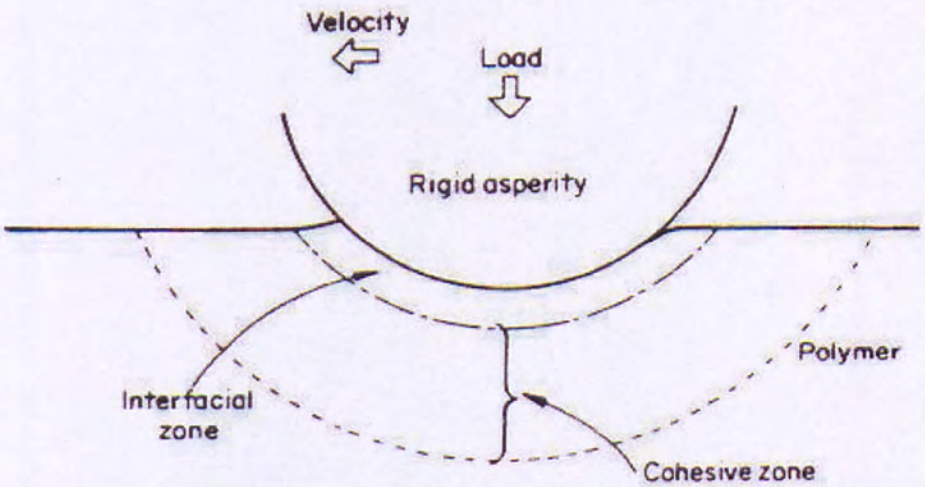

Figure 2.27: Interfacial and cohesive wear zones when a hard circular asperity slides against a polymer[177].

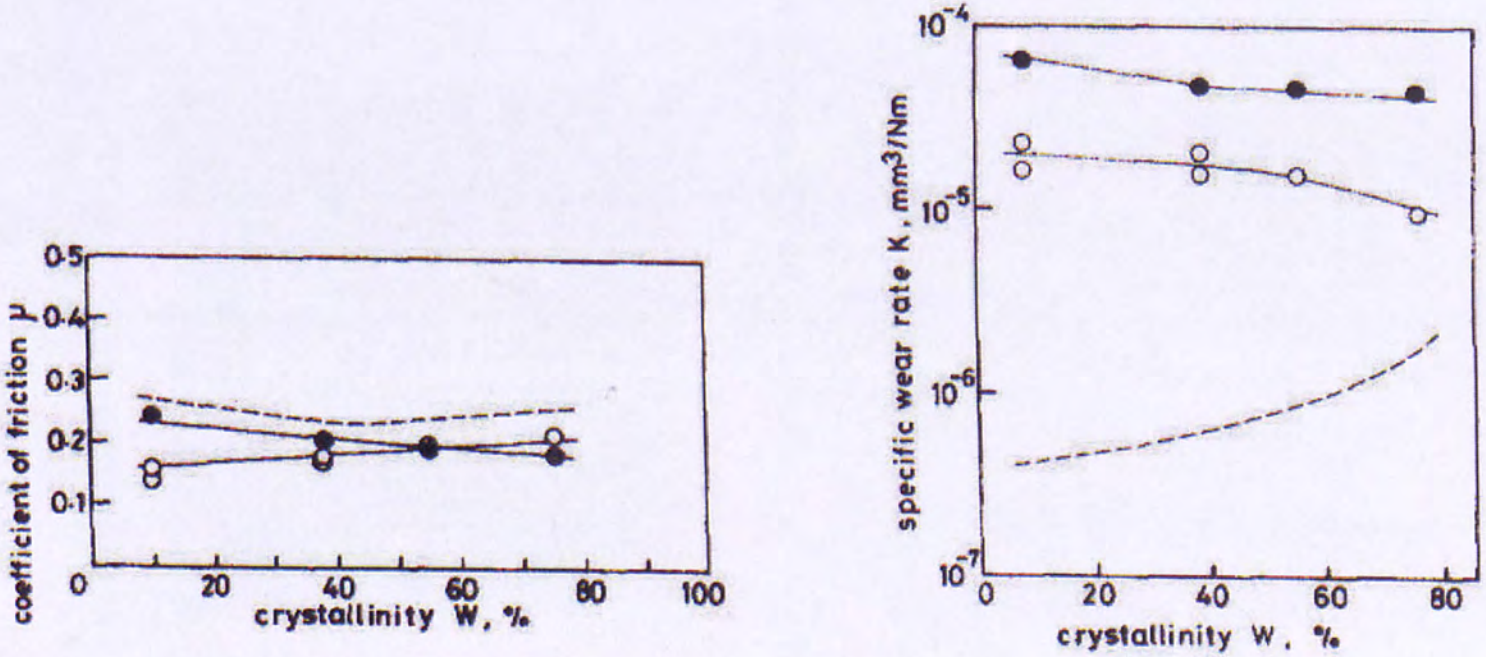

Figure 2.28: Coefficient of friction (right) and specific wear rate (left) in the case of water lubricated PET (0.1 m / sec) open circles, water lubricated PET (0.01 m / sec) closed circles and unlubricated PET (0.1 m / sec) broken line[185].

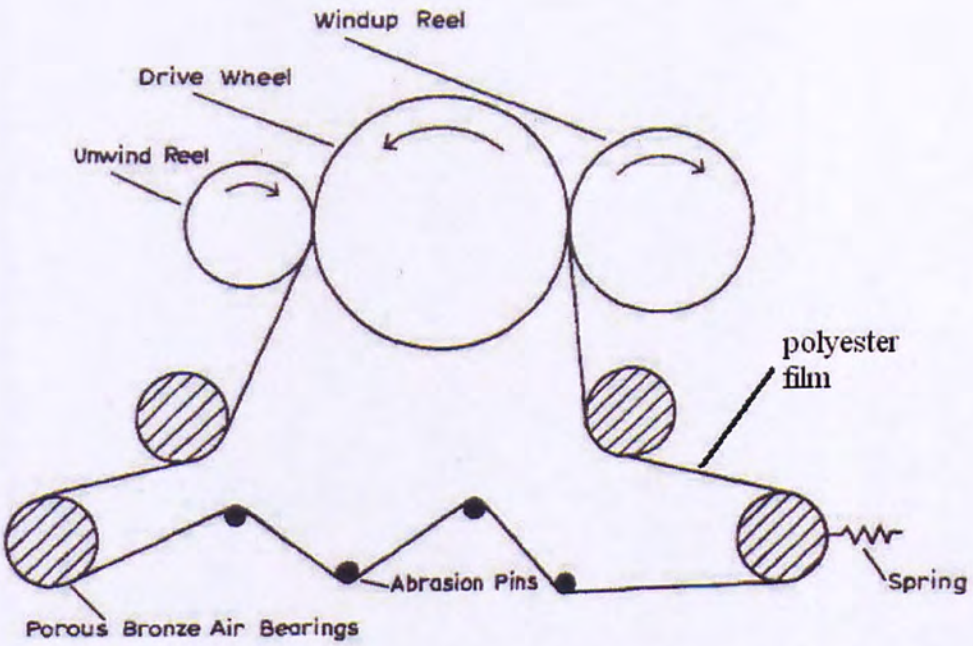

Figure 2.29: Apparatus used to measure wear of polyester films when they are passing over stationary pins[189].

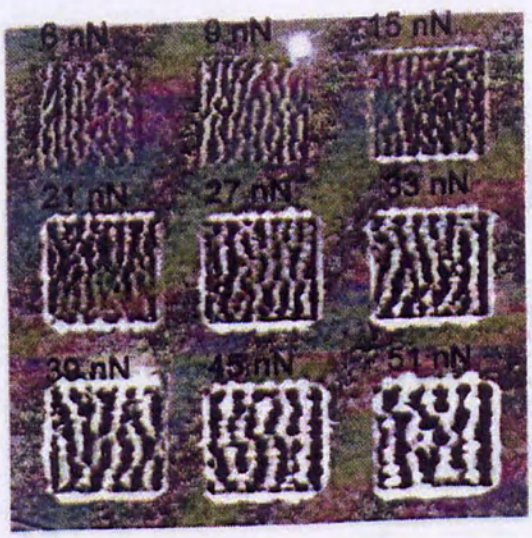

Figure 2.30: Nine different, 1 μm^2, areas repeatedly scanned for 10 times at different loads ranging from 6 to 51 nN. The ridges become more pronounced as the load increases[194].

Appendix 3

(Figures and tables from Chapter 3)

	Applications
PET Melinex 506	Adhesion promoting pre-treatment on both surfaces
PET Melinex ST506	Heat stabilized film pre-treated on both surfaces for graphics and circuitry layers for membrane touch switches
PEN Kaladex S1020	Adhesion promoting pre-treatment on one side only, heat stabilized. Pre-treated surface offers enhanced adhesion to solvent based inks and coatings such as hard coats
PEN Teonex Q65	One-side adhesion promoters. Optically clear films.

Table 3.1: Available flexible polyester substrates.

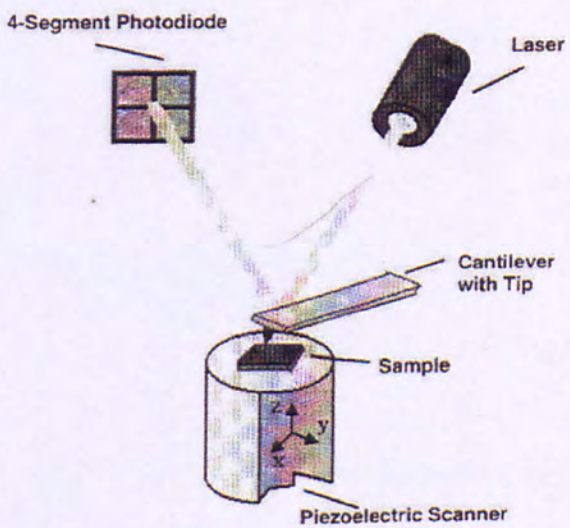

Figure 3.1: Schematic of an AFM showing the optical lever principle[219].

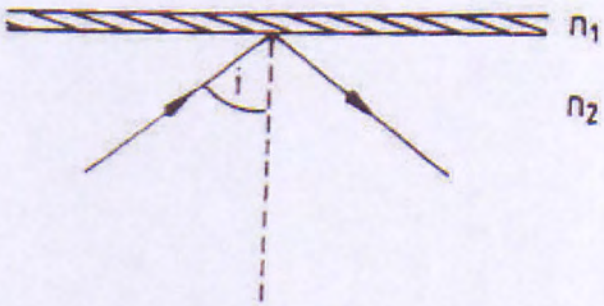

Figure 3.2: Total reflection[201] of radiation in a medium of refractive index n_2 by a thin film of refractive index n_1.

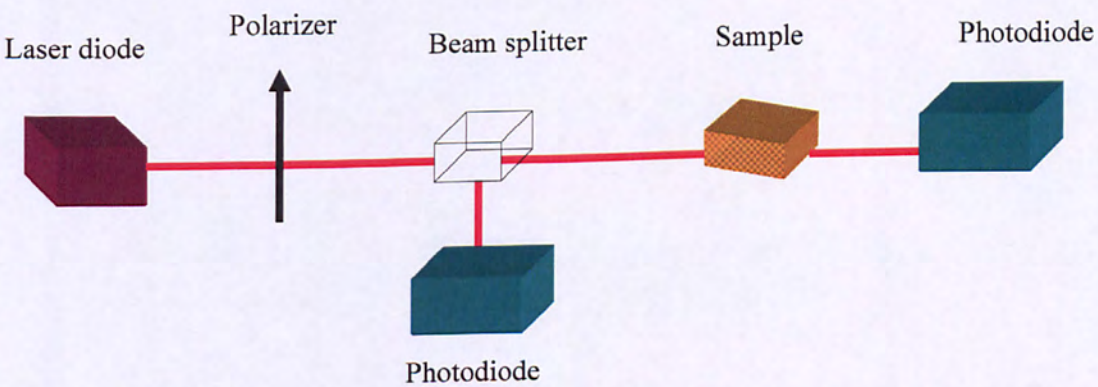

Figure 3.3: Schematic of the optical transmission measurement system.

Figure 3.4: Photograph of the pulsed laser deposition system.

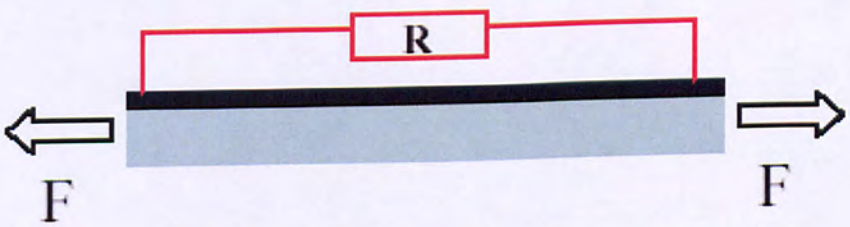

Figure 3.5: Uniaxial tensile electro-mechanical testing of ITO / polyester. F is uniaxially applied tensile force and R is electrical resistance of ITO.

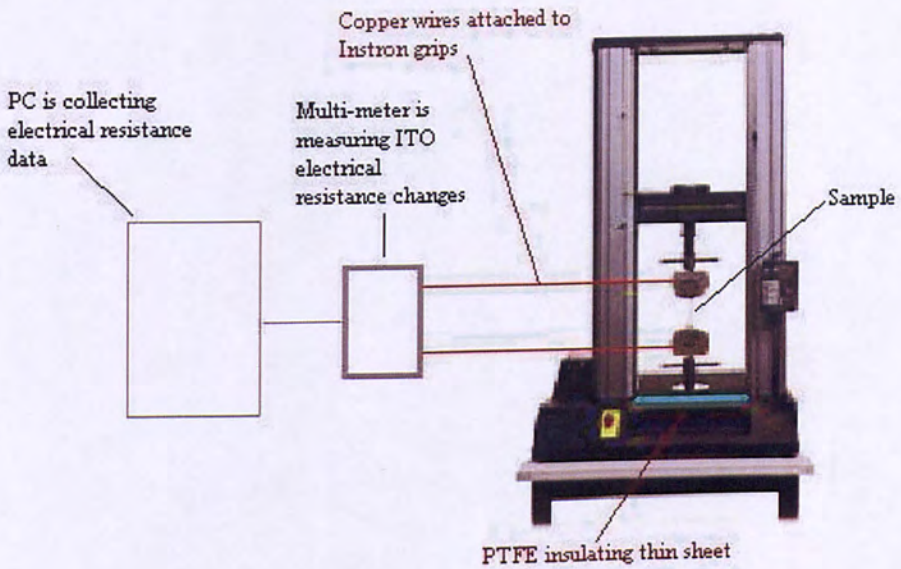

Figure 3.6: Instron mechanical tester after modifications.

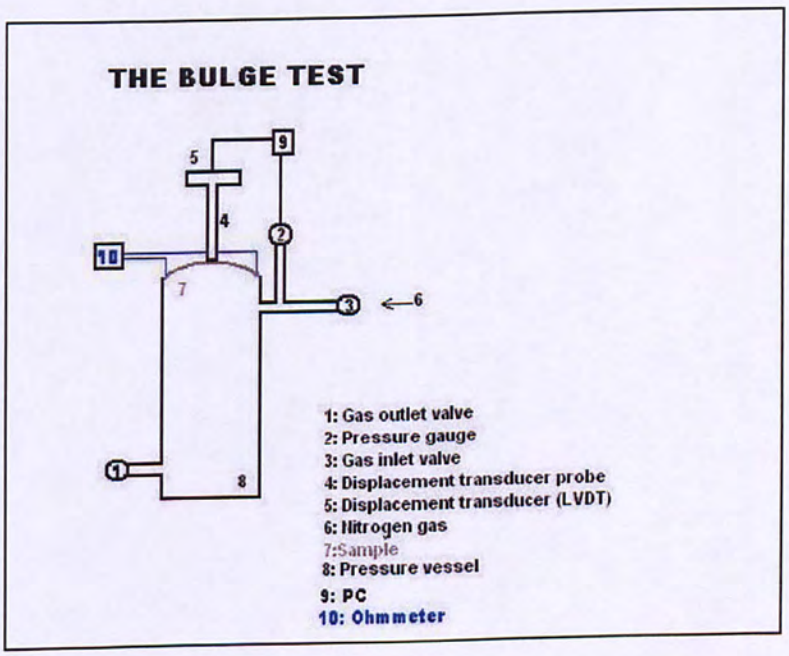

Figure 3.7: Schematic of the biaxial 'bulge' test apparatus.

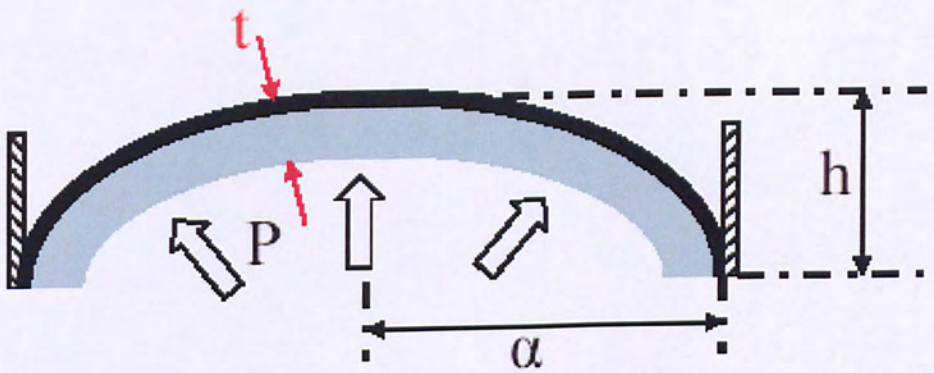

Figure 3.8: Biaxial tensile deformation of a thin film using the biaxial 'bulge' test.

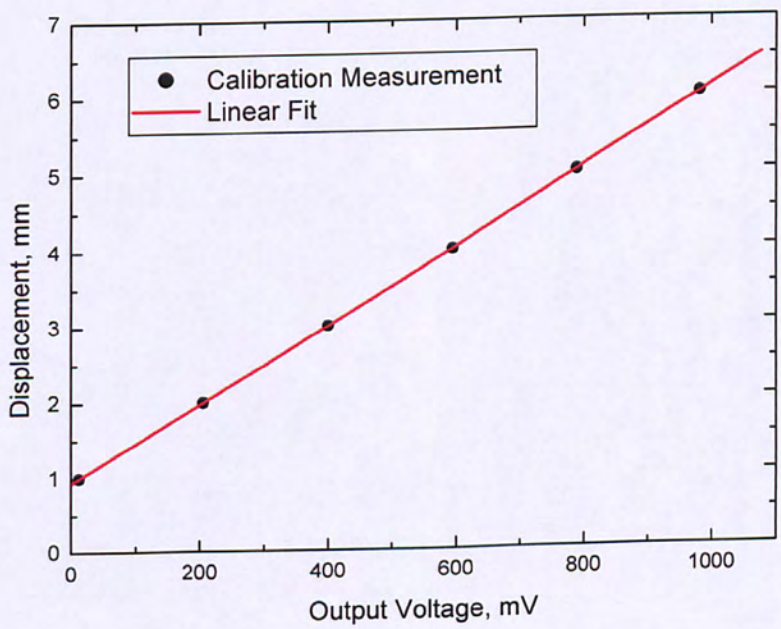

Figure 3.9: Calibration plot used for measuring central deflection, h.

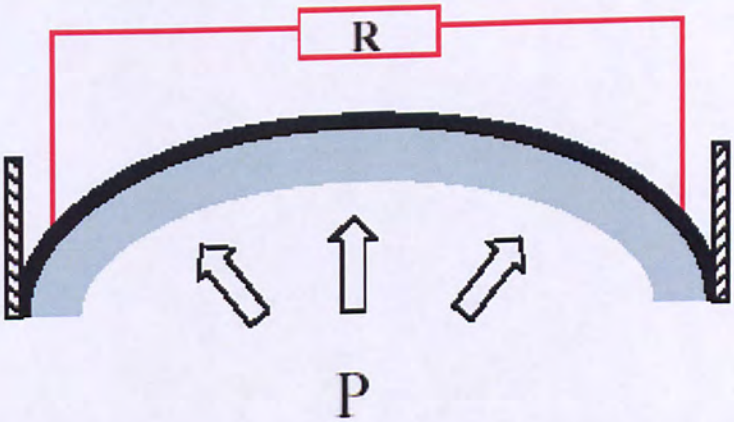

Figure 3.10: Schematic of biaxial testing coupled with electrical resistance in-situ monitoring.

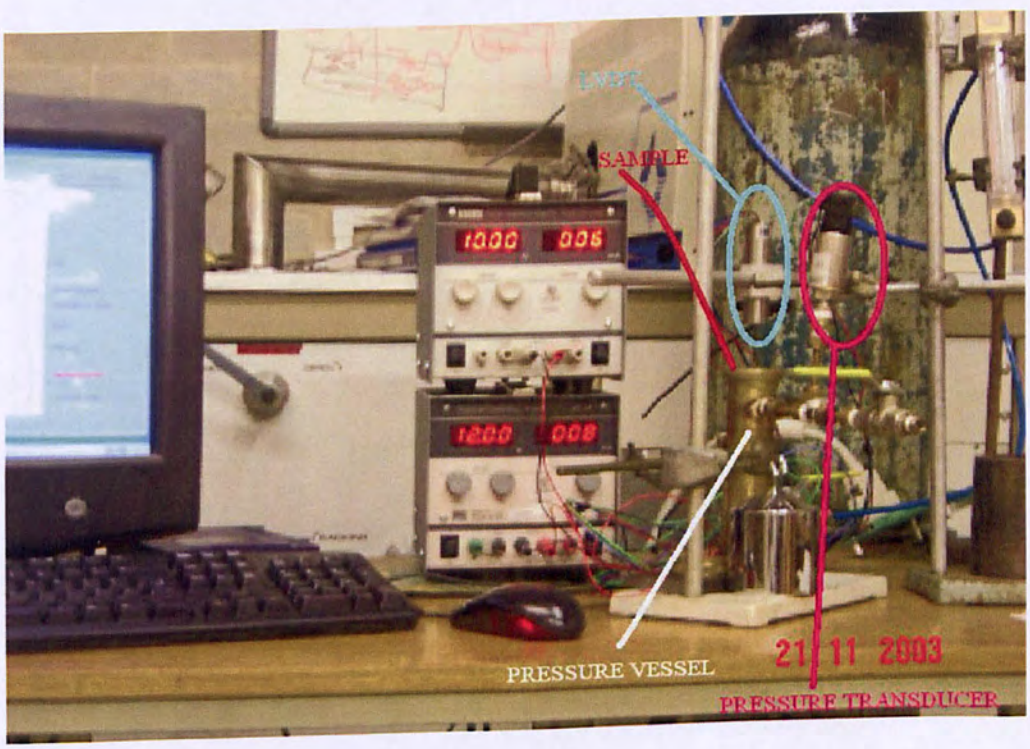

Figure 3.11: Photograph of the biaxial 'bulge' test system built in house.

Appendix 4

(Figures and tables from Chapter 4)

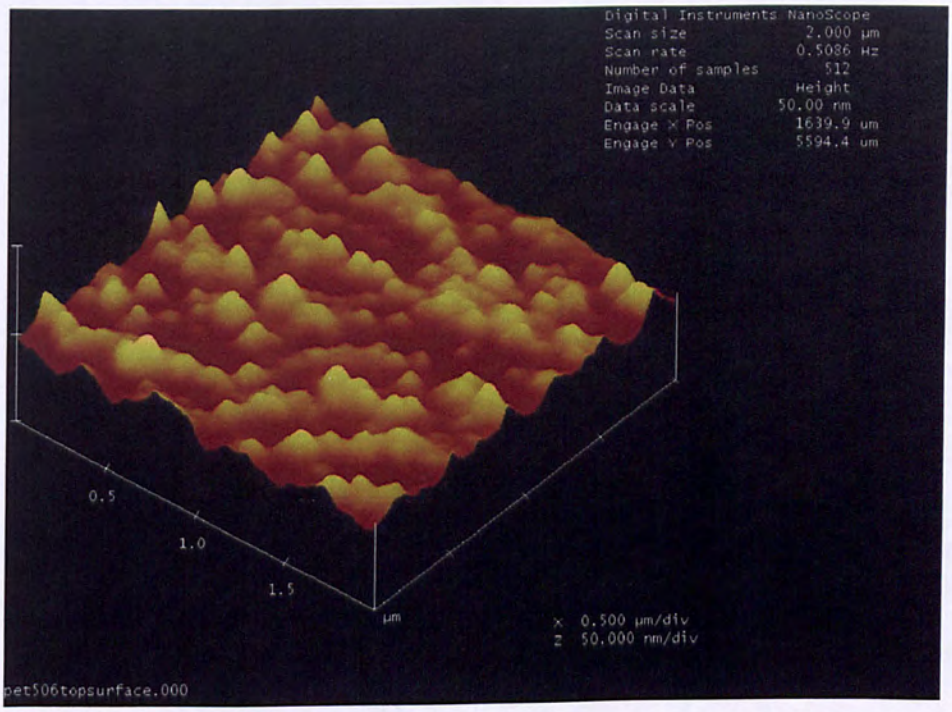

Figure 4.1: Three-dimensional contact-mode AFM image of the top PET 506 surface which is pre-treated in order to enhance adhesion.

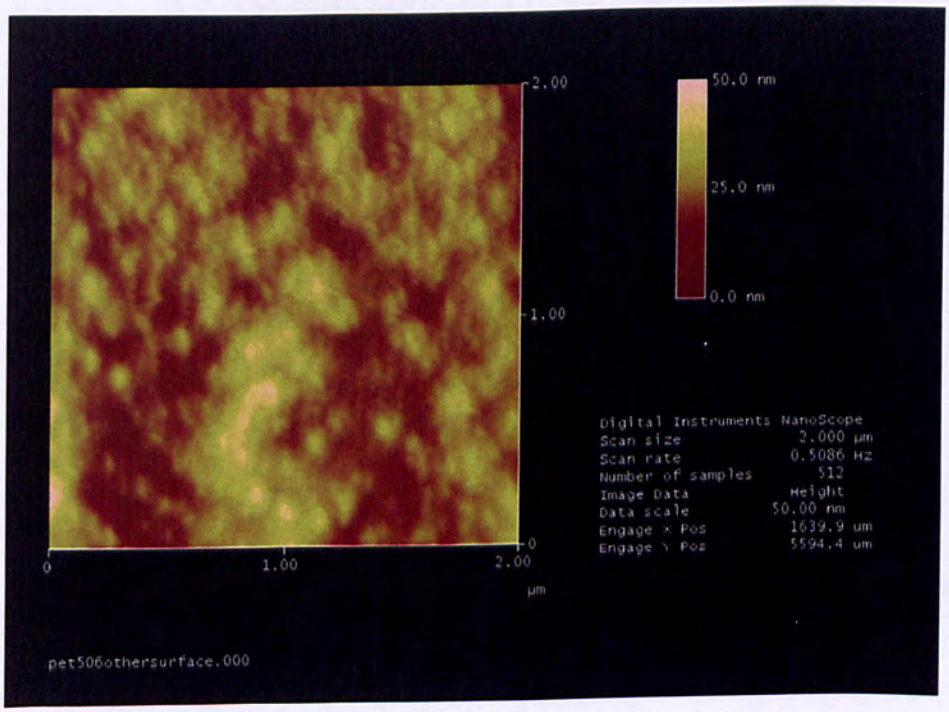

Figure 4.2: Two-dimensional contact-mode AFM image of the back PET 506 surface, which is also adhesion promotion, pre-treated.

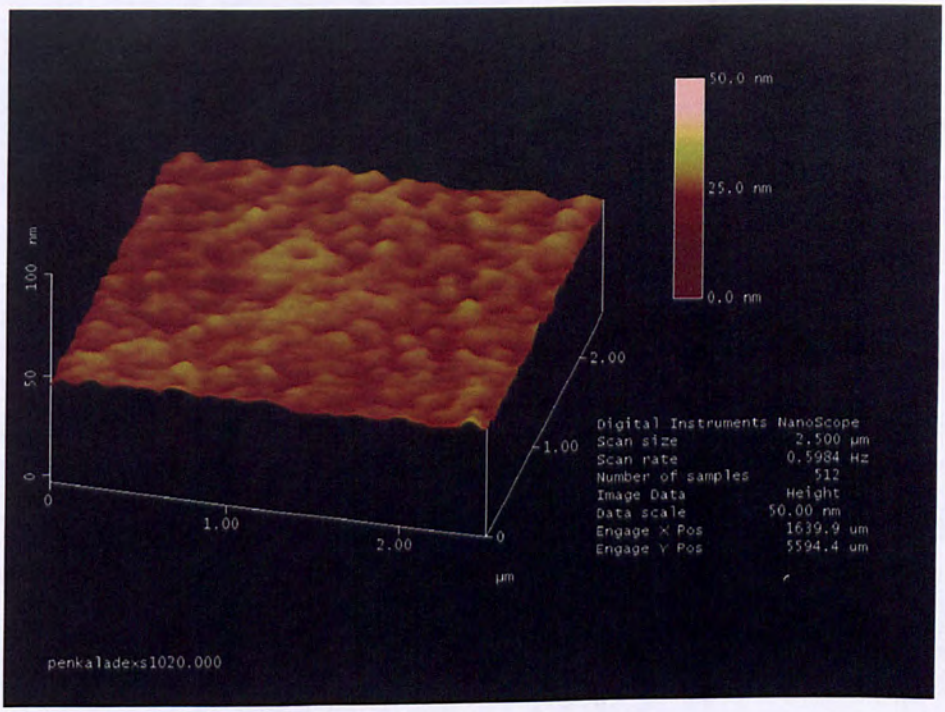

Figure 4.3: Three-dimensional AFM image showing the adhesion treated PEN Kaladex S1020 surface.

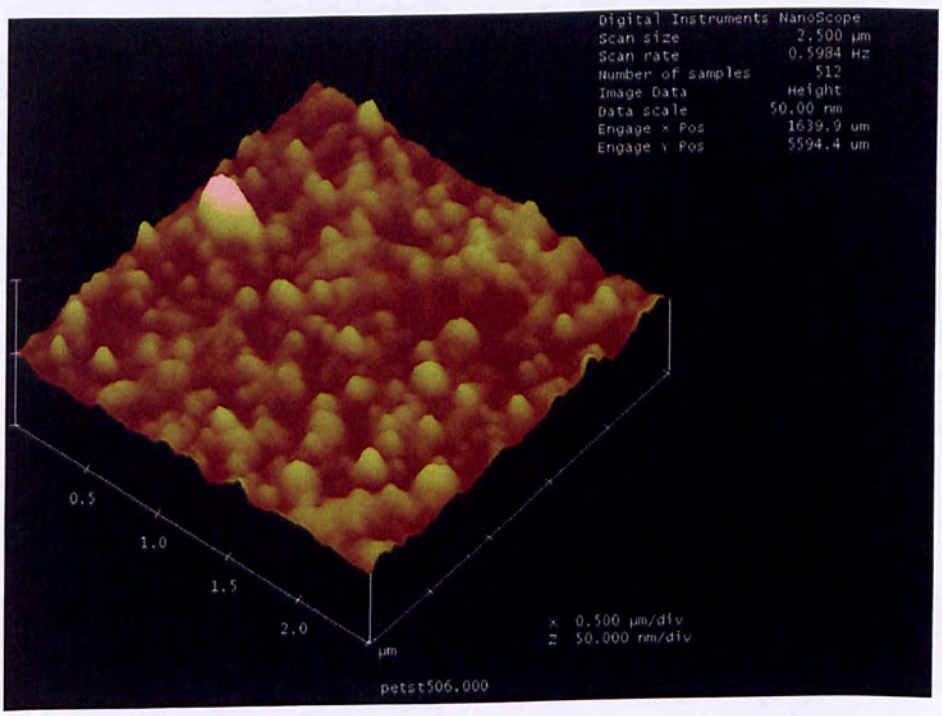

Figure 4.4: Three-dimensional AFM image of the heat-treated PET ST506 polymer surface.

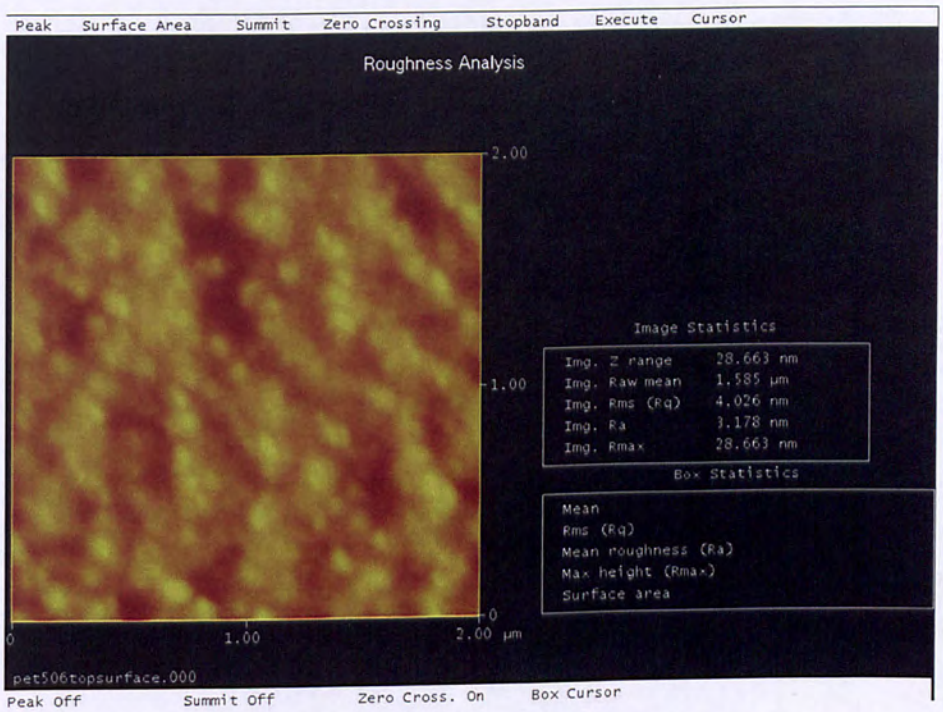

Figure 4.5: Roughness analysis of PET 506 adhesion treated top surface.

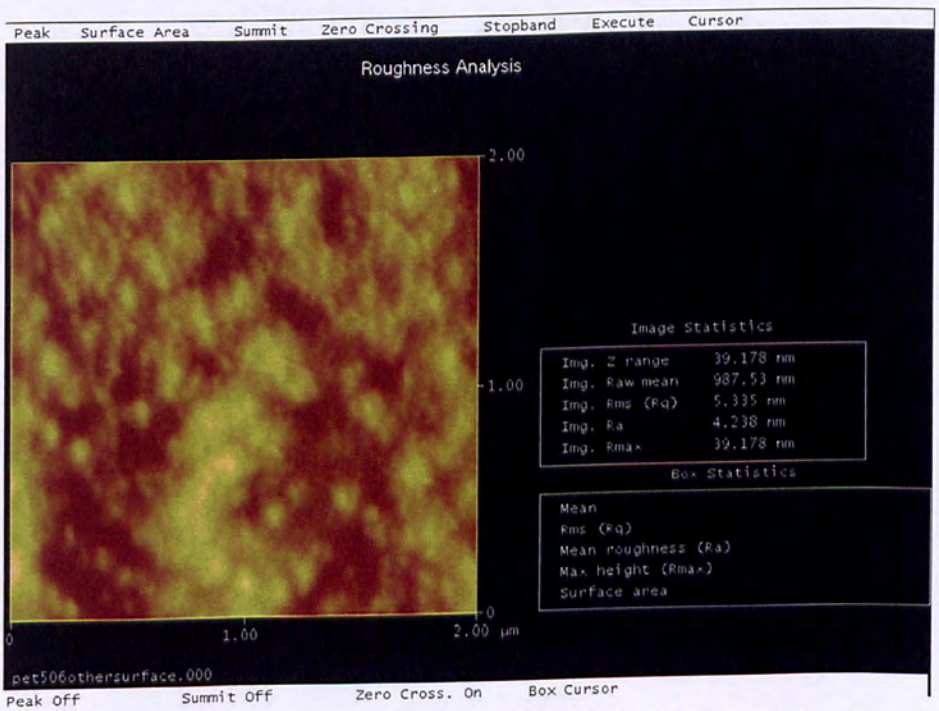

Figure 4.6: Roughness analysis data of PET 506 adhesion pre-treated back surface.

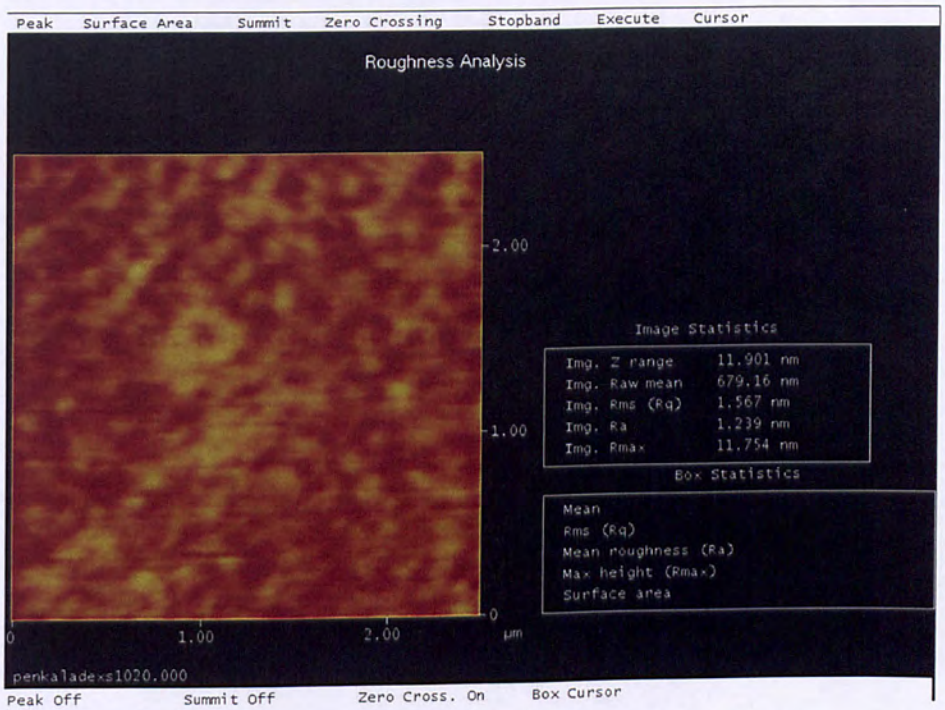

Figure 4.7: Contact-mode AFM roughness analysis of surface treated PEN Kaladex S1020 bare substrate.

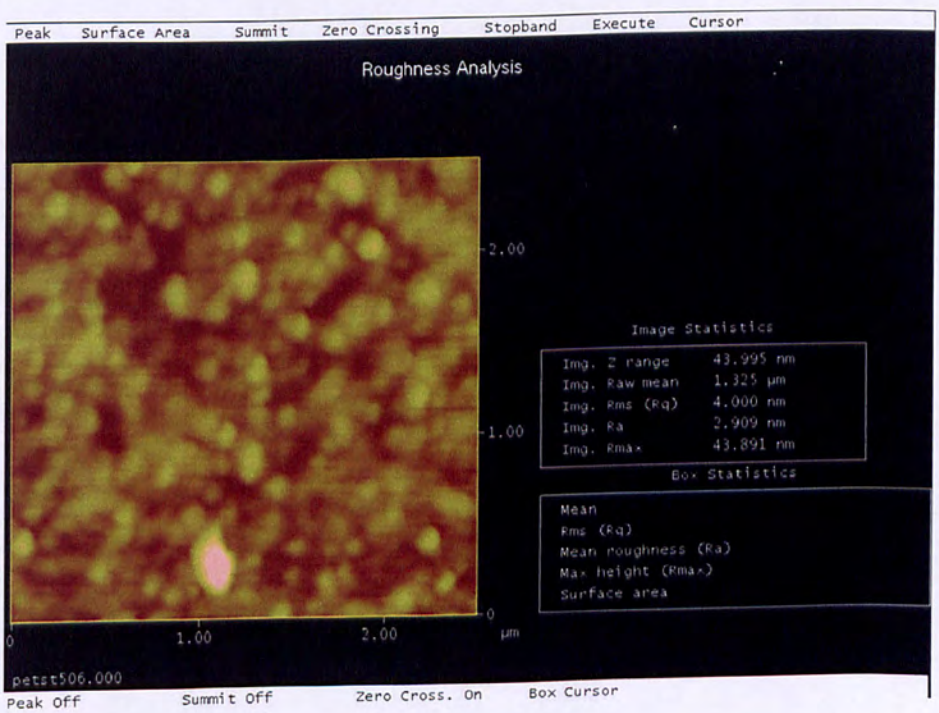

Figure 4.8: Roughness analysis, conducted by AFM, of the surface treated of the PET ST506 grade.

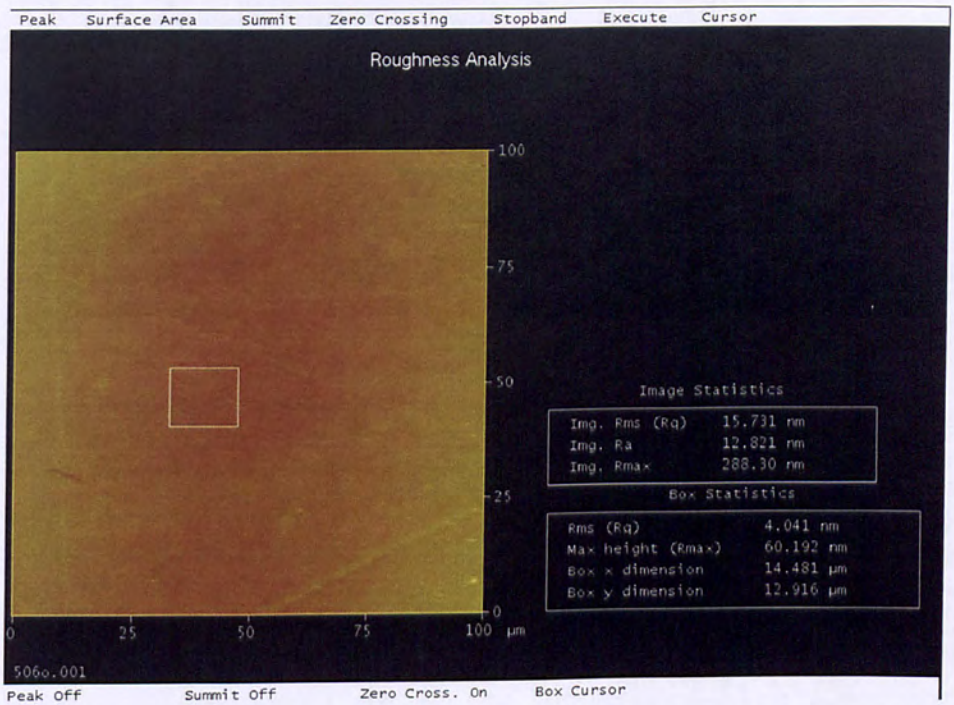

Figure 4.9: Roughness analysis of a relatively large, 100^2 μm^2, area of PET 506 bare substrate.

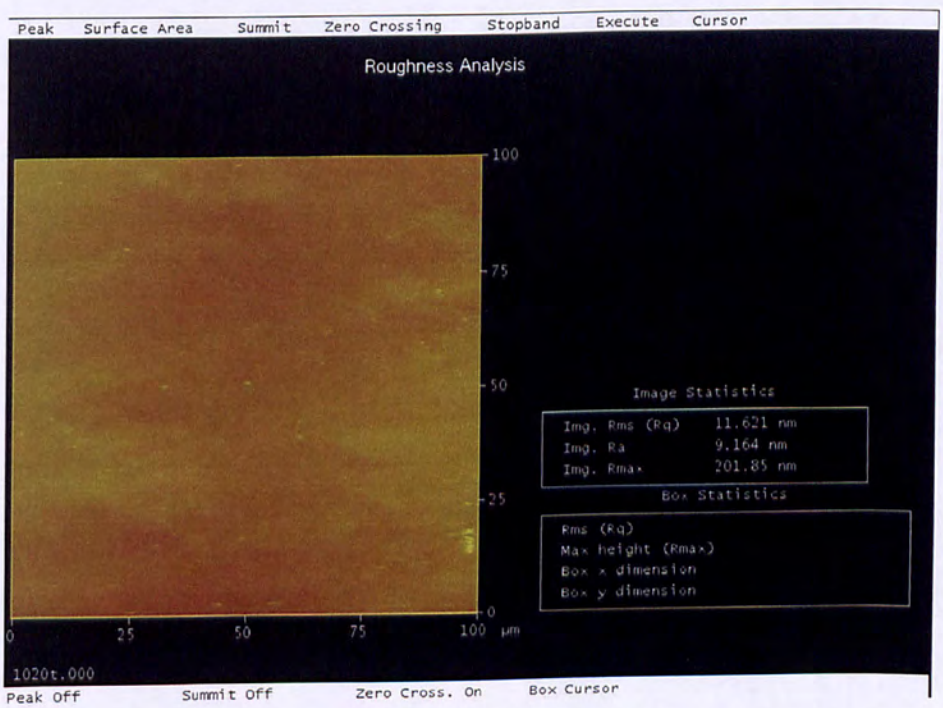

Figure 4.10: Roughness analysis of a relatively large, 100^2 μm^2, area of PEN Kaladex S1020 bare substrate.

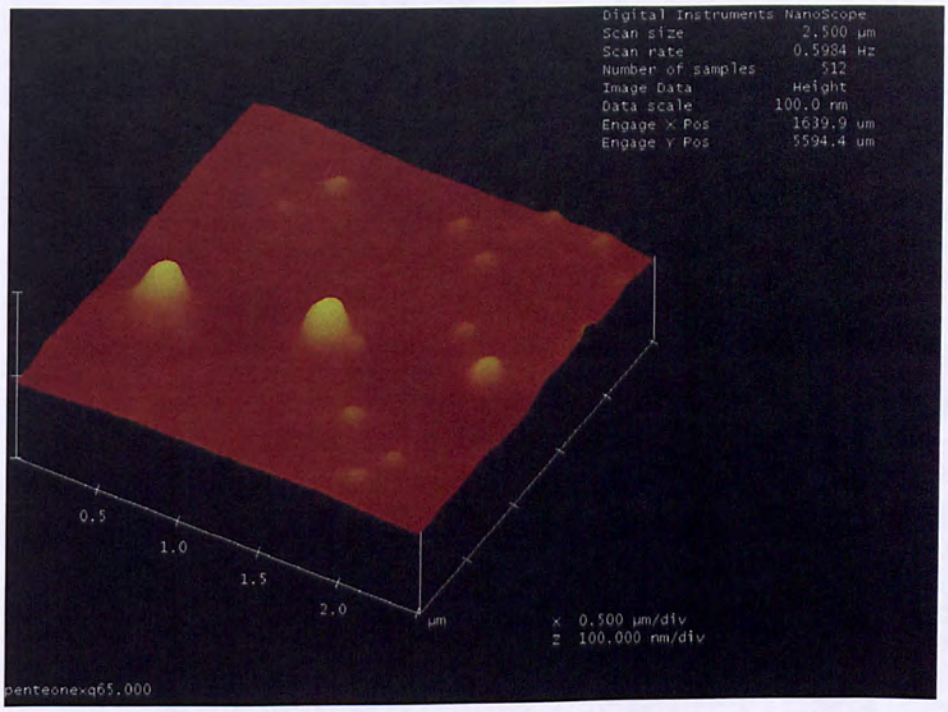

Figure 4.11: 3 – D AFM image showing the surface of PEN Teonex Q65 flexible substrate.

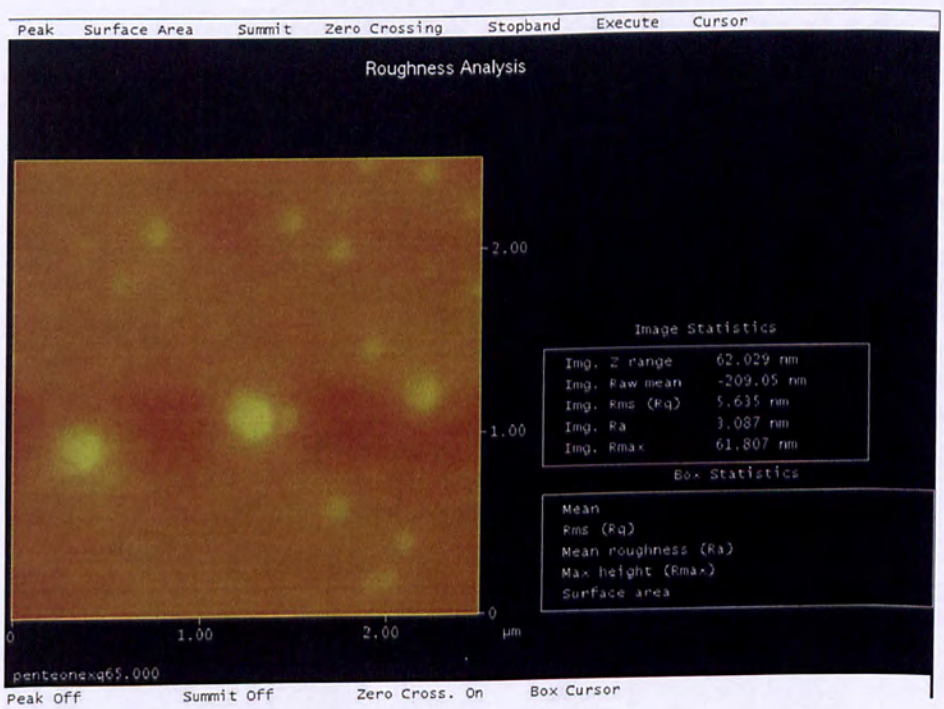

Figure 4.12: Roughness analysis, conducted by AFM, of the surface treated of the PEN Teonex Q65 grade.

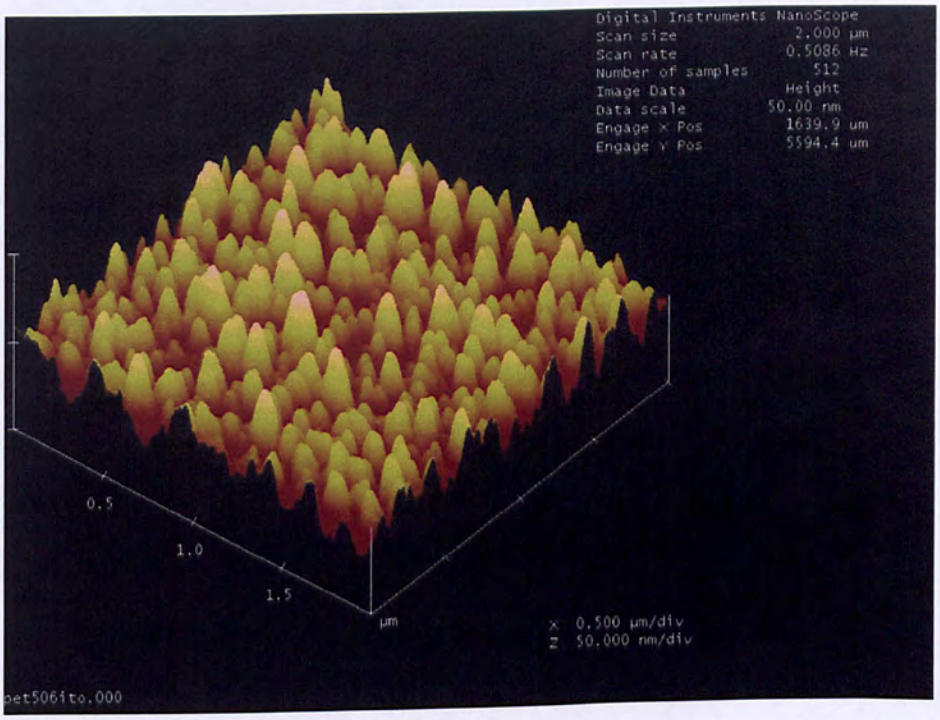

Figure 4.13: AFM three-dimensional image showing the ITO, deposited on PET 506, surface.

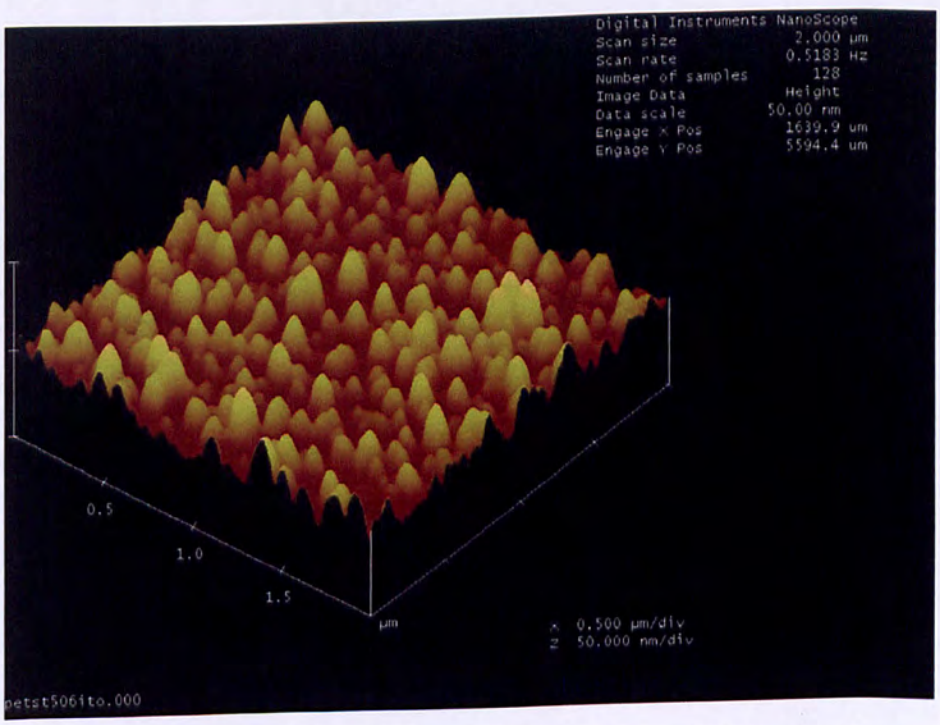

Figure 4.14: AFM image of the ITO surface deposited on PET ST506 flexible display substrate.

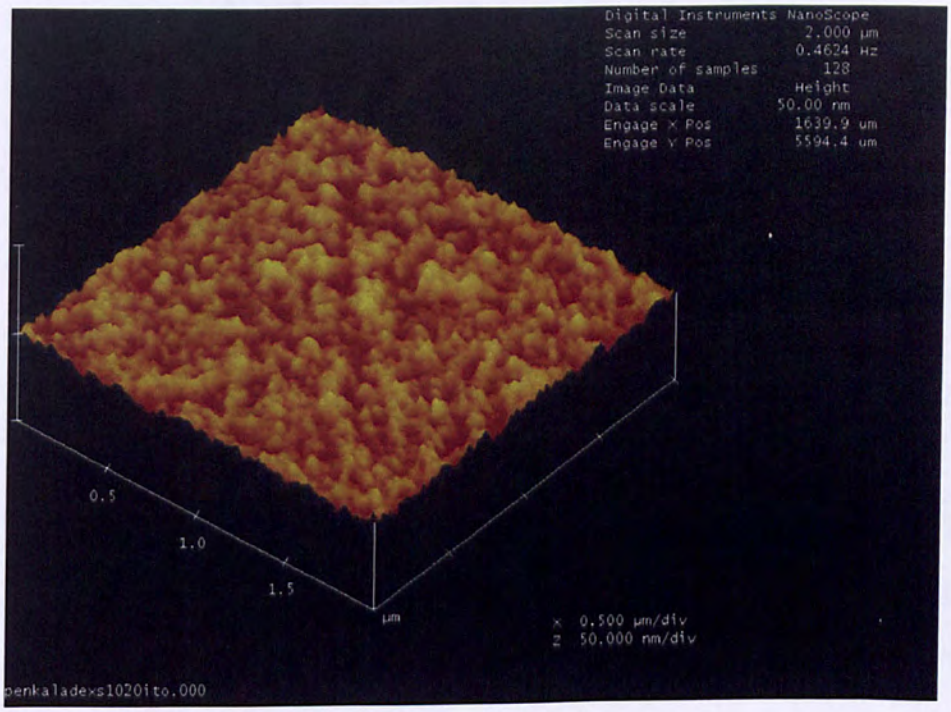

Figure 4.15: AFM image of an ITO surface deposited on PEN Kaladex S1020 polyester substrate.

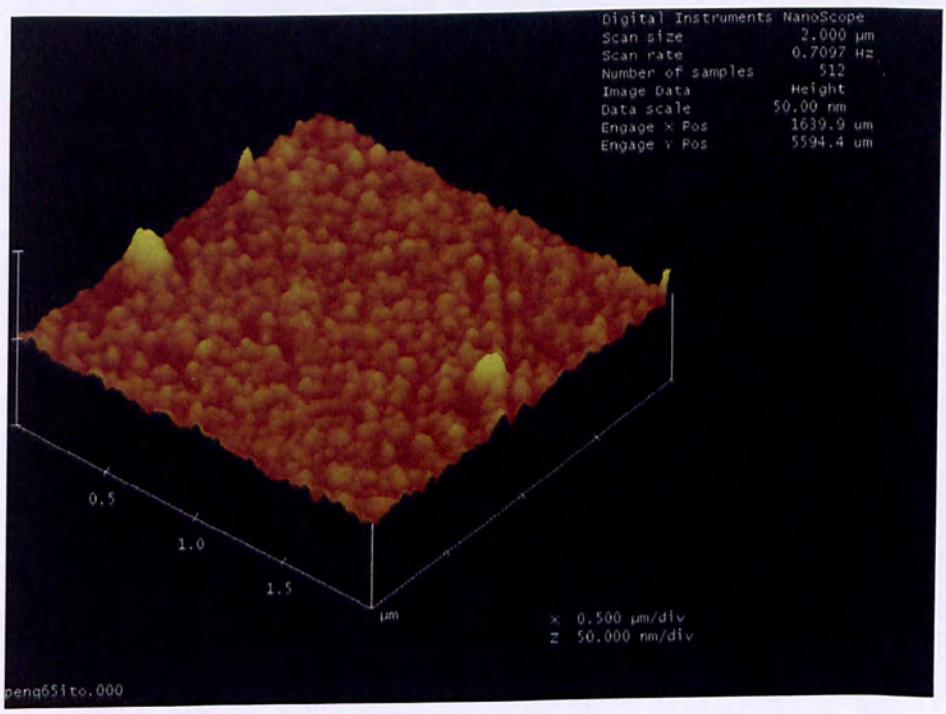

Figure 4.16: AFM contact-mode image showing the ITO, deposited on PEN TEONEX Q65, surface morphology.

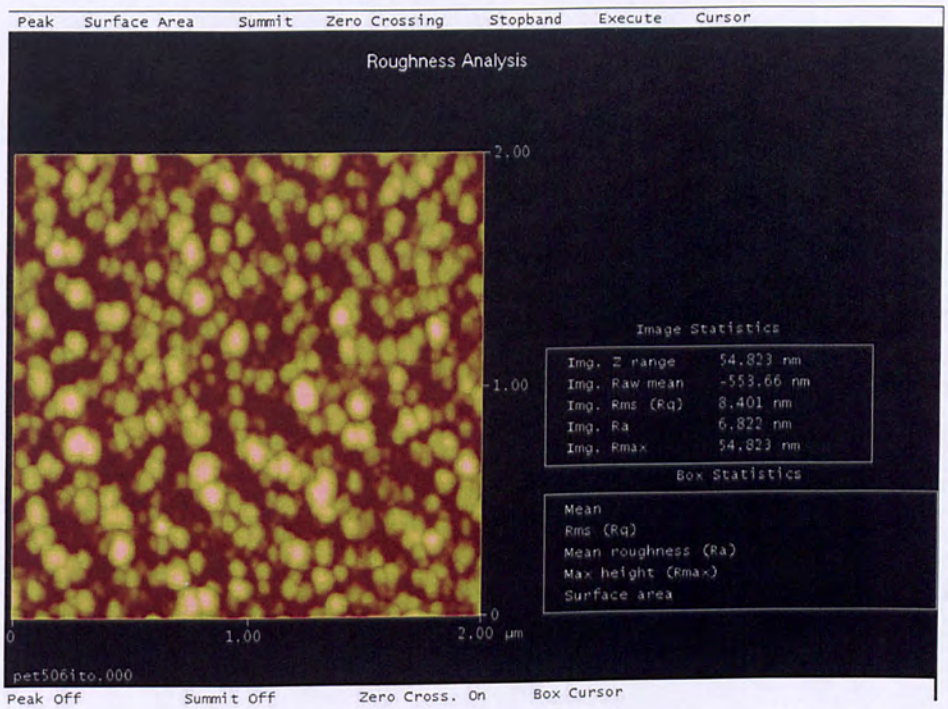

Figure 4.17: Roughness analysis of ITO, deposited on PET 506, surface.

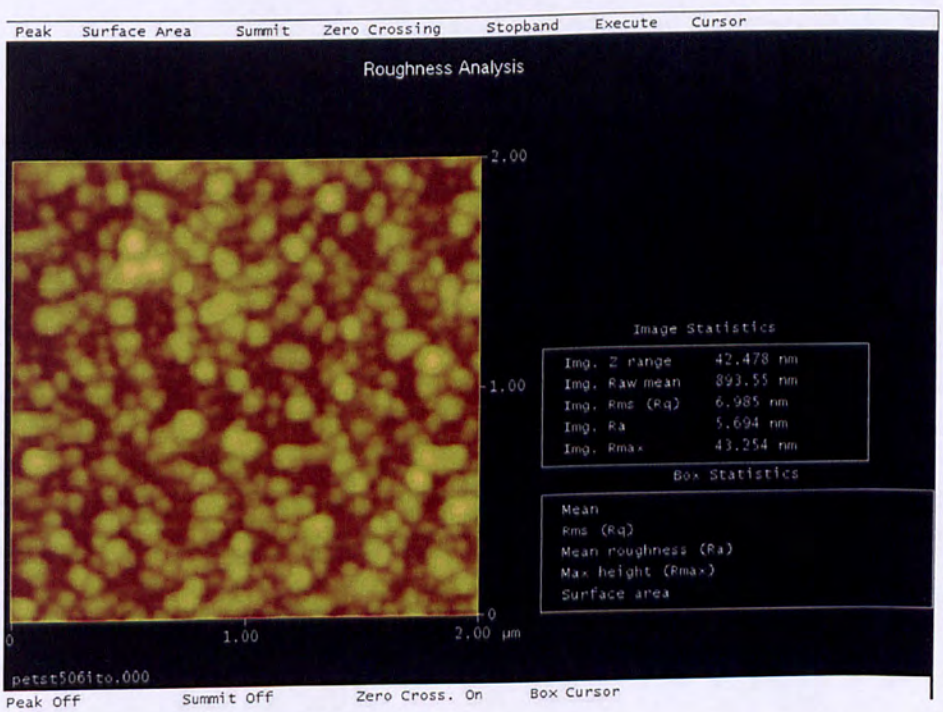

Figure 4.18: Roughness analysis of ITO surface sputtered on PET ST506 flexible display substrate.

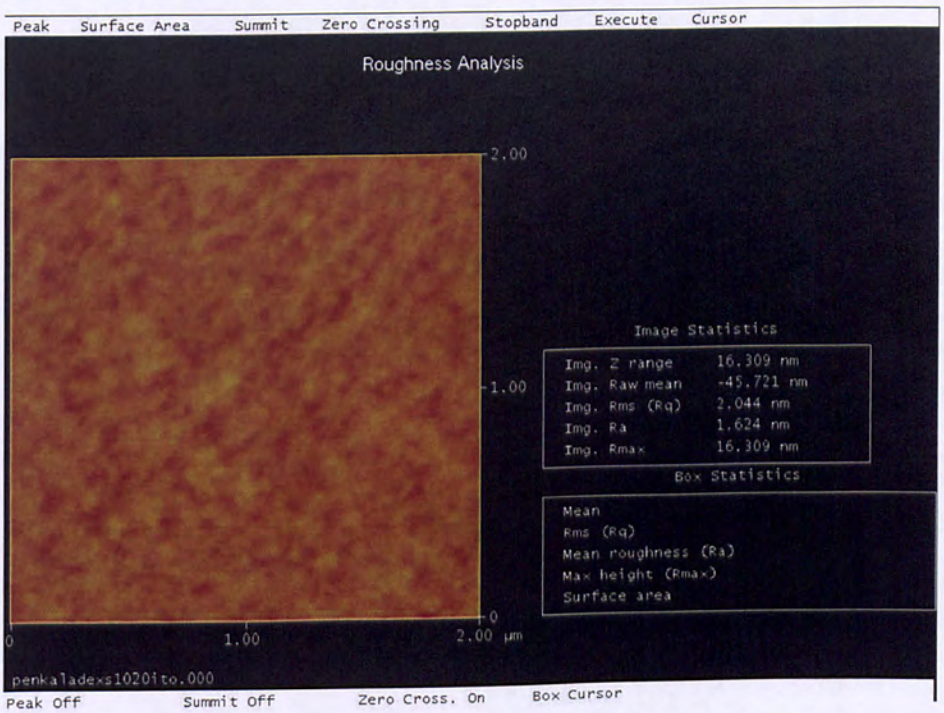

Figure 4.19: Roughness analysis of ITO surface magnetron sputtered on PEN Kaladex S1020 thin substrate.

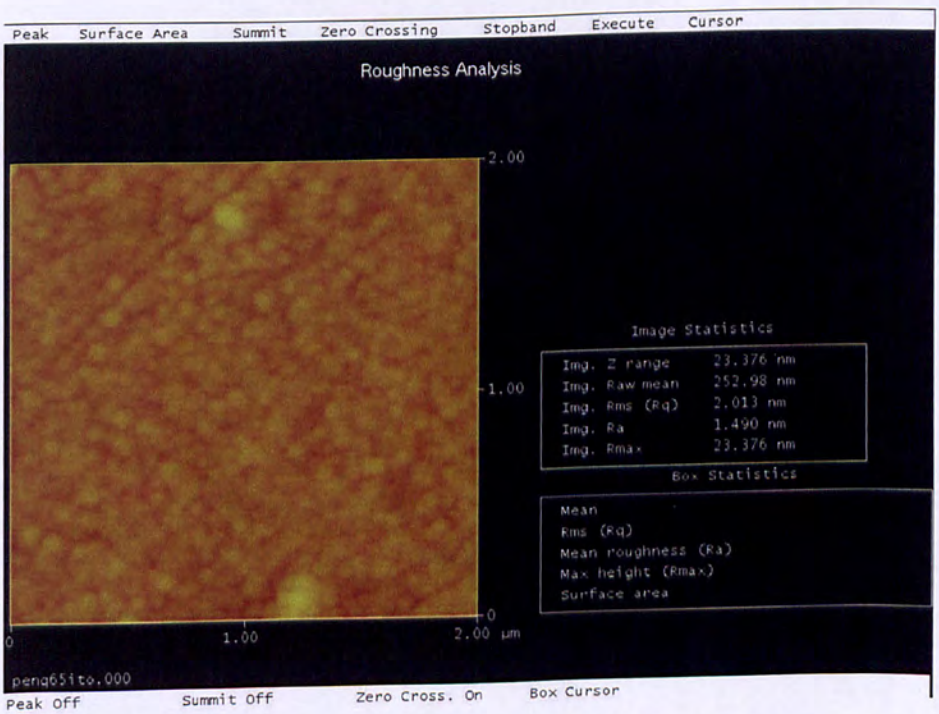

Figure 4.20: AFM surface roughness analysis image of ITO thin film deposited on PEN Teonex Q65 substrate.

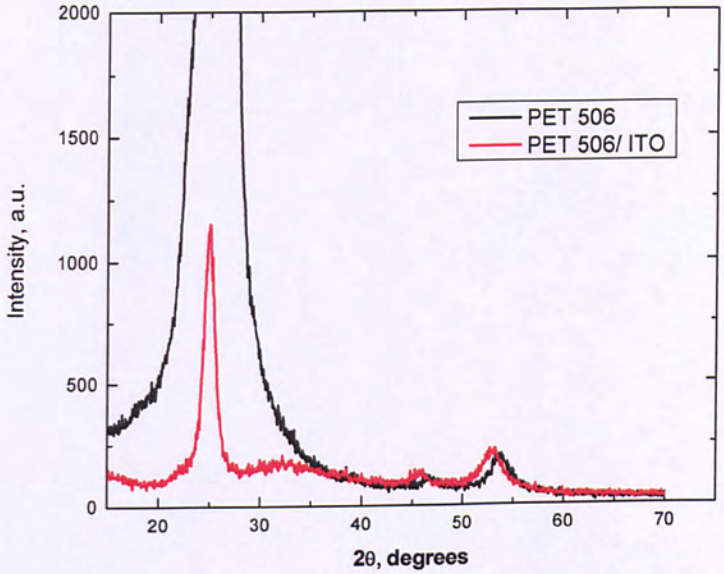

Figure 4.21: X-ray diffraction data of PET 506 substrate and PET 506/ITO composite film.

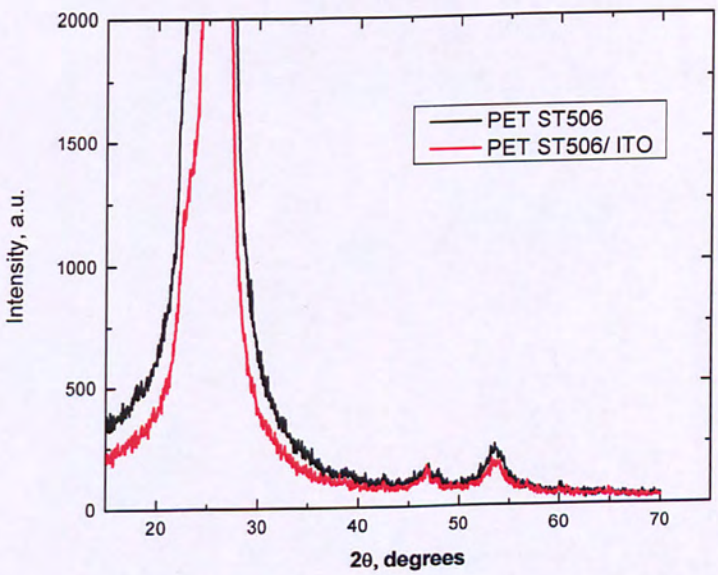

Figure 4.22: X-ray diffraction graph representing the PET ST506 substrate with and without ITO coating.

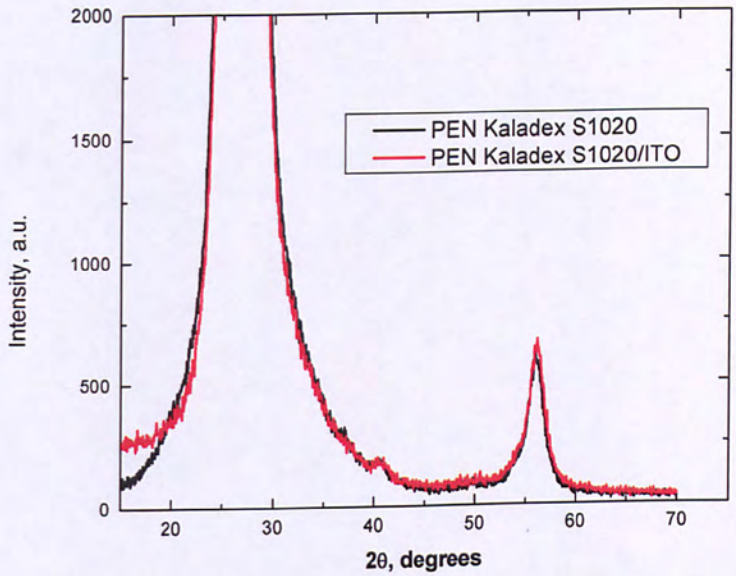

Figure 4.23: X-ray diffraction data of ITO coated and uncoated PEN Kaladex S1020 flexible substrate.

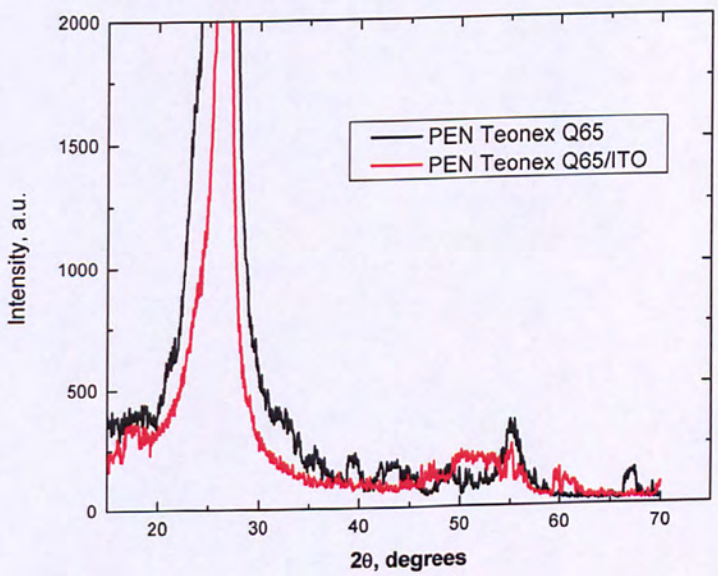

Figure 4.24: X-ray diffraction peaks associated with ITO coated and uncoated PEN Teonex Q65 flexible substrate.

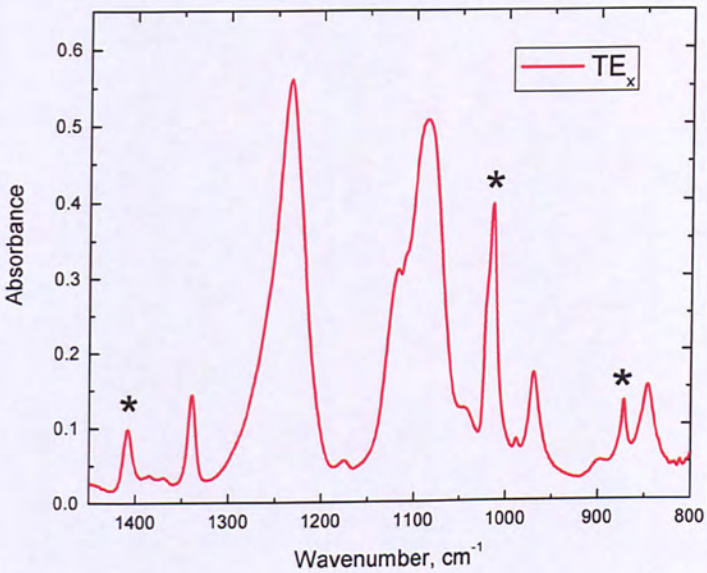

Figure 4.25: TE_x geometry FTIR – ATR spectrum obtained for the case of PET 506 substrate. The dichroic bands (1019 and 875 cm^{-1}) and the nondichroic 1410 cm^{-1} band are marked with an asterisk.

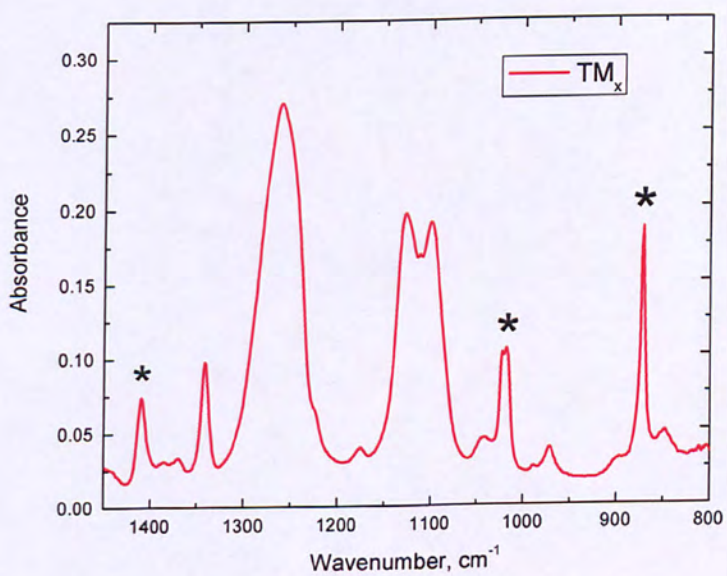

Figure 4.26: TM_x geometry FTIR – ATR spectrum obtained for the case of PET 506 substrate. The dichroic bands (1019 and 875 cm^{-1}) and the nondichroic 1410 cm^{-1} band are marked with an asterisk.

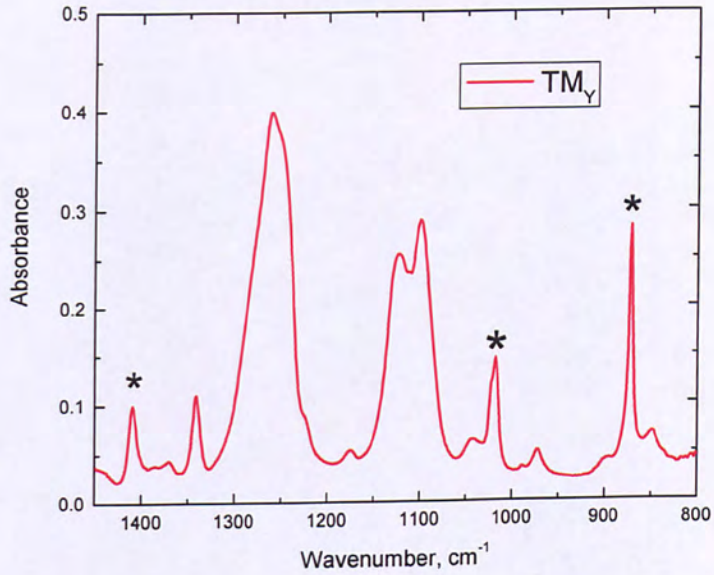

Figure 4.27: TM_y geometry FTIR – ATR spectrum obtained for the case of PET 506 substrate. The dichroic bands (1019 and 875 cm^{-1}) and the nondichroic 1410 cm^{-1} band are marked with an asterisk.

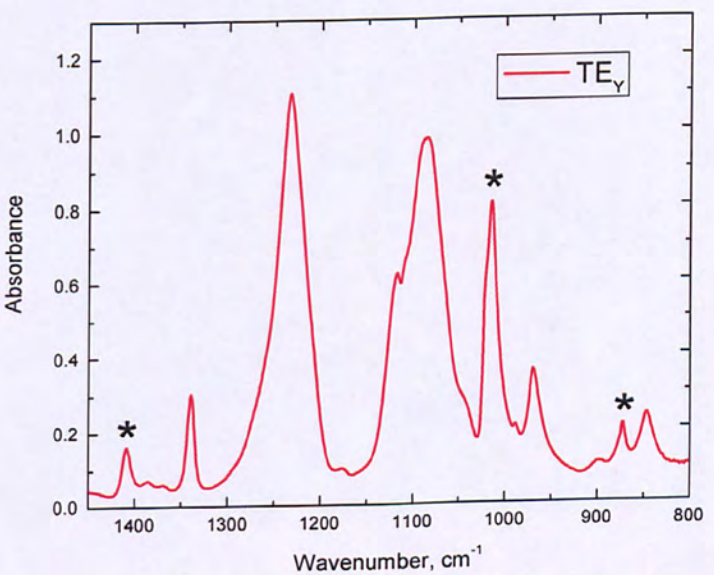

Figure 4.28: TE_y geometry FTIR – ATR spectrum obtained for the case of PET 506 substrate. The dichroic bands (1019 and 875 cm^{-1}) and the nondichroic 1410 cm^{-1} band are marked with an asterisk.

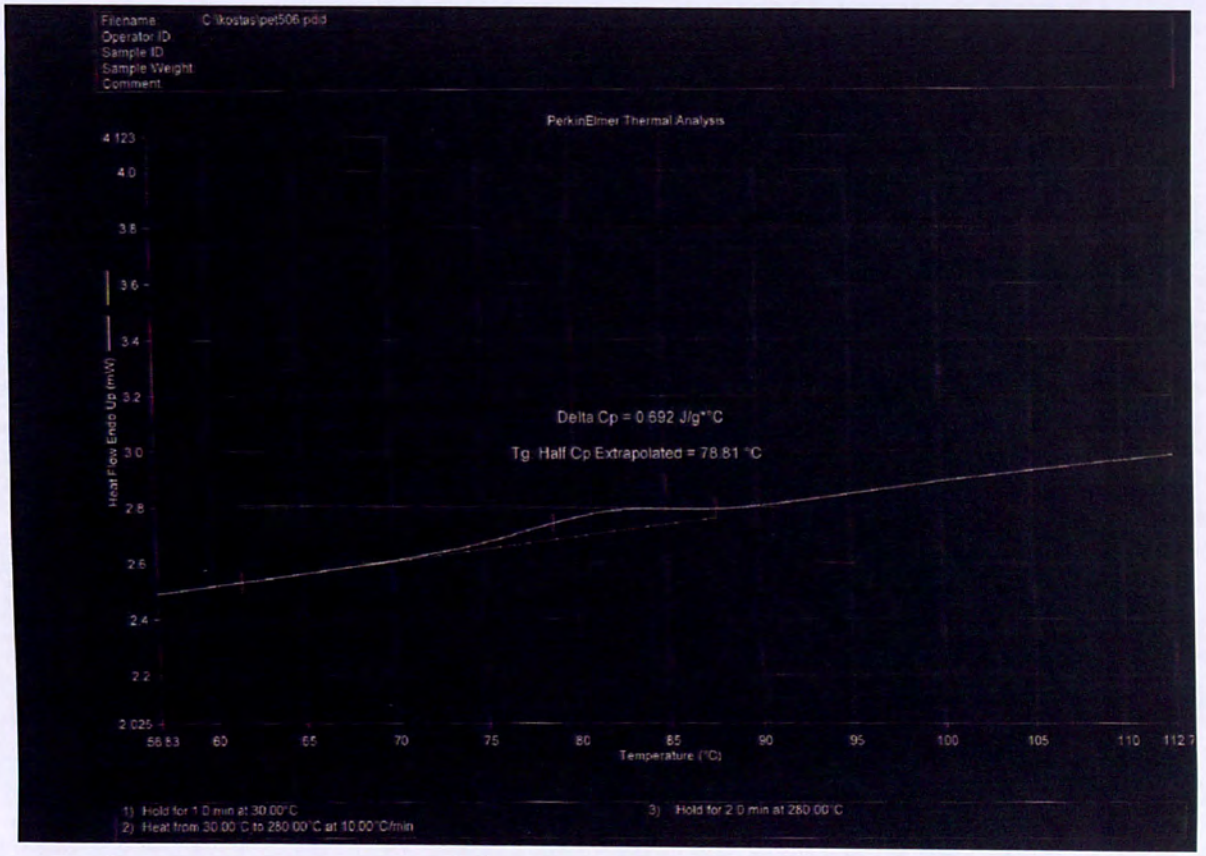

Figure 4.29: Differential scanning calorimeter graph showing the glass transition, T_g, temperature of PET 506 polyester film.

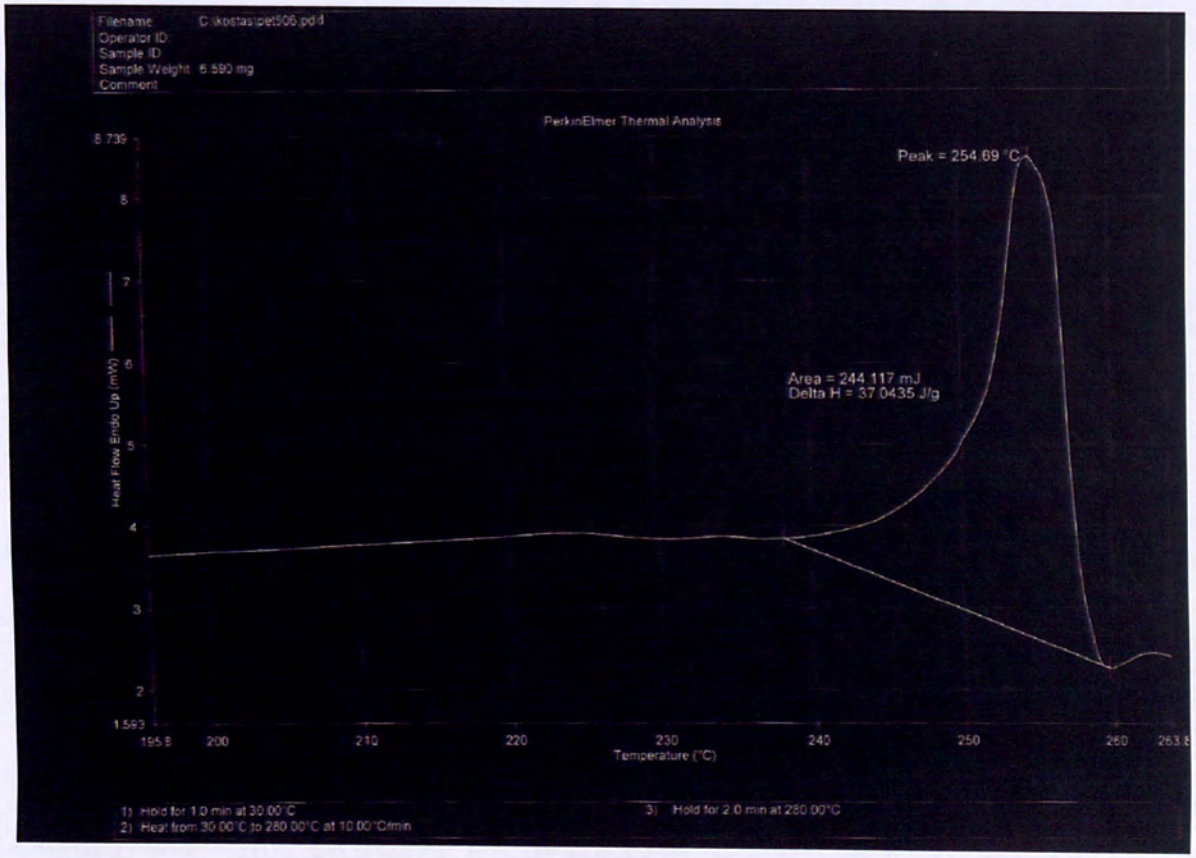

Figure 4.30: Differential scanning calorimeter graph presenting the melting peak observed for PET polyester film.

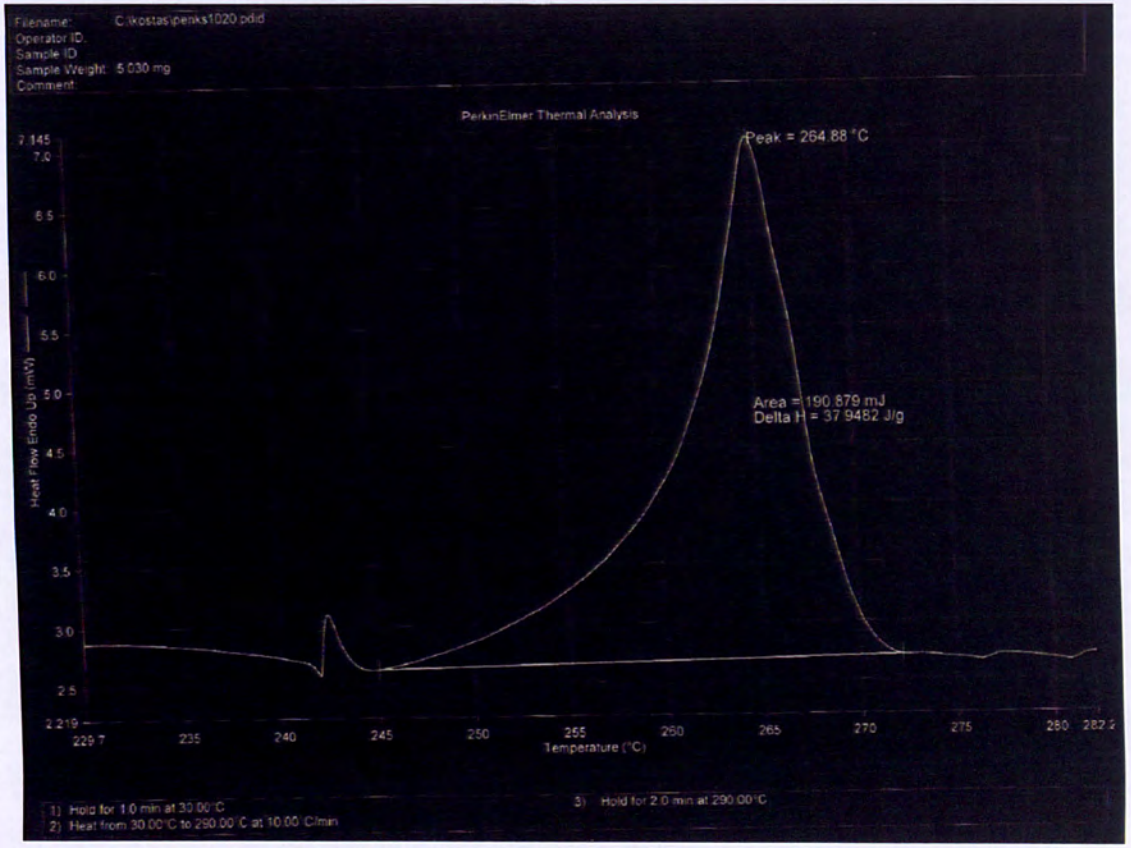

Figure 4.31: Differential scanning calorimeter graph presenting the melting peak observed for PEN Kaladex S1020 polyester film.

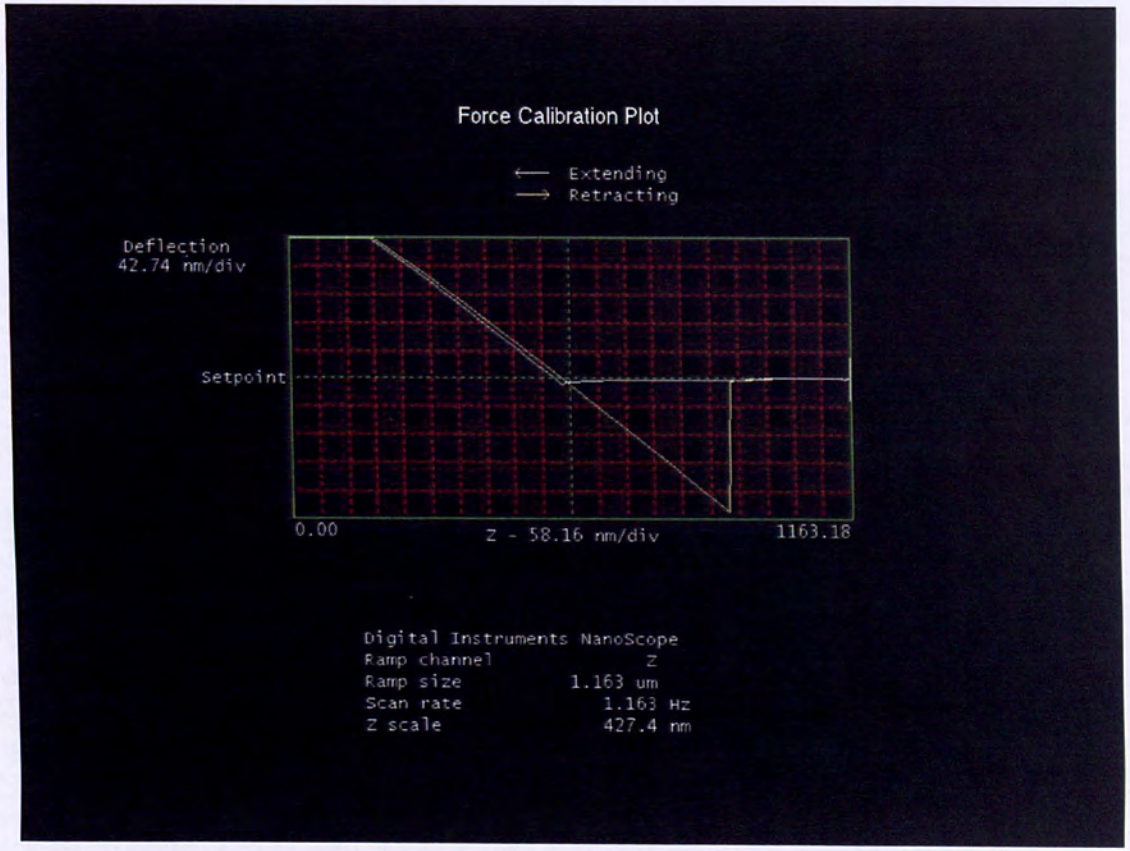

Figure 4.32: Pull off data for the case of PET ST506 flexible display bare substrate surface.

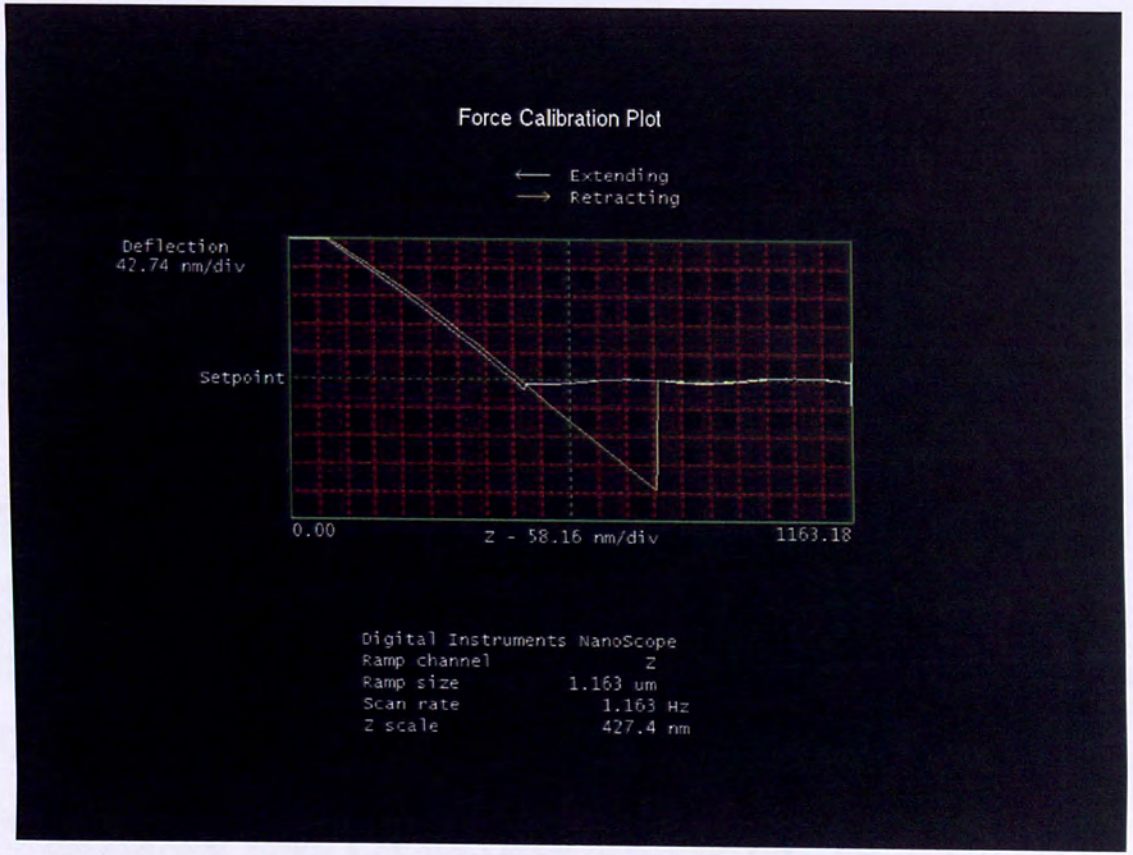

Figure 4.33: Surface adhesion measurement, using c-m AFM, for the case of PEN Kaladex S1020 flexible display film.

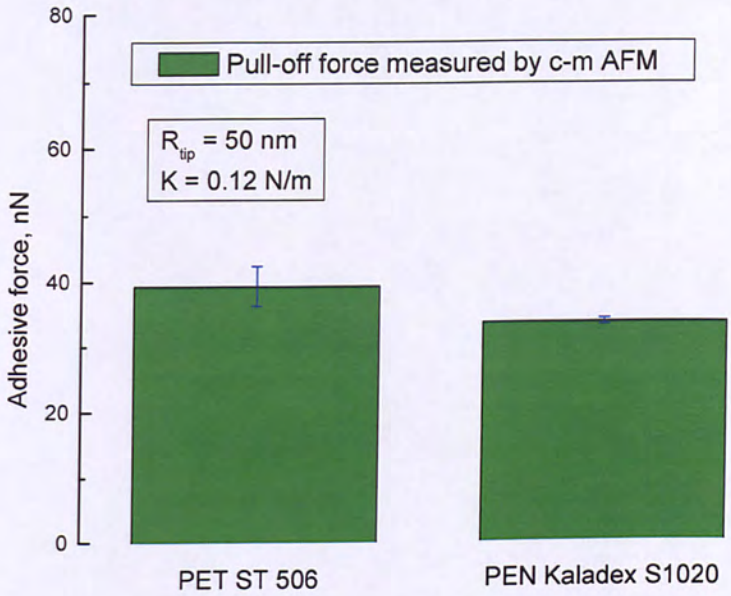

Figure 4.34: Comparison of adhesive, pull-off force, measured by c-m AFM for the case of PET ST506 and PEN Kaladex S1020 substrate. Error bars indicate the standard deviation of measured data.

Sample	*Minimum resistivity (Ω cm)*	*Maximum resistivity (Ω cm)*
ITO on PET 506	4.26×10^{-4}	4.62×10^{-4}
ITO on PET ST506	1.12×10^{-3}	1.6×10^{-3}
ITO on PEN Kaladex S1020	2.68×10^{-3}	3.11×10^{-3}
ITO on PEN Teonex Q65	1.87×10^{-3}	2.03×10^{-3}

Table 4.1: Minimum and maximum ITO resistivities measured using the four – probe system.

Sample	*Transparency (%)*
PET 506	89
PEN Kaladex S1020	85.5
ITO on PET 506	90
ITO on PEN Kaladex S1020	87

Table 4.2: Transparency measurement for ITO coated and uncoated polyester substrates.

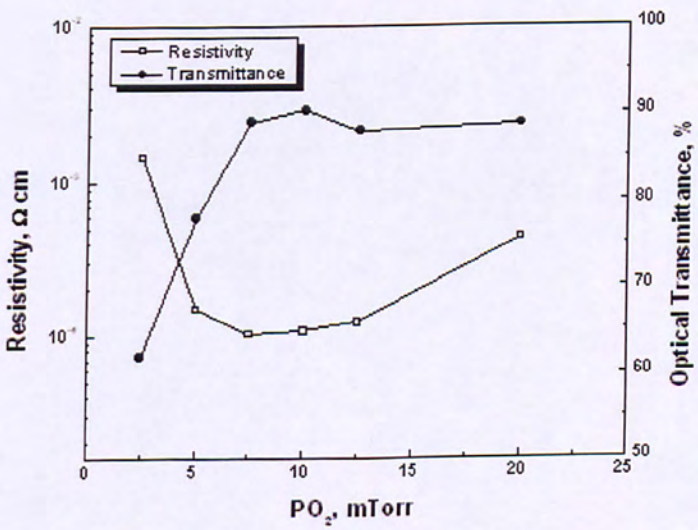

Figure 4.35: ITO resistivity and optical transmittance values for ITO deposited on PEN Kaladex S1020 by PLD at room temperature.

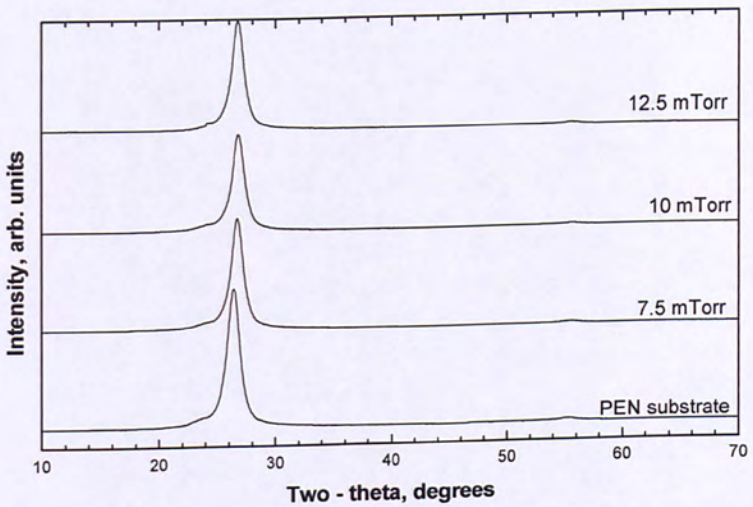

Figure 4.36: XRD diffraction patterns of bare PEN substrate and of ITO films deposited at various oxygen pressures.

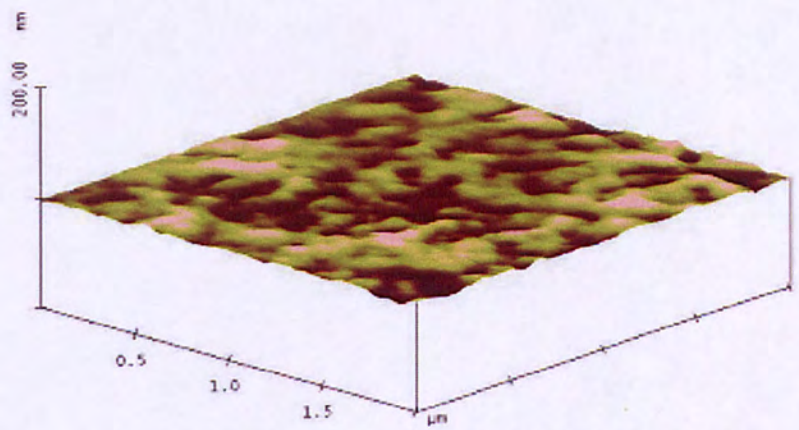

Figure 4.37: ITO layer surface morphology at 10 mTorr background pressure, as imaged by contact – mode AFM.

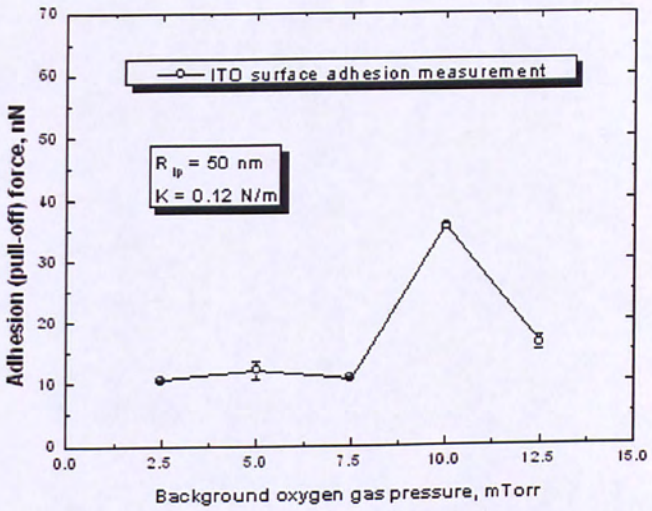

Figure 4.38: Pull – off force, as measured by c – m AFM, against oxygen pressure for ITO films deposited on PEN Kaladex S1020 at room temperature.

Appendix 5

(Figures and tables from Chapter 5)

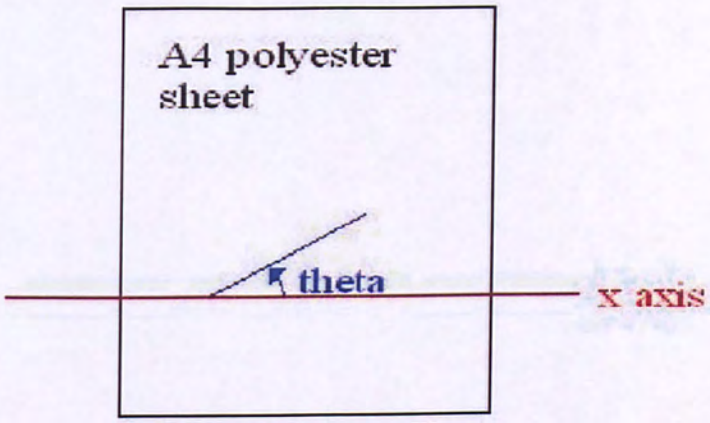

Figure 5.1: Definition of x –axis and angle θ regarding the A4 polyester biaxially oriented sheets.

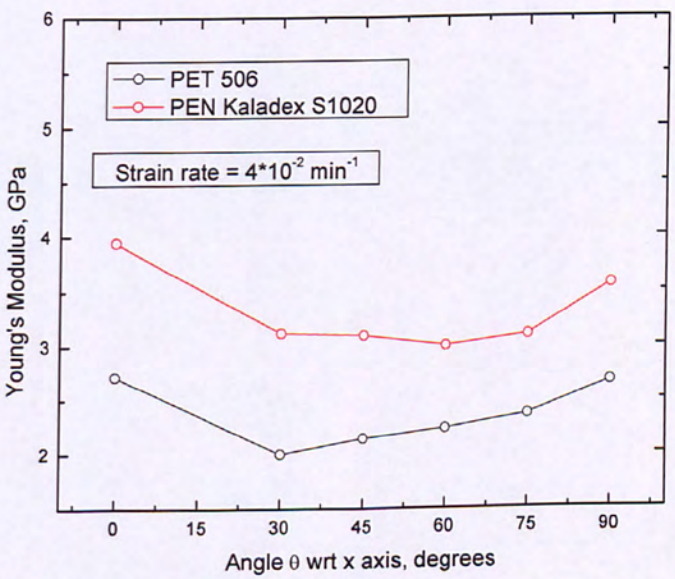

Figure 5.2: Young moduli versus angle θ, for uniaxially tensile tested PET 506 and PEN Kaladex S1202 bare substrates.

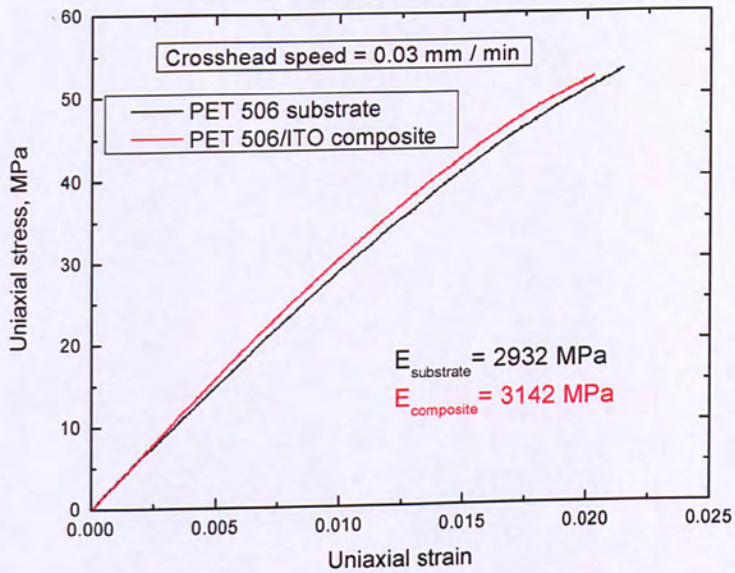

Figure 5.3: Tensile testing of ITO coated and uncoated PET 506 substrates tested at 0.03 mm / min crosshead speed.

Sample	*Coating elastic modulus (GPa)*
ITO on PET 506	220 GPa
ITO on PET ST506	215 GPa
ITO on PEN Kaladex S1020	180 GPa
ITO on PEN Teonex Q65	175 GPa

Table 5.1: ITO, on different polyester substrates, elastic modulus as calculated using the rule of mixtures (These values are only indicative).

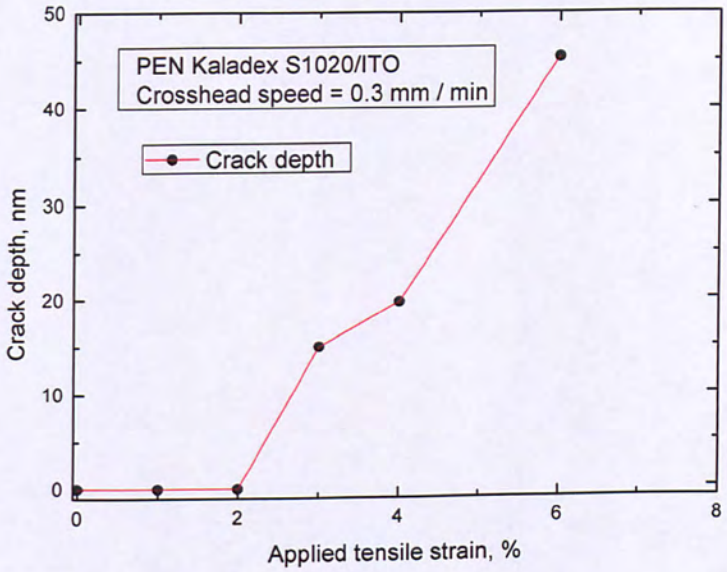

Figure 5.4: Ex-situ experimentally measured, by c-m AFM, non-recovered ITO, on PEN Kaladex S1020 crack depth versus applied uniaxial tensile strain.

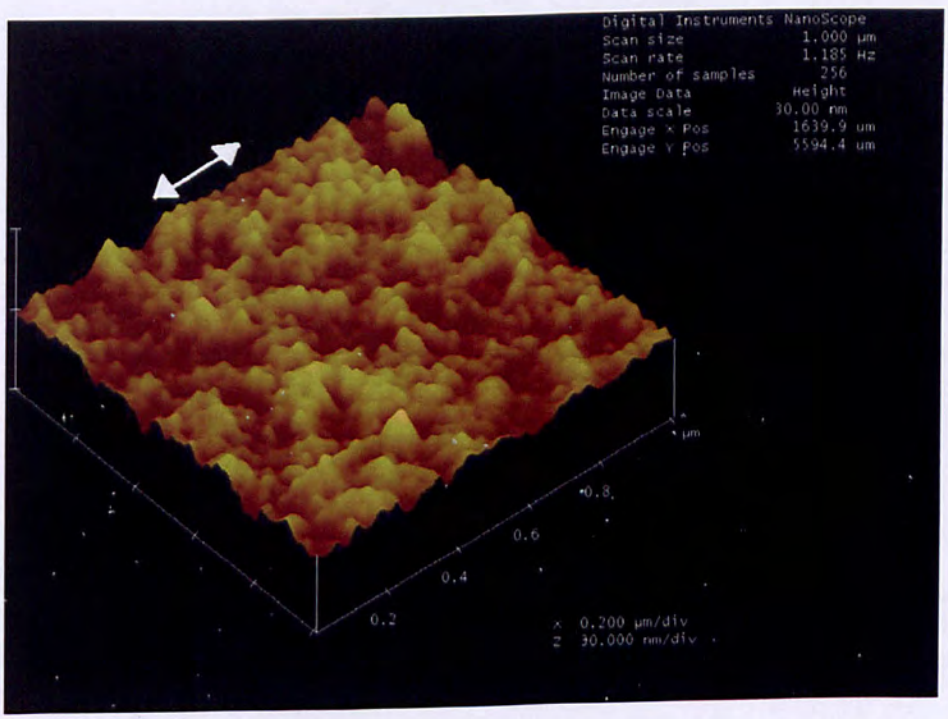

Figure 5.5: ITO on PEN Kaladex S1020 c-m AFM image, 1µm^2 area, when a 2 % uniaxial tensile strain is applied (white arrows indicate the tensile direction).

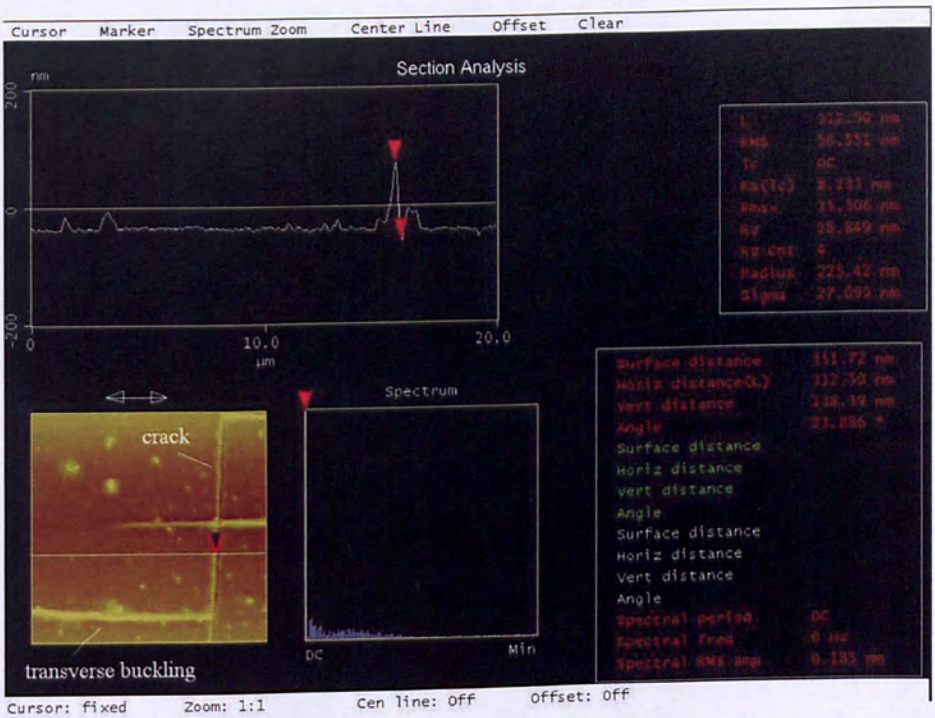

Figure 5.6: ITO on PEN Kaladex S1020, ex-situ, c-m AFM image and cross-section showing a recovered crack and transverse buckling formation. The applied uniaxial tensile strain is 3 %.

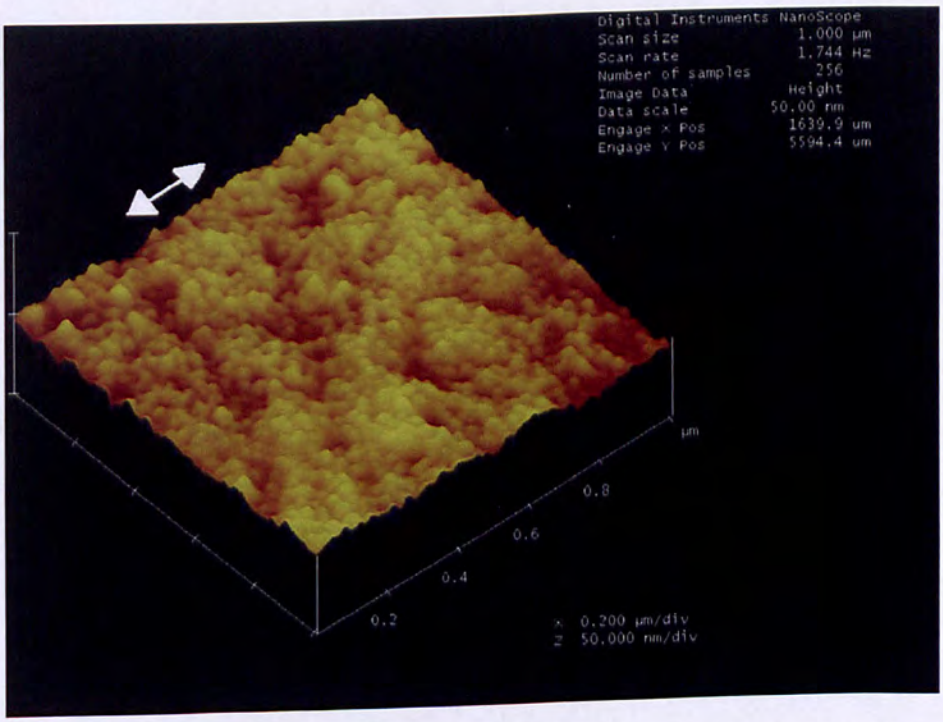

Figure 5.7: ITO intact surface on PEN Kaladex S1020 c-m AFM image, 1µm^2 area, when a 4 % uniaxial tensile strain is applied (white arrows indicate the tensile direction).

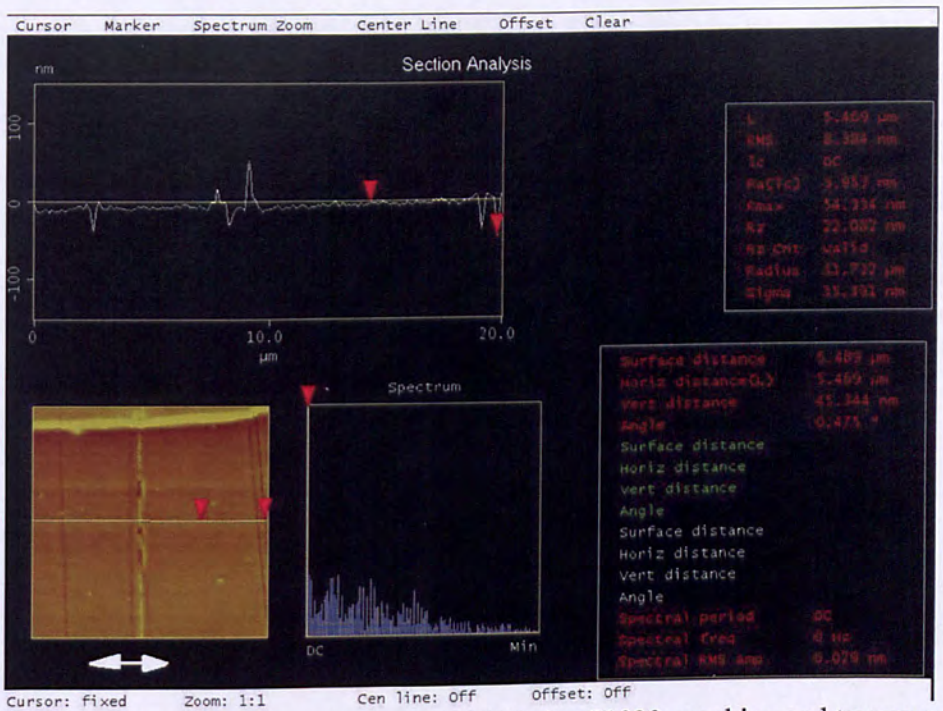

Figure 5.8: ITO surface, deposited on PEN Kaladex S1020, cracking and transverse buckling formation as imaged by c-m AFM. Applied tensile strain is 6 % in this case (arrows indicate tensile force direction).

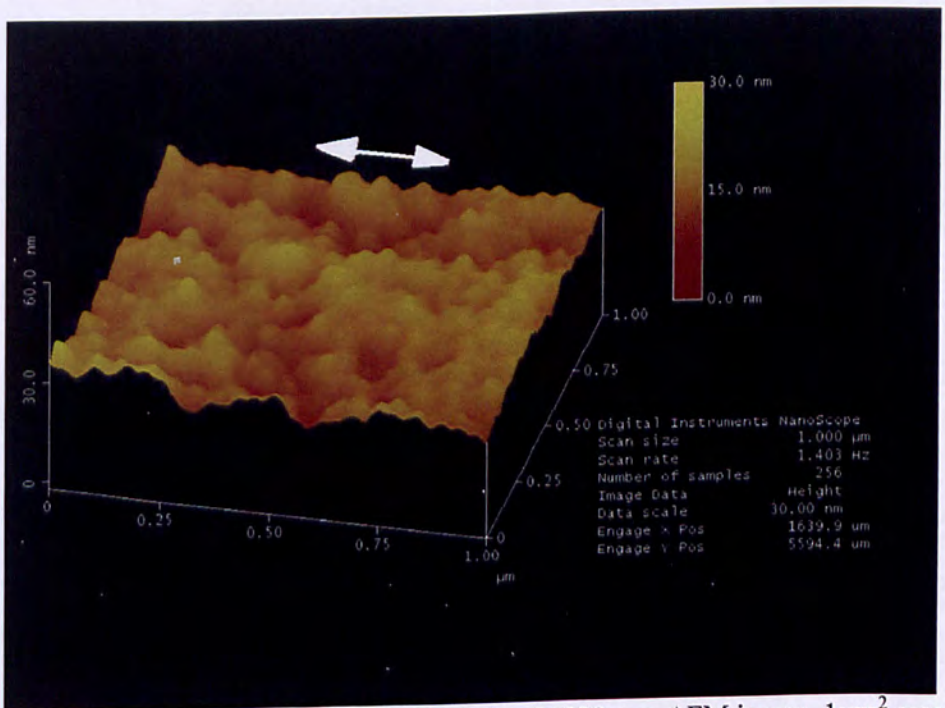

Figure 5.9: ITO intact surface on PEN Kaladex S1020 c-m AFM image, 1µm^2 area, when a 6 % uniaxial tensile strain is applied (white arrows indicate the tensile direction).

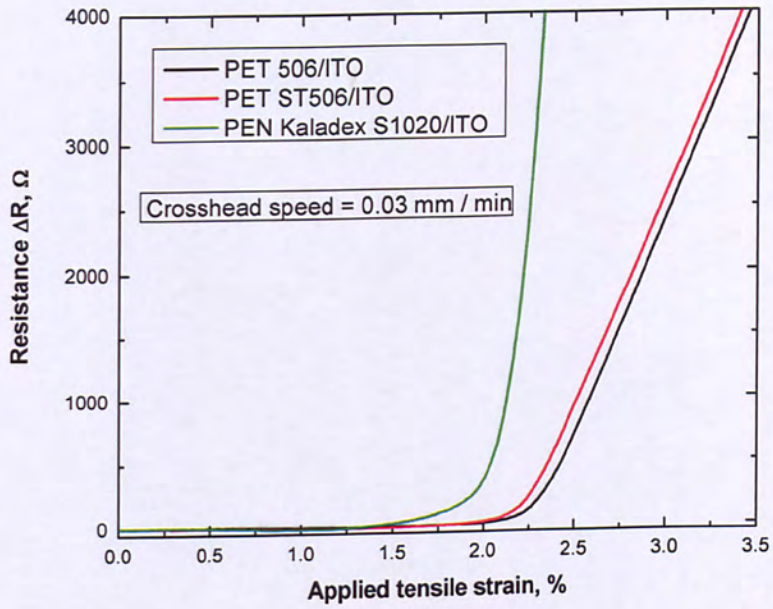

Figure 5.10: Resistance versus applied tensile strain, for ITO films deposited on different polyester substrates, at a crosshead speed of 0.03 mm / min.

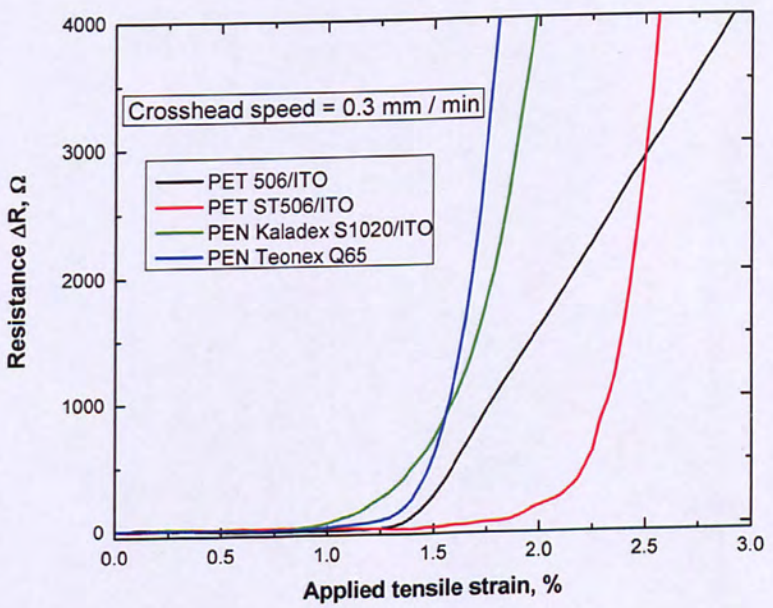

Figure 5.11: Resistance against applied tensile strain, for ITO films deposited on different polyester substrates, for 0.3 mm / min crosshead speed.

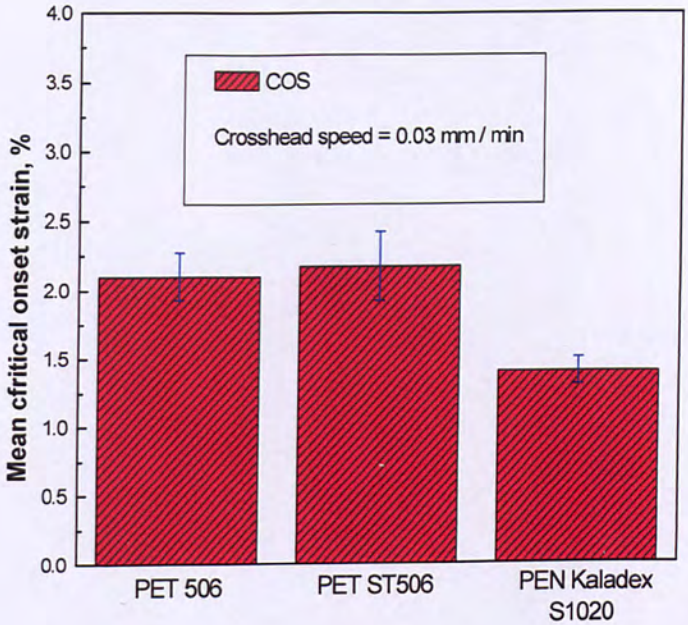

Figure 5.12: Mean values of critical onset strain for ITO conductive failure, at a crosshead speed of 0.03 mm / min, considering different polyester flexible substrates.

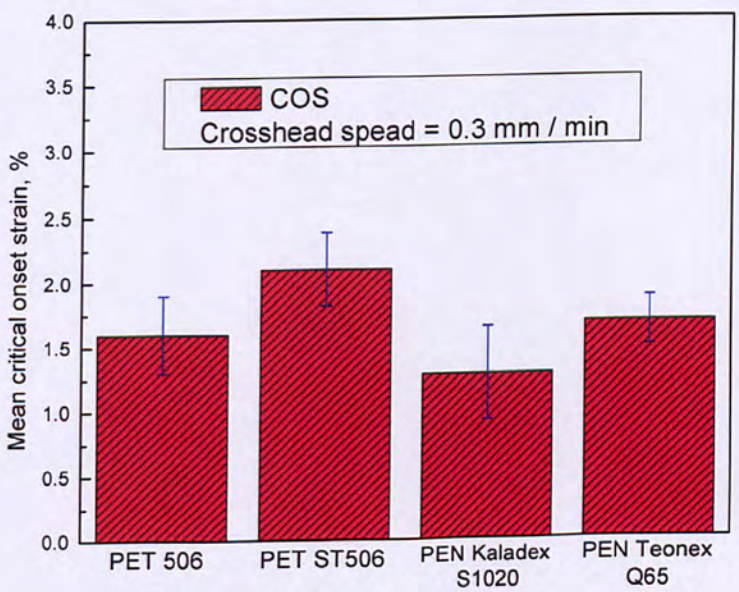

Figure 5.13: Mean values of critical onset strain for ITO conductive failure, at a crosshead speed of 0.3 mm / min, considering the effect of different polyester display substrates.

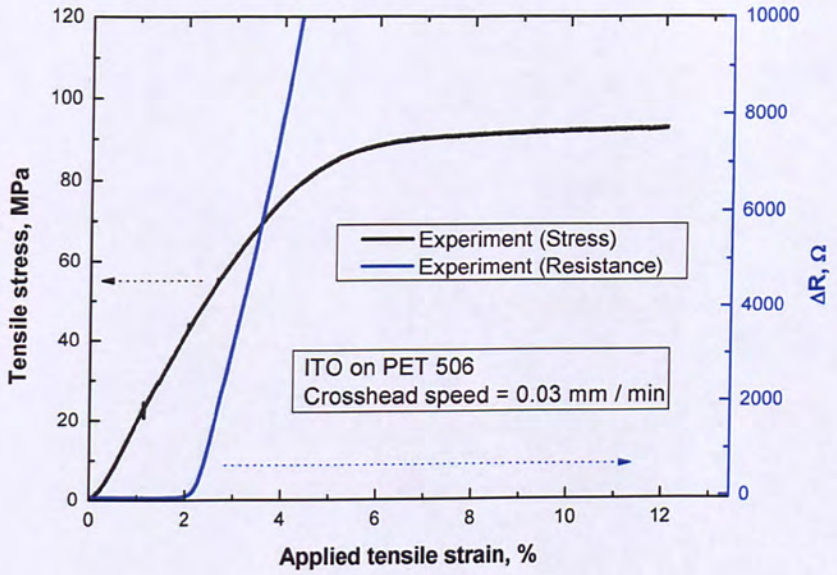

Figure 5.14: Typical electro-mechanical graph of ITO on PET 506 tensile tested to 12% strain at a crosshead speed of 0.03 mm / min.

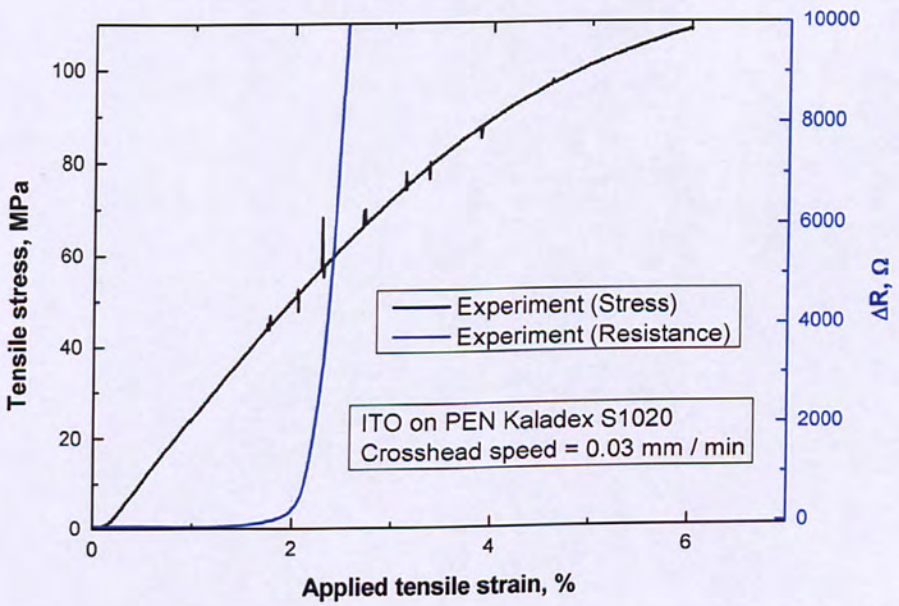

Figure 5.15: Stress – strain curve for composite PEN Kaladex S1020/ITO thin film anode, combined with electrical resistance in-situ monitoring, strained till 6% at 0.03 mm / min crosshead speed.

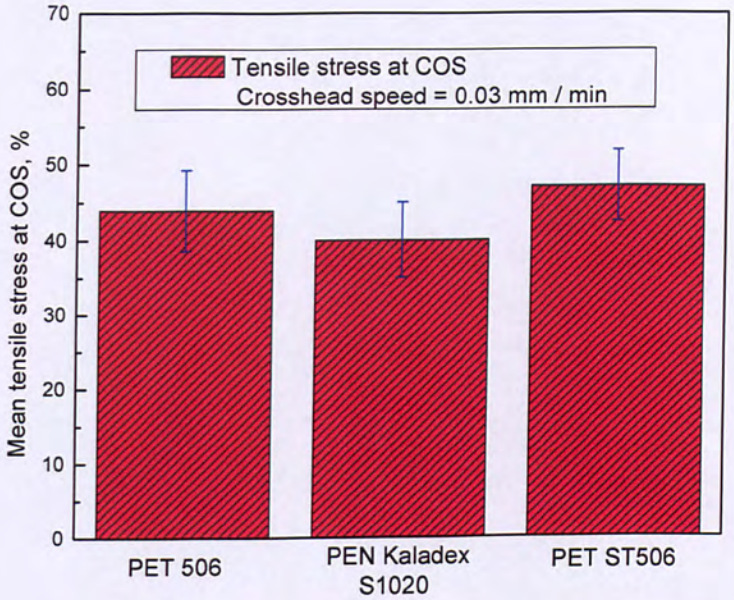

Figure 5.16: Mean tensile stress values corresponding to the critical onset strain for different base substrates and same crosshead speed of 0.03 mm / min.

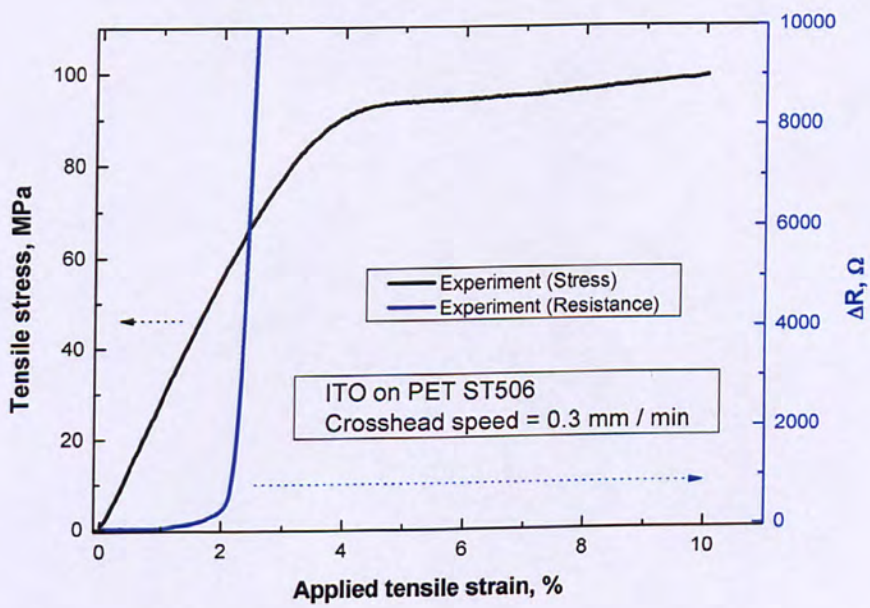

Figure 5.17: Typical electro-mechanical graph showing the behaviour of an ITO/PET ST 506 flexible display anode strained till 10% at 0.3 mm / min crosshead speed.

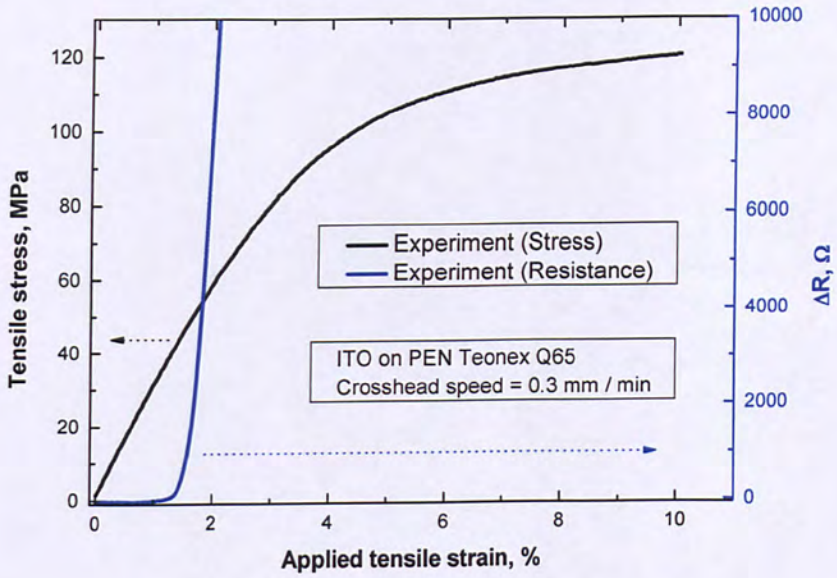

Figure 5.18: Typical electro-mechanical response of ITO coated PEN Teonex Q65 flexible display component strained till 10% at 0.3 mm / min crosshead speed.

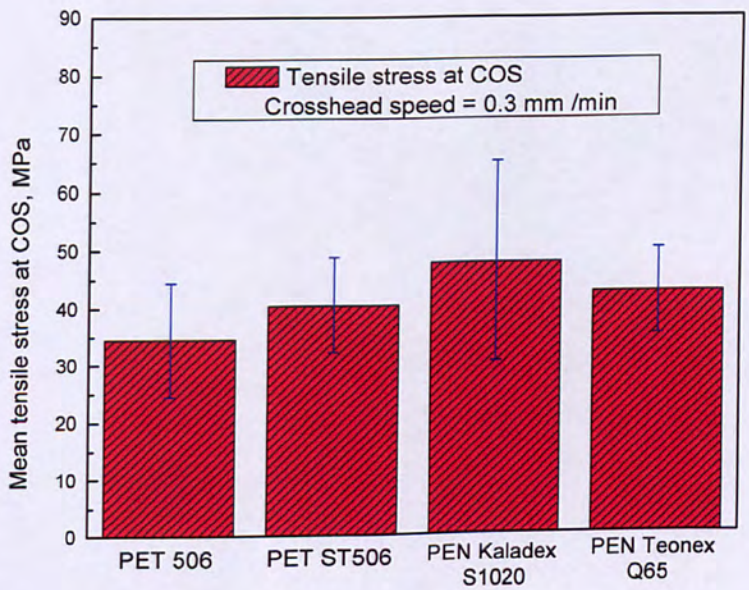

Figure 5.19: Mean tensile stress values corresponding to critical onset strain values for different substrates tensile tested at 0.3 mm /min crosshead speed.

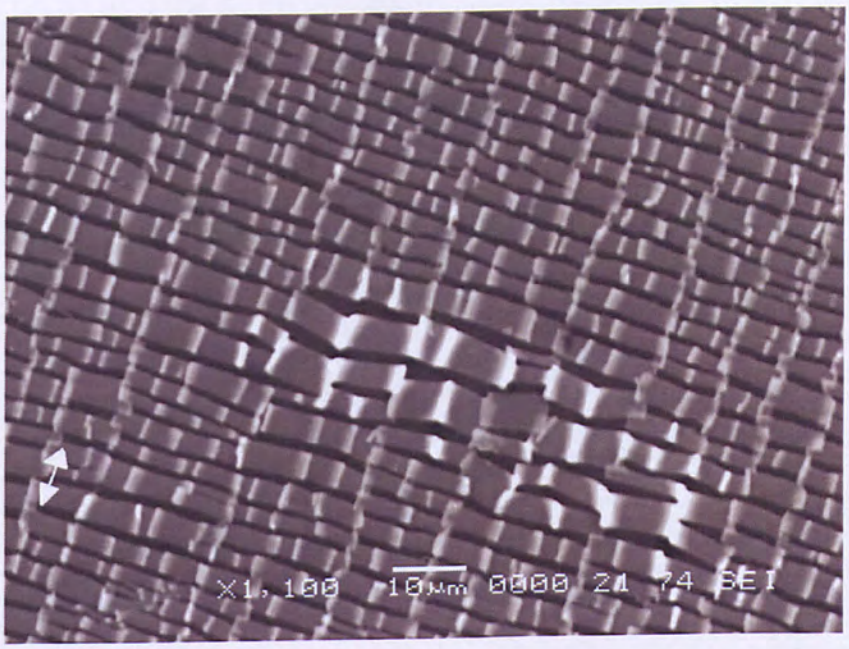

Figure 5.20: SEM image of an ITO surface deposited on PET ST506 substrate strained at 75 % for 1.5 mm / min crosshead speed (white arrows indicate straining direction).

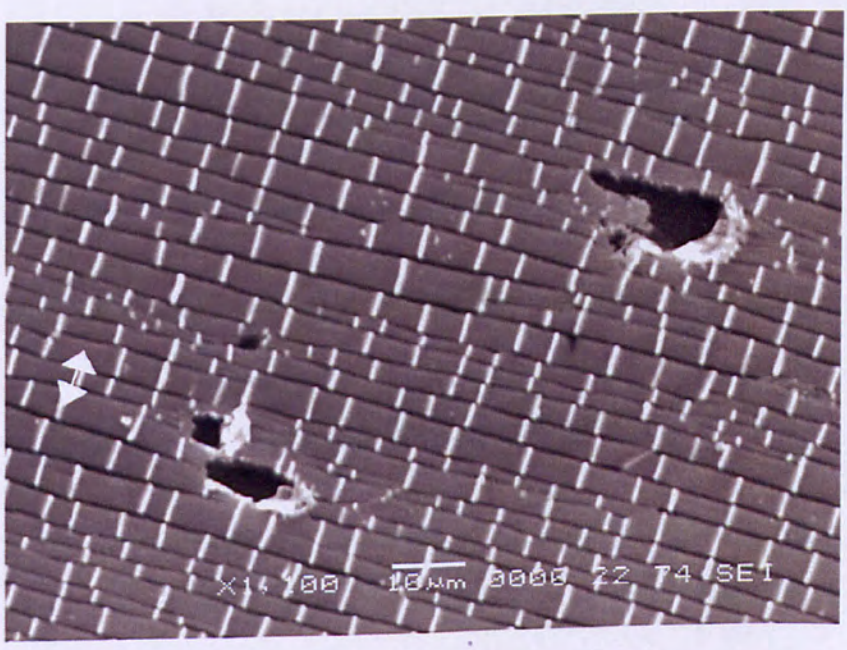

Figure 5.21: SEM micrograph of an ITO surface sputtered on PEN Kaladex S1020 substrate strained at 35 % for 1.5 mm / min crosshead speed (white arrows indicate the straining direction).

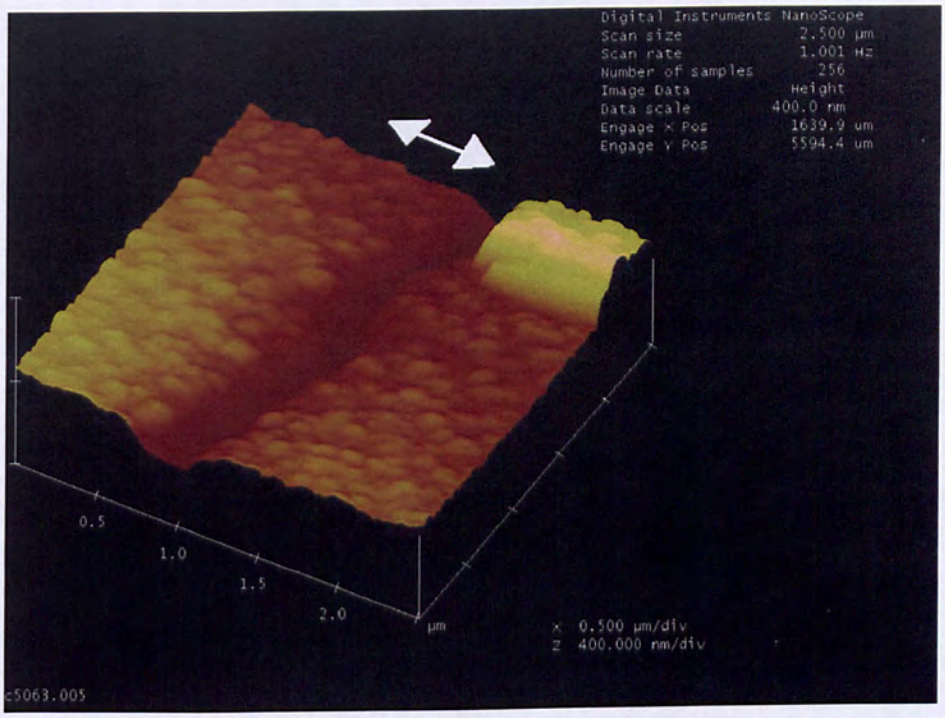

Figure 5.22: 3D c-m AFM image showing an ITO, on PET 506, crack morphology and part of a buckling pattern. The sample was strained up to 40 % with 1 mm / min crosshead speed (arrows indicate tensile direction).

Figure 5.23: ITO crack cross – sectional view. The surface is the same as in figure 5.22.

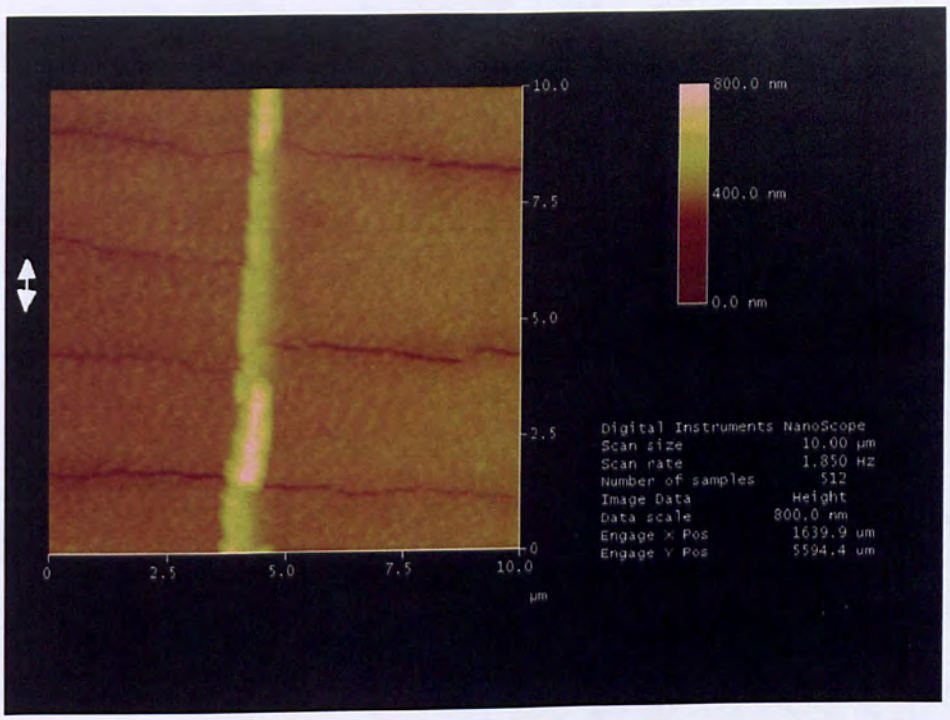

Figure 5.24: Contact – mode AFM image of an ITO surface deposited on PET 506 flexible substrate. The sample was strained till 20% at 0.3 mm / min crosshead speed (white arrows indicate direction of uniaxial tensile force).

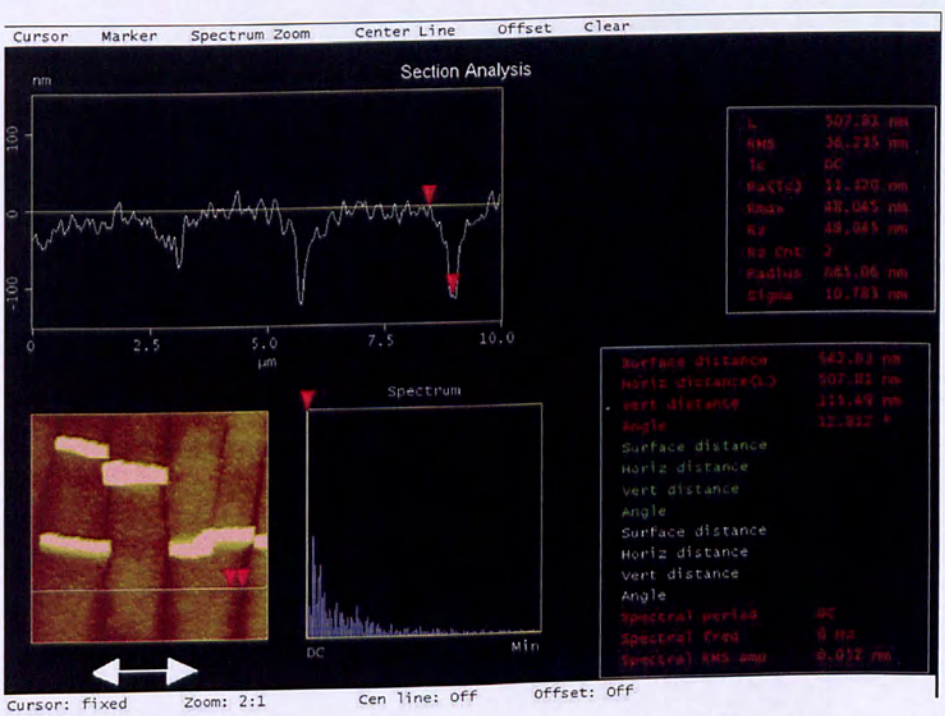

Figure 5.25: Crack cross –sectional view of ITO, on PET 506, obtained by using c-m AFM. The sample was uniaxially tensile strained till 30% at 0.3 mm / min crosshead speed.

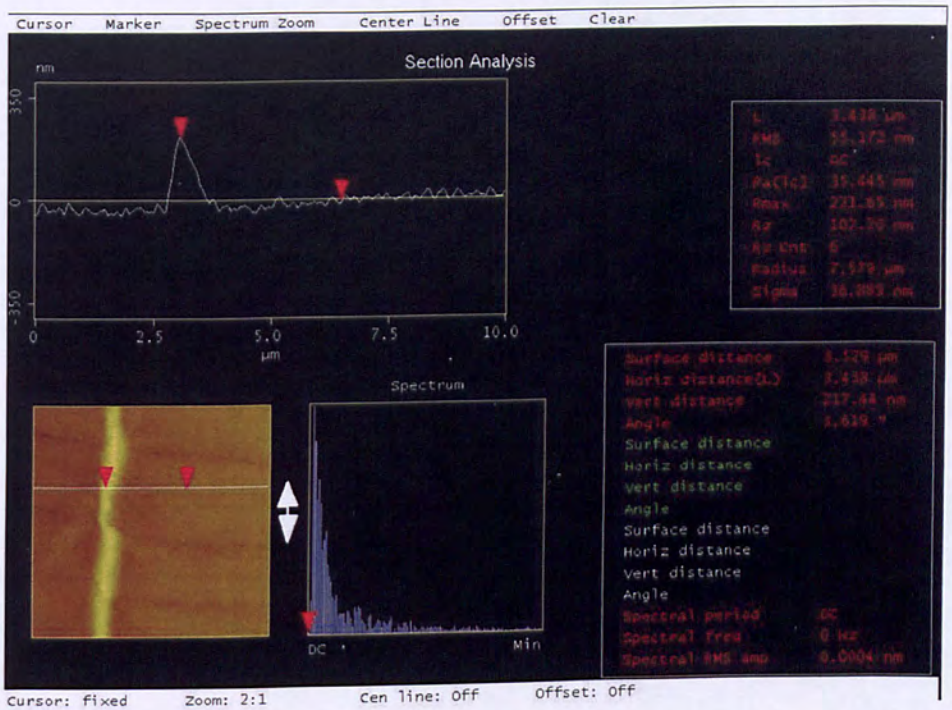

Figure 5.26: Cross – sectional AFM view of a buckled zone for an ITO on PET ST506 sample strained to 10% at 0.3 mm / min speed (white arrows indicate tensile force direction).

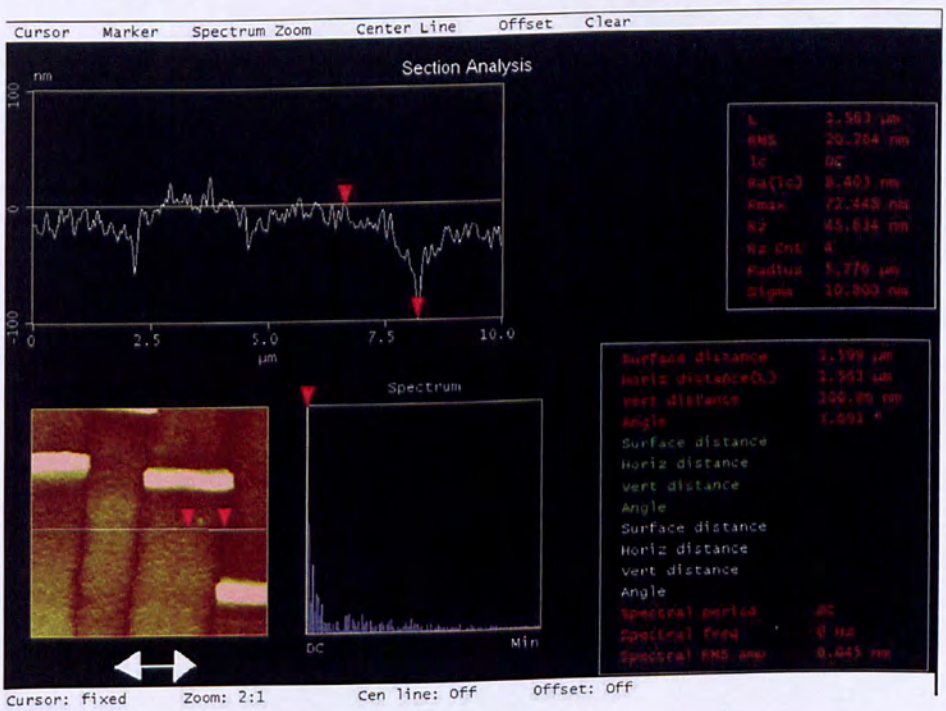

Figure 5.27: Crack formation cross – section as imaged by using c-m AFM for an ITO, sputtered on PET ST506, strained till 20% at 0.3 mm / min crosshead speed.

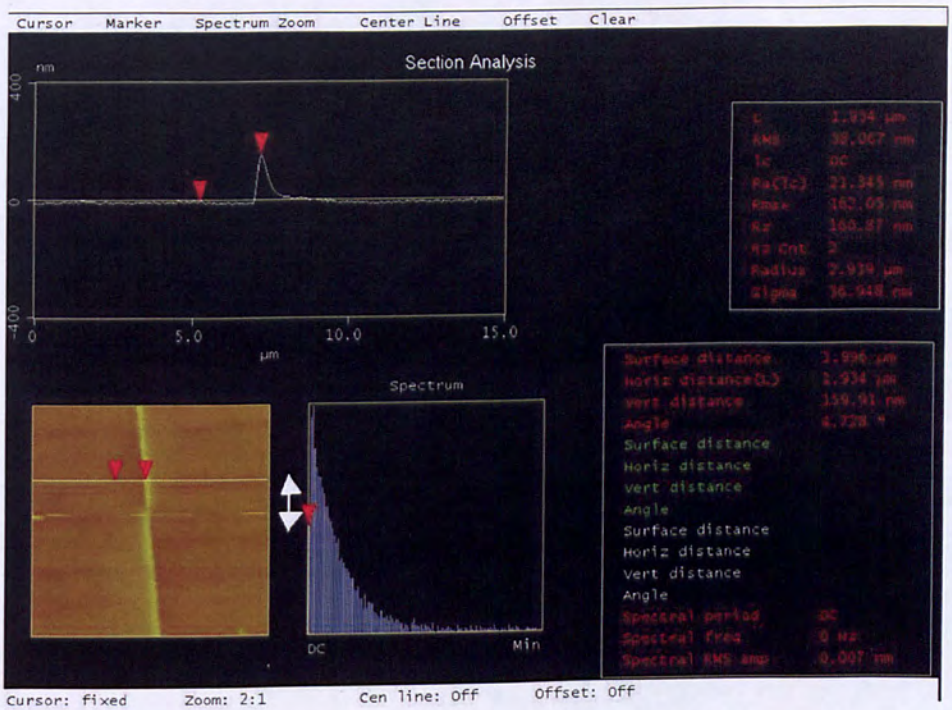

Figure 5.28: Buckling zone cross – section obtained by c-m AFM for an ITO deposited on PEN Kaladex S1020 sample tested under uniaxial tension to 12% strain at 0.03 mm / min speed (white arrows indicate tensile force direction).

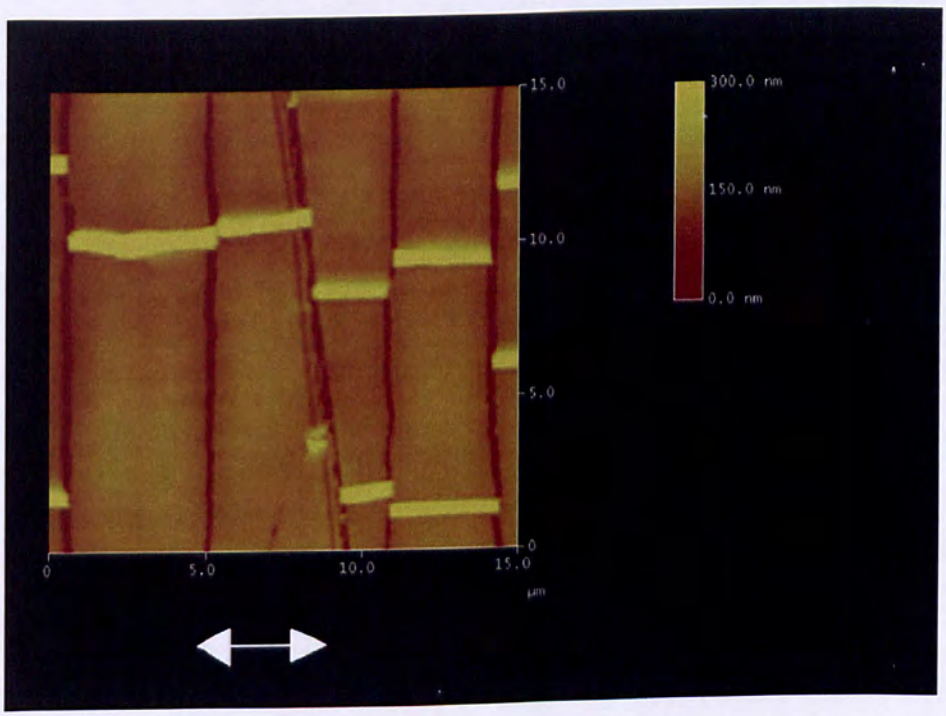

Figure 5.29: Cracking and buckling zone formation, as observed by c-m AFM, of ITO on PEN Kaladex S1020 strained till 30% at 0.03 mm / min crosshead speed.

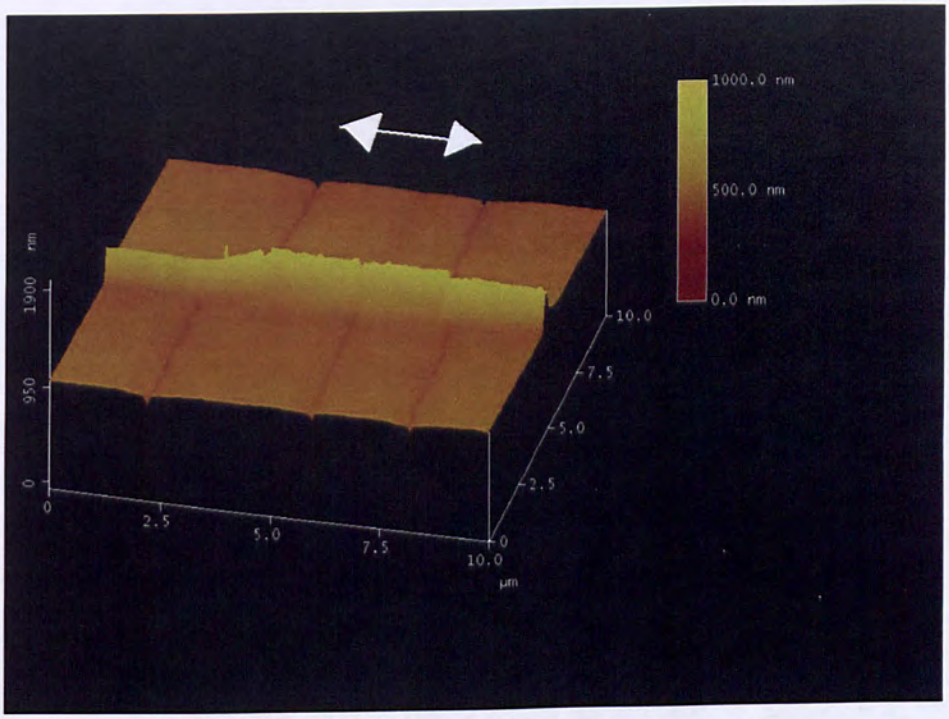

Figure 5.30: 3D contact mode AFM image showing cracking and transverse buckle zone formation for an ITO on PEN Teonex Q65 sample uniaxially strained till 20% at 0.3 mm / min speed (white arrows indicate tensile testing direction).

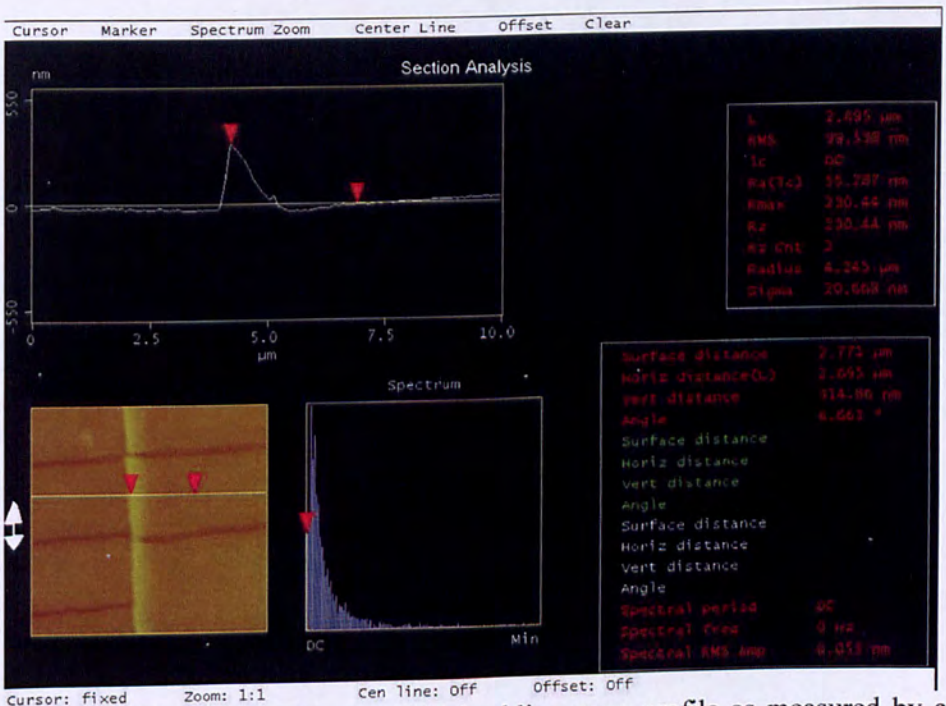

Figure 5.31: ITO on PEN Teonex Q65 buckling zone profile as measured by c-m AFM. The sample was strained till 30% of uniaxial strain at a 0.3 mm / min crosshead speed.

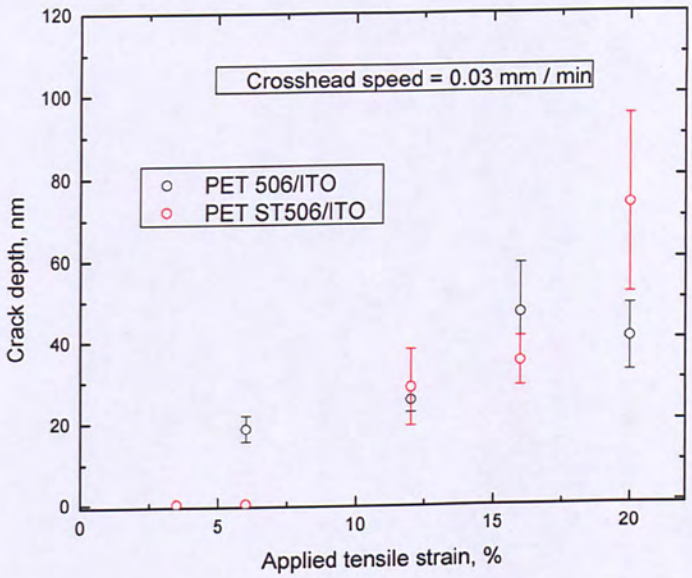

Figure 5.32: ITO coating crack depth, as measured by c-m AFM, against applied uniaxial tensile strain for different PET substrates at 0.03 mm / min speed.

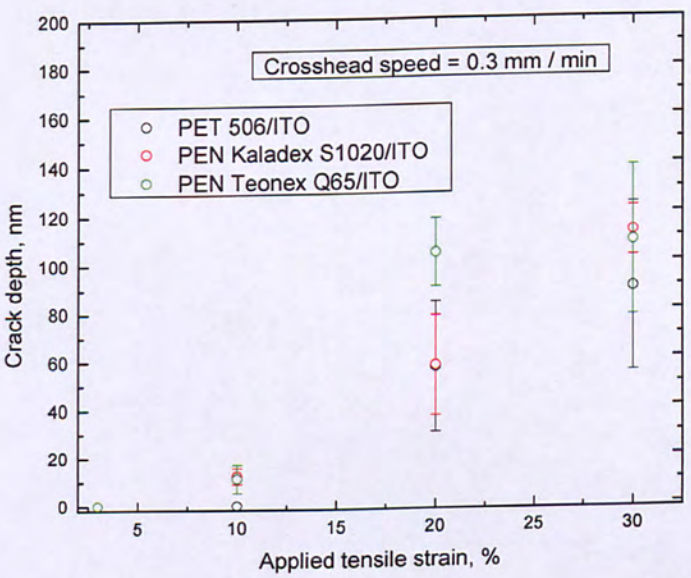

Figure 5.33: Crack depth of ITO coatings deposited on various polyester substrates as measured by c-m AFM. The crosshead speed is 0.3 mm /min.

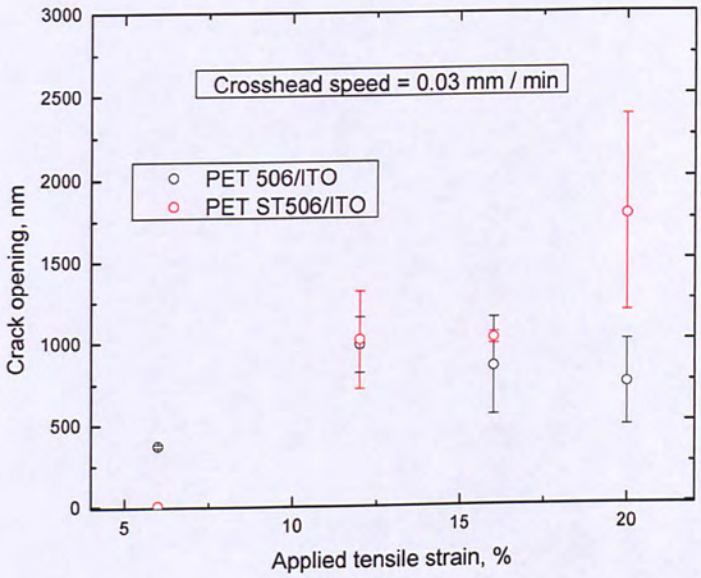

Figure 5.34: ITO crack opening, as measured by c-m AFM, for 0.03 mm /min speed and different PET substrates.

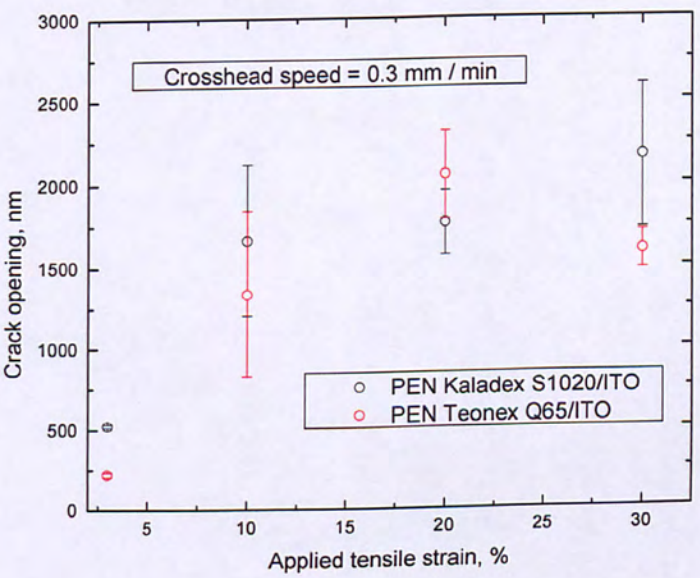

Figure 5.35: AFM measured crack opening of ITO coatings, on different PEN substrates, strained at 0.3 mm / min speed.

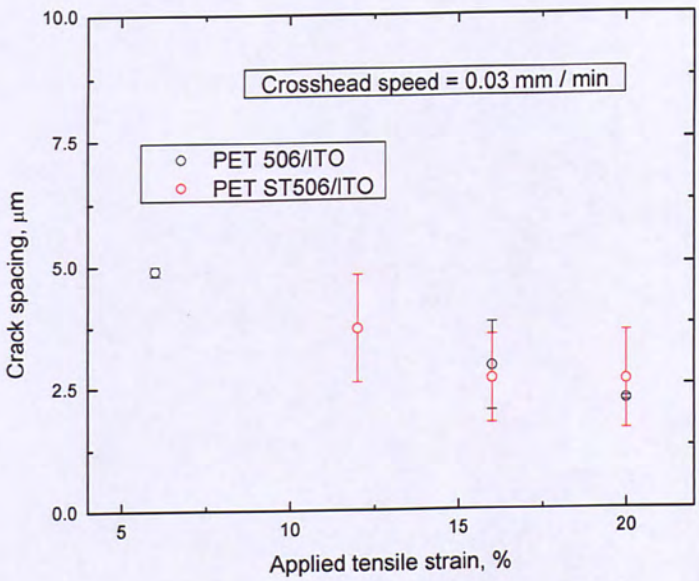

Figure 5.36: Distance of neighboring ITO cracks deposited on two different PET substrates as a function of applied uniaxial strain. The crosshead speed is 0.03 mm /min.

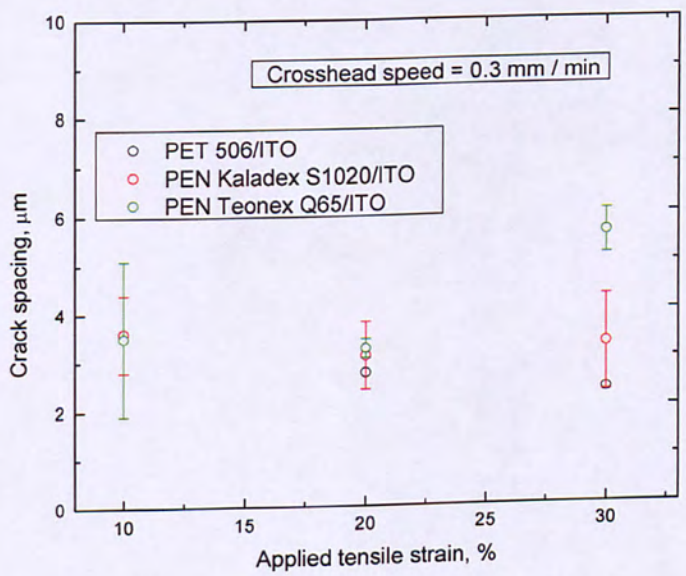

Figure 5.37: ITO crack spacing deposited on different PET and PEN substrates against applied tensile uniaxial strain. The crosshead speed is 0.3 mm /min.

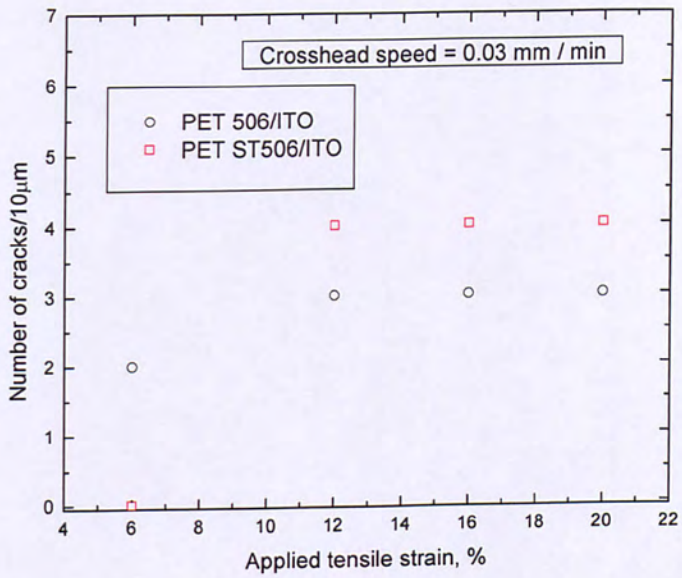

Figure 5.38: Number of ITO, on different PET substrates, cracks per 10 microns as a function of applied strain. The crosshead speed is 0.03 mm /min.

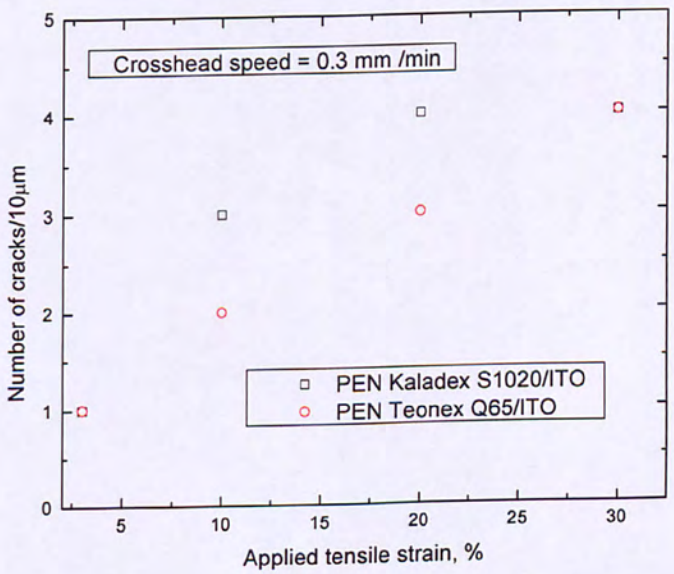

Figure 5.39: Number of ITO, on different PEN substrates, cracks against uniaxial tensile strain. The crosshead speed is 0.3 mm /min.

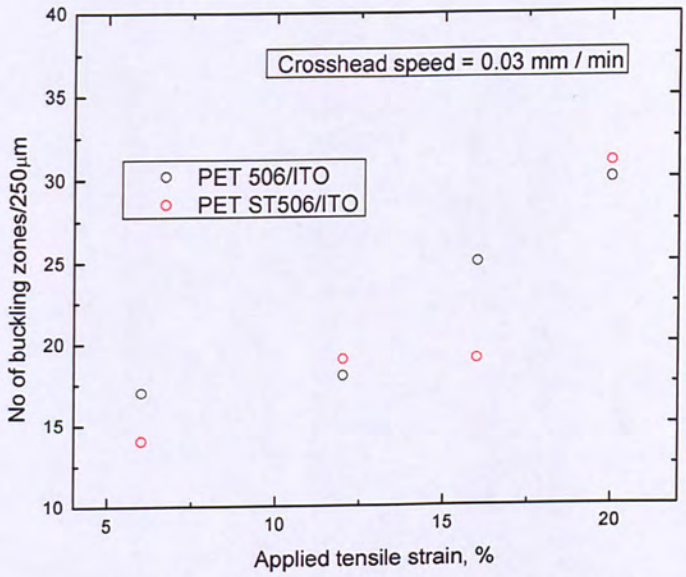

Figure 5.40: Number of transverse ITO, on different PET substrates, buckling zones per 250 microns against applied tensile strain. Crosshead speed is 0.03 mm / min.

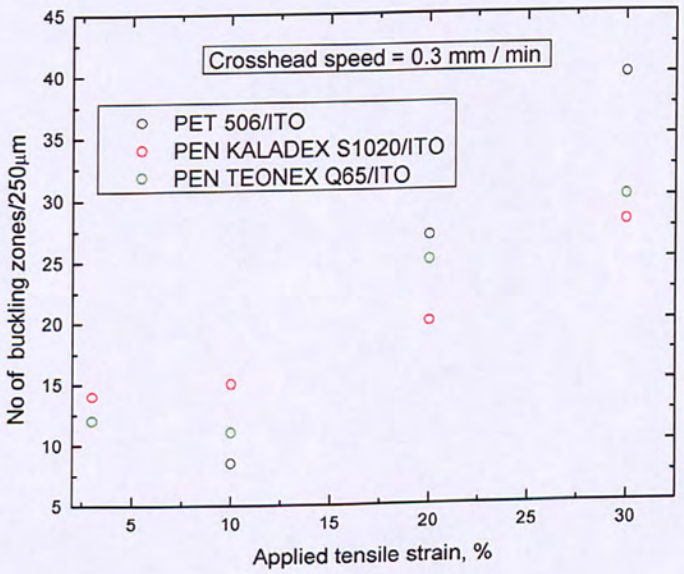

Figure 5.41: Number of ITO buckling zones per 250 microns for different polyester substrates as a function of uniaxial strain. Crosshead speed is 0.3 mm /min.

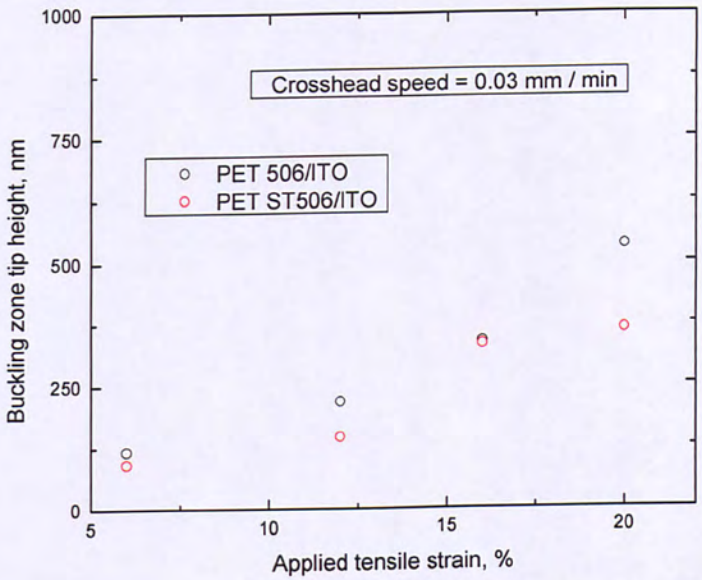

Figure 5.42: AFM measured ITO buckling zone tip heights for different PET substrates against applied uniaxial tensile strain. Crosshead speed is 0.03 mm / min.

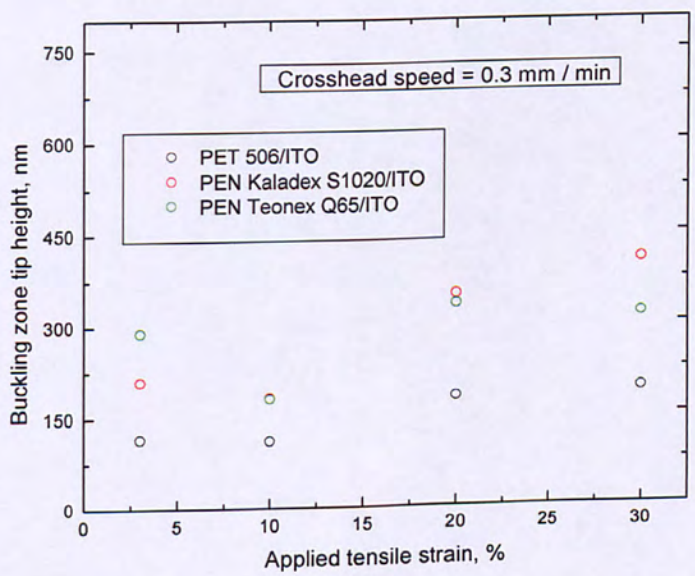

Figure 5.43: ITO buckling zone tip height as measured by contact mode AFM for different polyester substrates as a function of applied tensile strain. Crosshead speed is 0.3 mm / min.

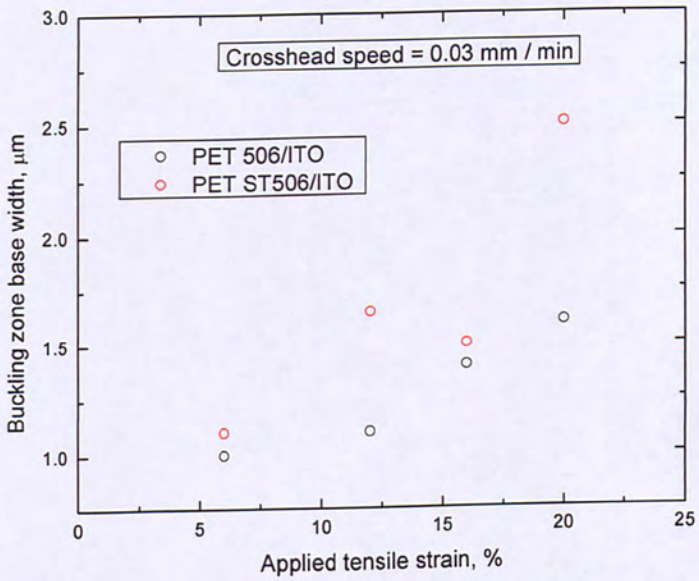

Figure 5.44: Buckling zone base width against applied strain, as measured by c – m AFM, for PET substrates and 0.03 mm / min crosshead speed.

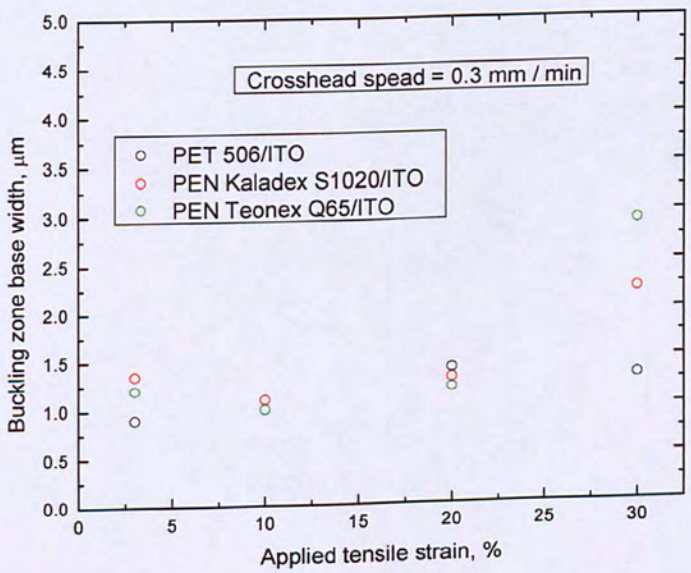

Figure 5.45: Buckling zone base width against applied strain, as measured by c – m AFM, for polyester substrates and 0.3 mm/min crosshead speed.

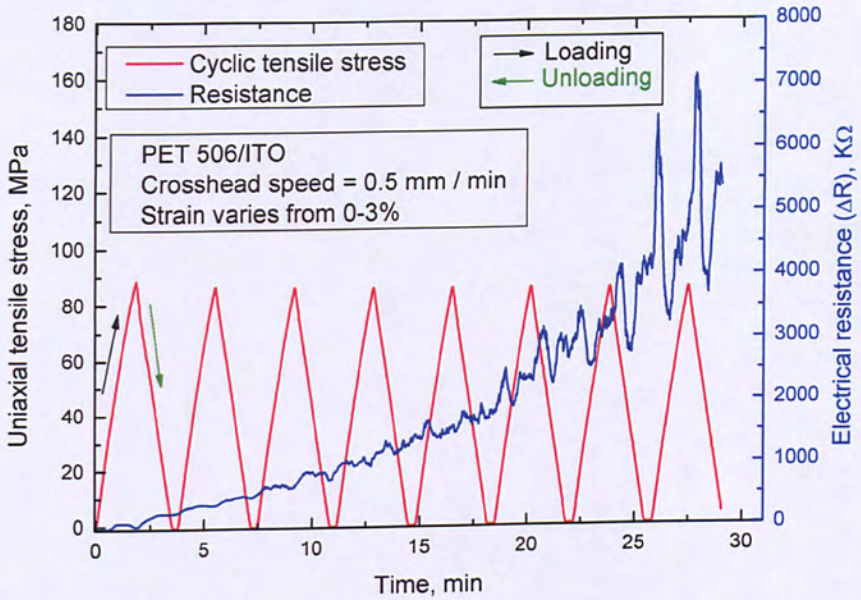

Figure 5.46: Stress-time-electrical resistance electromechanical graph considering PET506/ITO flexible display anode strained between 0-3% for 8 cycles.

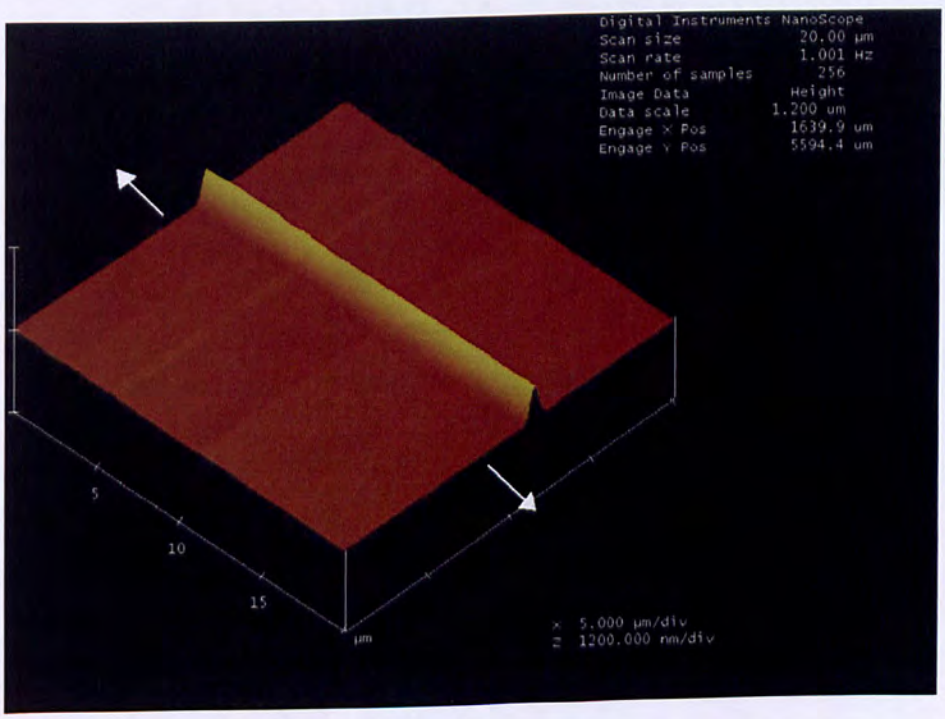

Figure 5.47: Contact-mode AFM image showing the surface of ITO on PET506 after tensile cyclic loading between 0-3% of strain. Transverse buckling and coating folding are observed. White arrows indicate the uniaxial tensile stress direction.

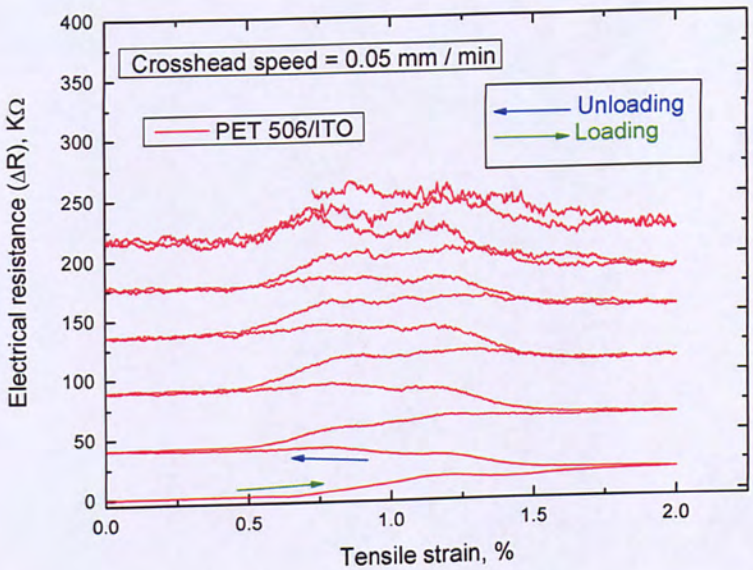

Figure 5.48: Electrical resistance against cyclic, 0-2%, tensile strain for 6 cycles in the case of PET 506/ITO flexible electrode. Crosshead speed is 0.05 mm / min.

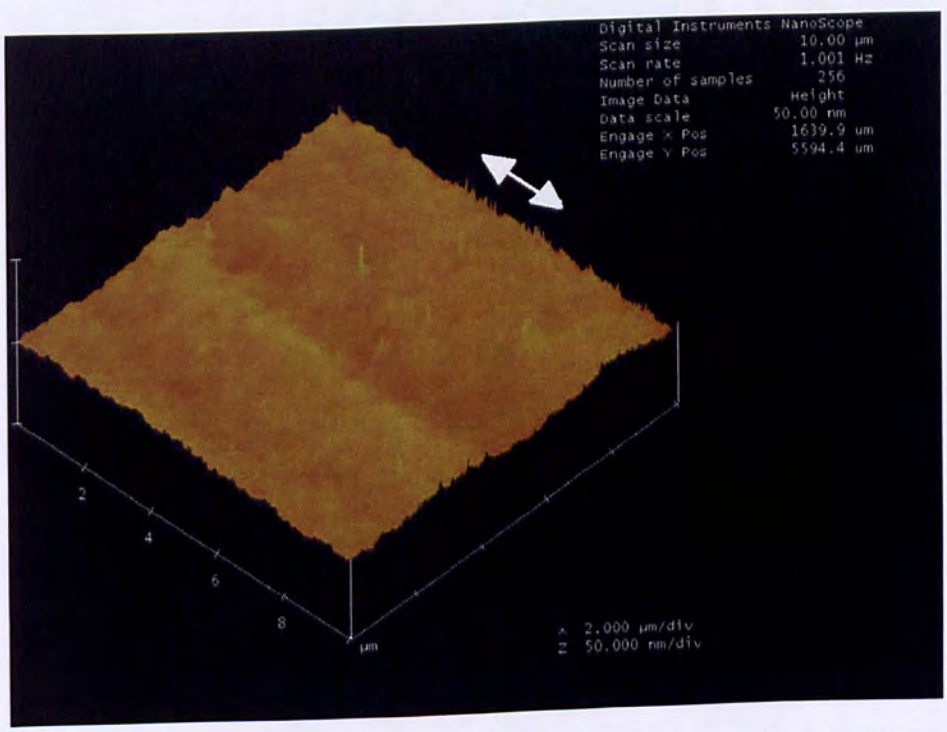

Figure 5.49: Intact surface of ITO on PET 506 as observed by using c-m AFM. The sample was tensile strained for 6 cycles between 0-2%. The corresponding electromechanical behaviour is presented in figure 5.48.

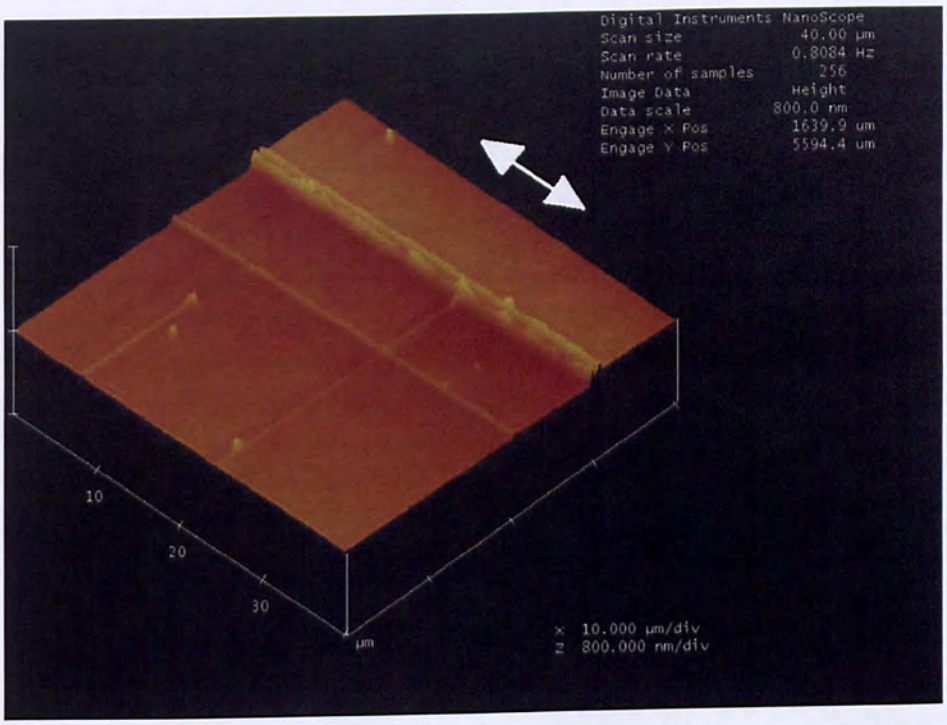

Figure 5.50: ITO on PET 506 as observed by using c-m AFM. The sample was tensile strained for 6 cycles between 0-2%. Parallel and perpendicular, to the tensile direction, adhesive failure as well as coating folding is clearly visible. The corresponding electromechanical behaviour is presented in figure 5.48.

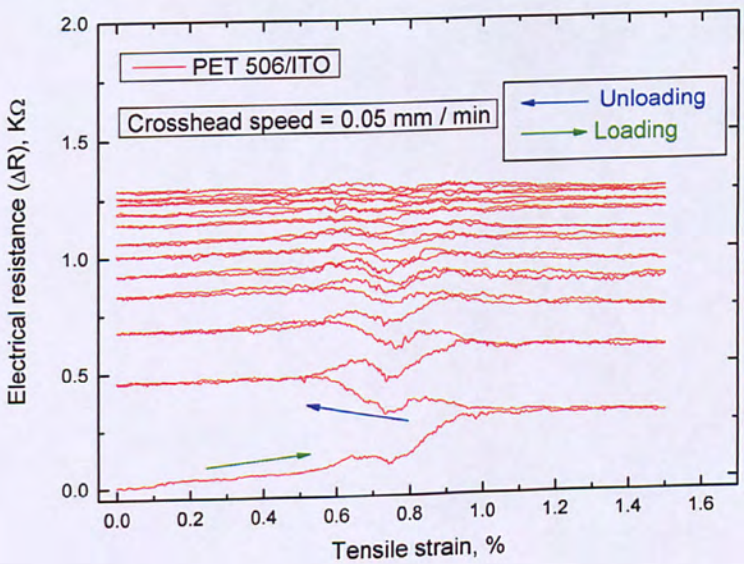

Figure 5.51: Electrical resistance against cyclic, 0-1.5%, tensile strain for 11 cycles in the case of PET 506/ITO flexible electrode. Crosshead speed is 0.05 mm / min.

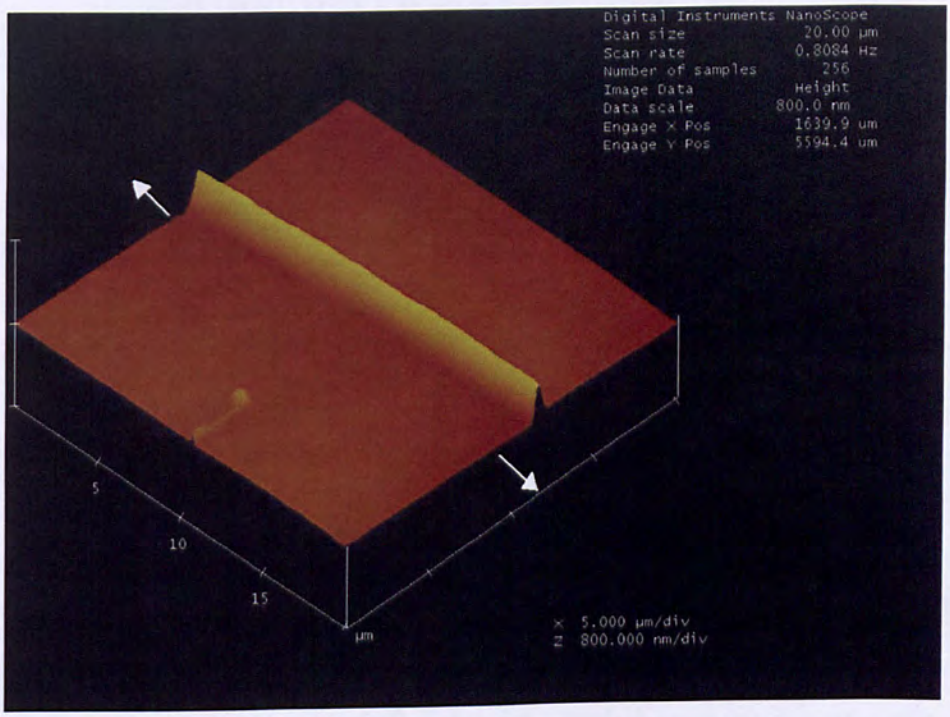

Figure 5.52: ITO on PET 506 as observed by using c-m AFM. The sample was tensile strained for 11 cycles between 0-1.5%. Transverse buckling formation is observed. The corresponding electromechanical behaviour is presented in figure 5.51.

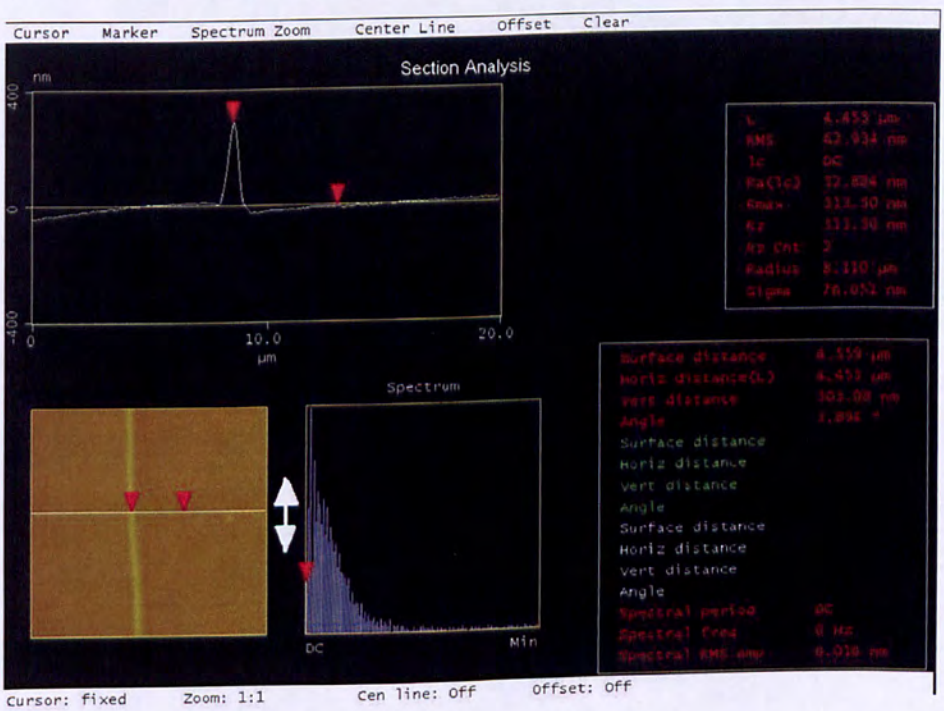

Figure 5.53: Cross section of the transverse buckling of ITO, on PET 506, as measured by ex-situ c-m AFM. The corresponding electromechanical behaviour is presented in figure 5.51.

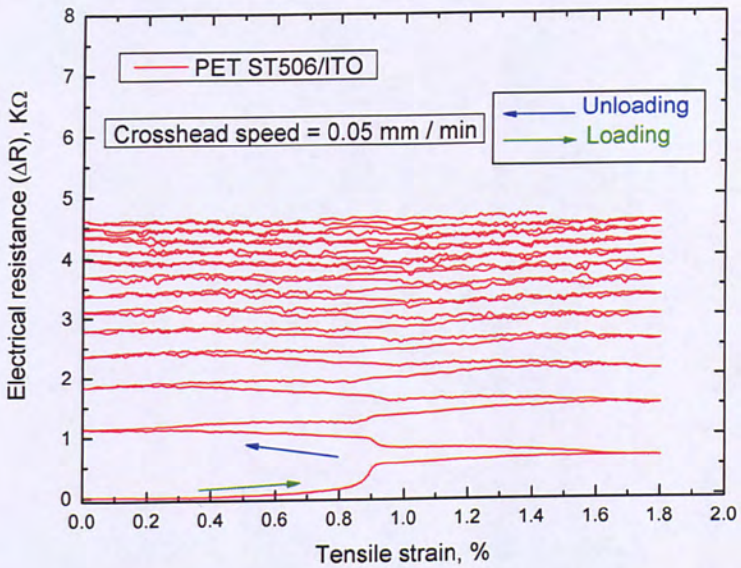

Figure 5.54: Uniaxial tensile cyclic, 12 cycles, loading with in-situ monitoring of the resistance of an ITO functional coating deposited on PET ST506 substrate. The cyclic tensile strain is between 0% and 1.8%.

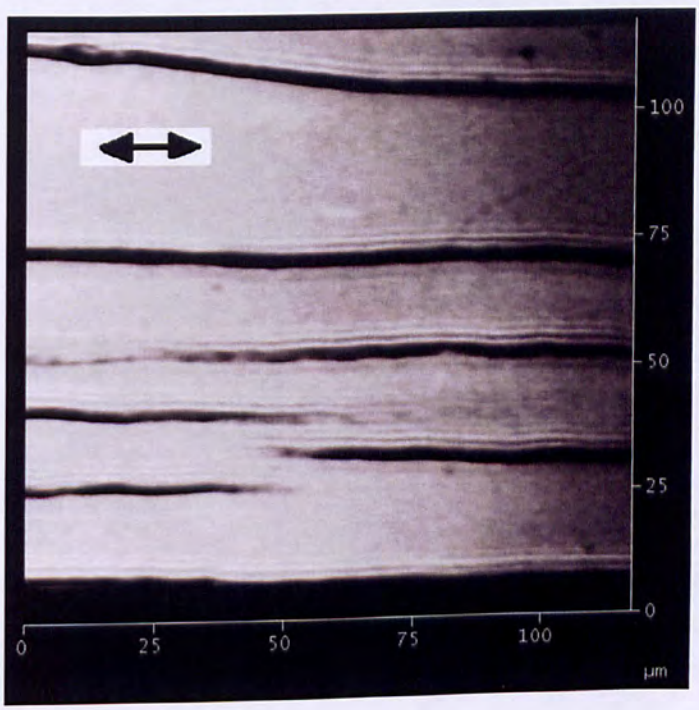

Figure 5.55: Optical micrograph showing the ITO, on PET ST506, surface strained for 12 cycles between 0% and 1.8% tensile strain at 0.05 mm / min crosshead speed.

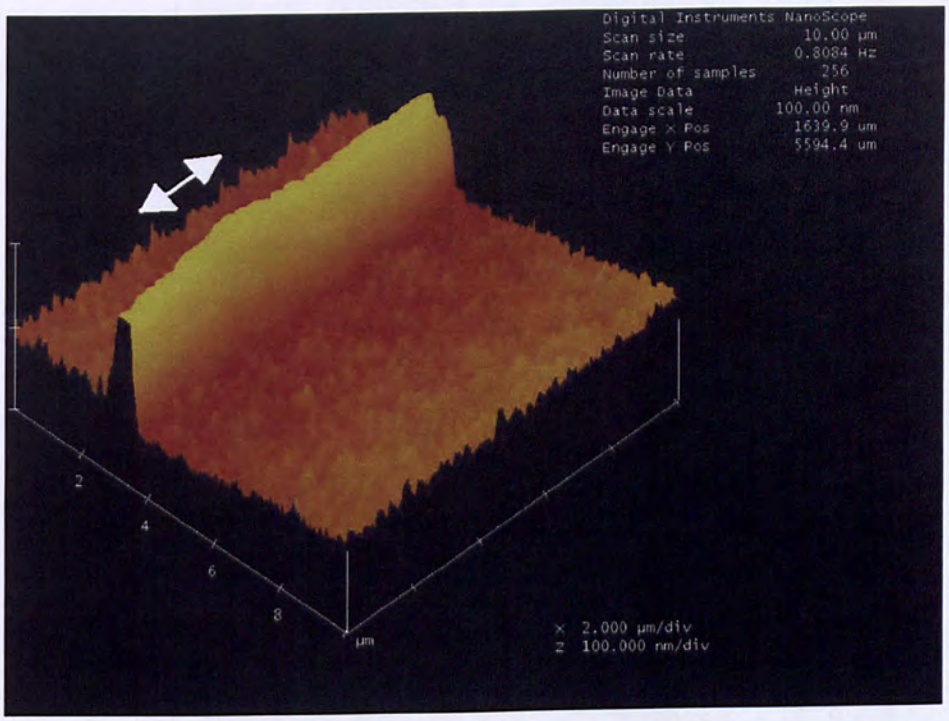

Figure 5.56: Contact-mode 3D image showing the transverse buckling formation for the case of ITO on PET ST506. The corresponding electromechanical graph is presented in figure 5.54.

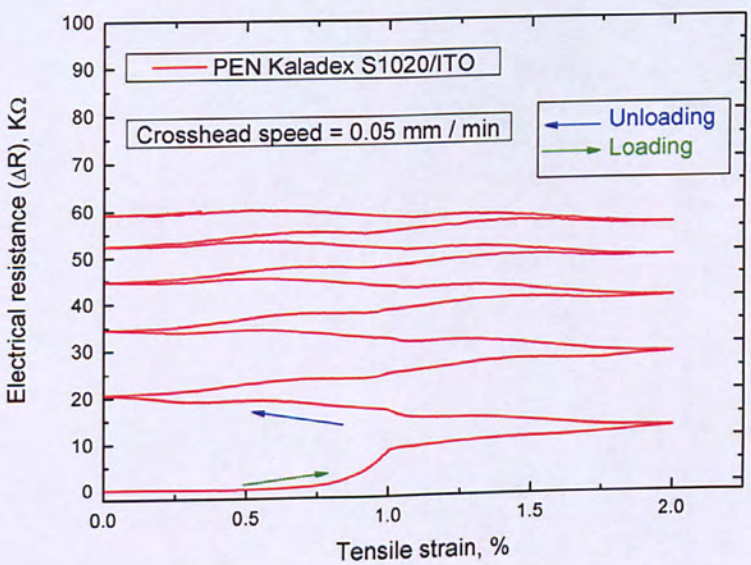

Figure 5.57: Uniaxial tensile cyclic, 5 cycles, loading with in-situ monitoring of the resistance of an ITO functional coating deposited on PEN Kaladex S1020 substrate. The cyclic tensile strain is between 0% and 2%.

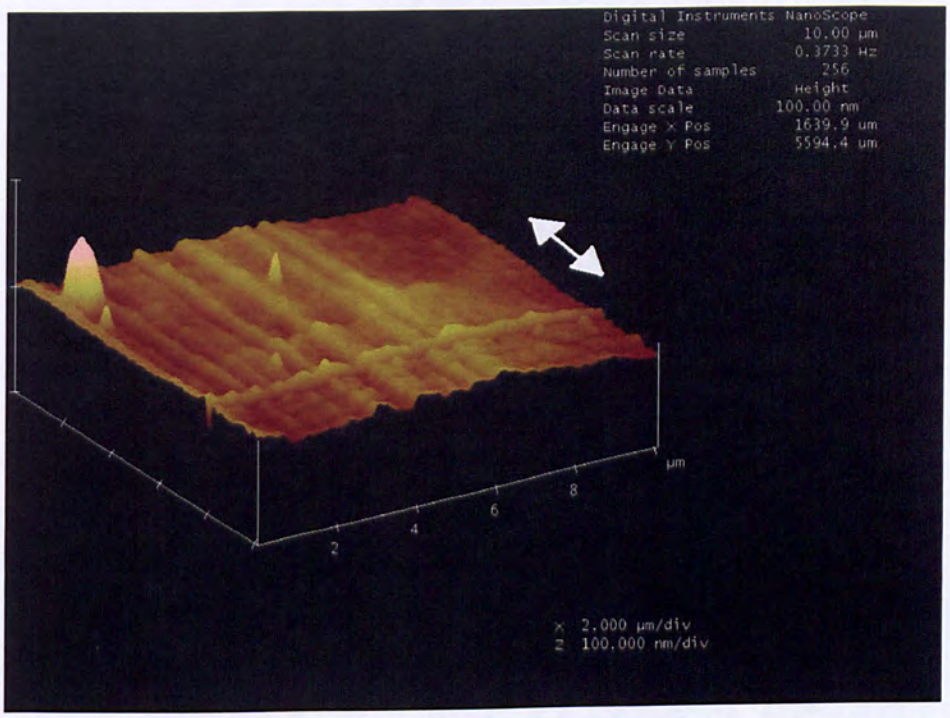

Figure 5.58: Contact-mode 3D image showing transverse buckling formation and folded cracking for the case of ITO on PEN Kaladex. The corresponding electromechanical graph is presented in figure 5.57.

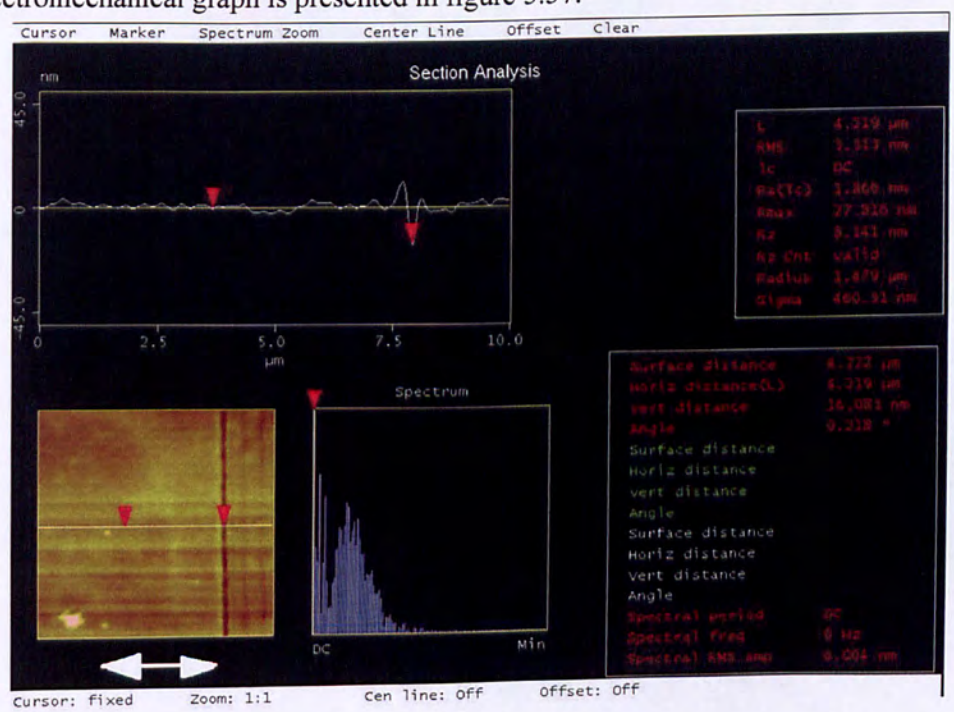

Figure 5.59: Cross-section of an ITO surface crack as measured by c-m AFM for the case of PEN Kaladex S1020/ITO flexible display anode. The cyclic, 5 cycles, strain is between 0% and 2% as presented in figure 5.57.

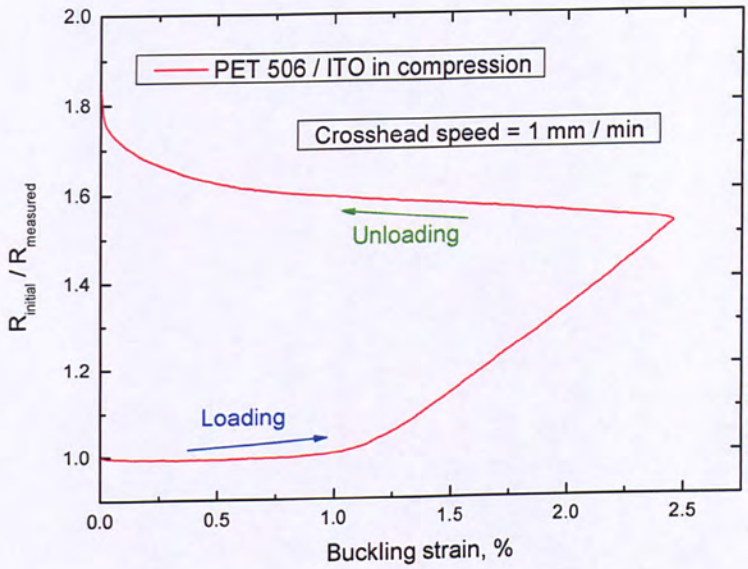

Figure 5.60: Controlled, 1 cycle, buckling behaviour of ITO, surface in compression, deposited on PET 506.

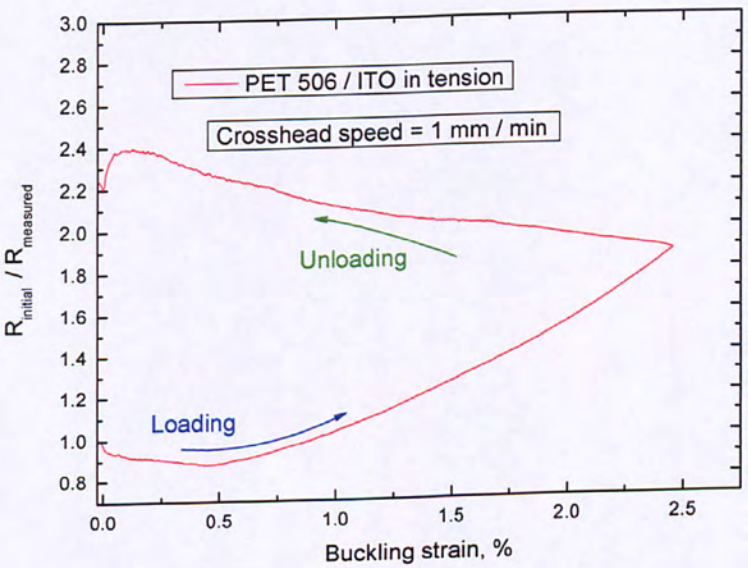

Figure 5.61: Controlled, 1 cycle, buckling behaviour of ITO, surface in tension, deposited on PET 506.

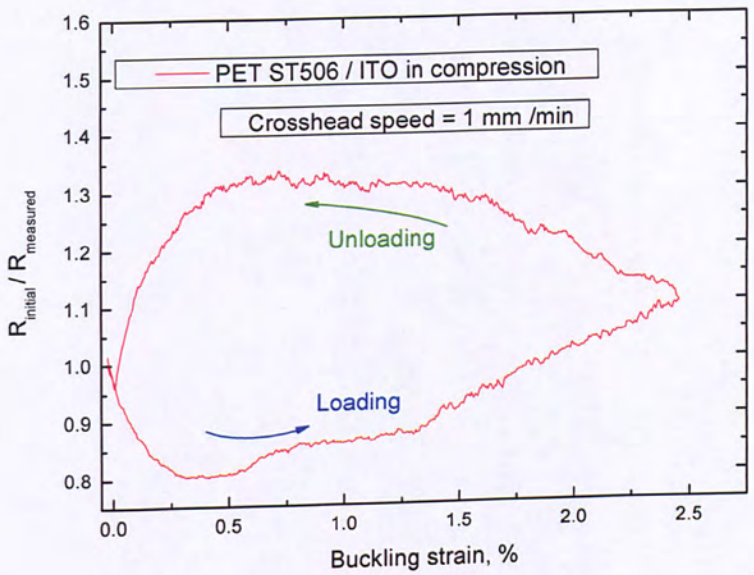

Figure 5.62: Controlled, 1 cycle, buckling behaviour of ITO, surface in compression, deposited on PET ST506.

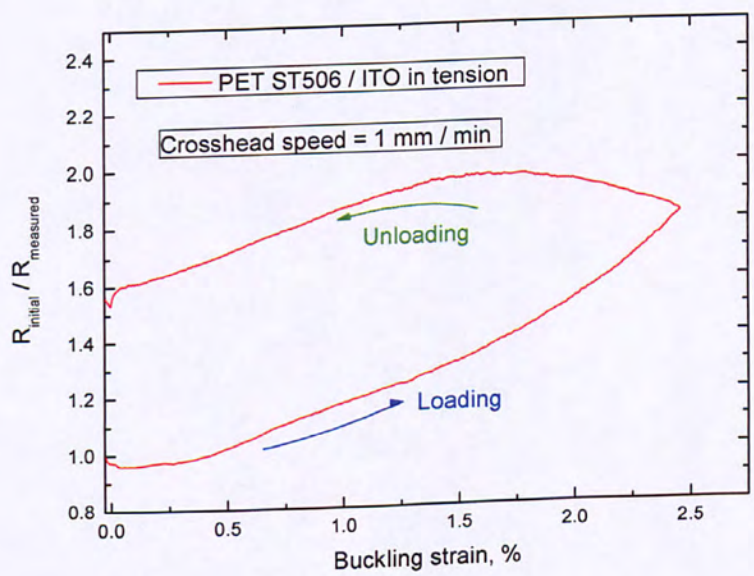

Figure 5.63: Controlled, 1 cycle, buckling behaviour of ITO, surface in tension, deposited on PET ST506.

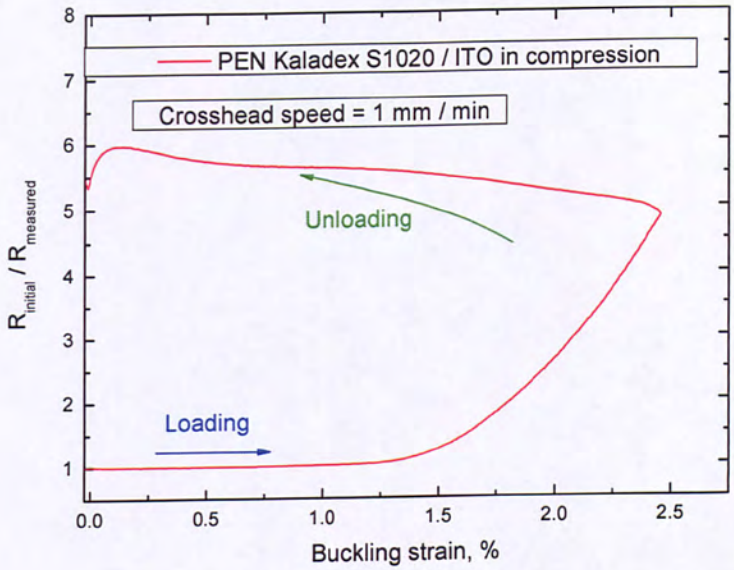

Figure 5.64: Controlled, 1 cycle, buckling behaviour of ITO, surface in compression, deposited on PEN Kaladex S1020.

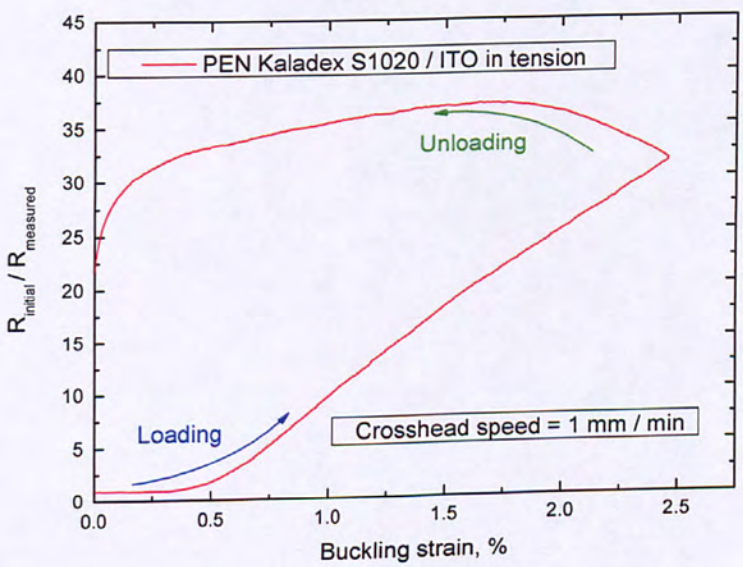

Figure 5.65: Controlled, 1 cycle, buckling behaviour of ITO, surface in tension, deposited on PEN Kaladex S1020.

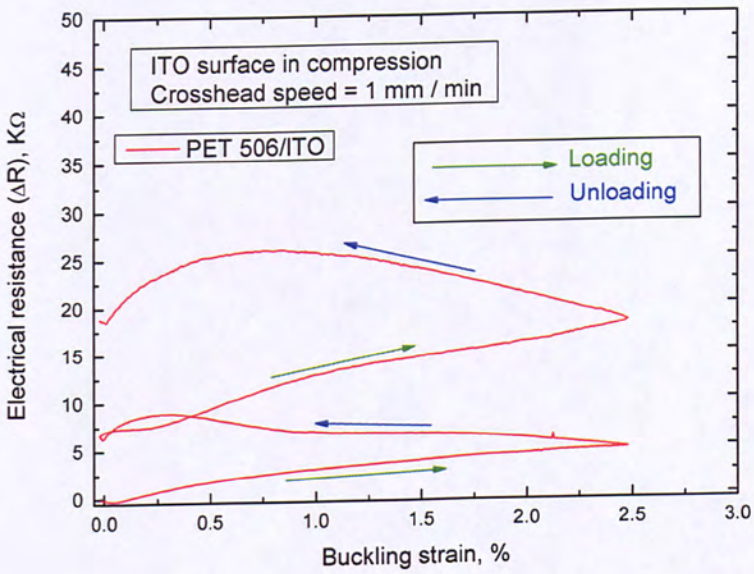

Figure 5.66: Cyclic, 2 cycles, electromechanical measurement of a PET 506/ITO flexible display electrode when the ceramic coating is under compression.

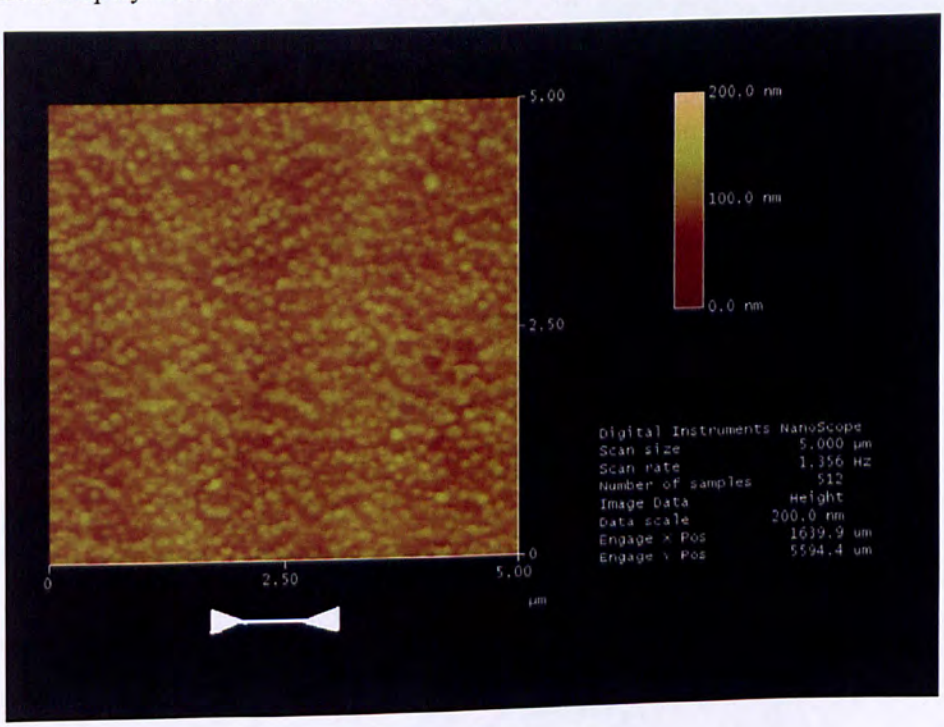

Figure 5.67: Intact surface fragment of buckled ITO surface deposited on PET 506. ITO surface is under compression. White arrows indicate direction of compressive force. Electromechanical behaviour presented in figure 5.66.

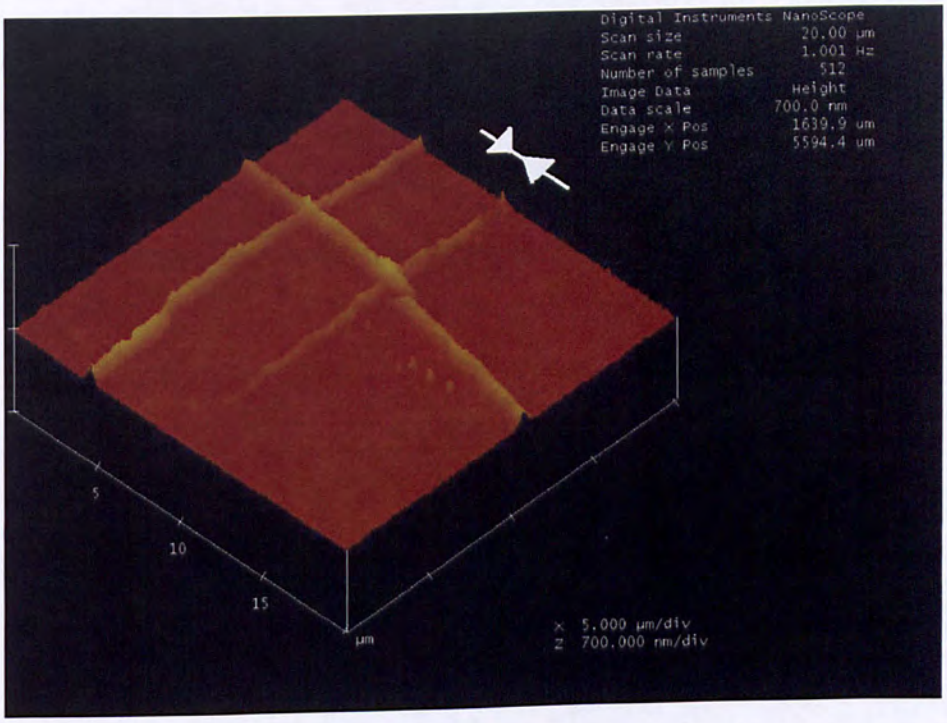

Figure 5.68: Larger, 20µm*20µm, c-m AFM image of buckled ITO surface deposited on PET 506. Parallel and perpendicular, to uniaxial compressive direction, buckled zones are clearly visible. ITO surface is under compression. Electromechanical behaviour presented in figure 5.66.

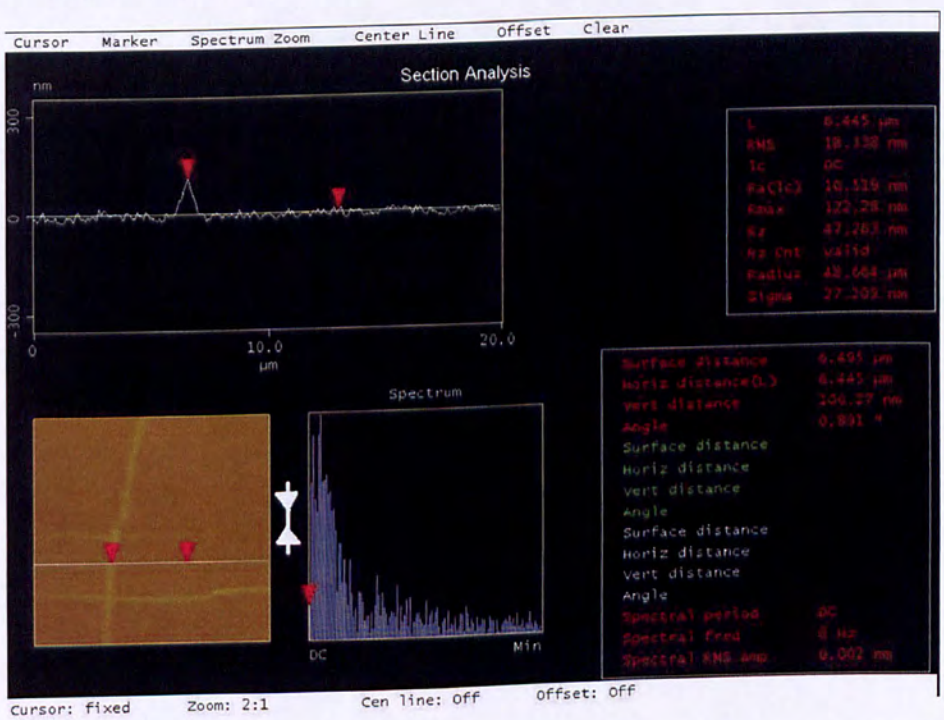

Figure 5.69: Cross sectional view of a buckled zone of the ITO surface corresponding to the electromechanical behaviour of figure 5.66.

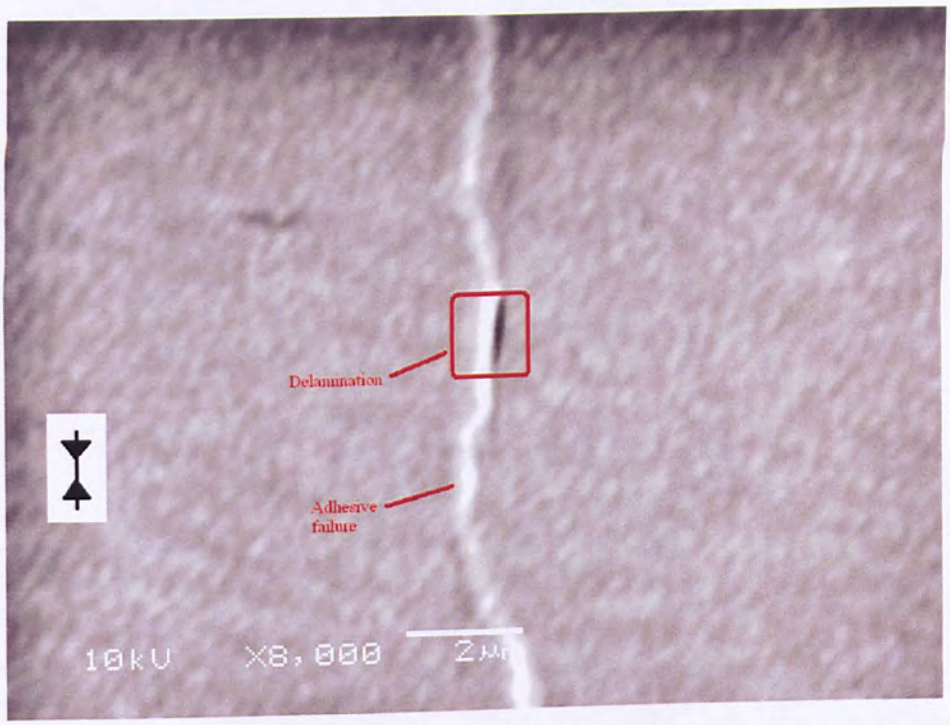

Figure 5.70: SEM micrograph showing the ITO, sputtered on PET 506 flexible substrate, surface. The electromechanical behaviour of this sample is presented in figure 5.66. Black arrows indicate the direction of the uniaxial, externally applied, compressive stress.

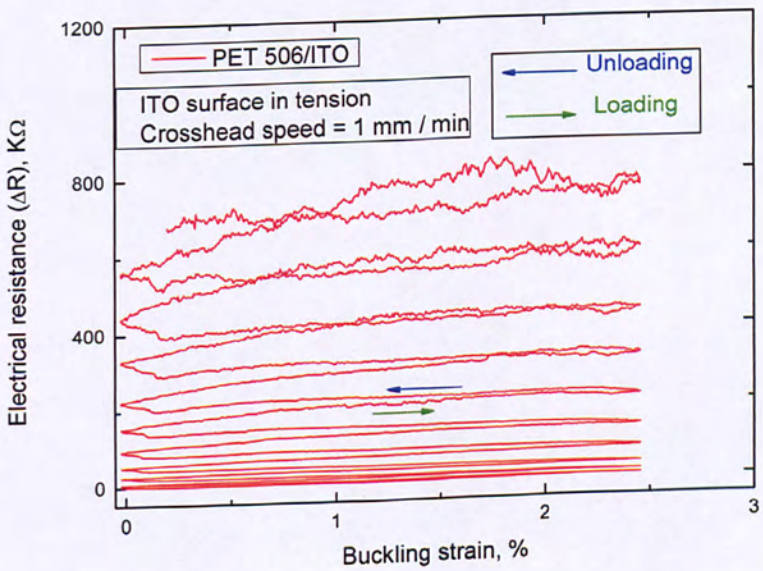

Figure 5.71: Electromechanical behaviour of ITO, deposited on PET 506, surface in tension. Cyclic loading, 10 cycles in total. The maximum buckling strain is 2.45%.

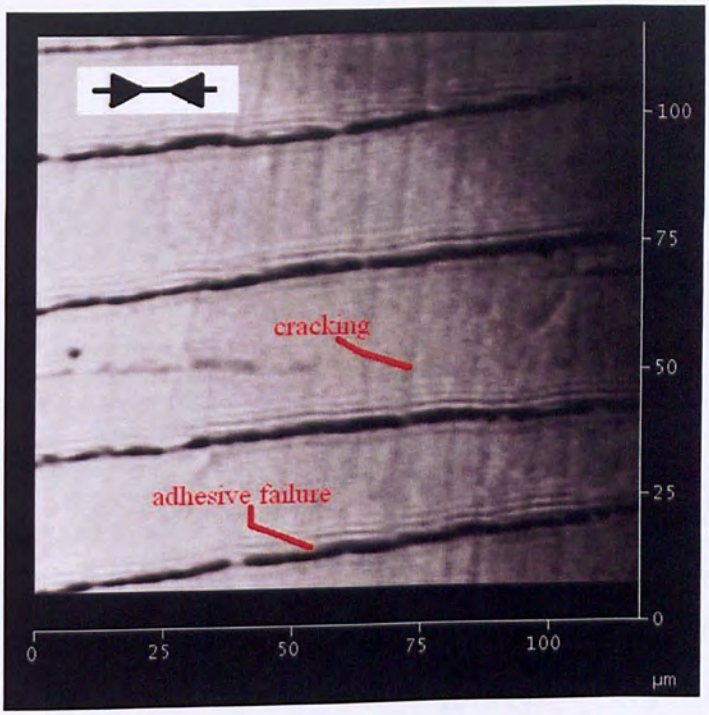

Figure 5.72: Optical image ITO surface on PET 506. The electromechanical behaviour of the sample is presented in figure 5.71. Cracking perpendicular to the applied stress and adhesive failure parallel to the applied stress is clearly visible.

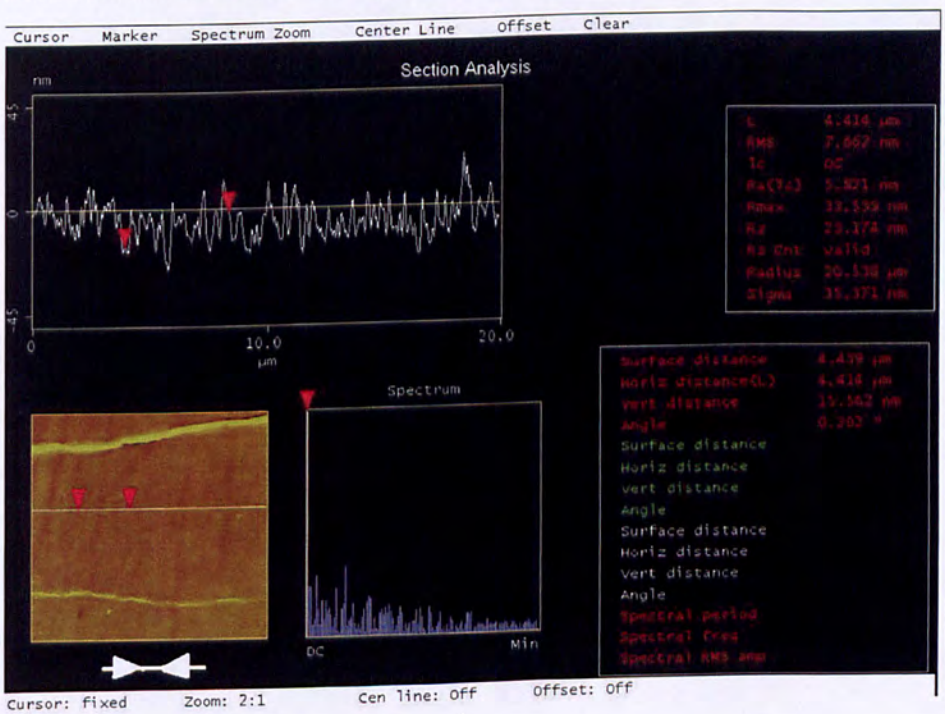

Figure 5.73: Crack profiles obtained by c-m AFM for ITO surface, sputtered on PET 506. The sample was under compressive cyclic loading for 10 cycles and its electromechanical behaviour is presented in figure 5.71.

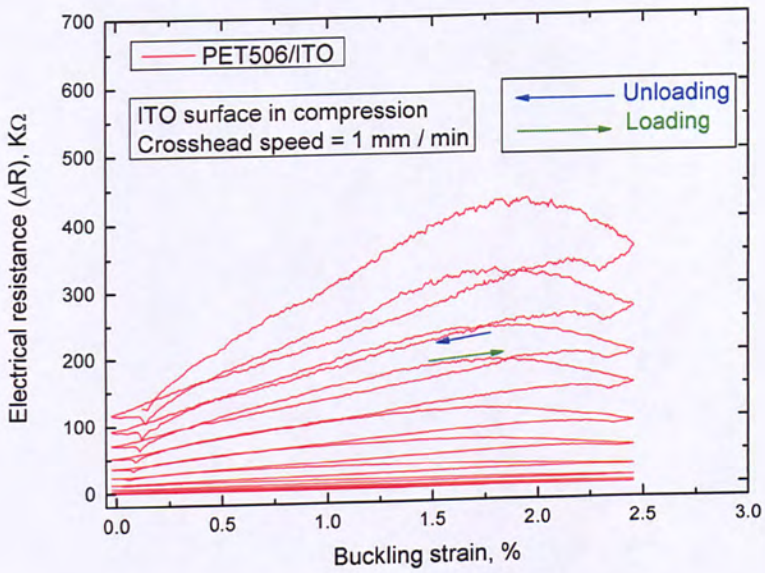

Figure 5.74: Electromechanical controlled, 9 cycles, buckling behaviour of a PET 506/ITO flexible electrode. The functional layer is under compression. Note the significant decrease in resistance during unloading.

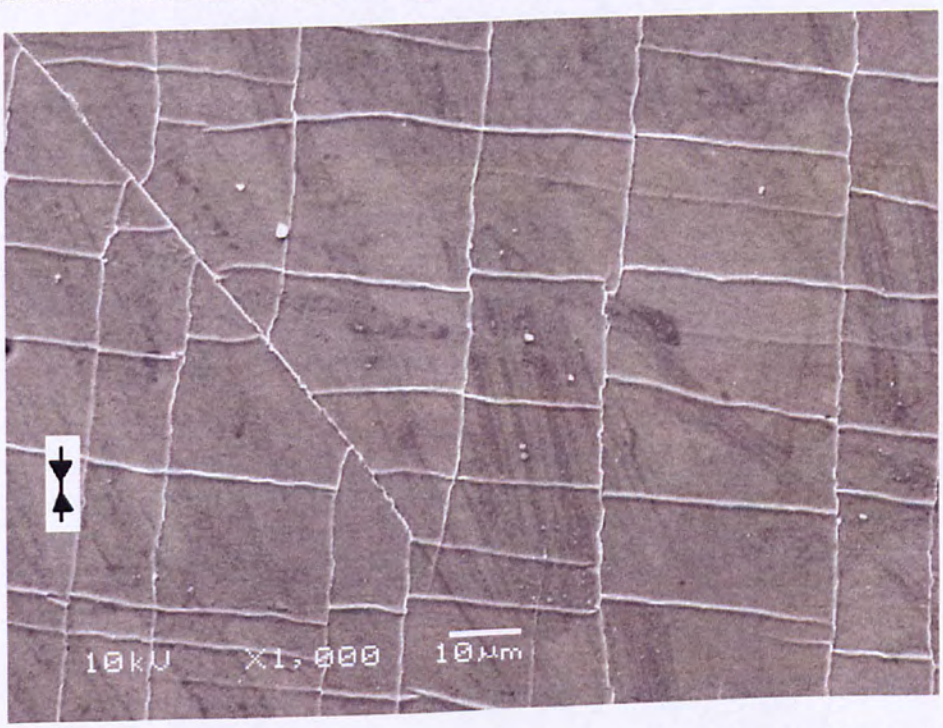

Figure 5.75: Ex-situ SEM image showing ITO, on PET 506, adhesive failure after 9 cycles of controlled buckling loading. Black arrows indicate the compressive external stress direction. Detailed electromechanical behaviour is presented in figure 5.74.

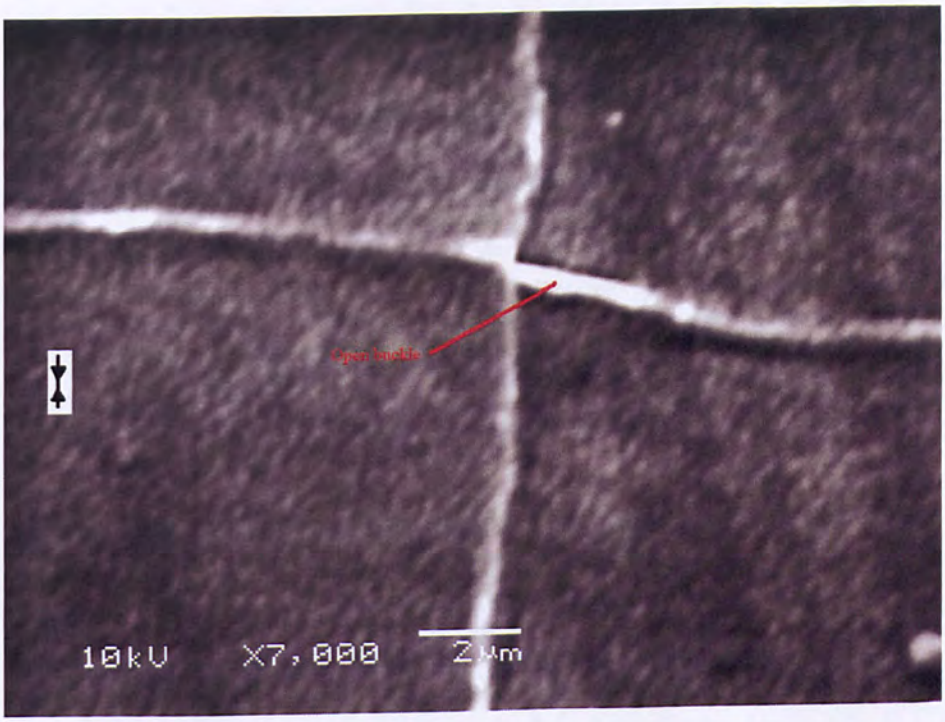

Figure 5.76: Higher magnification ex-situ SEM image showing ITO, on PET 506, adhesive failure. Closed and open buckling zones parallel and perpendicular to the applied compressive stress dominate adhesive failure. Detailed electromechanical behaviour is presented in figure 5.74.

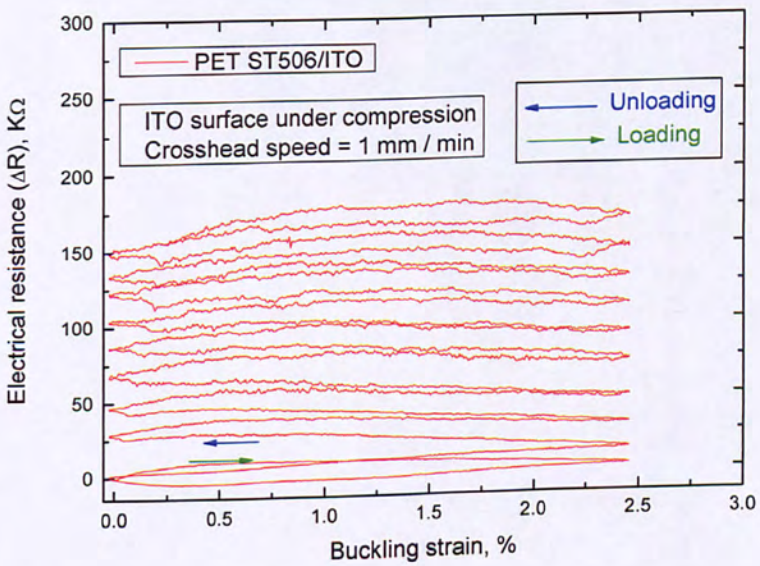

Figure 5.77: Electromechanical controlled, 10 cycles, buckling behaviour of a PET ST506/ITO flexible electrode. The functional layer is under compression.

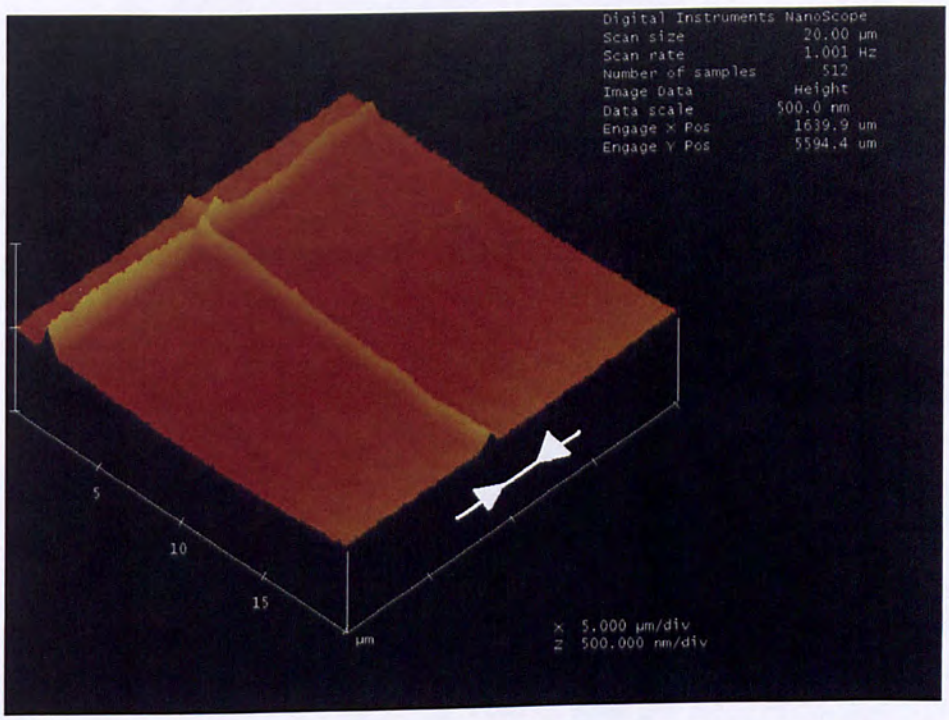

Figure 5.78: Parallel and perpendicular, adhesive ITO failure, to the applied compressive force direction as captured ex-situ by c-m AFM. The ITO coating was sputtered on PET ST506 flexible substrate. Detailed electromechanical behaviour shown in figure 5.77.

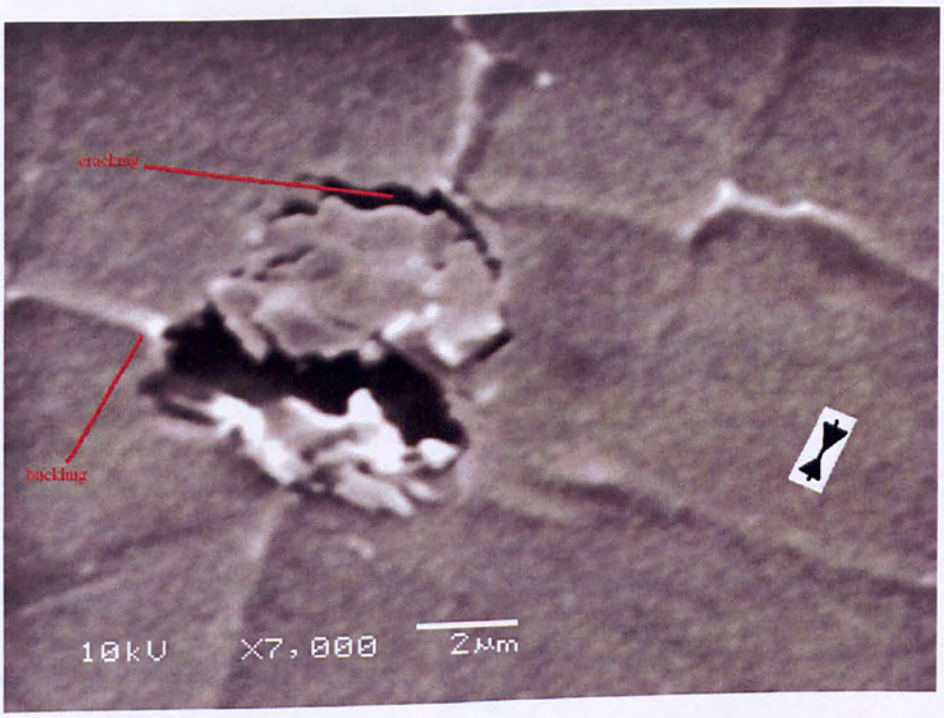

Figure 5.79: Higher magnification ex-situ SEM image showing ITO, on PET ST506, adhesive and cohesive coating failure. Detailed electromechanical behaviour shown in figure 5.77.

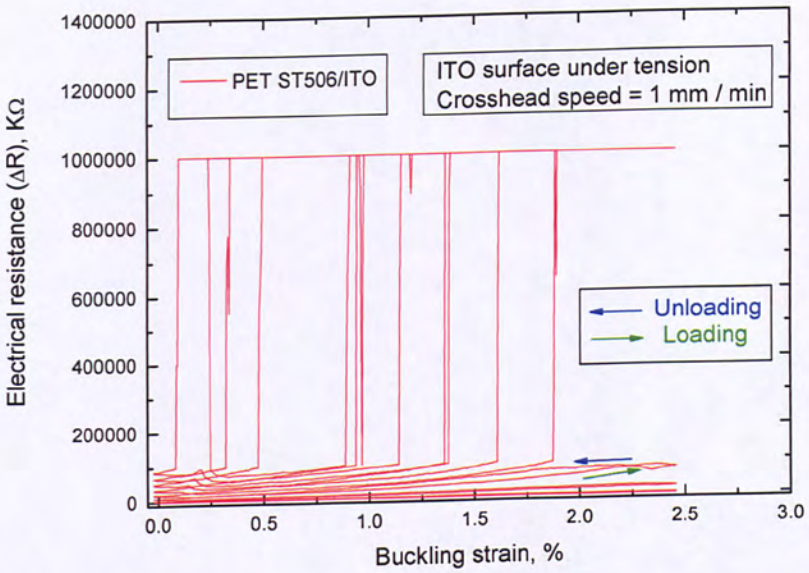

Figure 5.80: Electromechanical controlled, 10 cycles, buckling behaviour of a PET ST506/ITO flexible electrode. The functional layer is under tension. Note total electrical resistance degradation during the 4th cycle.

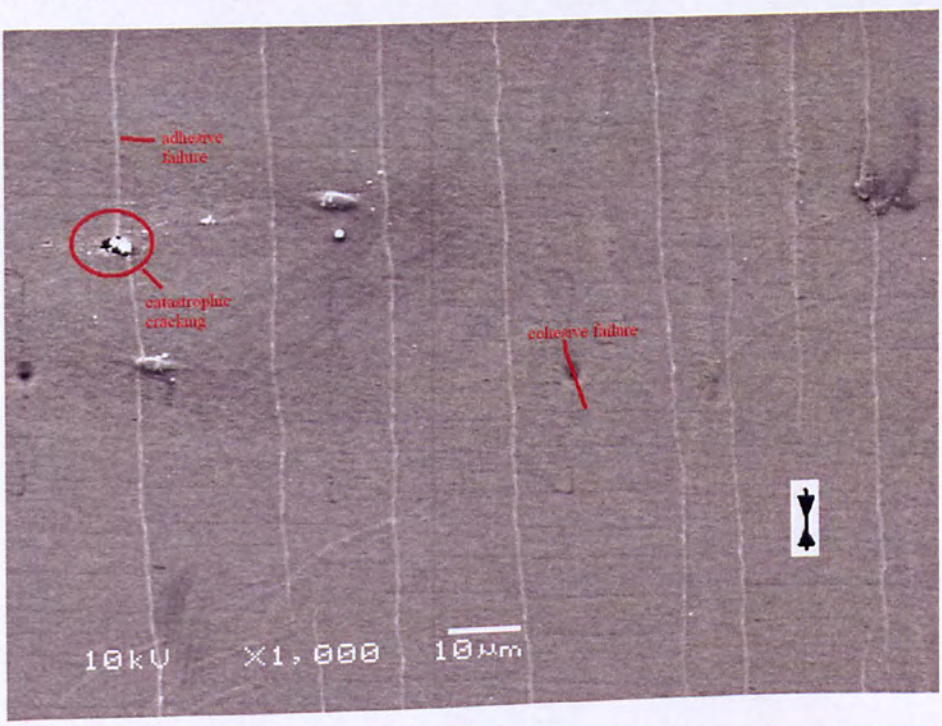

Figure 5.81: Low magnification ex-situ SEM micrograph showing the ITO, deposited on PET ST506, surface. Cohesive and adhesive failure is observed as well as catastrophic cracking. The electromechanical behaviour of the flexible anode material is presented in figure 5.80.

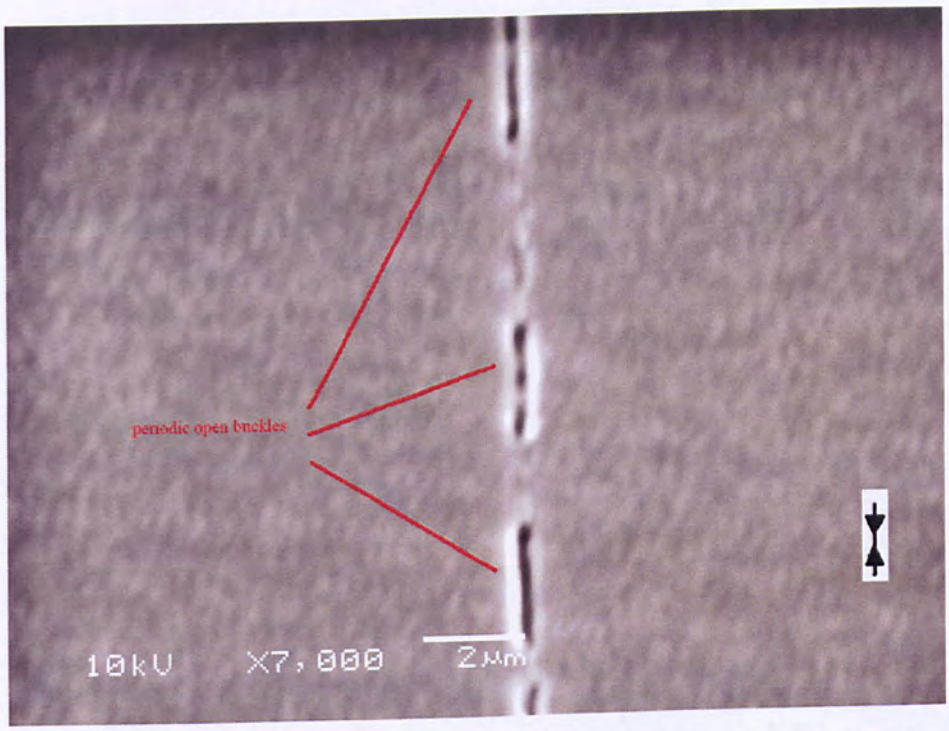

Figure 5.82: Higher magnification SEM image showing the formation of periodic open buckles, adhesive failure, for the case of a compressed PET ST506/ITO flexible display electrode. The functional layer is on the convex side. The electromechanical behaviour of the anode is presented in figure 5.80.

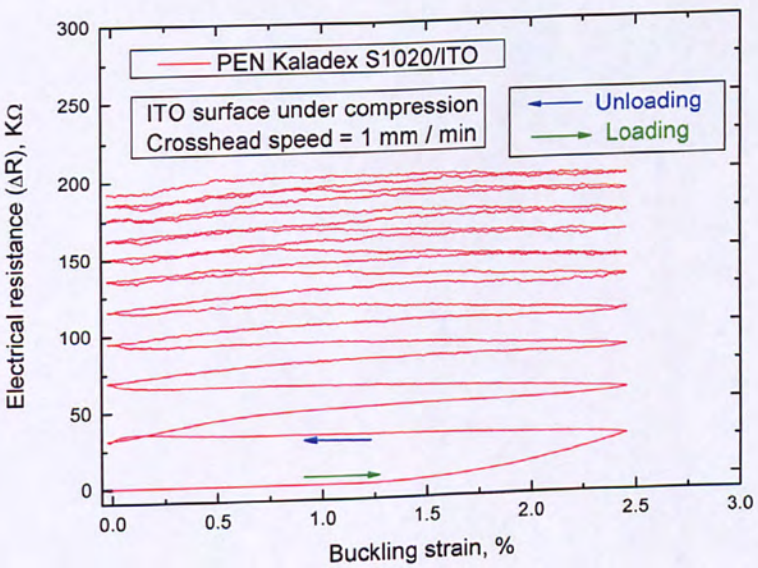

Figure 5.83: Electromechanical controlled, 10 cycles, buckling behaviour of a PEN Kaladex S1020/ITO flexible electrode. The ITO layer is on the concave side.

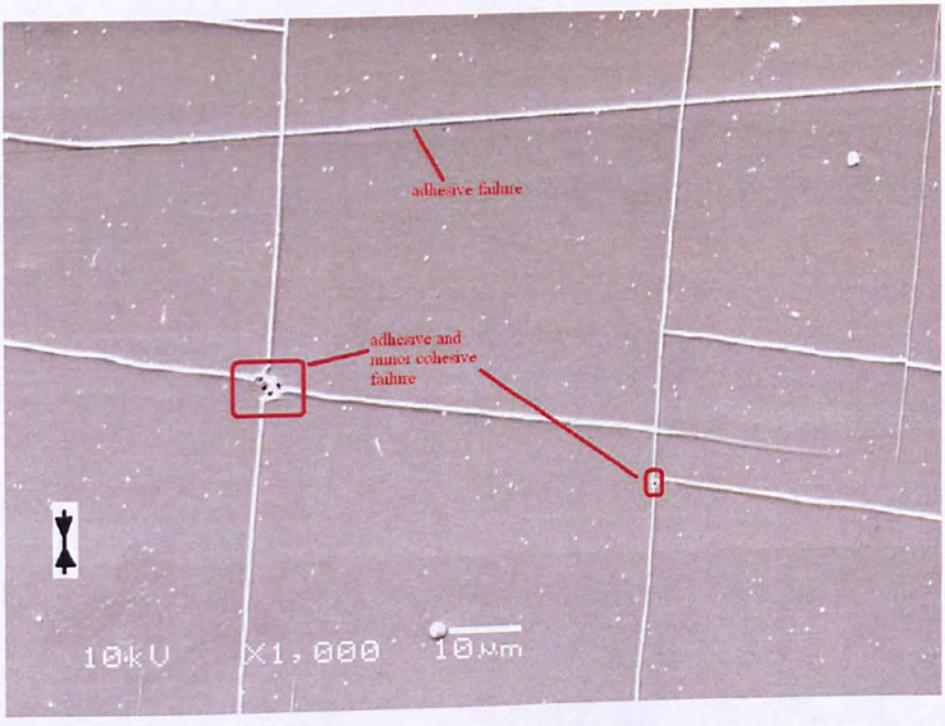

Figure 5.84: Low magnification ex-situ SEM micrograph showing the ITO, deposited on PEN Kaladex S1020, surface. Minor cohesive and major adhesive failure is observed. The electrical degradation, under cyclic buckling strain of 2.45%, is shown in figure 5.83.

Figure 5.85: Cross section of a buckling zone, for PEN Kaladex S1020/ITO flexible display electrode, as measured by c-m AFM after 10 cycles of externally applied buckling strain. The coating was on the concave side. Electromechanical behaviour is presented in figure 5.83.

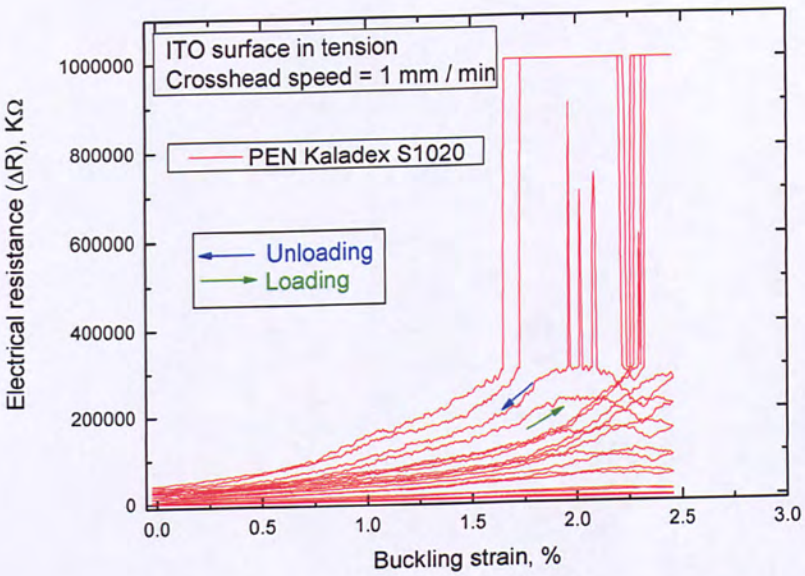

Figure 5.86: Electromechanical controlled, 10 cycles, buckling behaviour of a PEN Kaladex S1020/ITO flexible electrode. The ITO layer is on the convex side. Note coating total electrical degradation during the 8th cycle of the experiment.

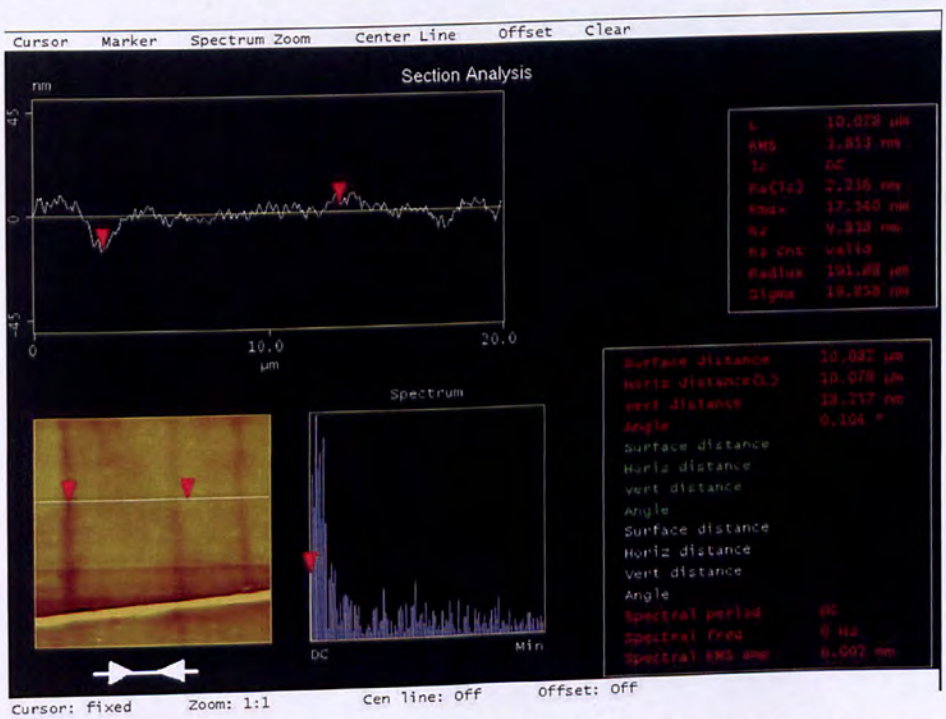

Figure 5.87: Cross section of cracks, for PEN Kaladex S1020/ITO flexible display electrode, as measured by c-m AFM after 10 cycles of externally applied buckling strain. The ITO layer is on the convex side and its electrical degradation is presented in figure 5.86.

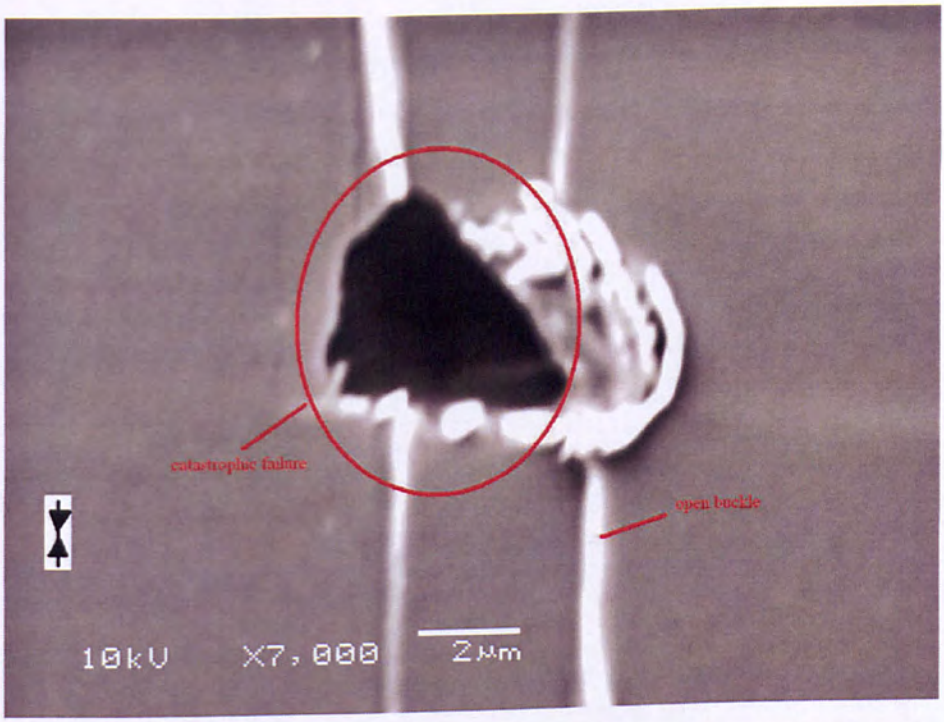

Figure 5.88: High magnification ex-situ SEM image showing catastrophic failure of ITO, sputtered on PEN Kaladex S1020, coating. Formation of open buckles is also evident. The corresponding electromechanical graph is presented in figure 5.86.

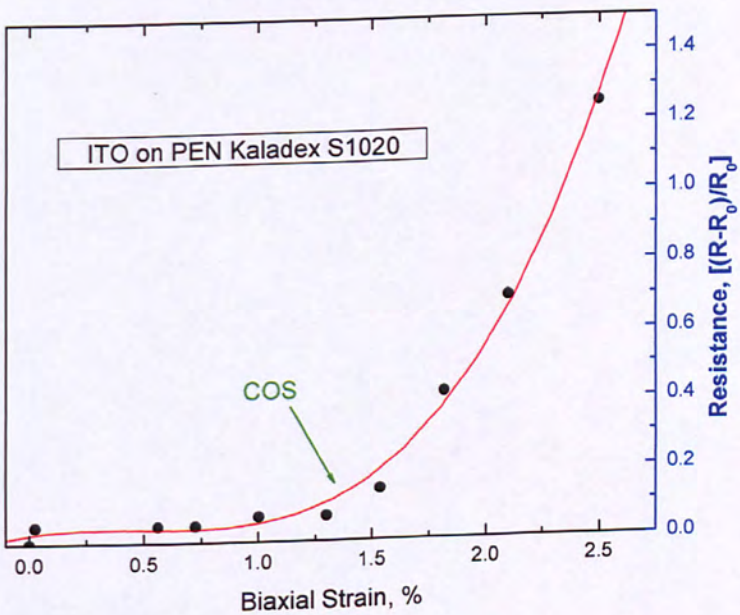

Figure 5.89: Electrical resistance versus biaxial strain for an ITO on PEN Kaladex S1020 flexible anode.

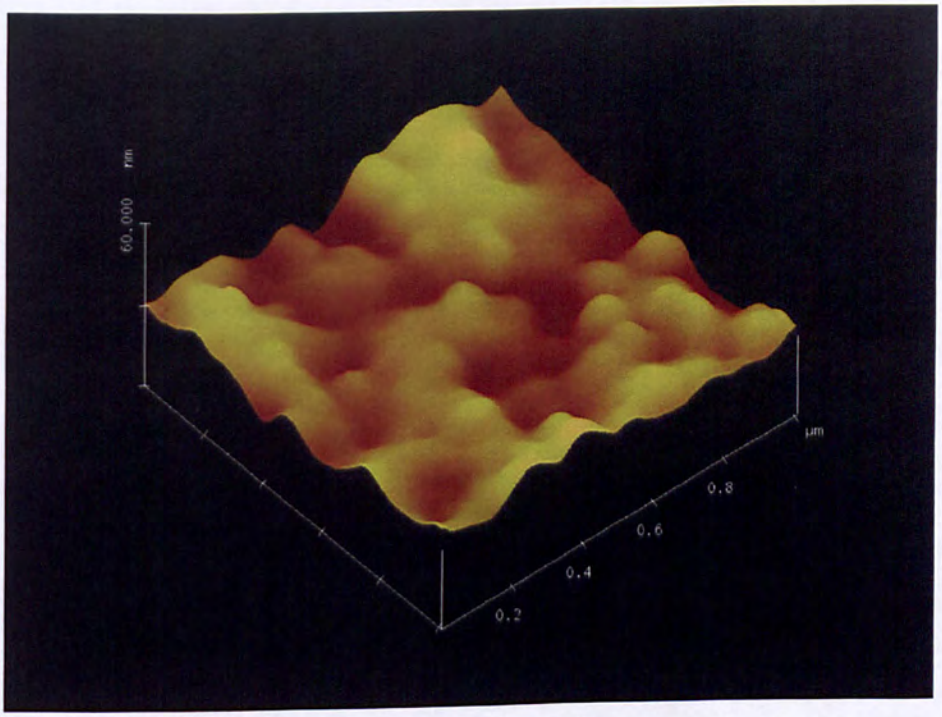

Figure 5.90: Intact fragment of ITO on PEN Kaladex surface tested under biaxial tension and imaged ex – situ by AFM.

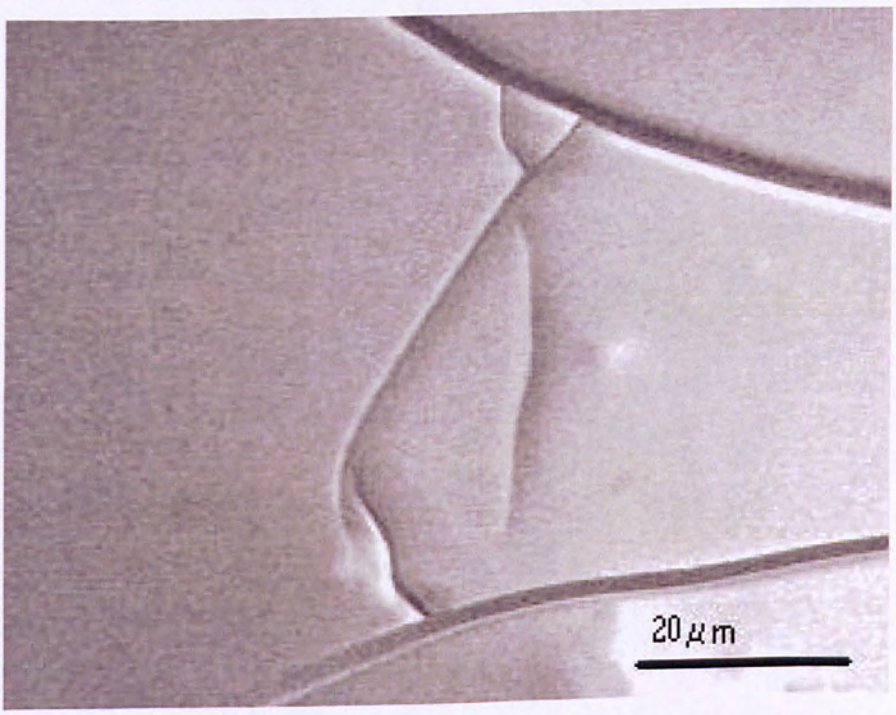

Figure 5.91: FEG – SEM image showing biaxial cracking of ITO on PEN Kaladex S1020 flexible anode.

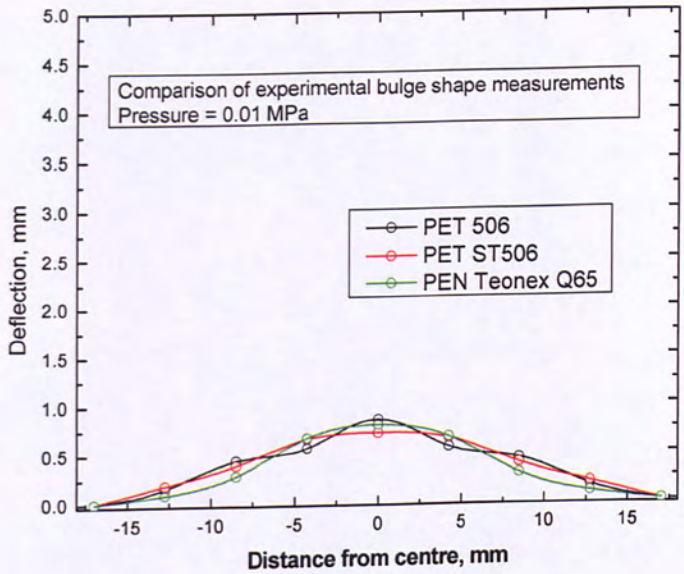

Figure 5.92: Comparison of experimentally measured bulge profiles, differential pressure is 0.01 MPa, for PET 506, PET ST506 and PEN Teonex Q65 bare flexible display substrate.

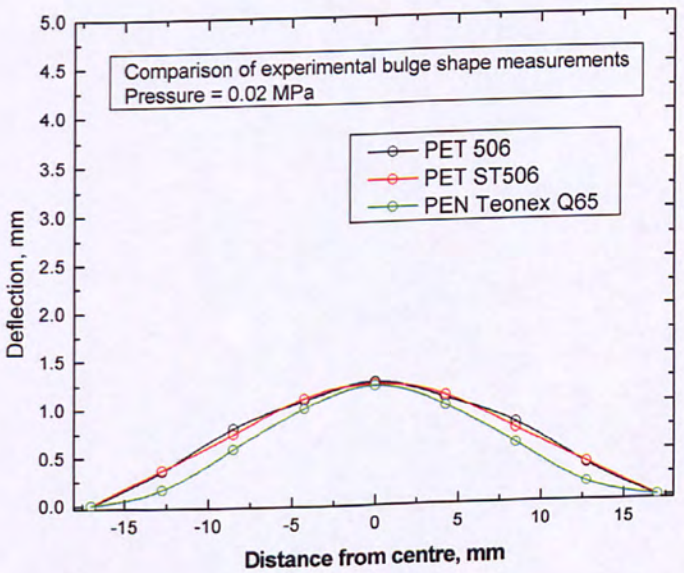

Figure 5.93: Comparison of experimentally measured bulge shapes for a differential pressure of 0.02 MPa, regarding PET 506, PET ST506 and PEN Teonex Q65 bare polyester circular substrates.

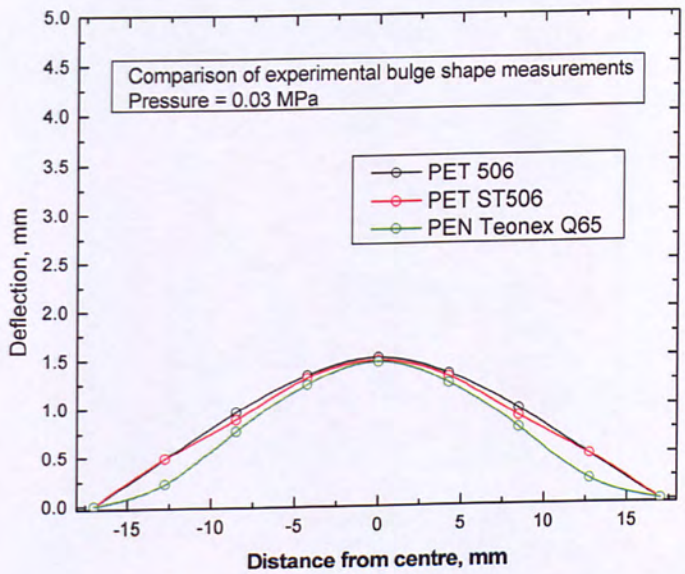

Figure 5.94: The bulge shapes, as measured experimentally, of PET 506, PET ST506 and PEN Teonex Q65 bare substrates for a differential pressure of 0.03 MPa.

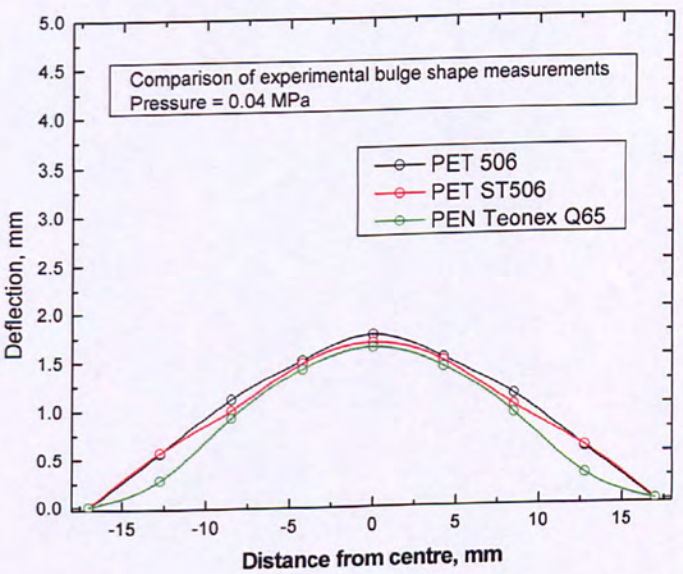

Figure 5.95: Comparison of experimentally measured bulge profiles, differential pressure is 0.04 MPa, for PET 506, PET ST506 and PEN Teonex Q65 bare flexible display substrate.

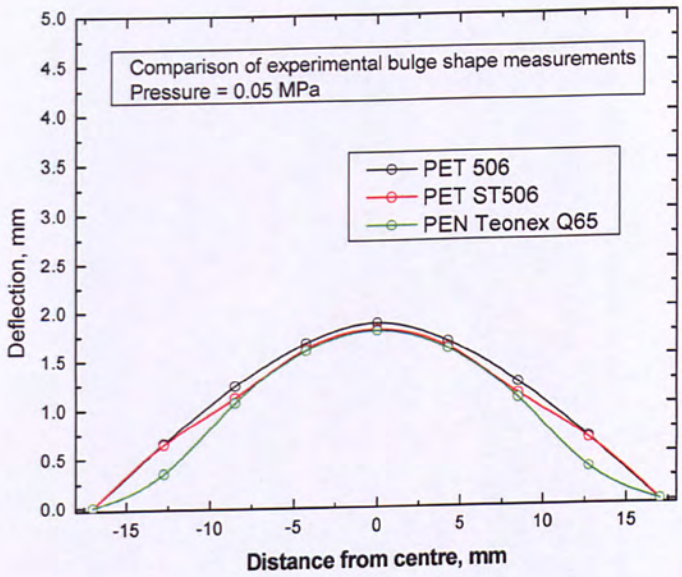

Figure 5.96: Comparison of experimentally measured bulge shapes for a differential pressure of 0.05 MPa, regarding PET 506, PET ST506 and PEN Teonex Q65 bare polyester circular substrates.

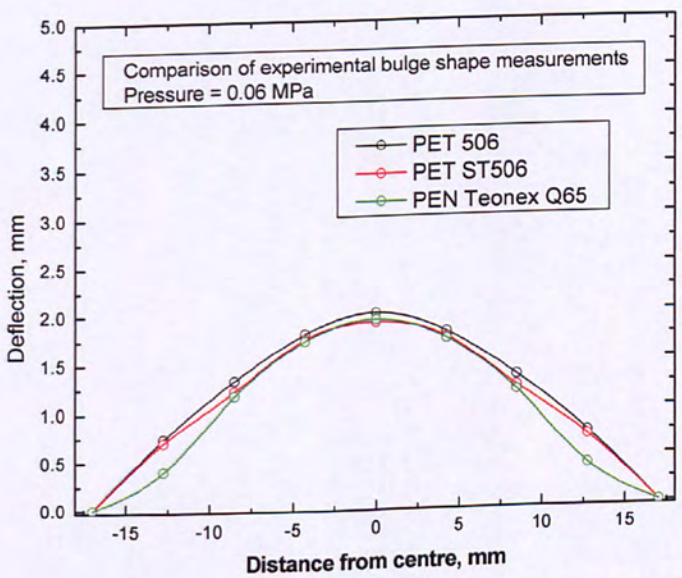

Figure 5.97: The bulge shapes, as measured experimentally, of PET 506, PET ST506 and PEN Teonex Q65 bare substrates for a differential pressure of 0.06 MPa.

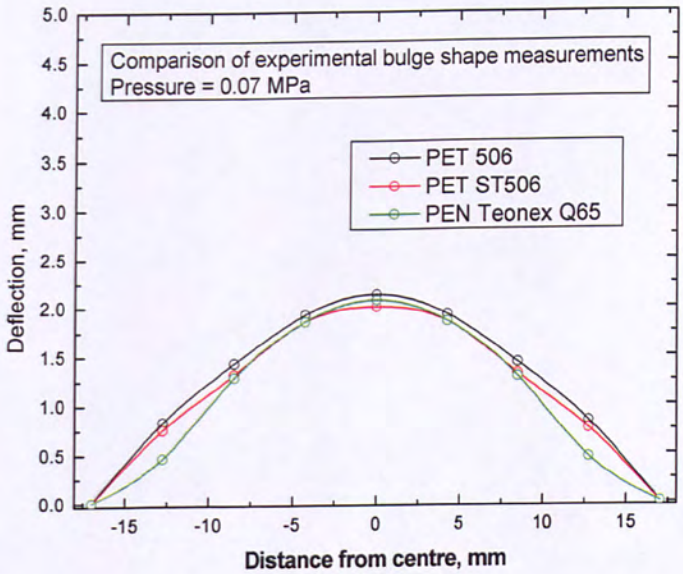

Figure 5.98: Comparison of experimentally measured bulge profiles, differential pressure is 0.07 MPa, for PET 506, PET ST506 and PEN Teonex Q65 bare flexible display substrate.

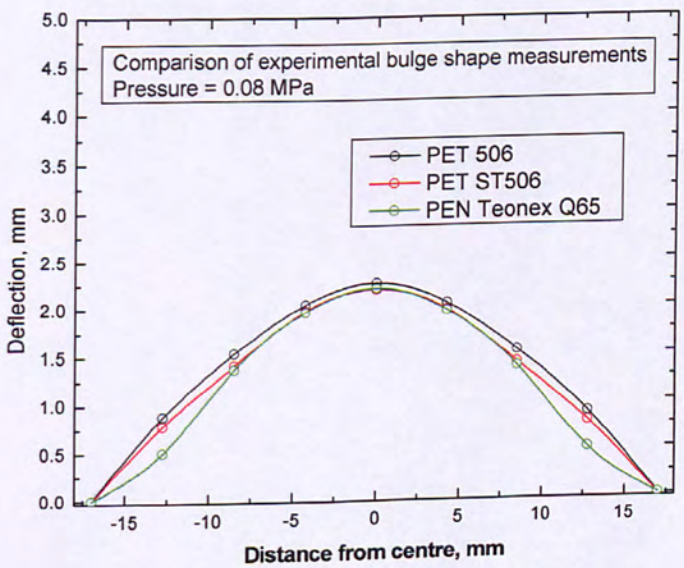

Figure 5.99: Comparison of experimentally measured bulge shapes for a differential pressure of 0.08 MPa, regarding PET 506, PET ST506 and PEN Teonex Q65 bare polyester circular substrates.

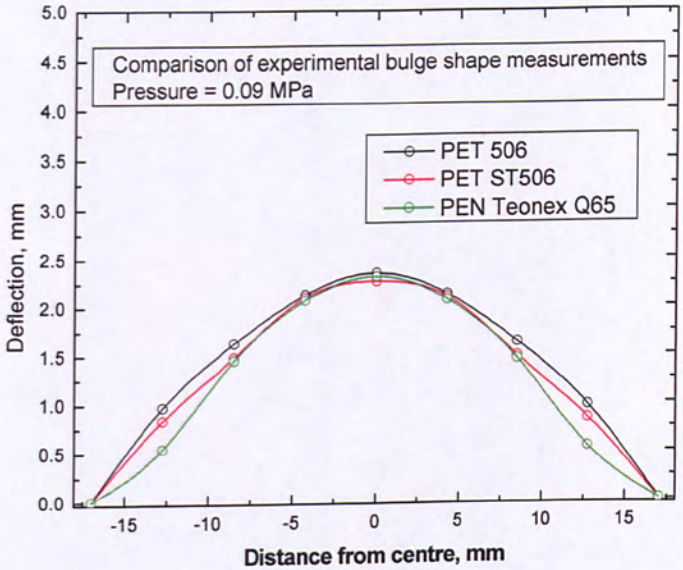

Figure 5.100: Comparison of experimentally measured bulge profiles, differential pressure is 0.09 MPa, for PET 506, PET ST506 and PEN Teonex Q65 bare flexible display substrate.

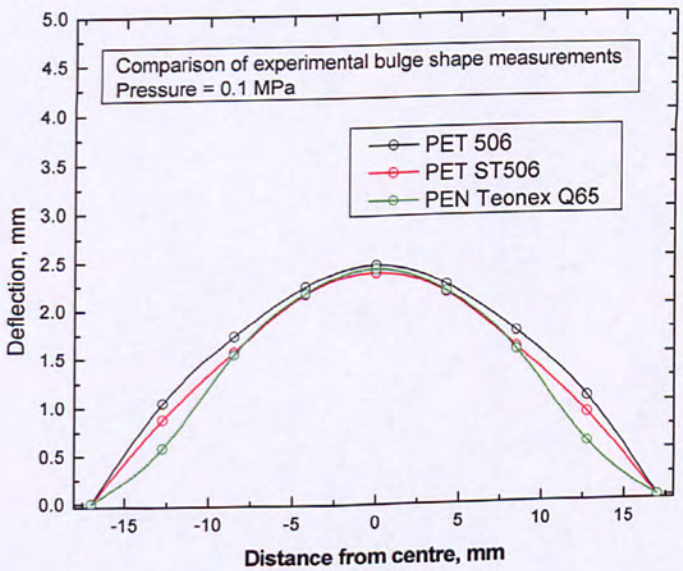

Figure 5.101: The bulge shapes, as measured experimentally, of PET 506, PET ST506 and PEN Teonex Q65 bare substrates for a differential pressure of 0.1 MPa.

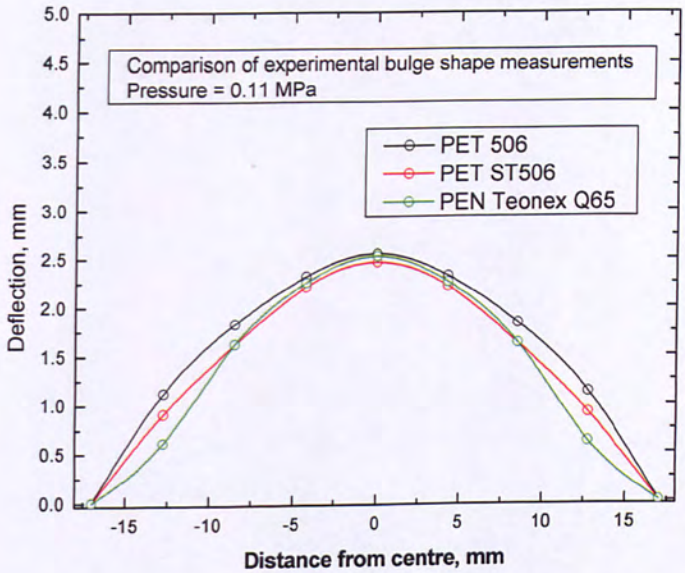

Figure 5.102: Comparison of experimentally measured bulge profiles, differential pressure is 0.11 MPa, for PET 506, PET ST506 and PEN Teonex Q65 bare flexible display substrate.

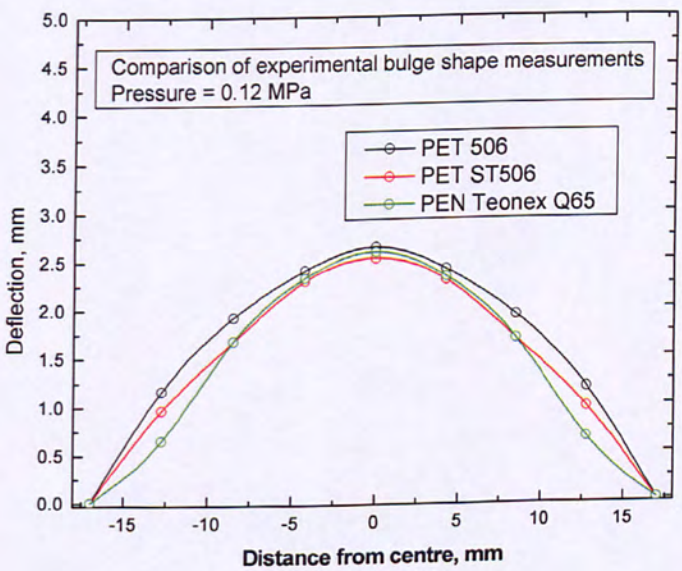

Figure 5.103: Comparison of experimentally measured bulge profiles, differential pressure is 0.12 MPa, for PET 506, PET ST506 and PEN Teonex Q65 bare flexible display substrate.

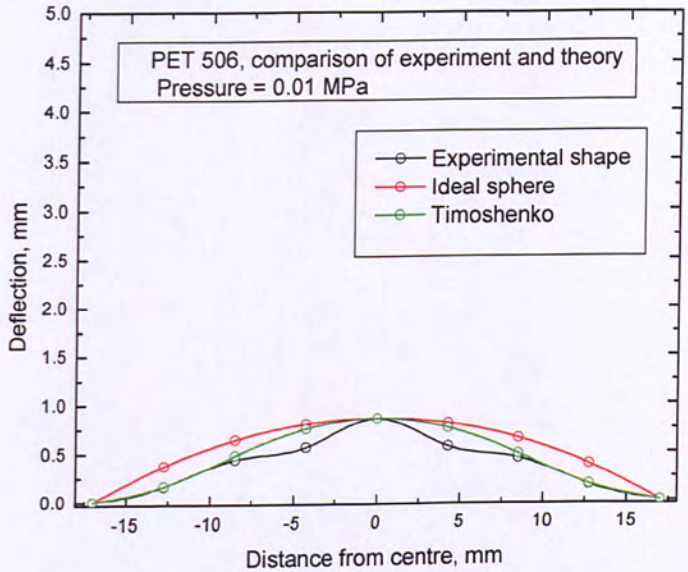

Figure 5.104: Comparison of experimentally measured bulge shape, for PET 506 bare film, with the spherical model and Timoshenko model considering 0.01 MPa of applied differential pressure.

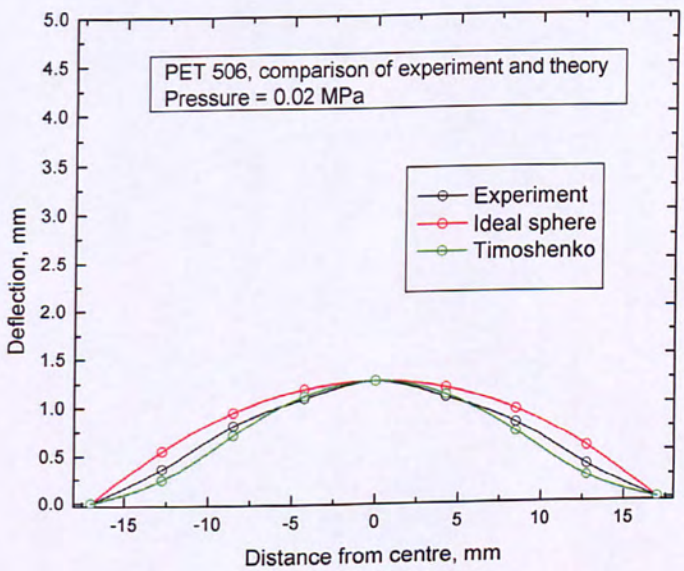

Figure 5.105: Experimentally measured bulge profile, 0.02 MPa pressure, as compared with the spherical shape and the Timoshenko predicted shape in the case of PET 506 flexible display substrate.

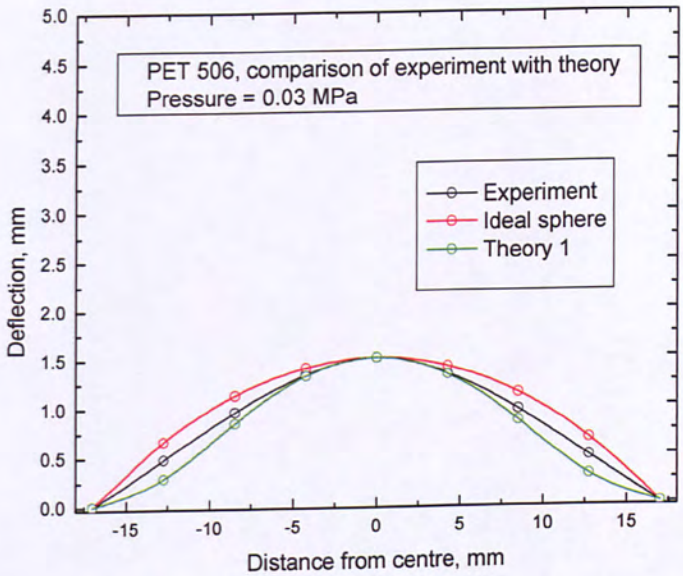

Figure 5.106: Comparison of theoretical shapes with experimentally measured shape for the case of PET 506 films and differential pressure of 0.03 MPa.

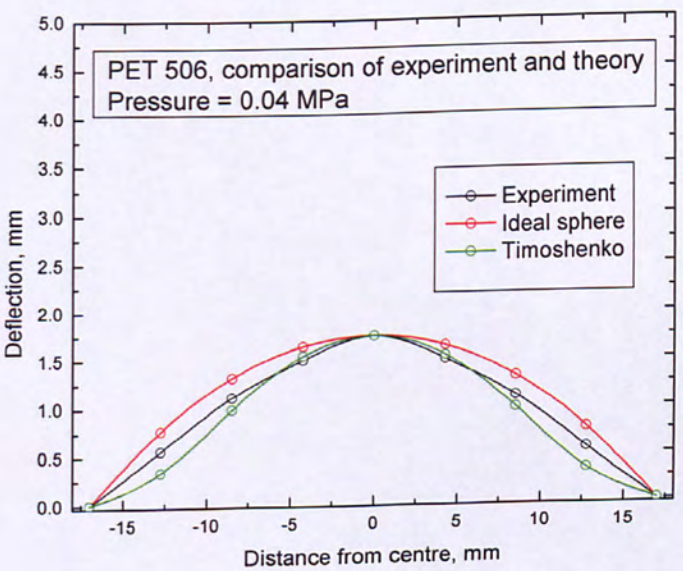

Figure 5.107: Experimentally measured bulge profile, 0.04 MPa pressure, as compared with the spherical shape and the Timoshenko predicted shape in the case of PET 506 flexible display substrate.

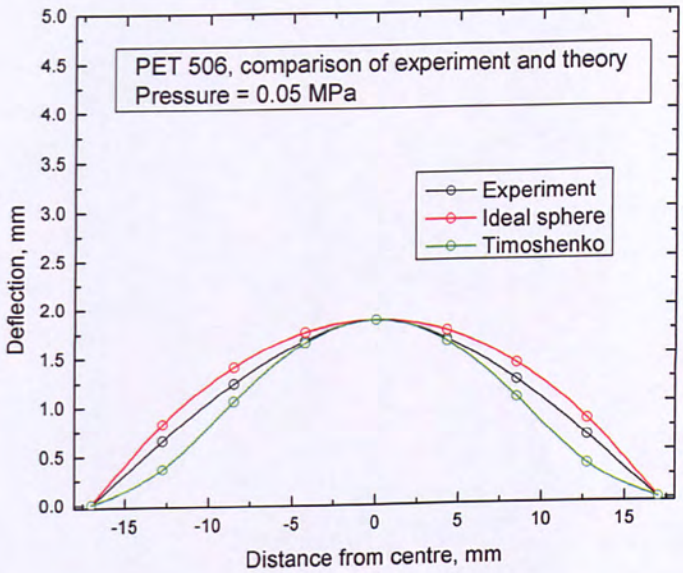

Figure 5.108: Comparison of experimentally measured bulge shape, for PET 506 bare film, with the spherical model and Timoshenko model considering 0.05 MPa of applied differential pressure.

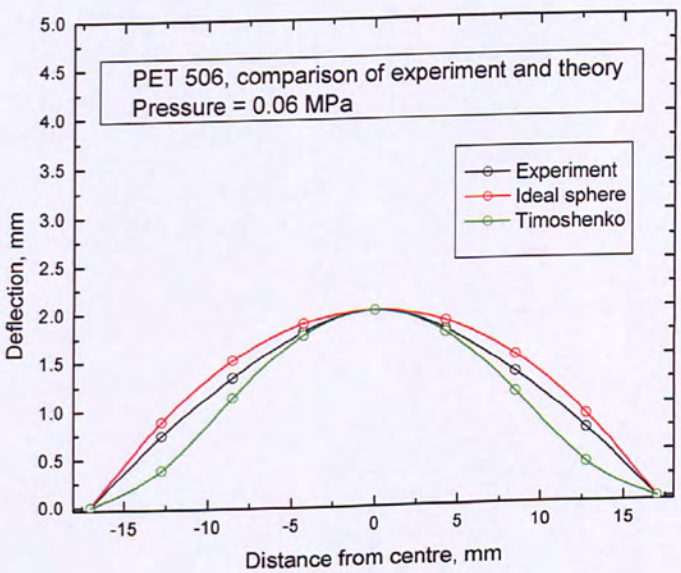

Figure 5.109: Comparison of theoretical shapes with experimentally measured shape for the case of PET 506 films and differential pressure of 0.06 MPa.

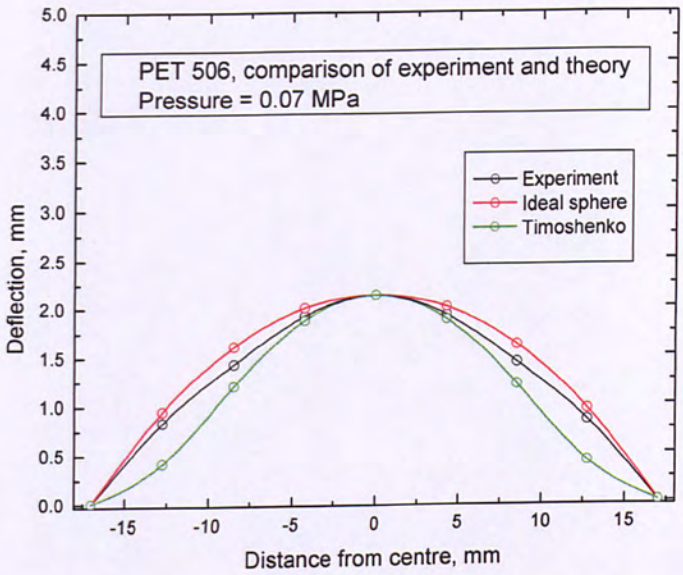

Figure 5.110: Experimentally measured bulge profile, 0.07 MPa pressure, as compared with the spherical shape and the Timoshenko predicted shape in the case of PET 506 flexible display substrate.

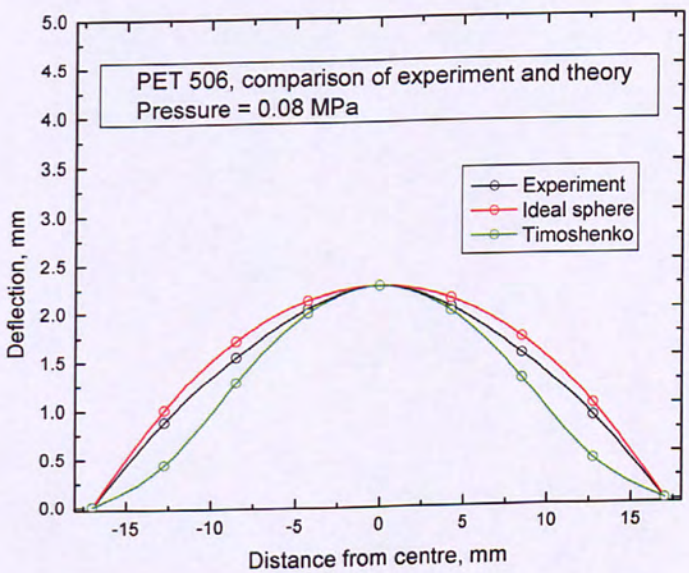

Figure 5.111: Experimentally measured bulge profile, 0.08 MPa pressure, as compared with the spherical shape and the Timoshenko predicted shape in the case of PET 506 flexible display substrate.

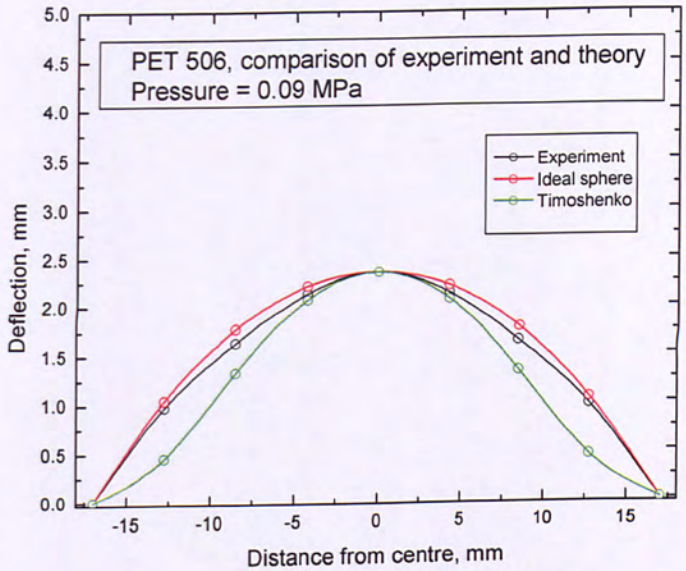

Figure 5.112: Comparison of experimentally measured bulge shape, for PET 506 bare film, with the spherical model and Timoshenko model considering 0.09 MPa of applied differential pressure.

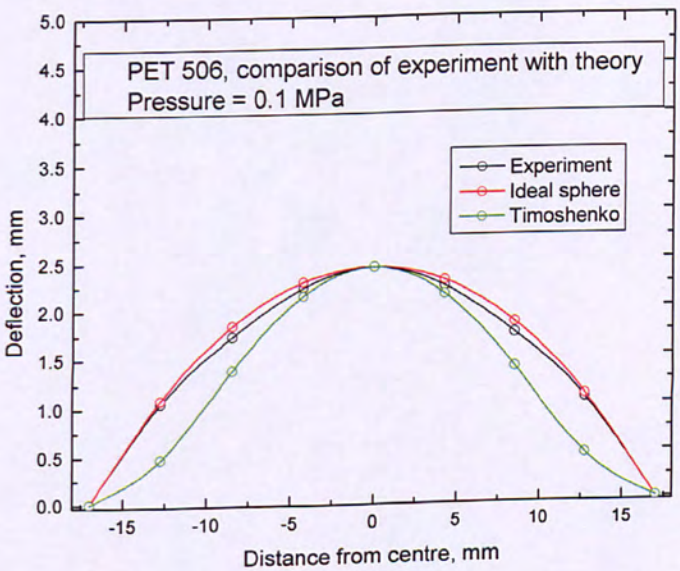

Figure 5.113: Experimentally measured bulge profile, 0.1 MPa pressure, as compared with the spherical shape and the Timoshenko predicted shape in the case of PET 506 flexible display substrate.

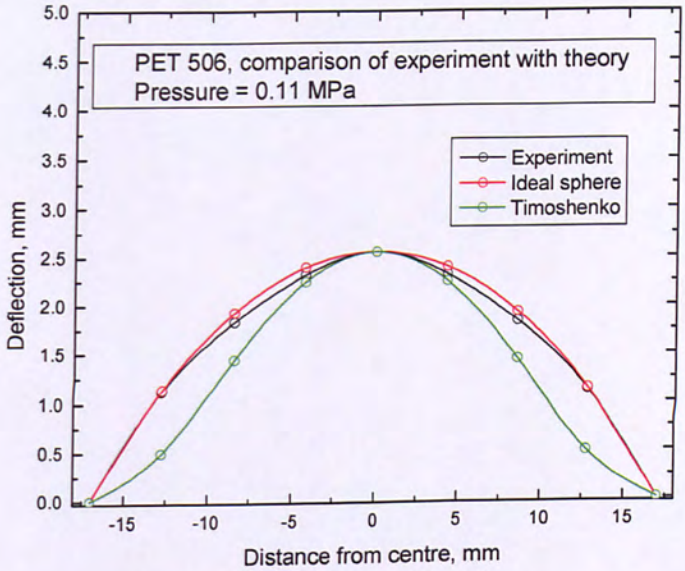

Figure 5.114: Experimentally measured bulge profile, 0.11 MPa pressure, as compared with the spherical shape and the Timoshenko predicted shape in the case of PET 506 flexible display substrate.

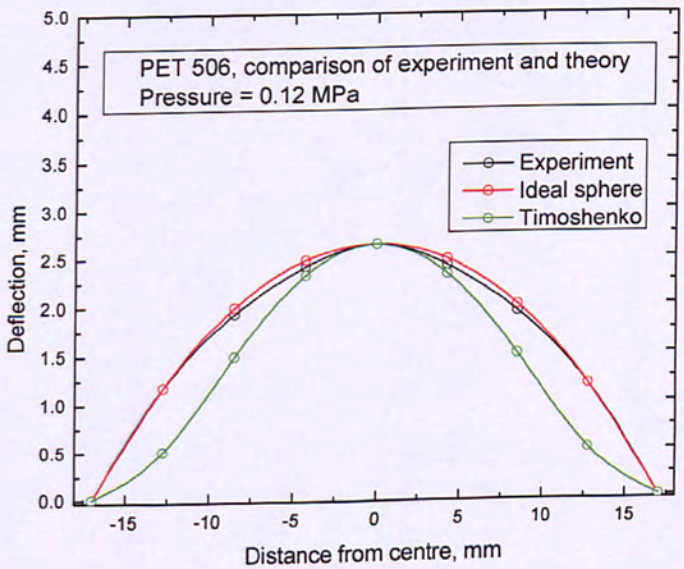

Figure 5.115: Comparison of experimentally measured bulge shape, for PET 506 bare film, with the spherical model and Timoshenko model considering 0.12 MPa of applied differential pressure.

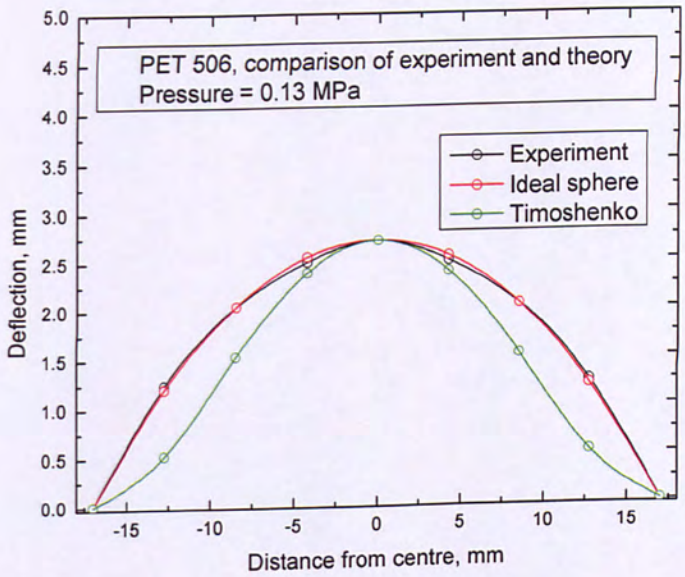

Figure 5.116: Comparison of theoretical shapes with experimentally measured shape for the case of PET 506 films and differential pressure of 0.13 MPa.

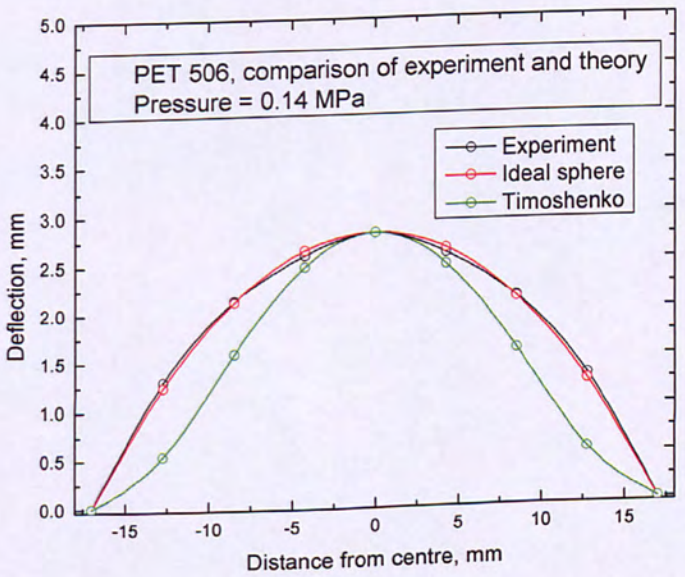

Figure 5.117: Comparison of theoretical shapes with experimentally measured shape for the case of PET 506 films and differential pressure of 0.14 MPa.

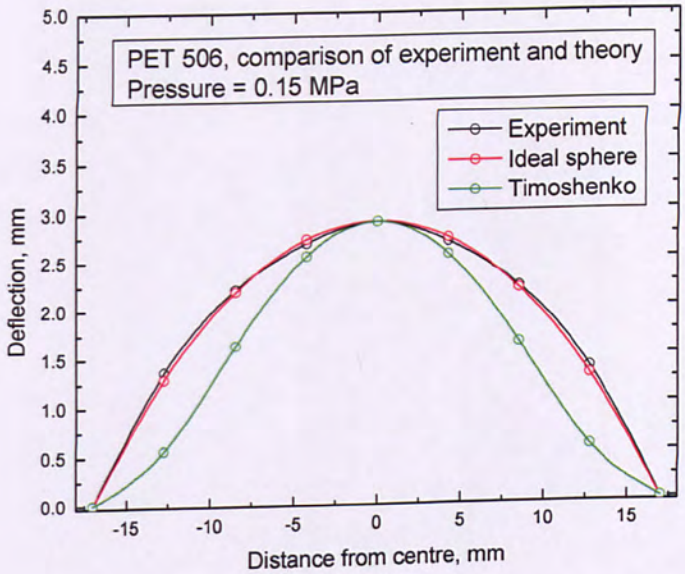

Figure 5.118: Experimentally measured bulge profile, 0.15 MPa pressure, as compared with the spherical shape and the Timoshenko predicted shape in the case of PET 506 flexible display substrate.

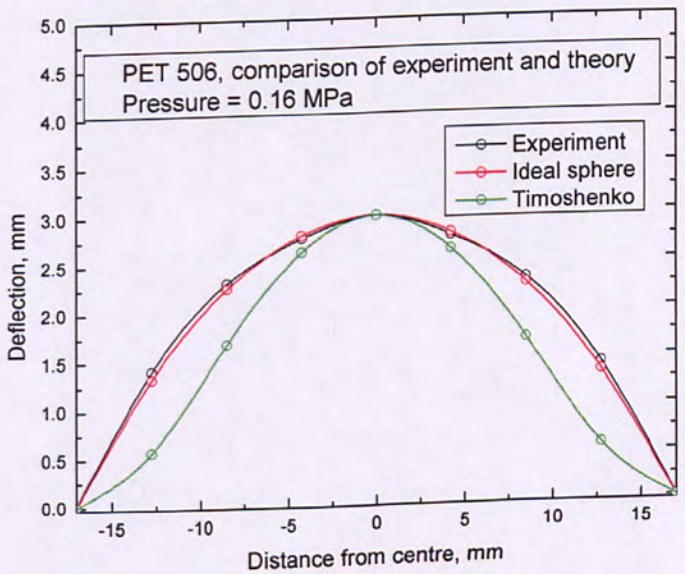

Figure 5.119: Comparison of experimentally measured bulge shape, for PET 506 bare film, with the spherical model and Timoshenko model considering 0.16 MPa of applied differential pressure.

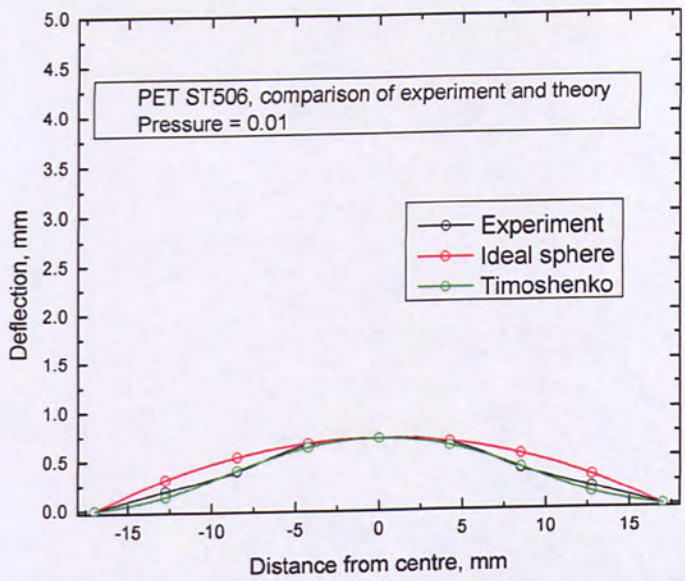

Figure 5.120: Comparison of experimentally measured bulge profile, for applied pressure of 0.01 MPa, with the spherical profile and the profile predicted by Timoshenko for PET ST506 flexible substrate.

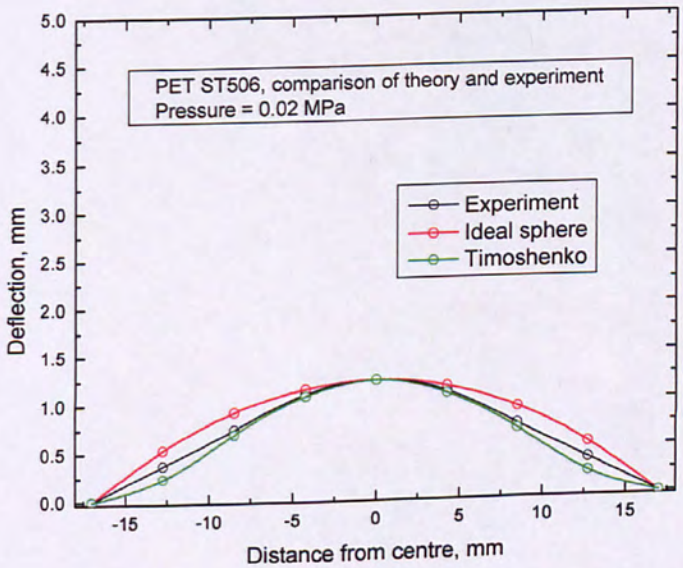

Figure 5.121: Experimental and theoretical, perfect sphere and Timoshenko, graphs, for PET ST506 bare display film, when the pressure is 0.02 MPa.

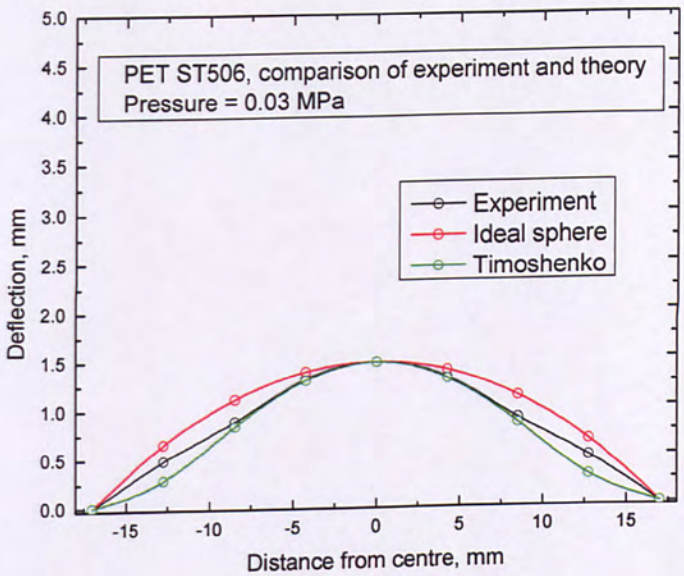

Figure 5.122: Comparison of experimentally measured bulge shape with spherical and Timoshenko predicted model for PET ST506 flexible base substrate and applied differential pressure of 0.03 MPa.

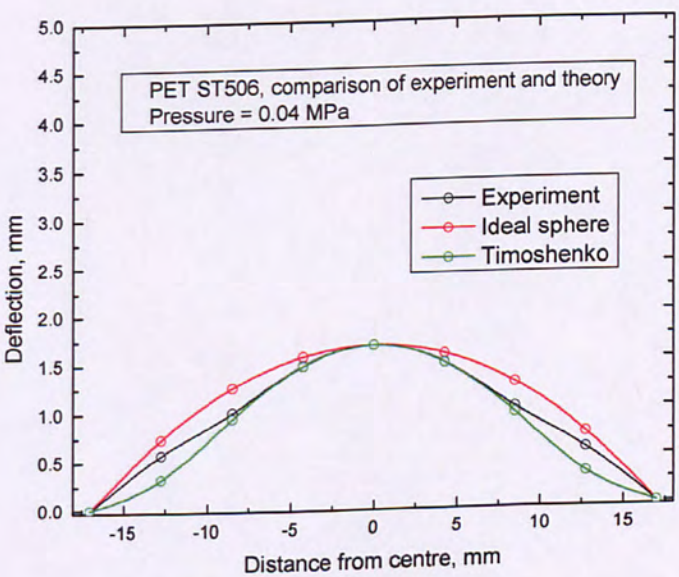

Figure 5.123: Graph showing the ideal spherical profile and the profile predicted by Timoshenko as opposed to the experimentally measured profile for the case of PET ST506 flexible thin film and pressure of 0.04 MPa.

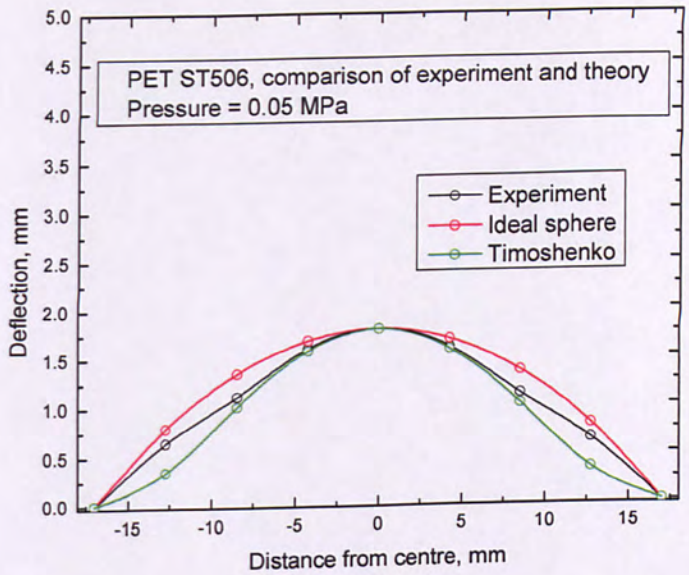

Figure 5.124: Comparison of experimentally measured bulge profile, for applied pressure of 0.05 MPa, with the spherical profile and the profile predicted by Timoshenko for PET ST506 flexible substrate.

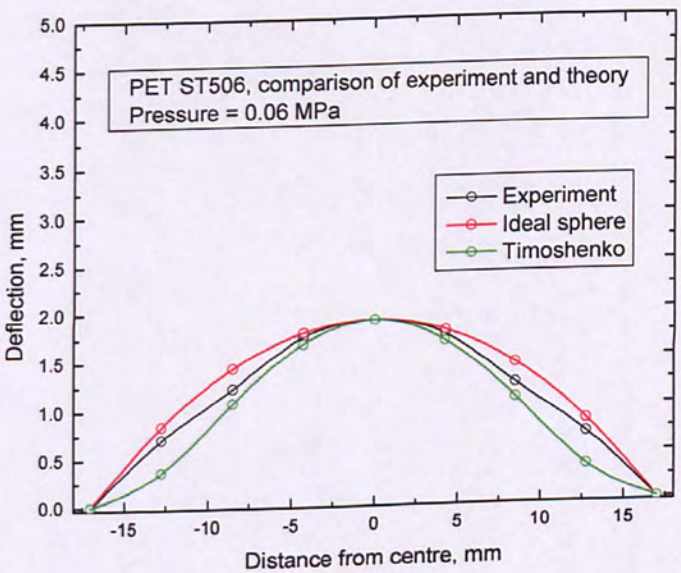

Figure 5.125: Experimental and theoretical, perfect sphere and Timoshenko, graphs, for PET ST506 bare display film, when the pressure is 0.06 MPa.

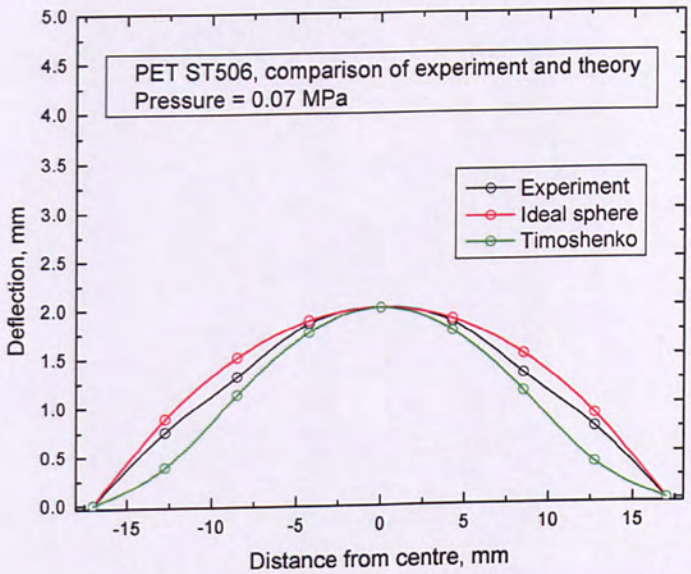

Figure 5.126: Comparison of experimentally measured bulge shape with spherical and Timoshenko predicted model for PET ST506 flexible base substrate and applied differential pressure of 0.07 MPa.

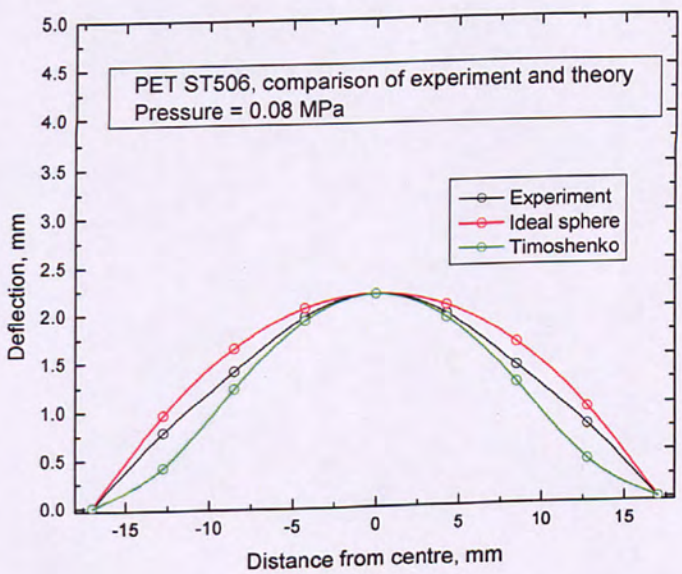

Figure 5.127: Graph showing the ideal spherical profile and the profile predicted by Timoshenko as opposed to the experimentally measured profile for the case of PET ST506 flexible thin film and pressure of 0.08 MPa.

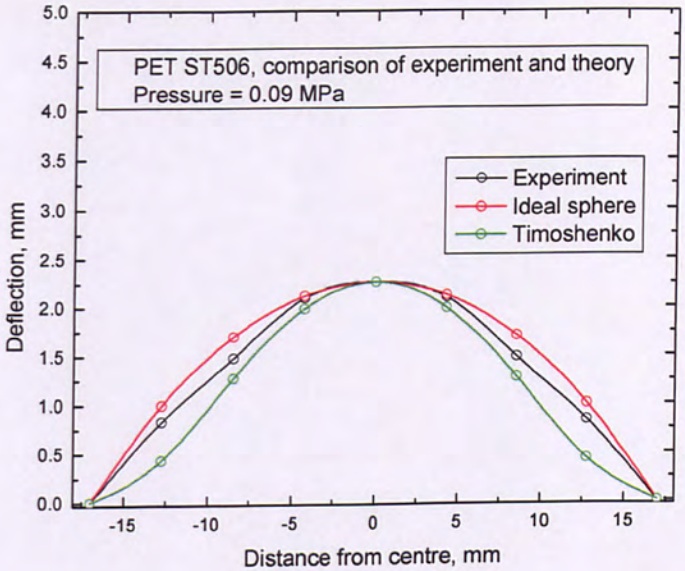

Figure 5.128: Comparison of experimentally measured bulge profile, for applied pressure of 0.09 MPa, with the spherical profile and the profile predicted by Timoshenko for PET ST506 flexible substrate.

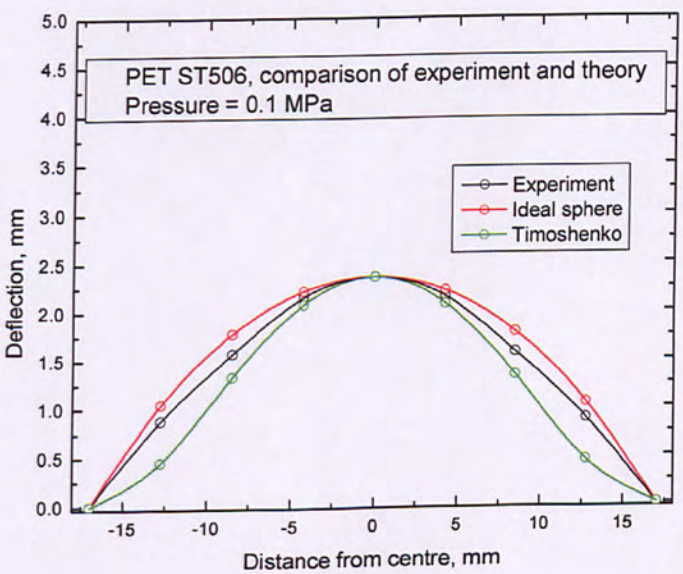

Figure 5.129: Experimental and theoretical, perfect sphere and Timoshenko, graphs, for PET ST506 bare display film, when the pressure is 0.1 MPa.

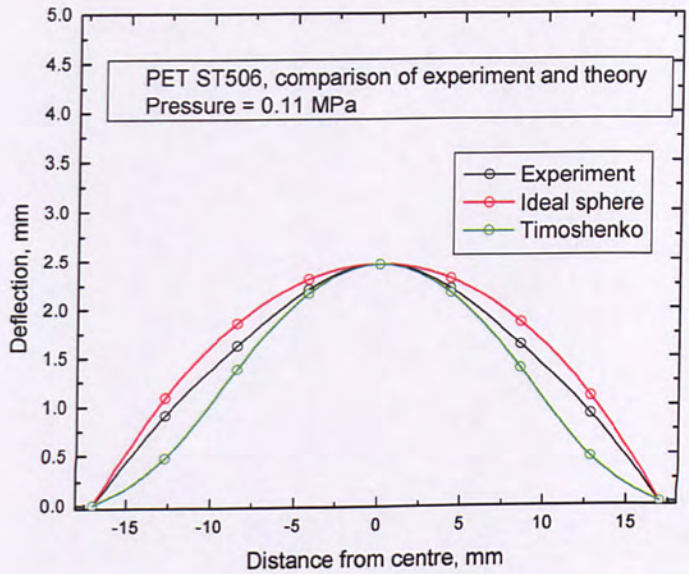

Figure 5.130: Comparison of experimentally measured bulge shape with spherical and Timoshenko predicted model for PET ST506 flexible base substrate and applied differential pressure of 0.11 MPa.

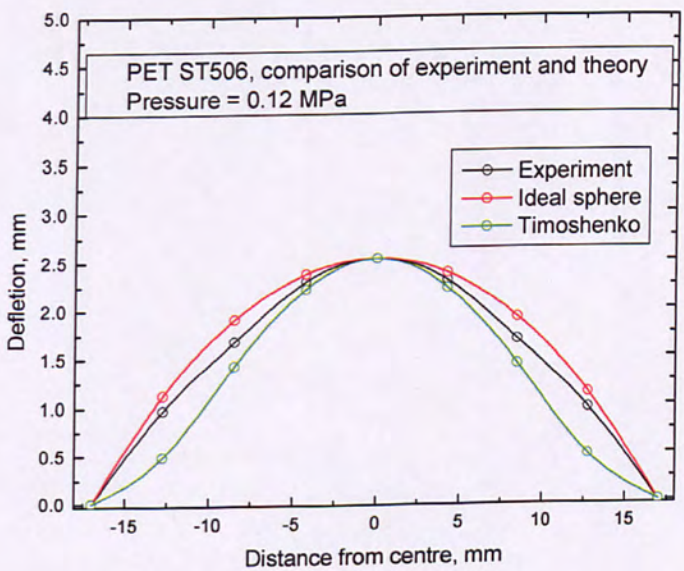

Figure 5.131: Graph showing the ideal spherical profile and the profile predicted by Timoshenko as opposed to the experimentally measured profile for the case of PET ST506 flexible thin film and pressure of 0.12 MPa.

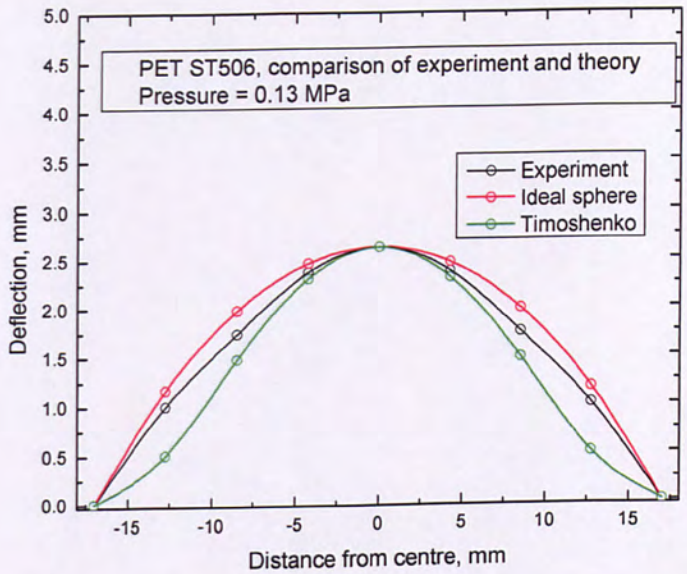

Figure 5.132: Experimental and theoretical, perfect sphere and Timoshenko, graphs, for PET ST506 bare display film, when the pressure is 0.13 MPa.

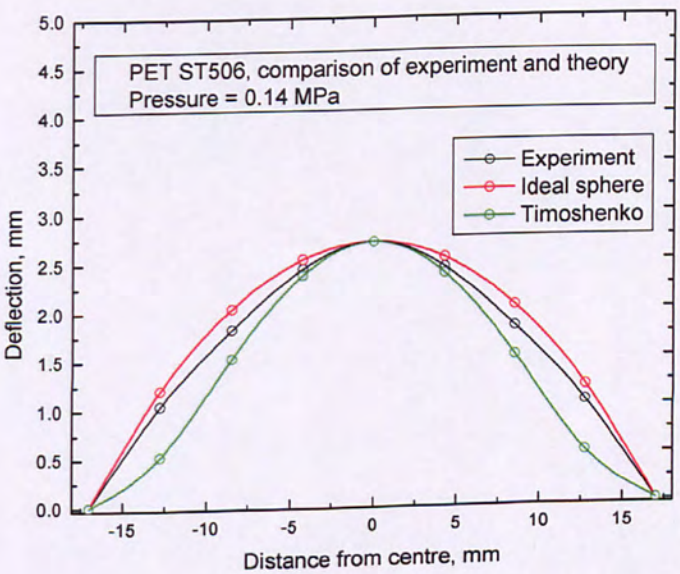

Figure 5.133: Comparison of experimentally measured bulge shape with spherical and Timoshenko predicted model for PET ST506 flexible base substrate and applied differential pressure of 0.14 MPa.

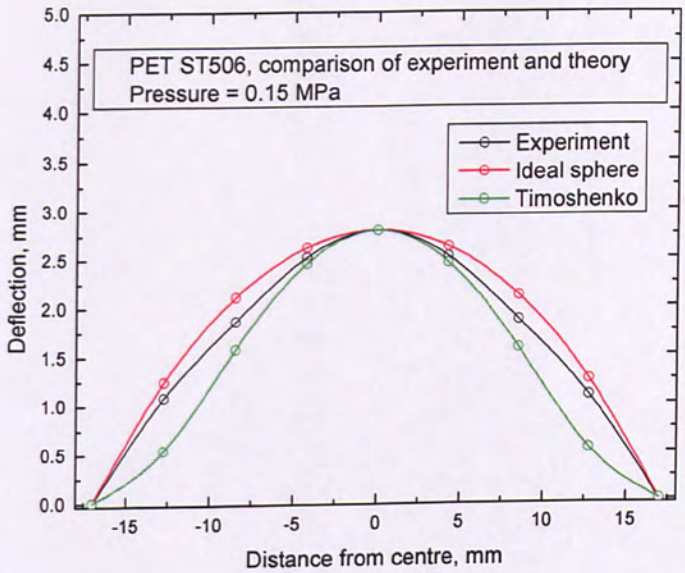

Figure 5.134: Graph showing the ideal spherical profile and the profile predicted by Timoshenko as opposed to the experimentally measured profile for the case of PET ST506 flexible thin film and pressure of 0.15 MPa.

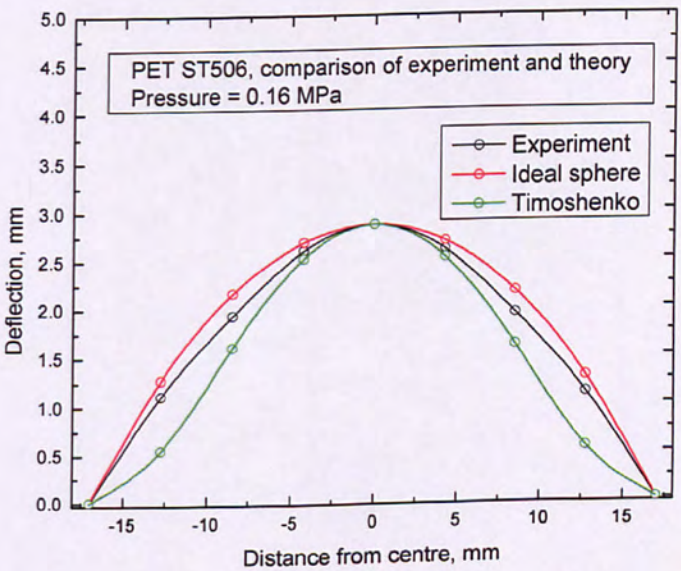

Figure 5.135: Experimental and theoretical, perfect sphere and Timoshenko, graphs, for PET ST506 bare display film, when the pressure is 0.16 MPa.

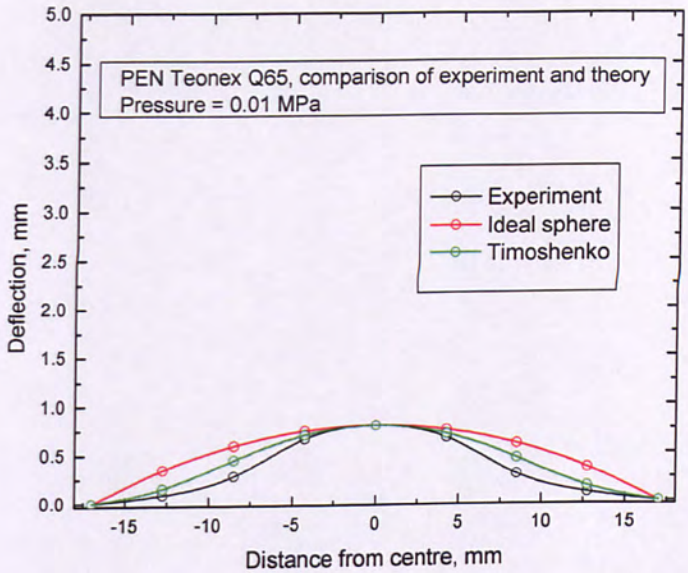

Figure 5.136: Comparison of experimentally measured bulge shape with ideal spherical shape and Timoshenko predicted shape for PEN Teonex Q65 and differential pressure of 0.01 MPa.

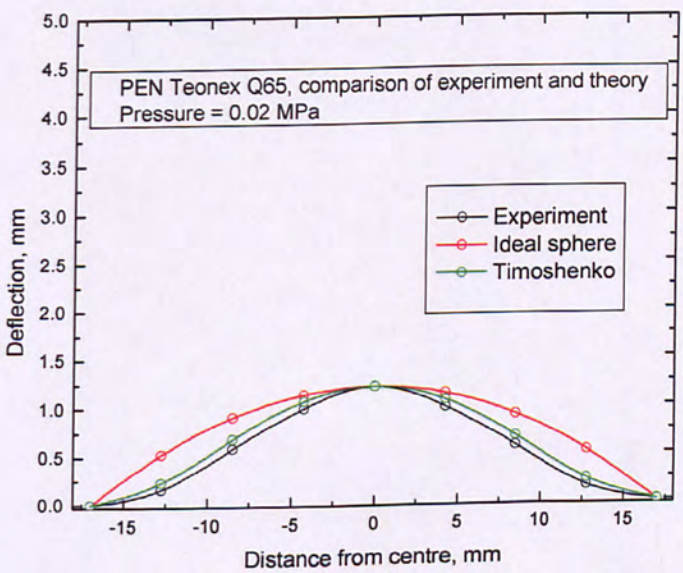

Figure 5.137: Experimentally measured film profile compared with the spherical profile and Timoshenko model for PEN Teonex Q65 display substrate and applied pressure of 0.02 MPa.

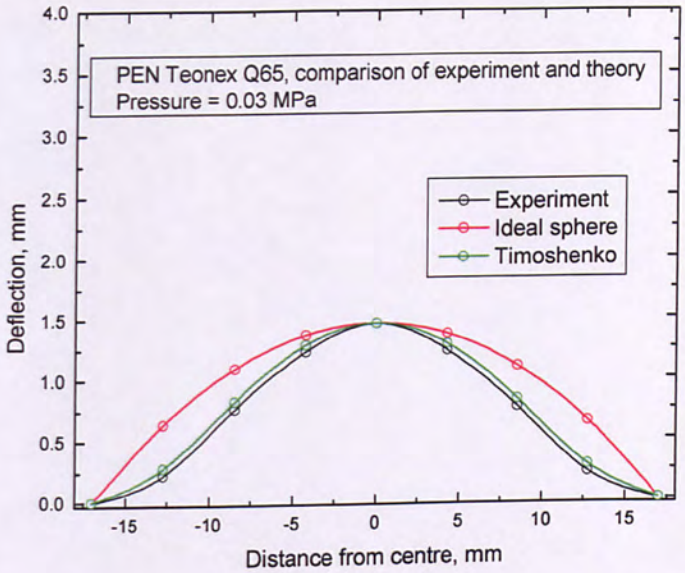

Figure 5.138: Graph showing the experimentally measured 2D shape as opposed to the spherical cap and Timoshenko predicted shape for PEN Teonex Q65 and external pressure of 0.03 MPa.

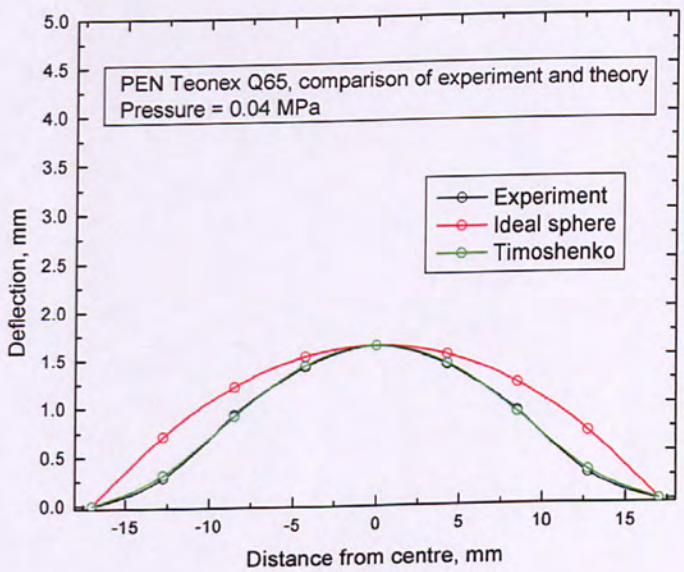

Figure 5.139: Data presenting the comparison of experimentally measured bulge profile with the perfect spherical profile and the Timoshenko predicted profile for PEN Teonex Q65 display bare base substrate and differential pressure of 0.04 MPa.

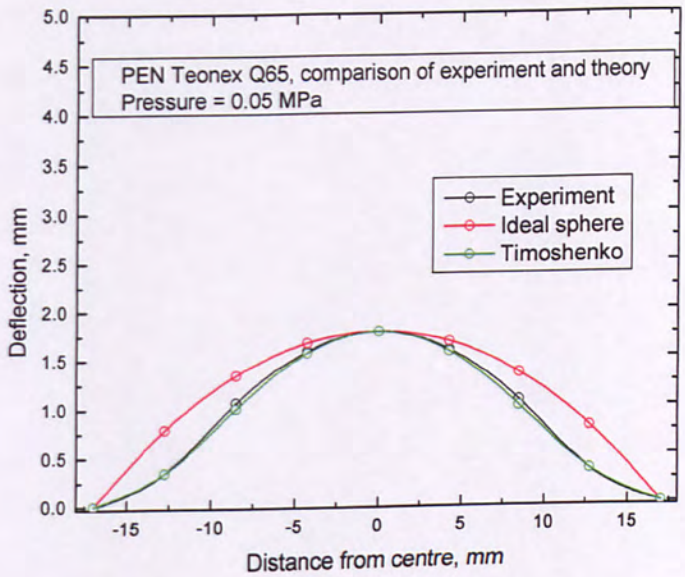

Figure 5.140: Comparison of experimentally measured bulge shape with ideal spherical shape and Timoshenko predicted shape for PEN Teonex Q65 and differential pressure of 0.05 MPa.

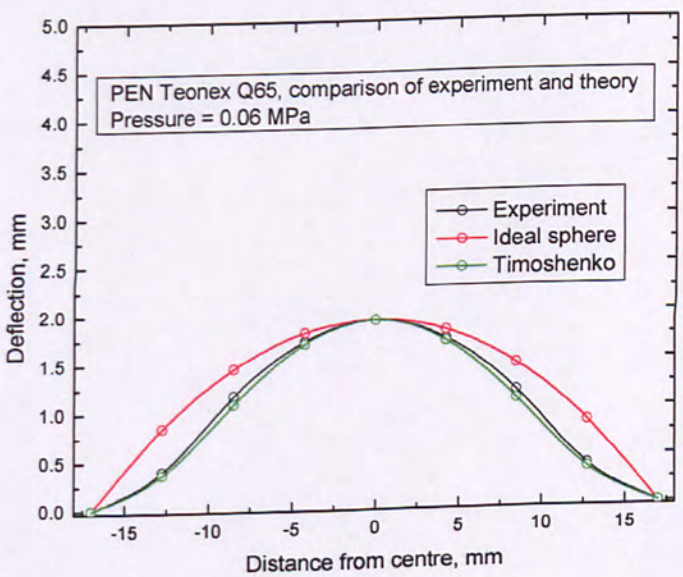

Figure 5.141: Experimentally measured film profile compared with the spherical profile and Timoshenko model for PEN Teonex Q65 display substrate and applied pressure of 0.06 MPa.

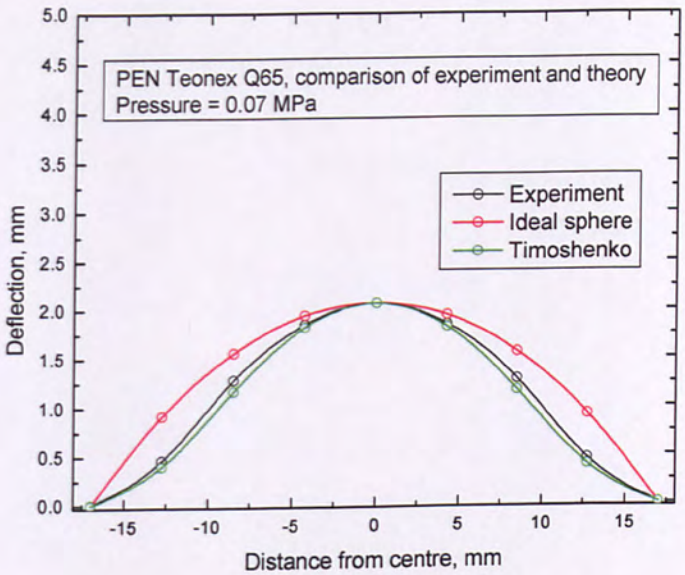

Figure 5.142: Graph showing the experimentally measured 2D shape as opposed to the spherical cap and Timoshenko predicted shape for PEN Teonex Q65 and external pressure of 0.07 MPa.

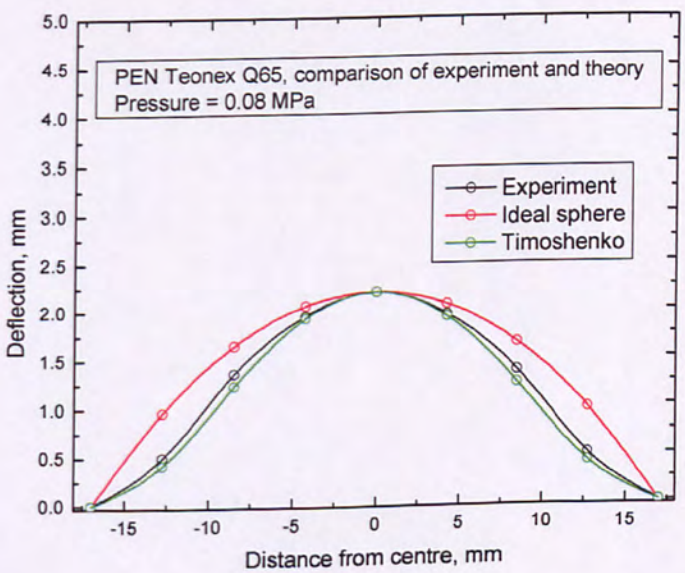

Figure 5.143: Data presenting the comparison of experimentally measured bulge profile with the perfect spherical profile and the Timoshenko predicted profile for PEN Teonex Q65 display bare base substrate and differential pressure of 0.08 MPa.

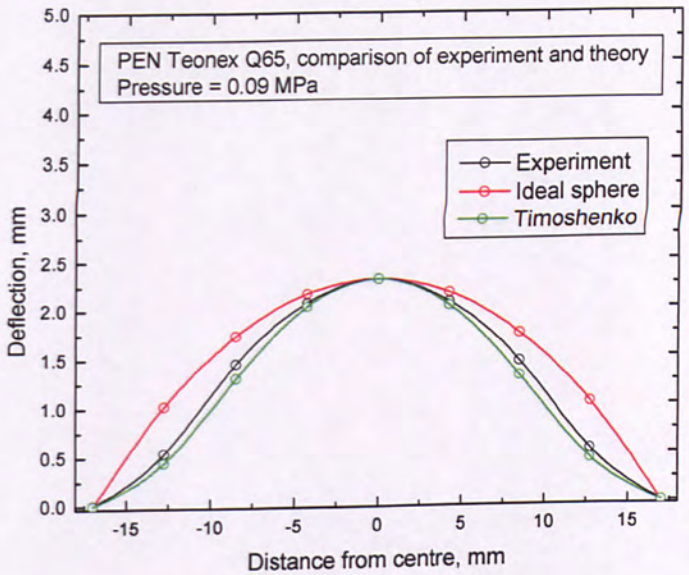

Figure 5.144: Comparison of experimentally measured bulge shape with ideal spherical shape and Timoshenko predicted shape for PEN Teonex Q65 and differential pressure of 0.09 MPa.

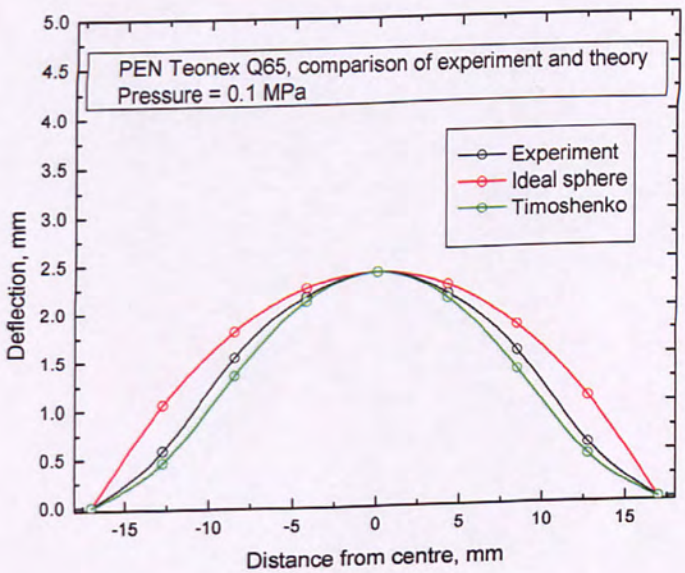

Figure 5.145: Experimentally measured film profile compared with the spherical profile and Timoshenko model for PEN Teonex Q65 display substrate and applied pressure of 0.1 MPa.

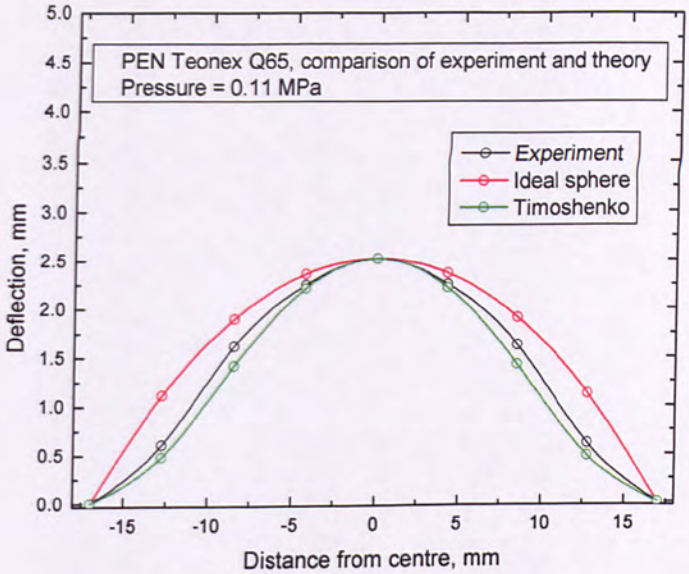

Figure 5.146: Graph showing the experimentally measured 2D shape as opposed to the spherical cap and Timoshenko predicted shape for PEN Teonex Q65 and external pressure of 0.11 MPa.

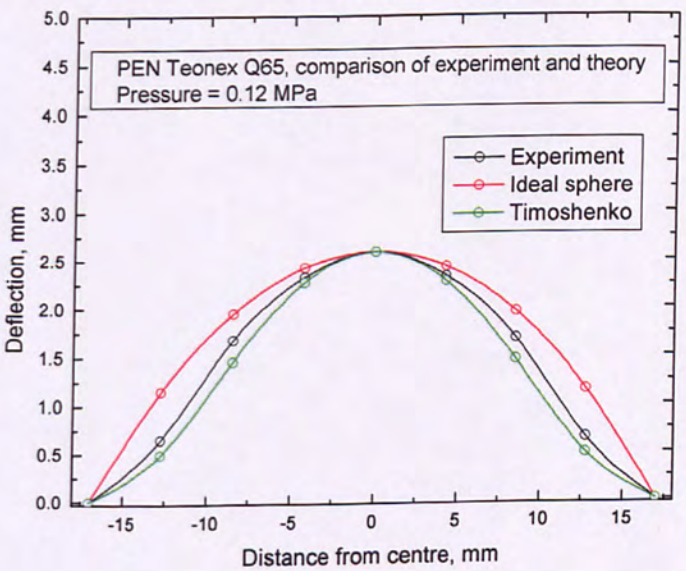

Figure 5.147: Data presenting the comparison of experimentally measured bulge profile with the perfect spherical profile and the Timoshenko predicted profile for PEN Teonex Q65 display bare base substrate and differential pressure of 0.12 MPa.

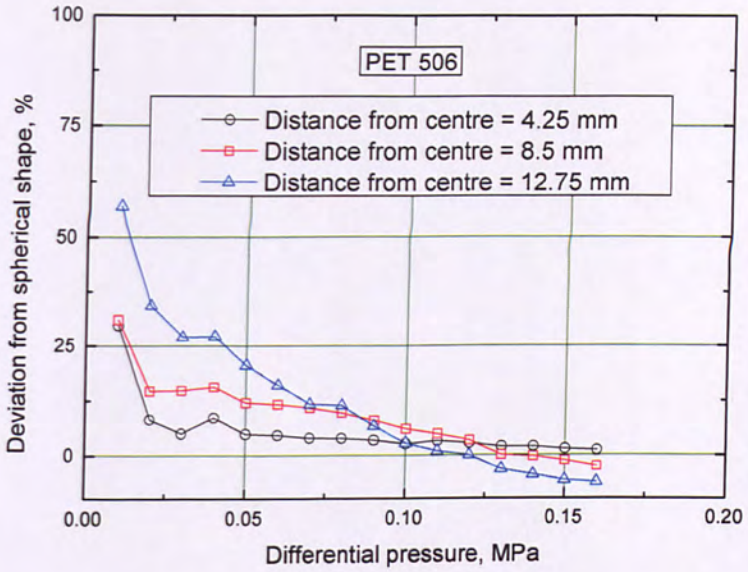

Figure 5.148: Deviation of experimental data from ideal spherical shape with respect to increasing pressure for the case of PET 506 substrate.

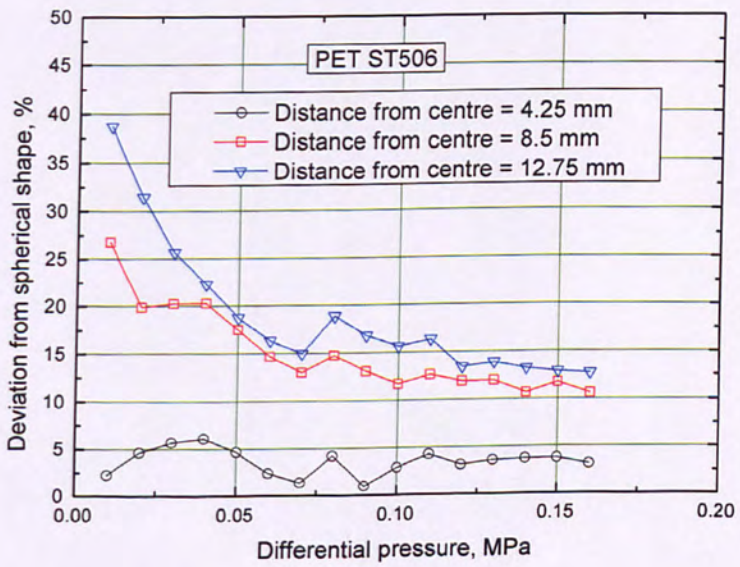

Figure 5.149: Deviation of the experimental bulge shape from the ideal spherical shape against differential pressure in the case of PET ST506 uncoated substrate.

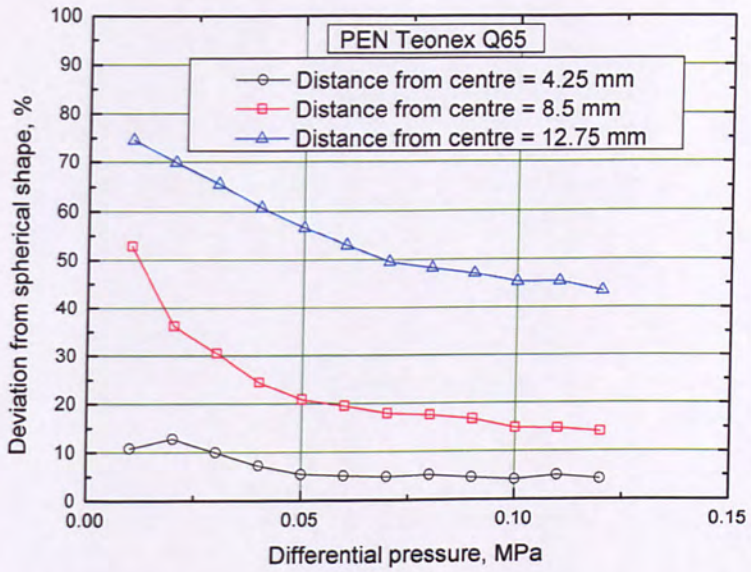

Figure 5.150: Deviation of experimental measured shape from the ideal spherical shape for the case of a PEN Teonex Q65 bare substrate.

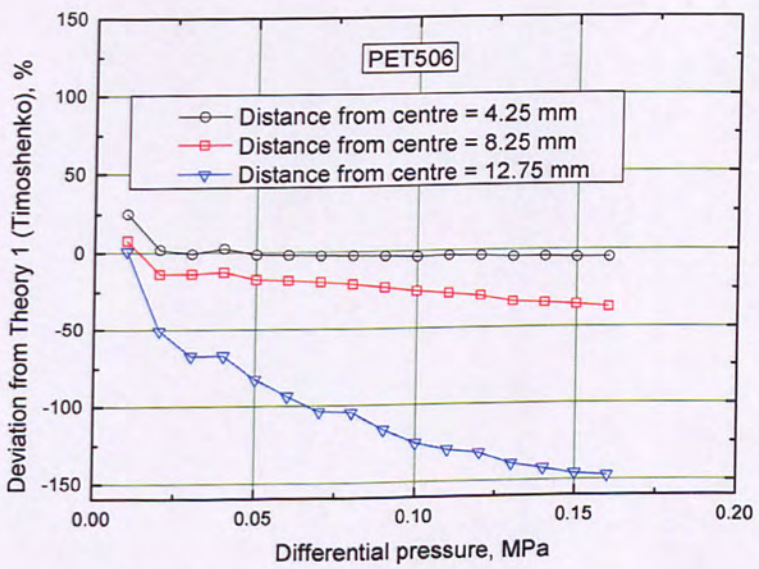

Figure 5.151: Deviation of experimentally measured bulge shape from Timoshenko's predicted shape with respect to differential pressure for the case of PET 506 bare substrate.

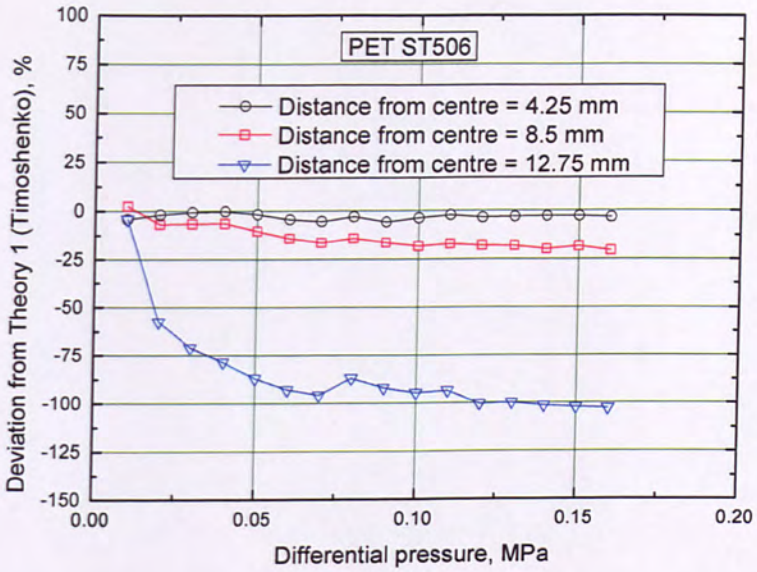

Figure 5.152: Deviation of experimental bulge shape data from theory 1, predicted by Timoshenko, plotted against differential pressure regarding PET ST506 flexible bare substrate.

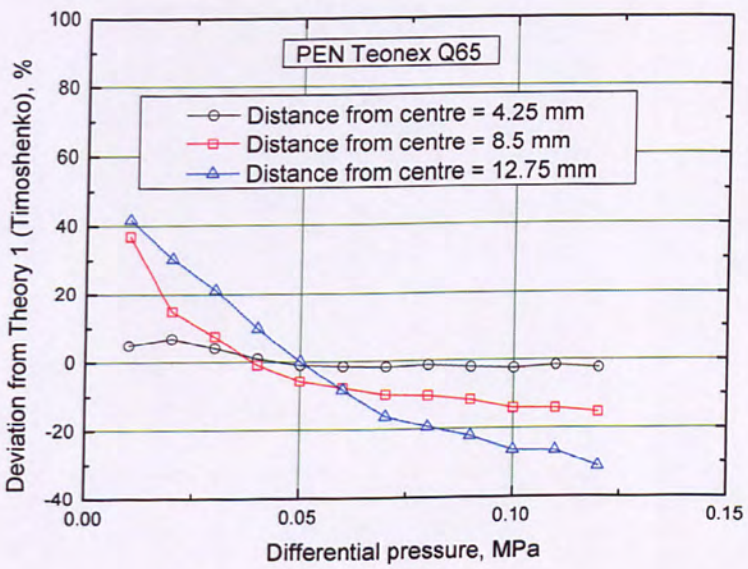

Figure 5.153: Deviation of experimental shape from Timoshenko's prediction with applied differential bulge pressure for the case of PEN Teonex Q65 polyester substrate.

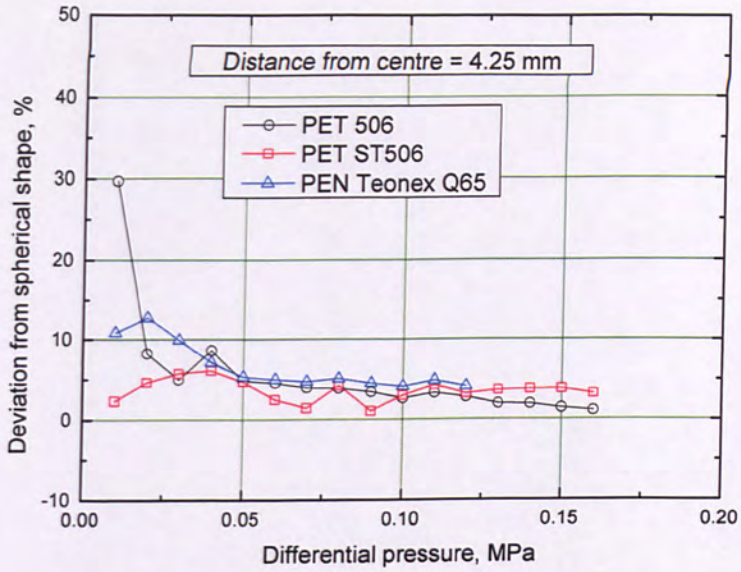

Figure 5.154: Deviation of experimentally measured deflection, distance is 4.25 mm from the centre of the circular film, from the ideal spherical shape with respect to pressure. The different polyester substrates are compared.

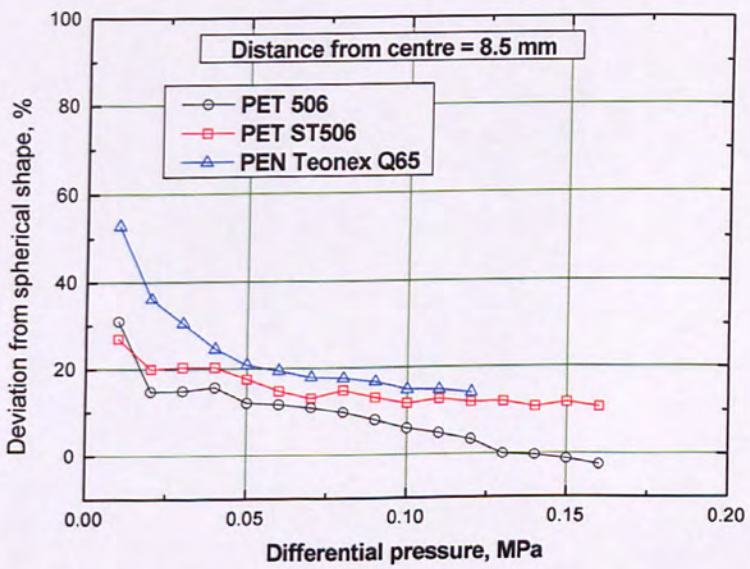

Figure 5.155: Deviation of experimentally measured deflection, 8.5 mm from the centre of the circular film, from the ideal spherical shape plotted against the differential bulge pressure. The three different bare substrates are compared.

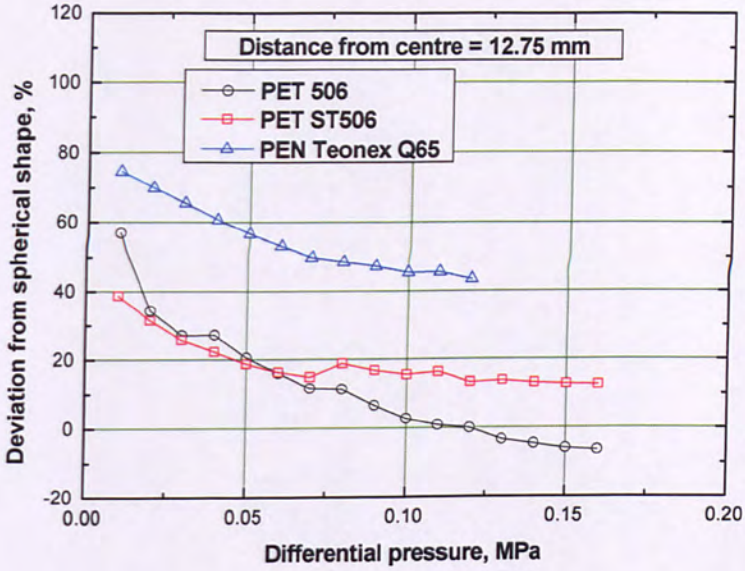

Figure 5.156: Deviation of experimentally measured deflection, distance is 12.75 mm from the centre of the circular film, from the ideal spherical shape with respect to pressure. The different flexible display substrates are compared.

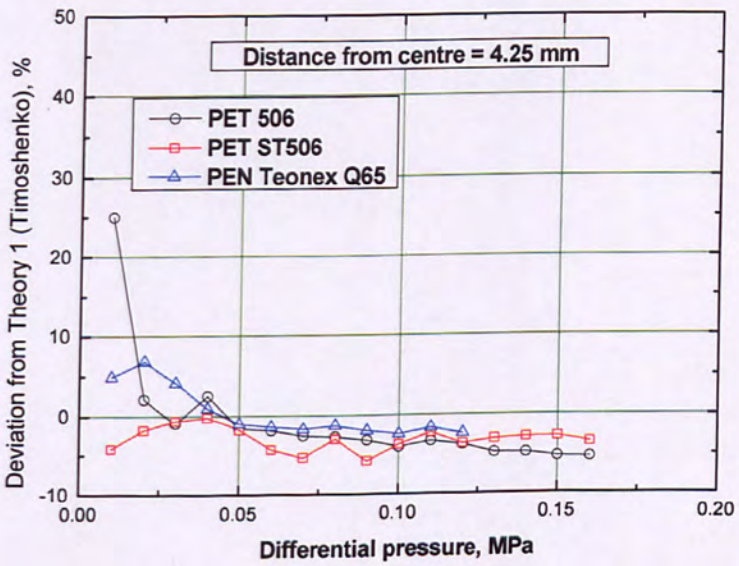

Figure 5.157: Deviation of experimentally measured deflection, distance is 4.25 mm from the centre of the circular film, from Timoshenko's predicted shape plotted against pressure. The different polyester substrates are compared.

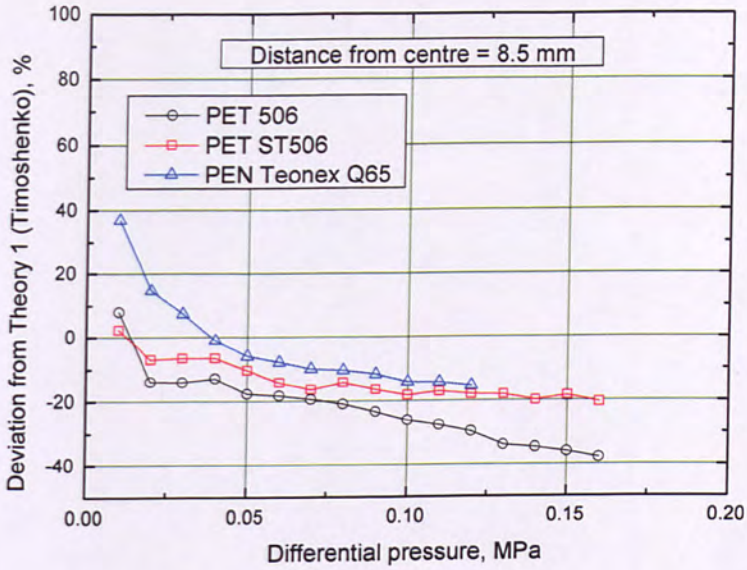

Figure 5.158: Deviation of experimentally measured deflection, 8.5 mm from the centre of the circular film, from the shape predicted by Timoshenko's theory 1 plotted against the differential bulge pressure. The three different bare display substrates are compared.

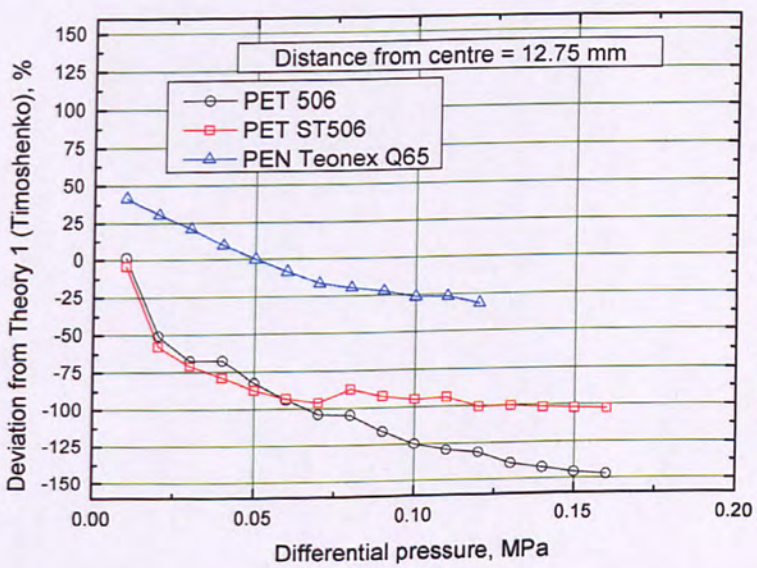

Figure 5.159: Deviation of experimentally measured deflection, distance is 4.25 mm from the centre of the circular film, from Timoshenko's predicted deflection plotted against pressure. The different thin substrates are compared.

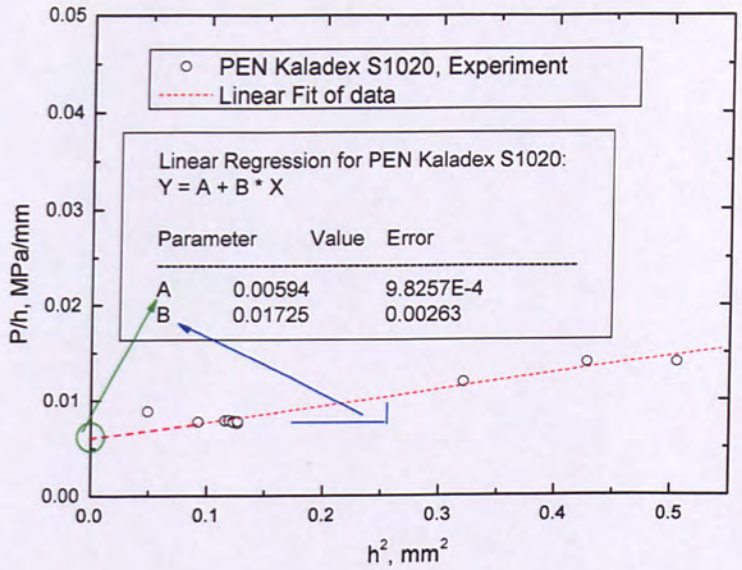

Figure 5.160: Typical linear fit of bulge test data in order to extract the initial stress and the biaxial modulus for the case of PEN Kaladex S1020 bare substrate.

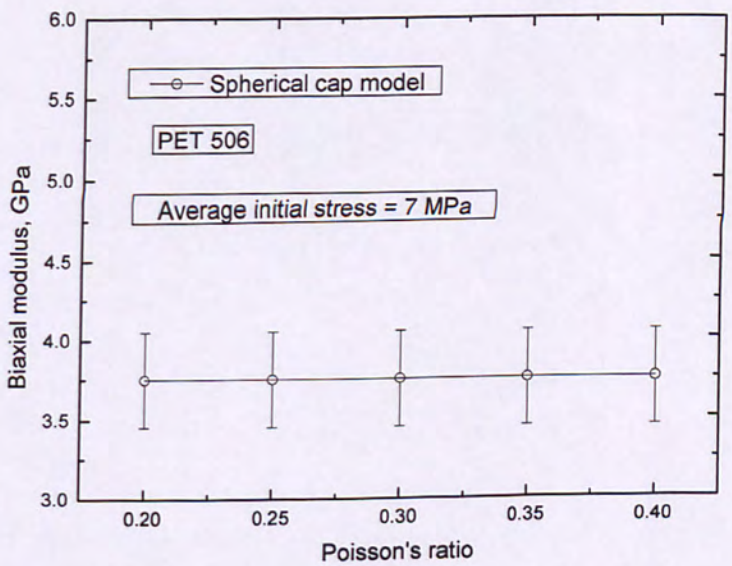

Figure 5.161: Biaxial modulus as a function of Poisson's ratio for the case of PET 506 using the spherical cap model.

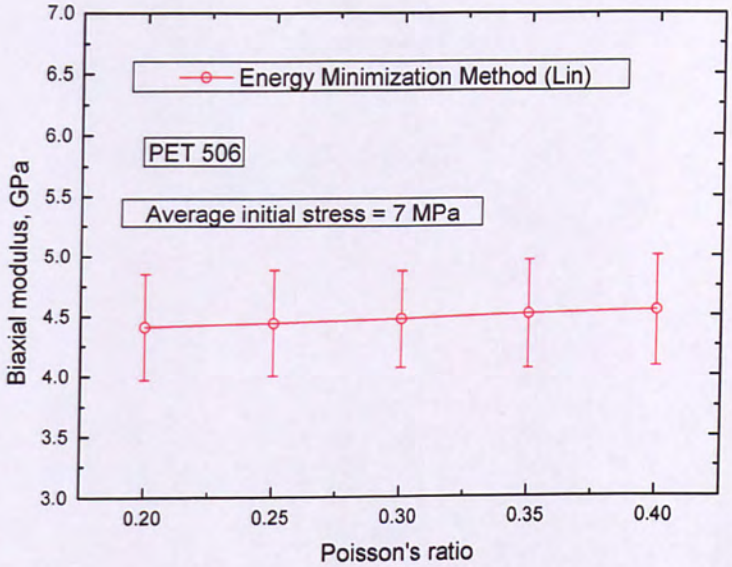

Figure 5.162: Variation of the biaxial modulus with respect to Poisson's ratio for the case of PET 506 using Lin's model.

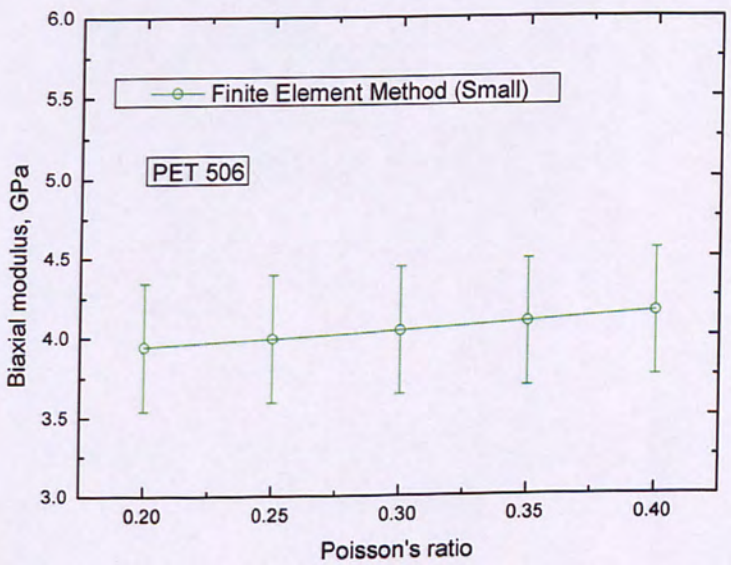

Figure 5.163: Dependence of biaxial modulus on Poisson's ratio for PET 506 as predicted by Small's finite element model.

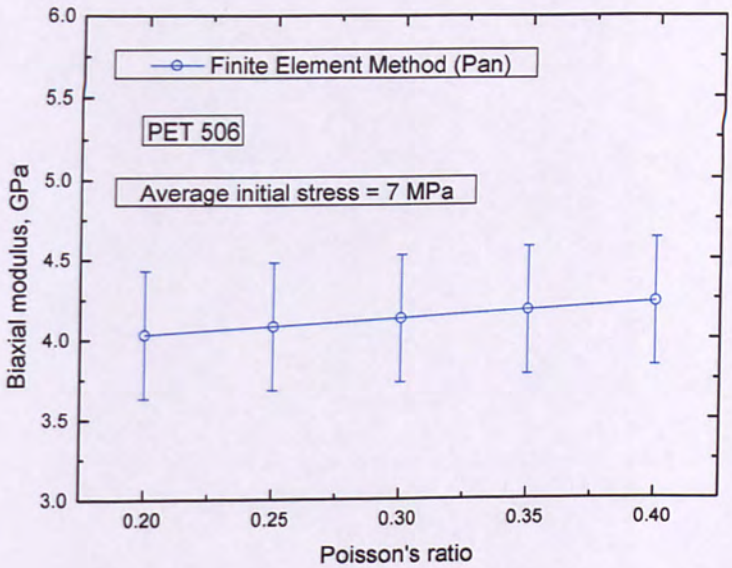

Figure 5.164: Biaxial modulus versus Poisson's ratio for PET 506 using Pan's model.

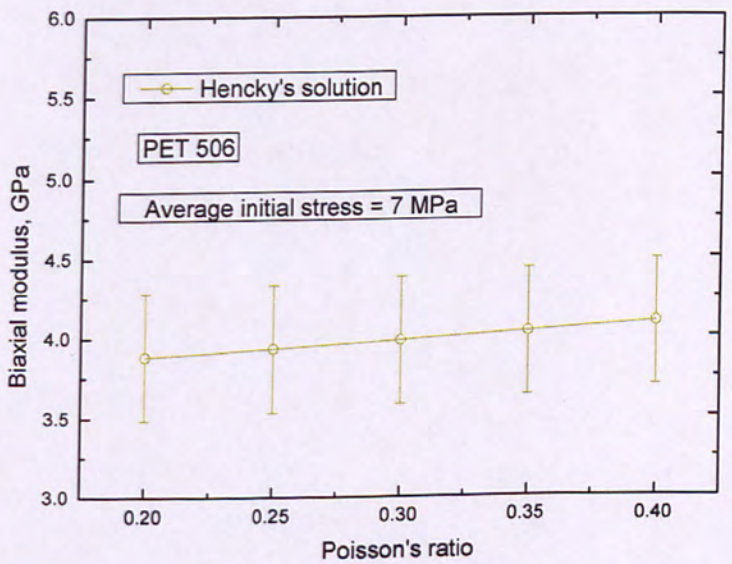

Figure 5.165: Variation of biaxial modulus against Poisson's ratio using Hencky's model regarding PET 506.

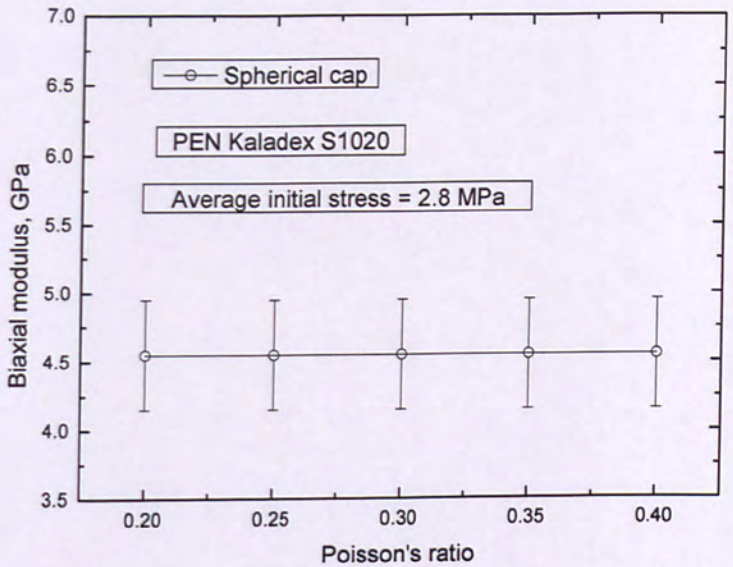

Figure 5.166: Biaxial modulus as a function of Poisson's ratio for the case of PEN Kaladex S1020 using the spherical cap model.

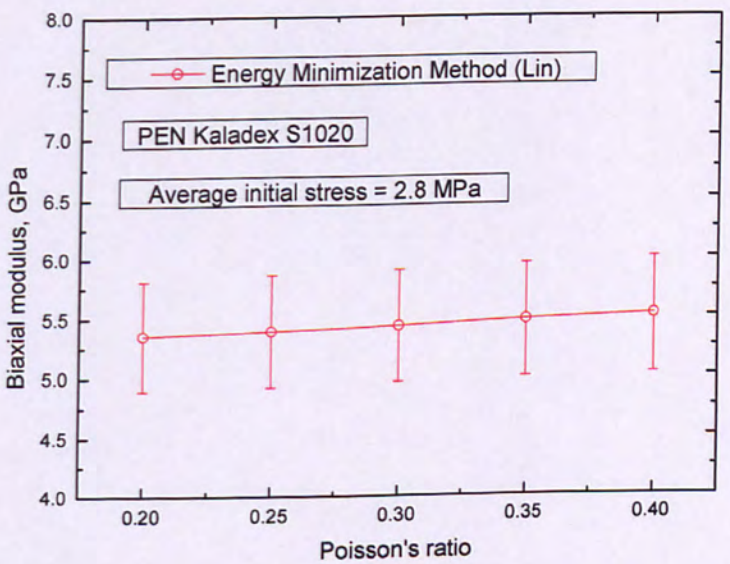

Figure 5.167: Variation of the biaxial modulus with respect to Poisson's ratio for the case of PEN Kaladex S1020 using Lin's model.

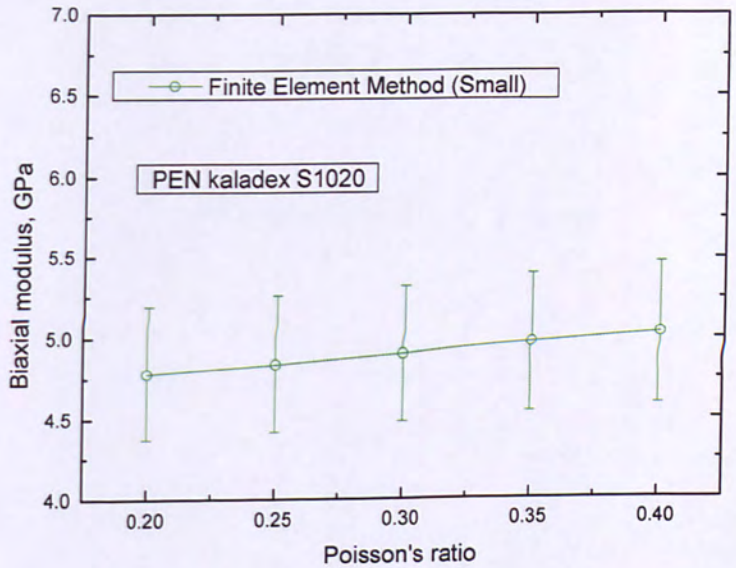

Figure 5.168: Dependence of biaxial modulus on Poisson's ratio for PEN Kaladex S1020 as predicted by Small's finite element model.

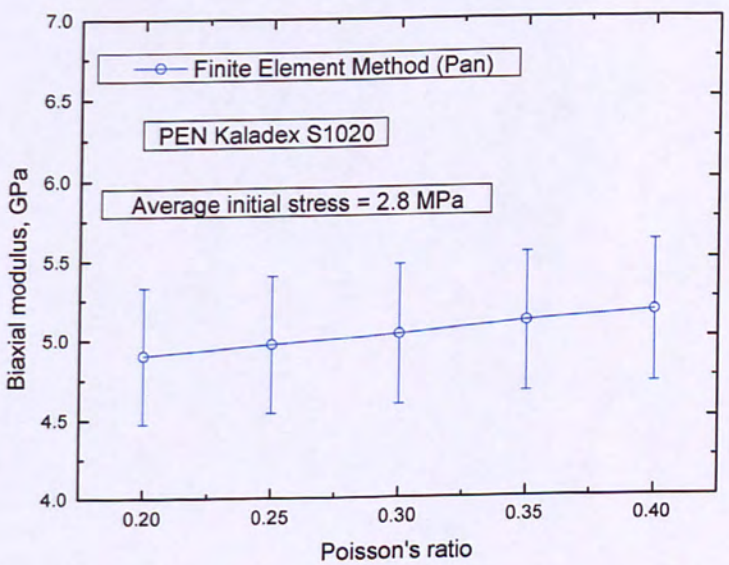

Figure 5.169: Biaxial modulus versus Poisson's ratio for PEN Kaladex S1020 using Pan's model.

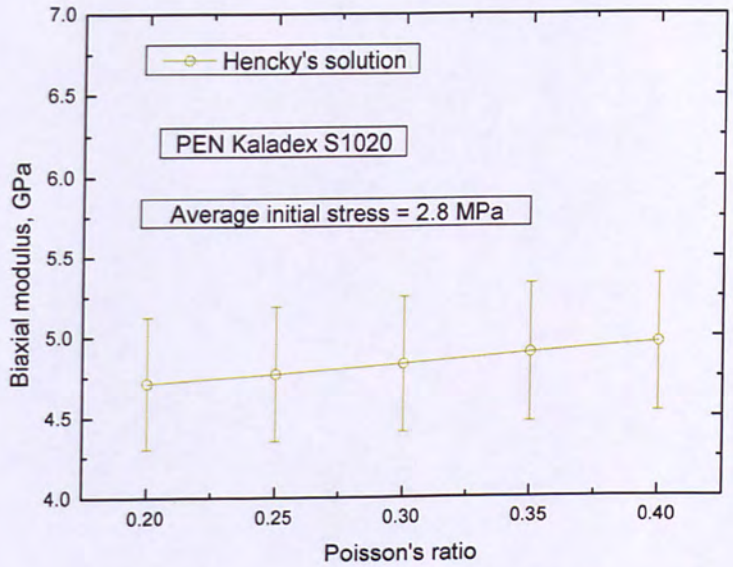

Figure 5.170: Variation of biaxial modulus against Poisson's ratio using Hencky's model regarding PEN Kaladex S1020.

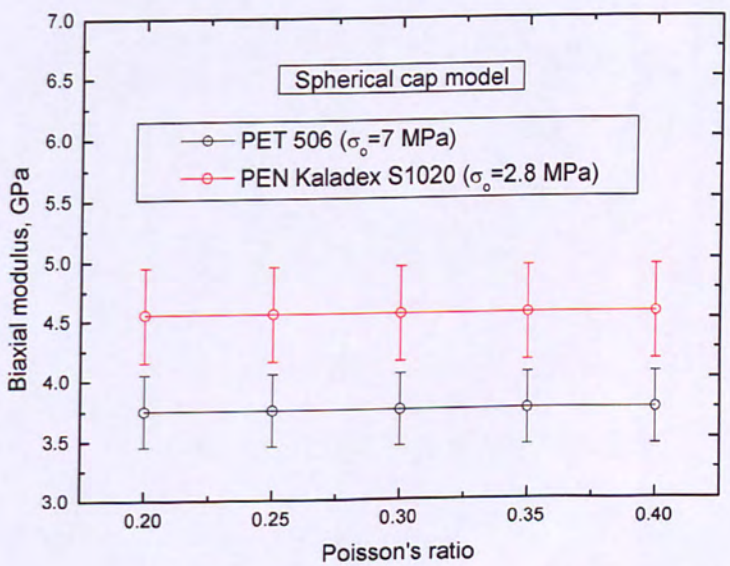

Figure 5.171: Comparison of biaxial moduli, against Poisson's ratio, of PET 506 and PEN Kaladex S1020 films, using the spherical cap model.

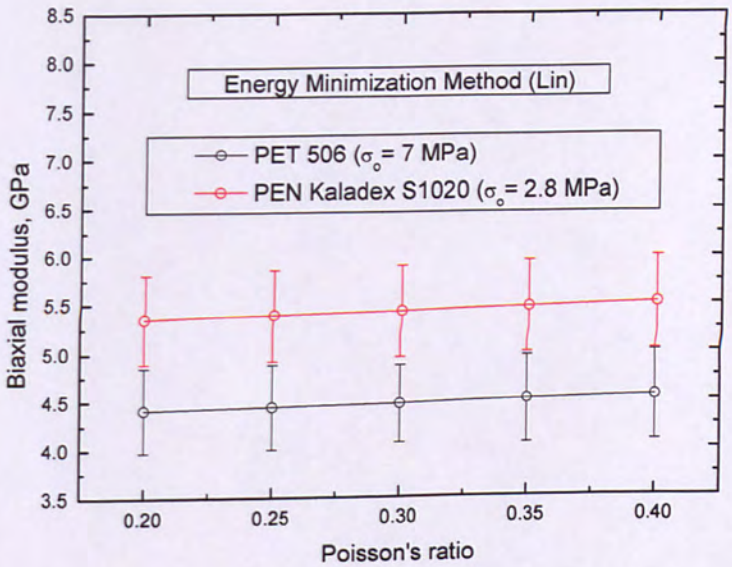

Figure 5.172: PET 506 and PEN Kaladex S1020 biaxial moduli comparison, plotted against Poisson's ratio, considering Lin's model.

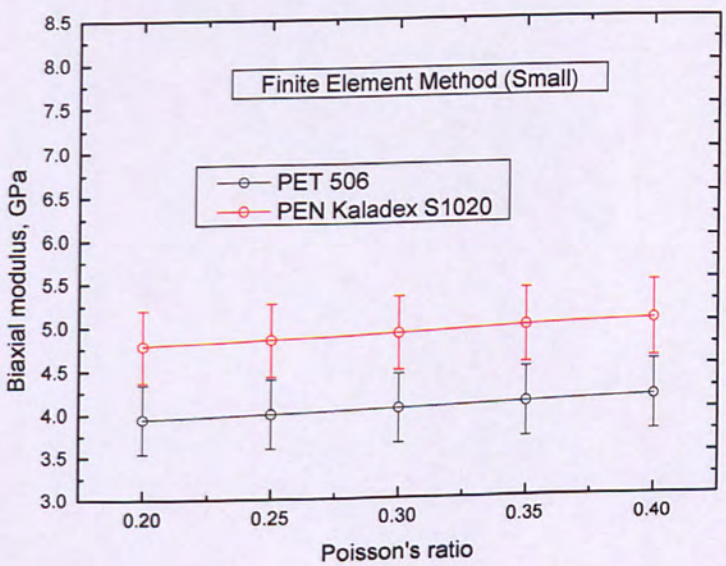

Figure 5.173: Biaxial moduli, against Poisson's ratio, for the case of PET 506 and PEN Kaladex S1020 substrates regarding Small's model.

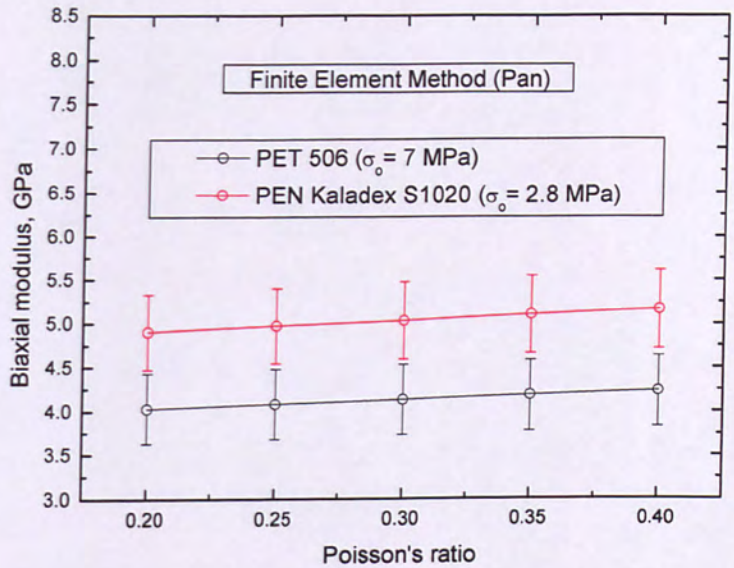

Figure 5.174: Comparison of PET 506 and PEN Kaladex S1020 biaxial moduli versus Poisson's ratio using Pan's model.

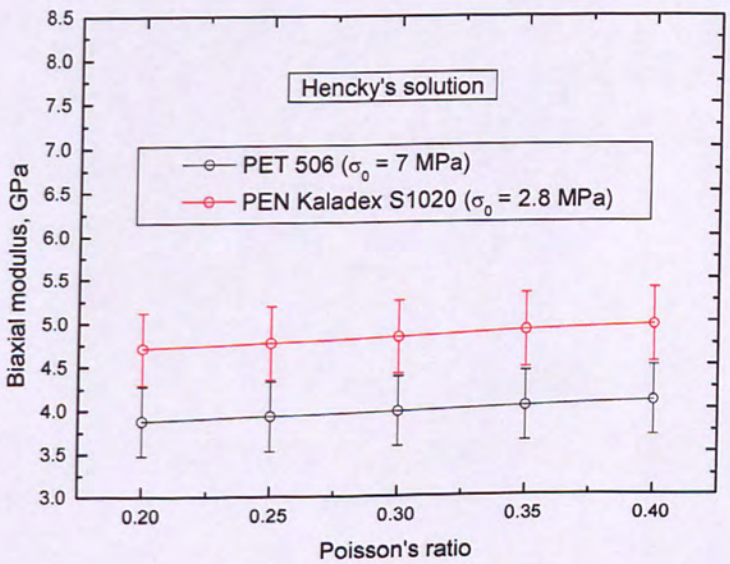

Figure 5.175: Biaxial moduli of PET 506 and PEN Kaladex S1020 substrates, against Poisson's ratio, using Henkcy's model.

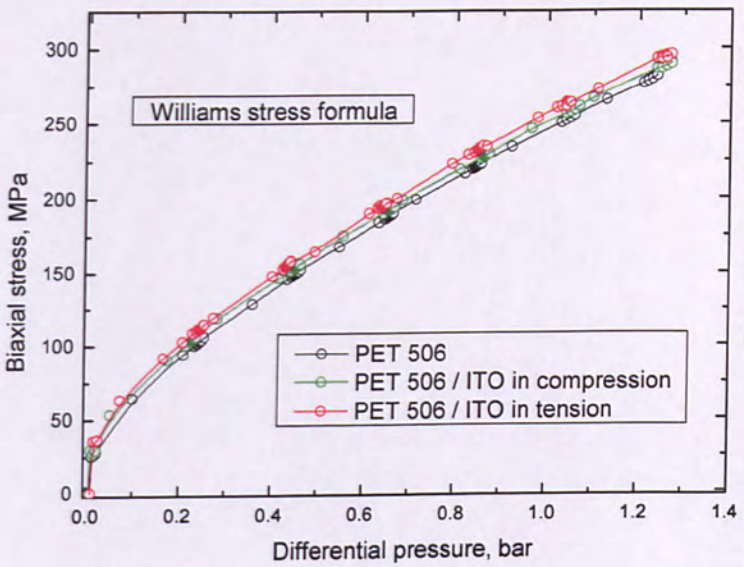

Figure 5.176: Biaxial stress versus differential applied pressure using Williams equation regarding uncoated and ITO coated PET 506.

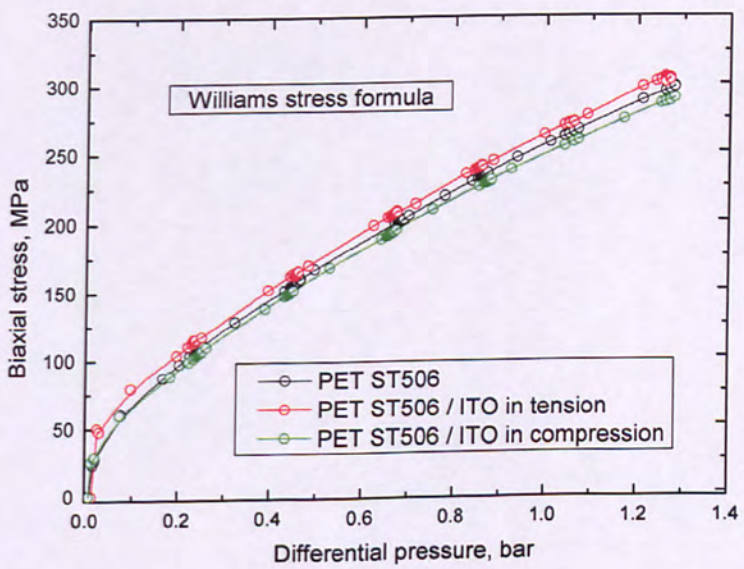

Figure 5.177: Biaxial stress versus differential applied pressure using Williams equation regarding uncoated and ITO coated PET ST506.

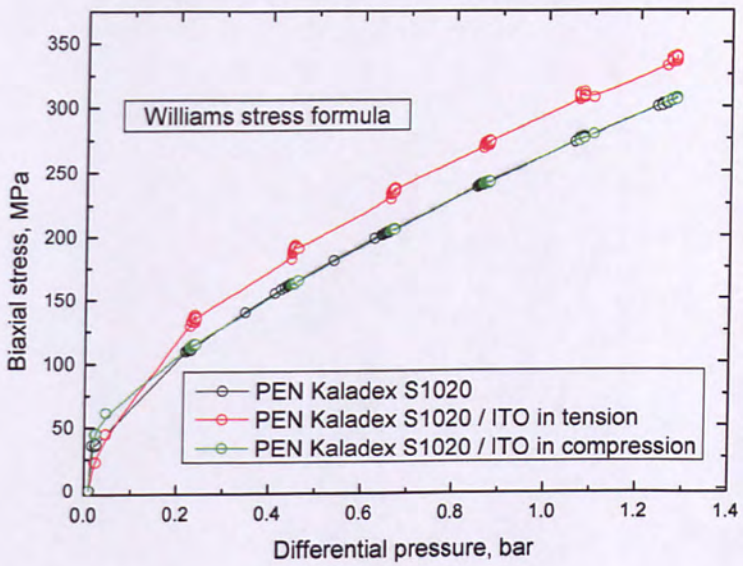

Figure 5.178: Biaxial stress versus differential applied pressure using Williams equation regarding uncoated and ITO coated PEN Kaladex S1020.

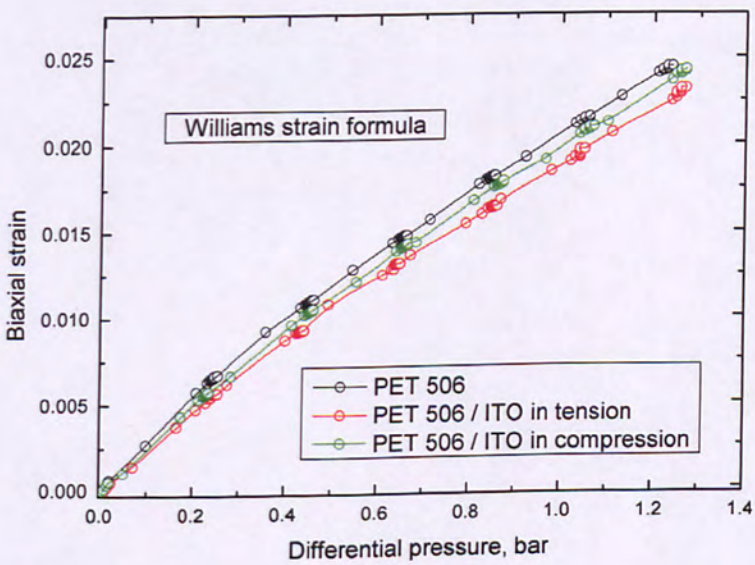

Figure 5.179: Mean biaxial strain against applied differential pressure obtained using Williams formula for uncoated and ITO coated PET 506 film substrates.

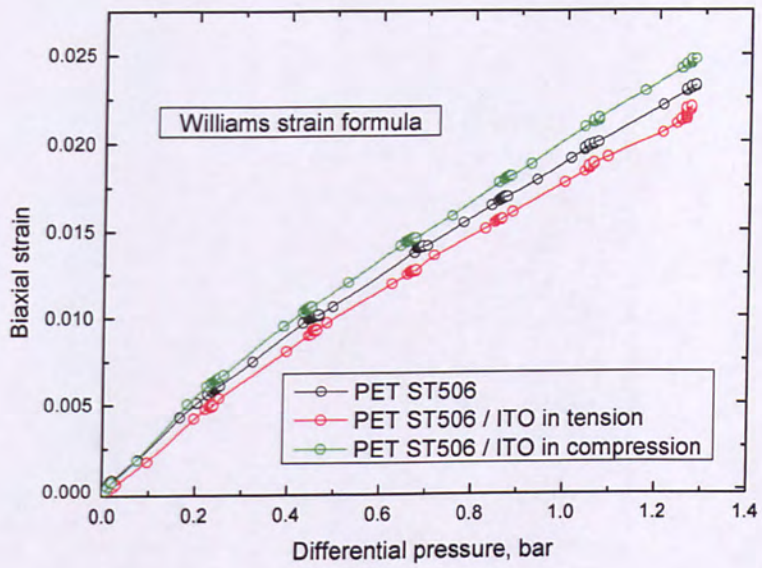

Figure 5.180: Mean biaxial strain against applied differential pressure obtained using Williams formula for uncoated and ITO coated PET ST506 film substrates.

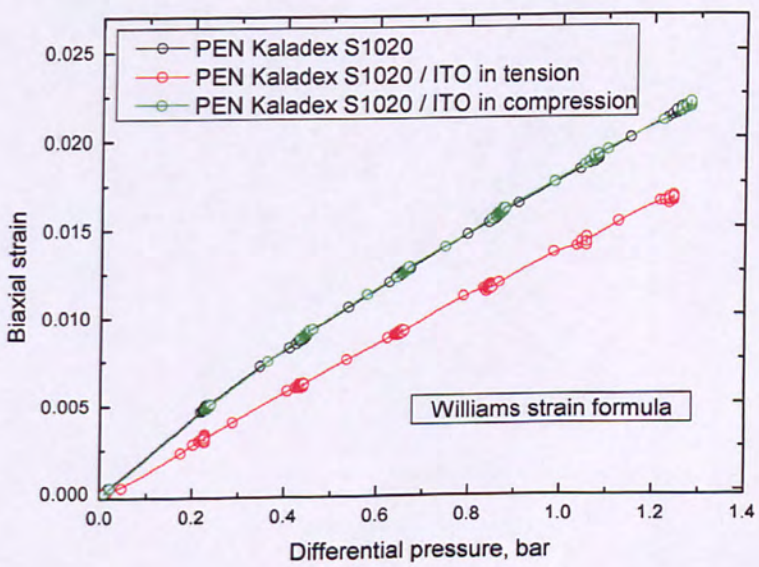

Figure 5.181: Mean biaxial strain against applied differential pressure obtained using Williams formula for uncoated and ITO coated PEN Kaladex S1020 film substrates.

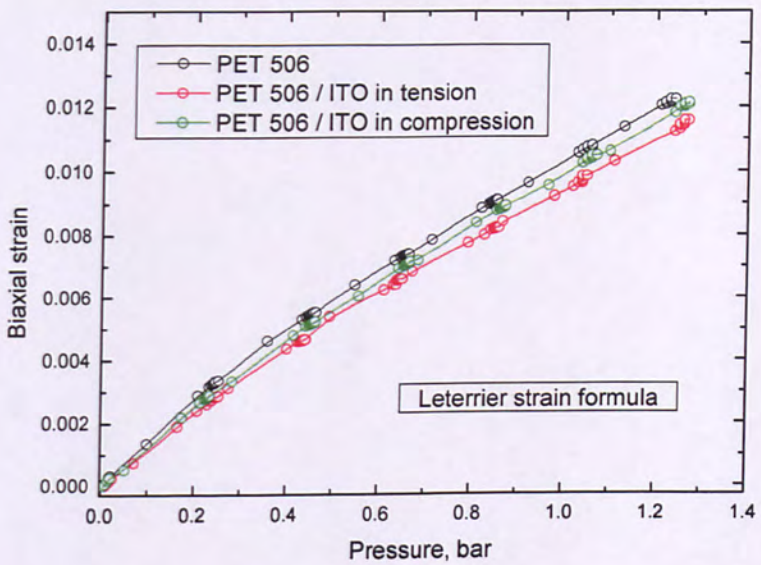

Figure 5.182: Mean biaxial strain against applied differential pressure obtained using Leterrier's formula for uncoated and ITO coated PET 506 film substrates.

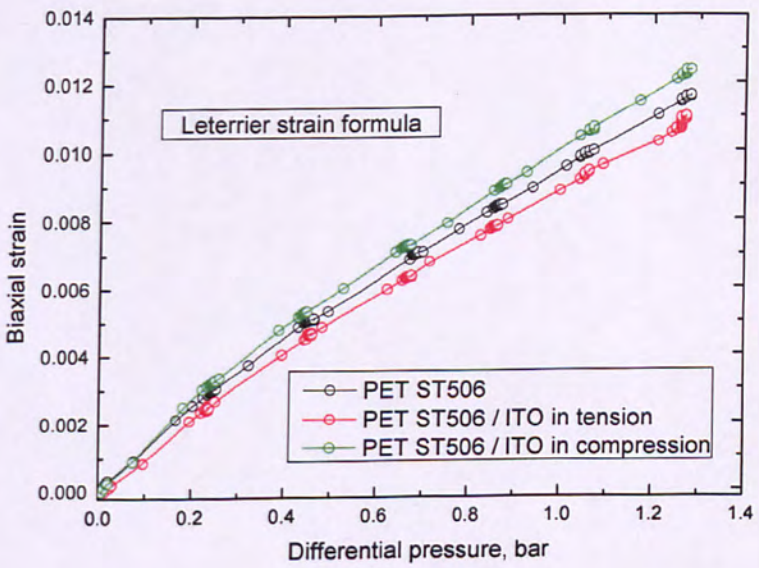

Figure 5.183: Mean biaxial strain against applied differential pressure obtained using Leterrier's formula for uncoated and ITO coated PET ST506 film substrates.

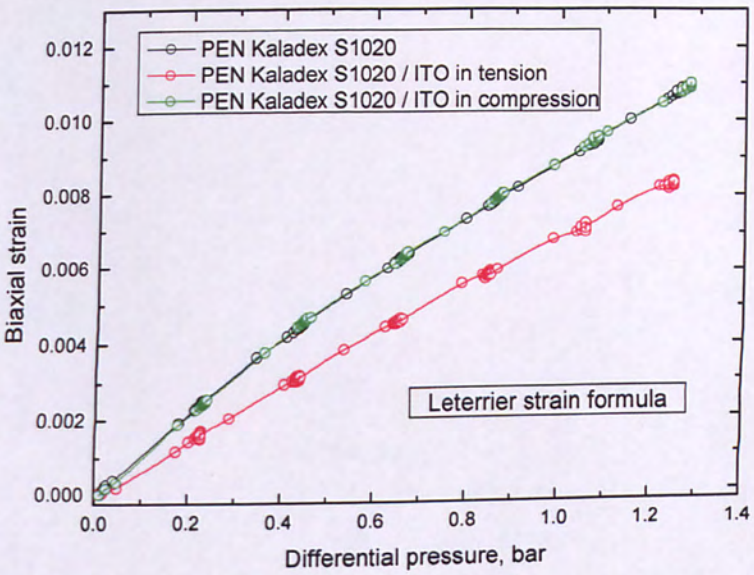

Figure 5.184: Mean biaxial strain against applied differential pressure obtained using Leterrier's formula for uncoated and ITO coated PEN Kaladex S1020 film substrates.

Appendix 6

(Figures and tables from Chapter 6)

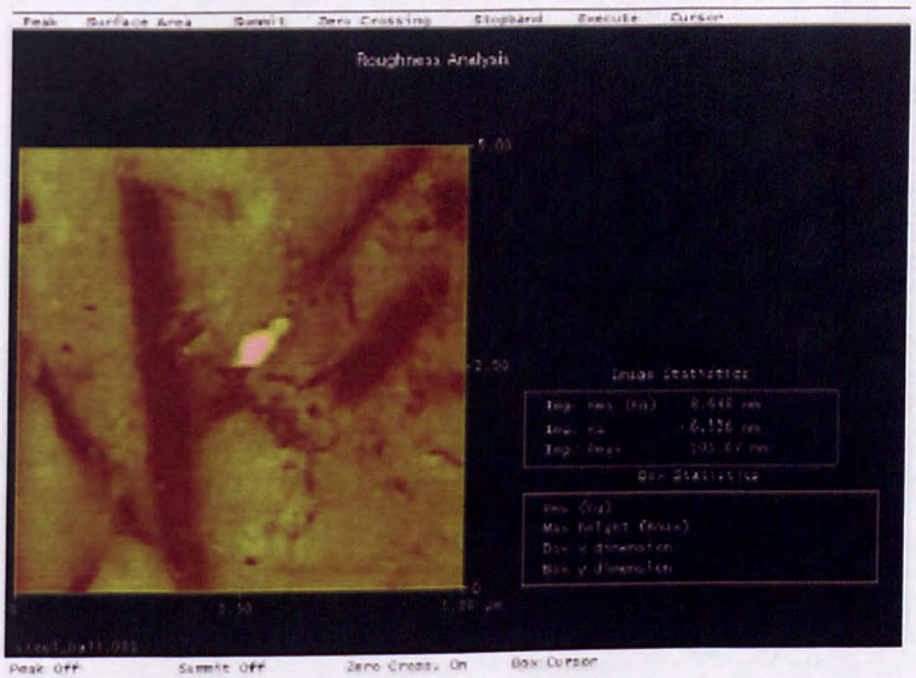

Figure 6.1: Contact – mode AFM image of a steel ball counterbody surface before testing.

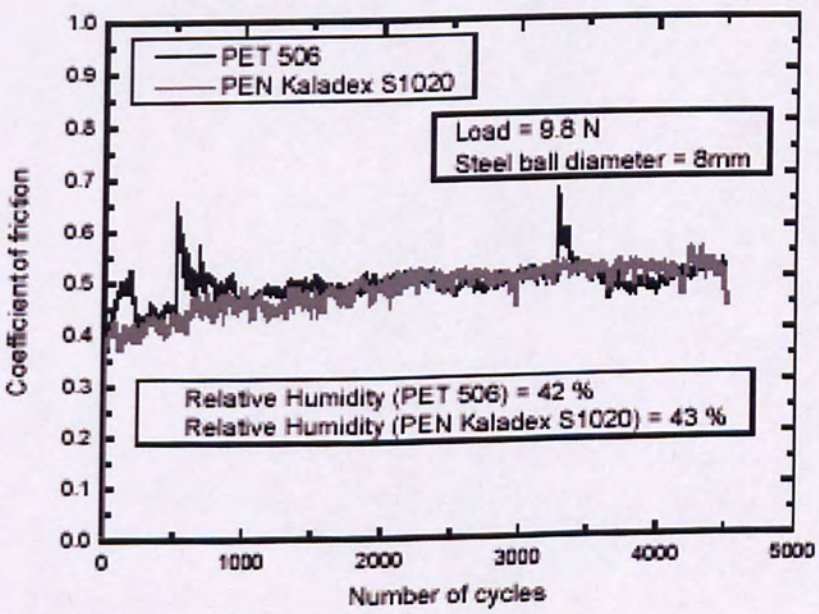

Figure 6.2: Coefficient of friction versus number of cycles for PET 506 and PEN Kaladex S1020 samples. Total number of cycles is 4500 and the normal load is 9.8 N.

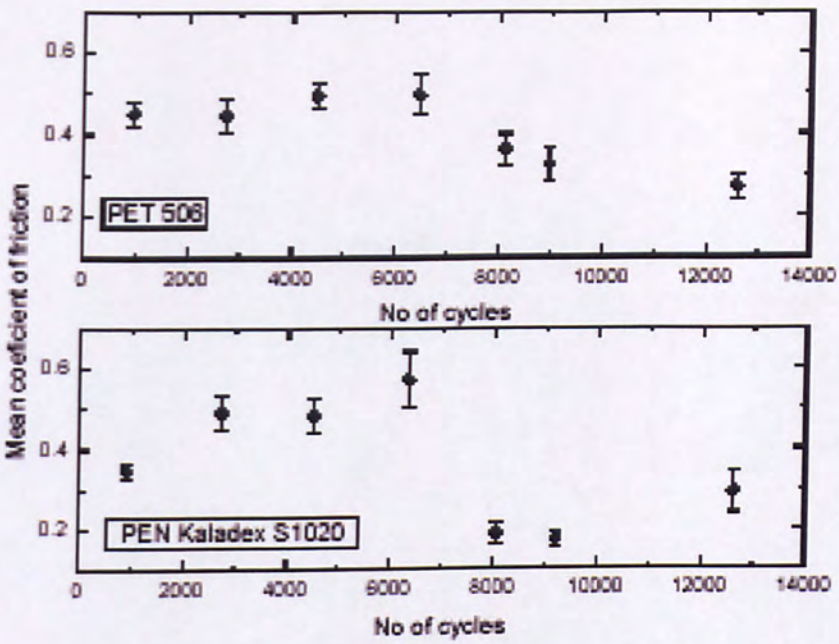

Figure 6.3: Mean coefficient of friction for PET 506, above, and PEN Kaladex S1020, below, against number of sliding cycles.

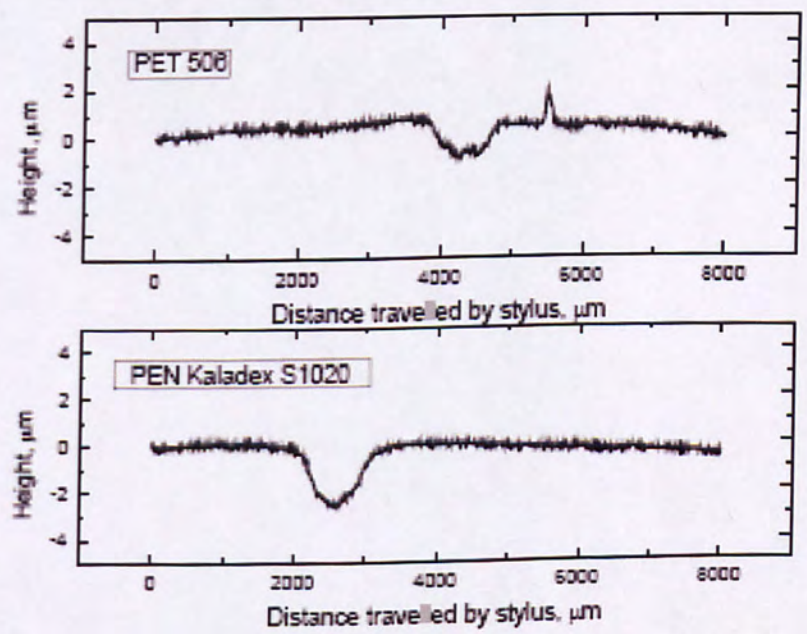

Figure 6.4: Typical wear track profiles measured by stylus profilometer for PET 506, above, and PEN Kaladex S1020, below, for 12600 cycles as measured by stylus profilometer.

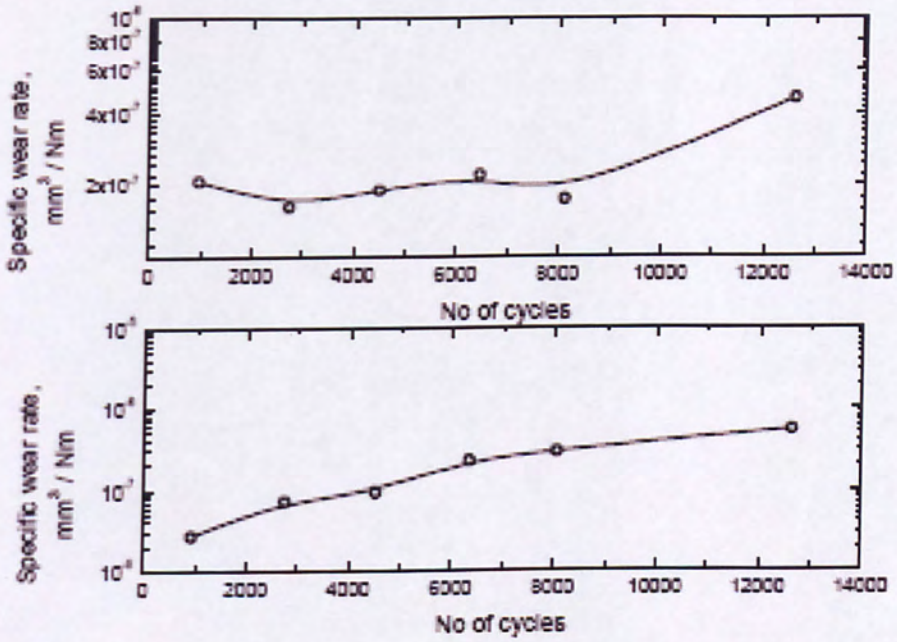

Figure 6.5: Specific wear rate versus number of sliding cycles for PET 506, above, and PEN Kaladex S1020, below.

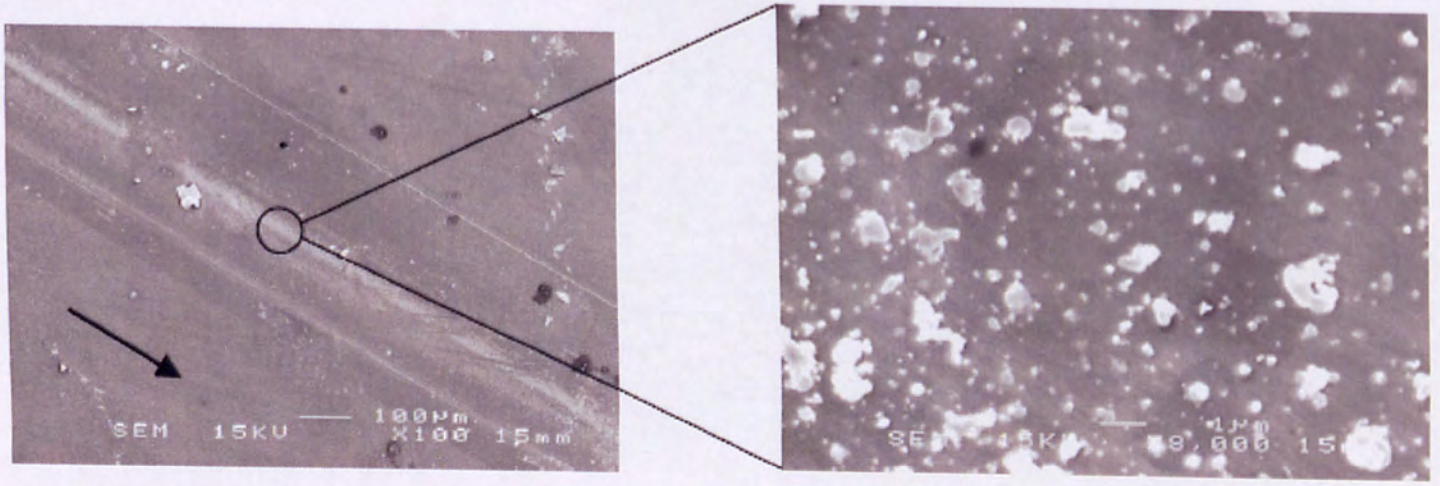

Figure 6.6: Low magnification SEM image, left, showing the wear track of PEN Kaladex S1020 tested against a steel ball for 925 cycles and high magnification image, right, of the centre of the wear track for the same sample. Arrow indicates the relative movement of the steel ball.

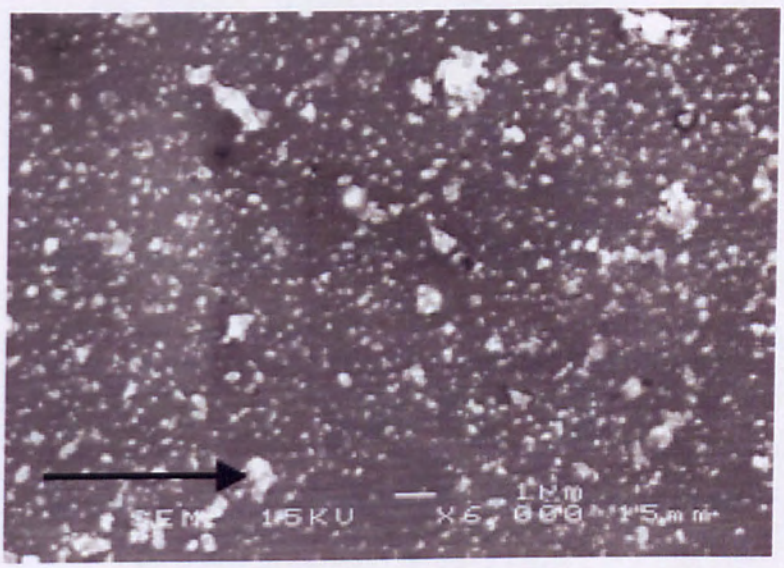

Figure 6.7: SEM image showing the wear track centre of PET 506 sliding against a steel ball for 965 cycles under a normal load of 9.8 N. Arrow indicate relative movement of steel ball.

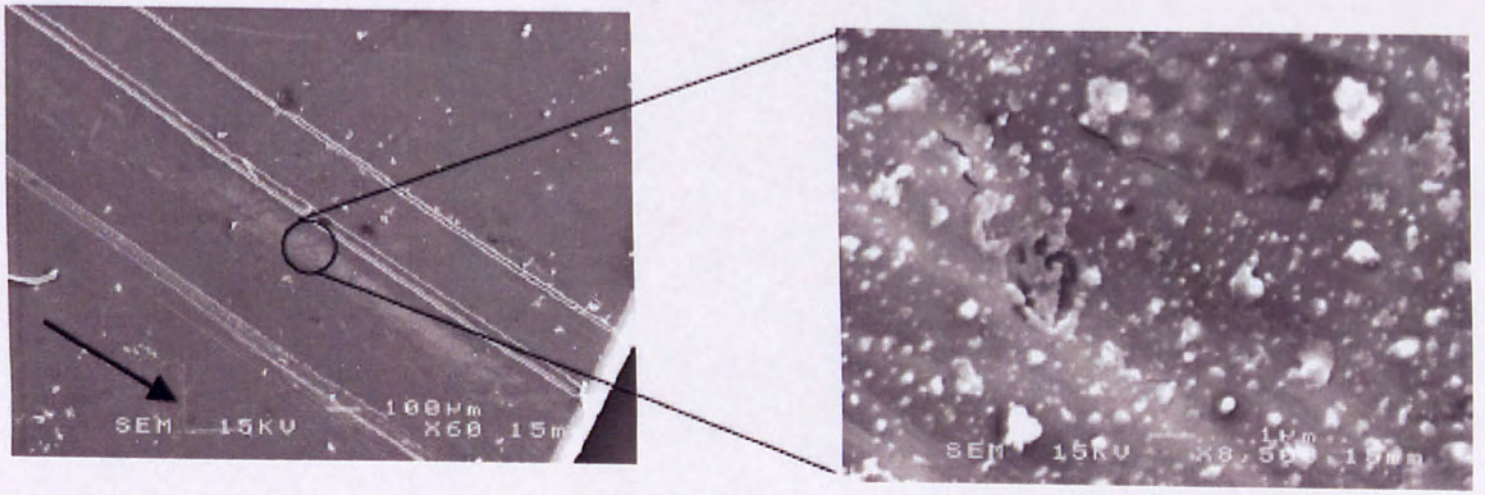

Figure 6.8: Low magnification SEM image, left, showing the wear track of PET 506 tested against a steel ball for 2740 cycles and high magnification image, right, of the centre of the wear track for the same sample. Arrow indicates the relative movement of the steel ball.

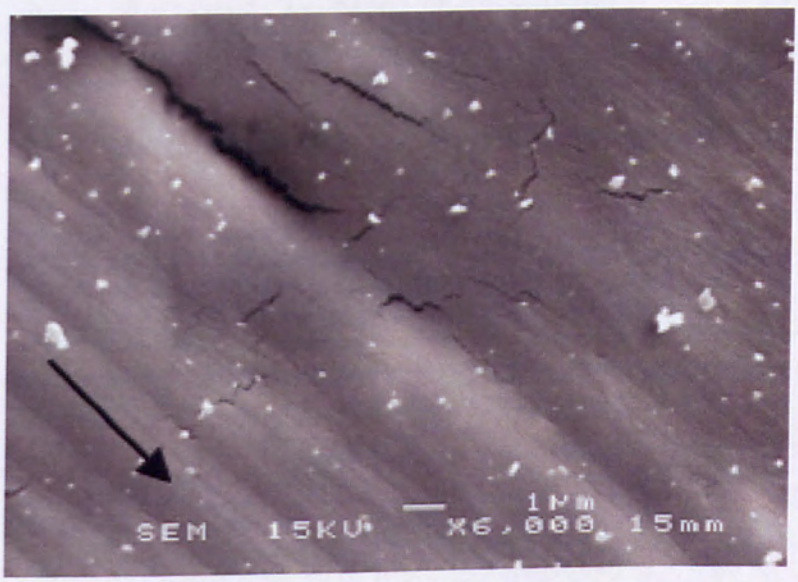

Figure 6.9: SEM micrograph showing the centre of the wear track in the case of PET 506 sliding against a steel ball for 4500 cycles. Arrow indicates the relative movement of steel ball.

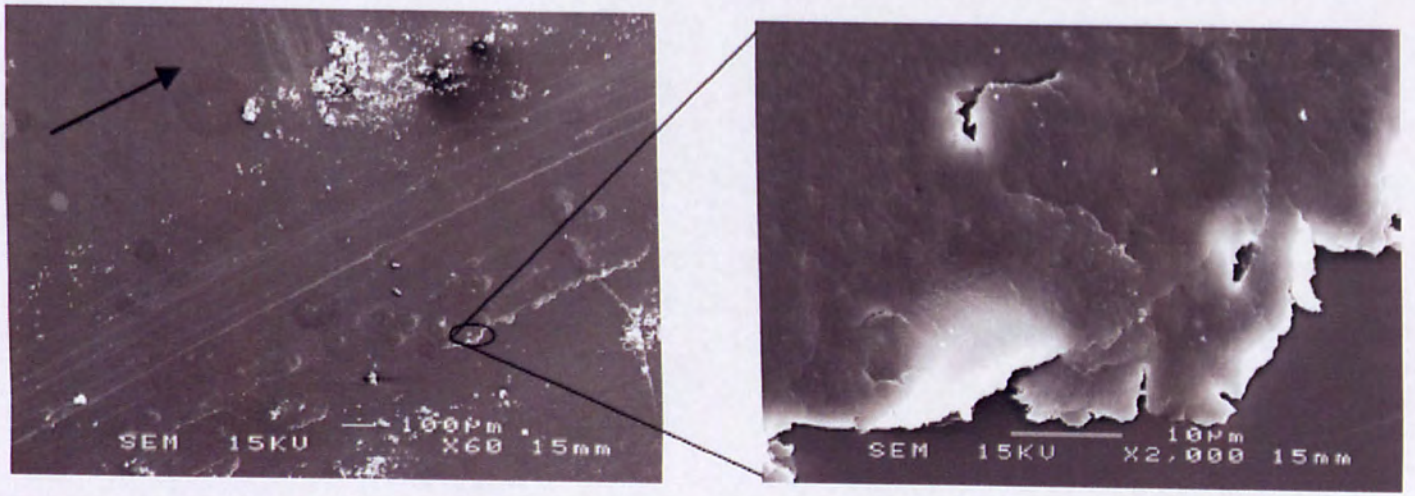

Figure 6.10: Low magnification SEM image, left, showing the wear track of PEN Kaladex S1020 tested against a steel ball for 4500 cycles and high magnification image, right, at the edge of the wear track for the same sample. Arrow indicates the relative movement of the steel ball.

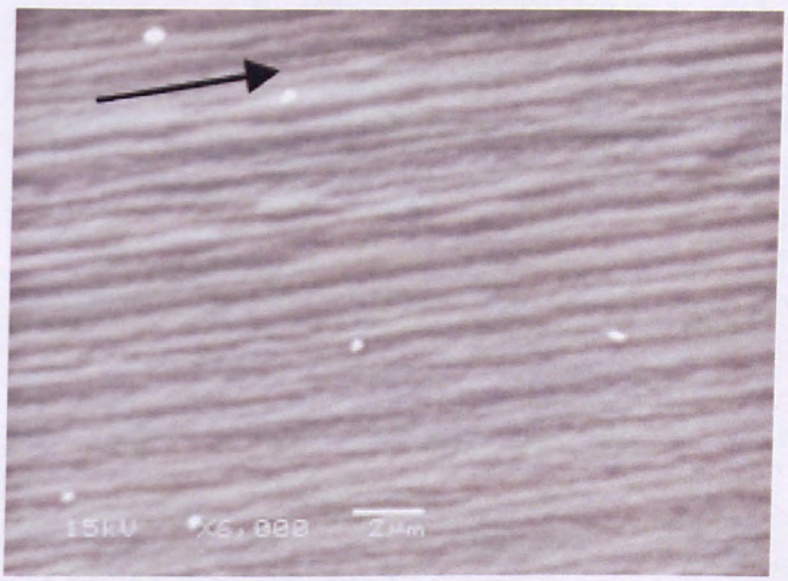

Figure 6.11: SEM image of the wear track centre for PEN Kaladex S1020 sliding against a smooth steel sphere for 8050 cycles. Arrow indicates the relative steel ball movement.

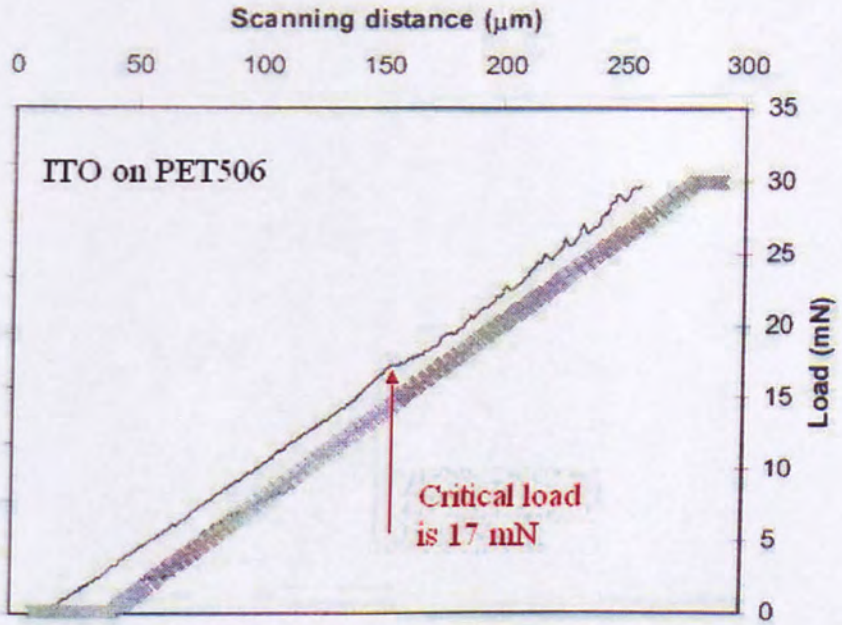

Figure 6.12: Load – distance scratching test graph of an ITO on PET 506 substrate.

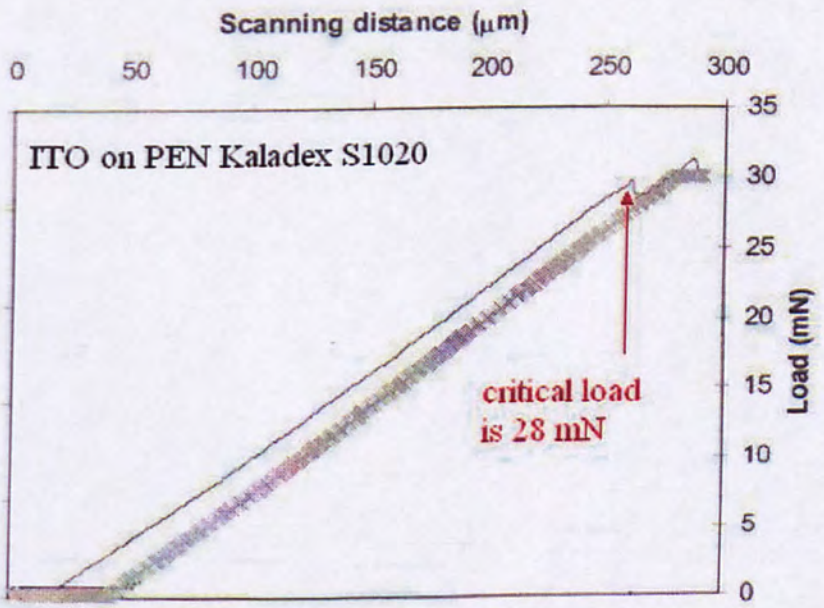

Figure 6.13: Load – distance scratching test graph of an ITO on PEN Kaladex S1020 substrate.

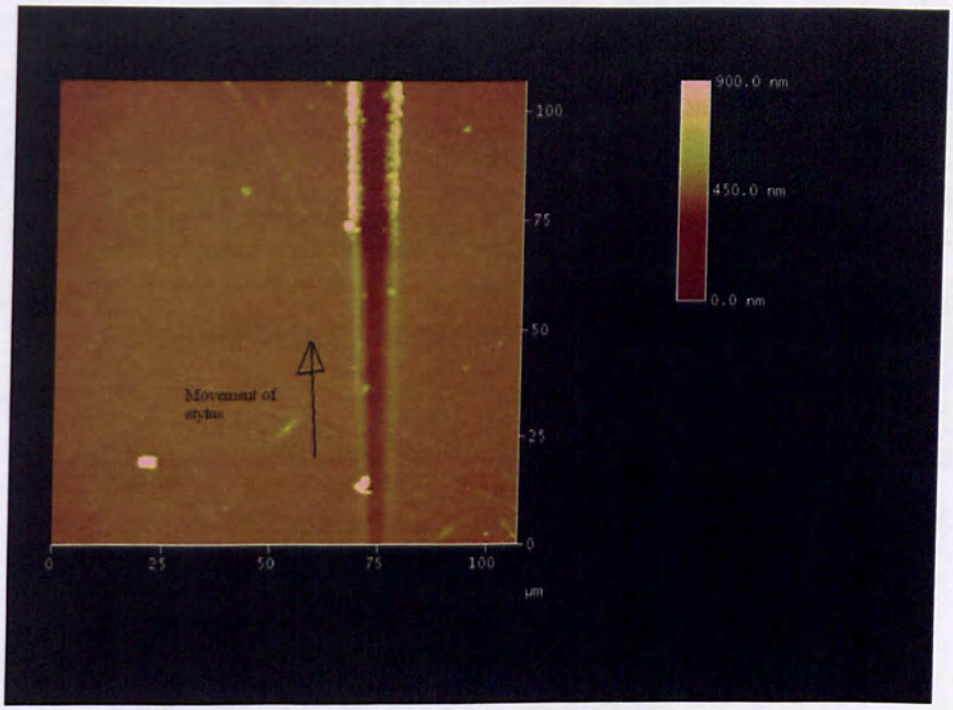

Figure 6.14: Contact – mode AFM image of a nano - scratched ITO, on PET 506, surface.

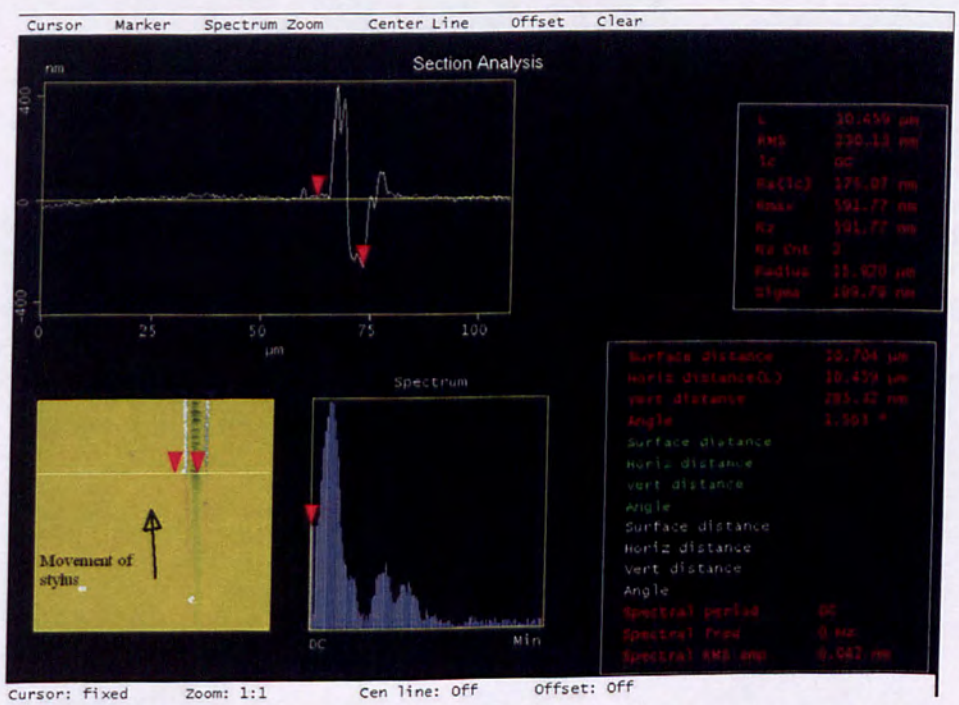

Figure 6.15: Contact – mode AFM cross - sectional measurement of a nano - scratched ITO, on PET 506, surface.

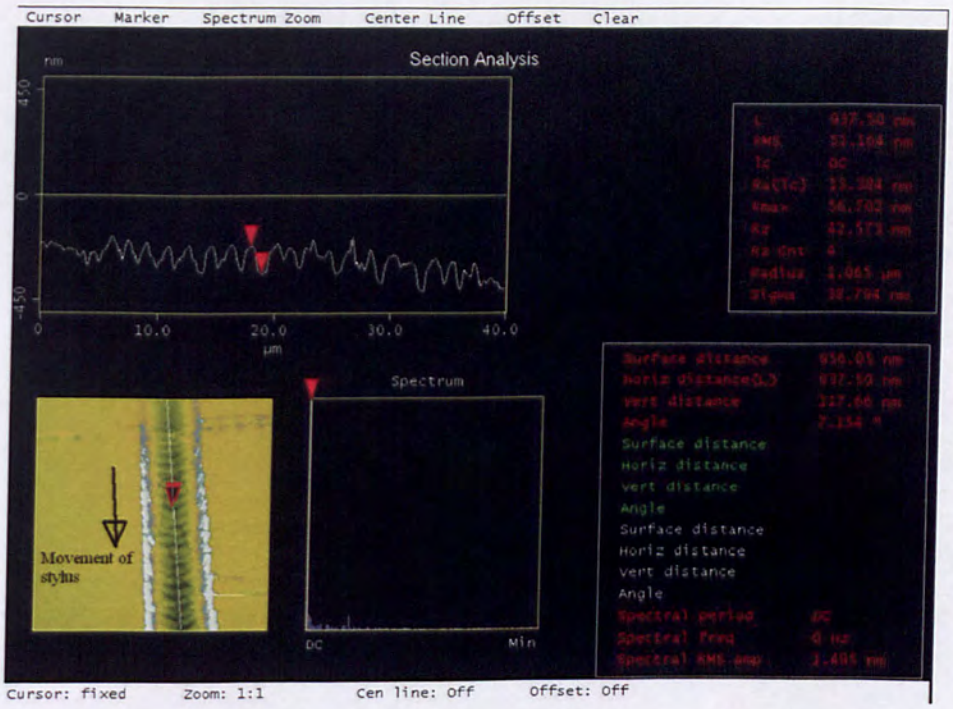

Figure 6.16: Contact – mode AFM cross - sectional measurement of a nano - scratched ITO, on PET ST506, surface.

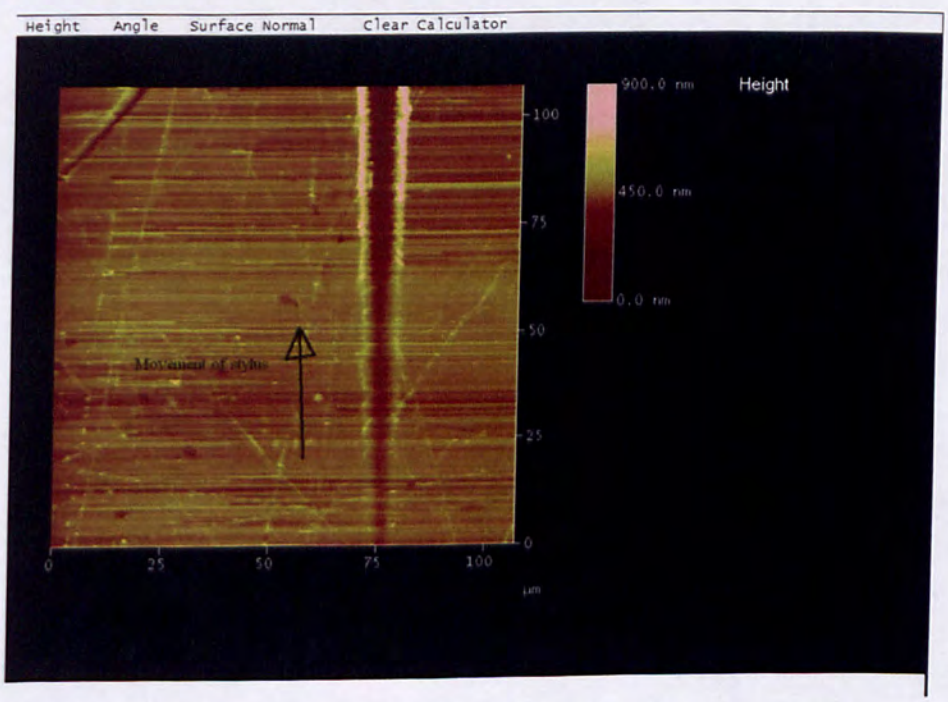

Figure 6.17: Contact – mode AFM image of a nano - scratched ITO, on PEN Kaladex S1020, surface.

Sample	*Critical load (mN)*
ITO on PET 506	17
ITO on PET ST506	14
ITO on PEN Kaladex S1020	28

Table 6.1: Critical ITO scratching loads for different flexible polyester substrates.

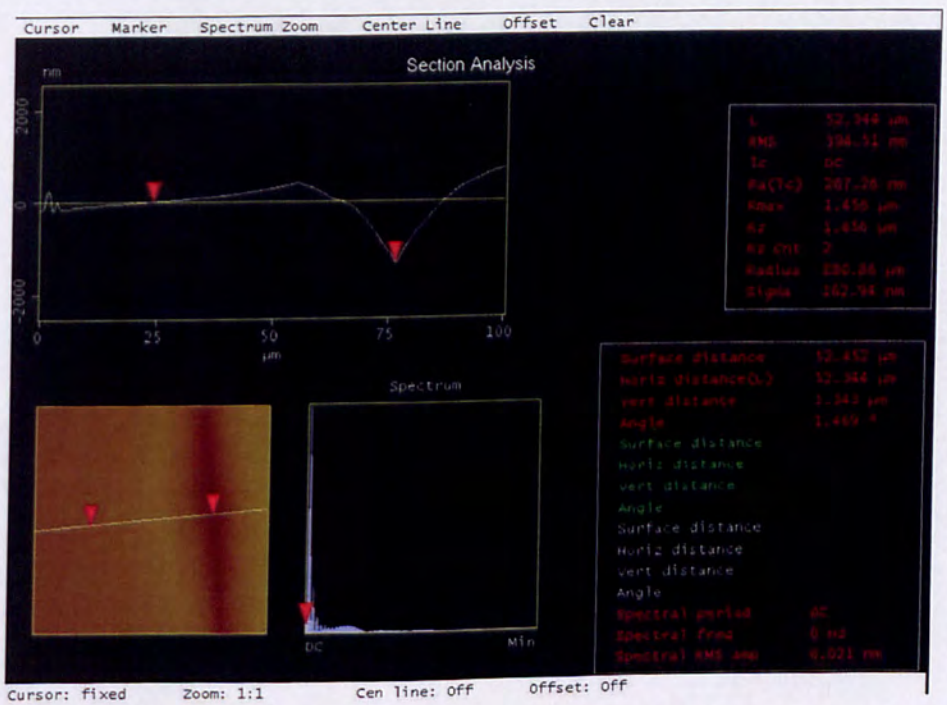

Figure 6.18: Contact – mode cross – sectional view of an ITO, on PET 506, nano – indented surface with 5 mN normal maximum load.

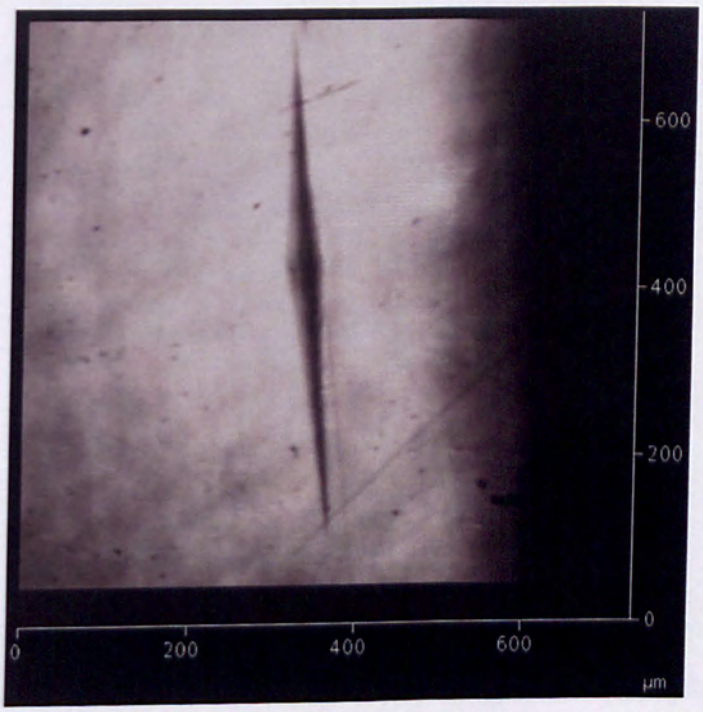

Figure 6.19: Optical micrograph of nanoindent of ITO on PEN Kaladex S1020.

Sample	*Maximum load 30 mN*		*Maximum load 5 mN*	
	Hardness, H (GPa)	E (GPa)	Hardness, H (GPa)	E (GPa)
PET 506	0.29 ± 0.00	2.51 ± 0.004	0.27 ± 0.003	2.51 ± 0.037
PET 506 / ITO	0.28 ± 0.004	2.96 ± 0.06	0.28 ± 0.004	2.83 ± 0.028
PEN Kaladex S1020	0.29 ± 0.00	2.98 ± 0.011	0.65 ± 0.007	4.32 ± 0.021
PEN K S1020 / ITO	0.29 ± 0.003	2.59 ± 0.019	0.56 ± 0.009	4.03 ± 0.032
PET ST506	0.29 ± 0.004	2.85 ± 0.013	0.54 ± 0.003	3.75 ± 0.017
PET ST506 / ITO	0.29 ± 0.00	2.91 ± 0.003	0.54 ± 0.003	4.14 ± 0.013

Table 6.2: Hardness values and Young modulus values, measured by nanoindentation, for ITO coated and uncoated polyester substrates.